

The Pennsylvania State University
The Graduate School
Department of Aerospace Engineering

NUMERICAL SIMULATION OF A CONFINED SUPERSONIC
SHEAR LAYER

A Thesis in
Aerospace Engineering
by
Dale A. Hudson

Submitted in Partial Fulfillment
of the Requirements
for the Degree of

Doctor of Philosophy

August 1996

We approve the thesis of Dale A. Hudson.

Date of Signature

Lyle N. Long
Associate Professor of Aerospace Engineering
Thesis Co-Adviser
Chair of Committee

Philip J. Morris
Boeing Professor of Aerospace Engineering
Thesis Co-Adviser

Vigor Yang
Professor of Mechanical Engineering

Dennis K. McLaughlin
Professor of Aerospace Engineering
Head of the Department of Aerospace Engineering

Abstract

Numerical simulations of confined supersonic shear layers have been conducted using advanced massively parallel computing systems and a high performance scientific programming language. The fundamental capability sought was the ability to model the steady and unsteady behavior of confined compressible shear layer mixing, at least to within the conventional guidelines for the resolution of important physical phenomena. The overall objective was fully achieved.

The development of the software was accomplished on a combination of a CM-200a situated at Penn State, the Numerical Aerodynamic Simulation Program's CM-5 at NASA Ames, and the National Center for Supercomputing Application's CM-5 at the University of Illinois at Urbana-Champaign. A system specific version of High Performance Fortran, CM Fortran, was used to code the software. The Euler equations were integrated with the MacCormack 2-4 numerical scheme applied over a Cartesian grid. Several new developments such as a modified Jameson Artificial Viscosity scheme, a new spatial extrapolation scheme, and new unsteady inlet boundary conditions, resulted in excellent comparison with experimental data. The supersonic shear layers were simulated using dense grids to provide a fine-grain resolution of the mixing layer. Grid densities were chosen to resolve the fundamental Kelvin-Helmholtz instability mode and the very thin shear layer near the inlet. The fine grain solutions utilize approximately 200,000 grid points in the 2-D cases and 5,250,000 grid points in the 3-D case.

Two compressible mixing layers were simulated and compared to experimental data collected under a separate effort. Similarly, single frequency excitation simulations were made to provide comparisons with linear stability theory. Both shear layers have moderate Reynolds numbers ($Re_{y_{\delta_w}}$) of 6600 and 9500, and have convective Mach numbers of 0.5 and 0.64, respectively. Excellent agreement between the two-dimensional simulation and experimental results were obtained for the mean velocity profiles, FFT spectra, shear layer growth rate, momentum fluctuation quantities and the Reynolds stresses. Examination of instantaneous and time-averaged field variables provided informative insight into; shear layer growth rate behavior, double peaked turbulence intensity profiles that are commonly

observed in experimental data, and shear layer excitation by standing Mach waves reflected from the confining channel walls.

TABLE OF CONTENTS

LIST OF FIGURES	vi
LIST OF TABLES	vii
Acknowledgments	viii
1 Introduction	1
1.1 Objectives and Overview	1
1.2 Background	2
1.3 Parallel Computing	7
1.4 The Simulation	12
1.5 Scope and Outline	16
2 Mathematical Formulation	19
2.1 Governing Equations	19
2.2 Boundary Conditions	21
2.2.1 Steady Boundary Conditions	23
2.2.2 Unsteady Boundary Conditions	26
2.2.3 Linear Theory Eigenfunctions	30
3 Numerical Formulation	33
3.1 MacCormack 2-4 Method	33
3.2 Artificial Viscosity	37
3.2.1 Modified Jameson	37
3.2.2 High Order Sankar Damping	38
3.3 Grid	39
3.4 Boundary Conditions	43
3.4.1 Unsteady Inflow	43
3.4.2 Wall Conditions	45

3.4.3	Outflow Conditions	45
3.4.4	Ghost Cell Determination	46
4	Shear Layer Single Frequency Excitation	52
4.1	Dynamics	52
4.1.1	Frequency Behavior and Auto-spectra	54
4.2	Time-averaged Behavior	55
4.2.1	Shear Layer Growth	55
4.2.2	Instantaneous Results	55
4.2.3	Time Averaged Results	56
5	Shear Layer Simulation Case I: $M_c = 0.5$	69
5.1	Dynamics	69
5.1.1	Frequency Behavior and Auto-spectra	71
5.2	Instantaneous and Time-averaged Behavior	77
5.2.1	Shear Layer Growth	77
5.2.2	Instantaneous Results	84
5.2.3	Time Averaged Results	94
5.2.4	Special Topics	114
5.3	Three-dimensional Simulation of Case I	119
5.3.1	Dynamics	120
5.3.2	Instantaneous and Time-averaged Behavior	122
6	Shear Layer Simulation Case II: $M_c = 0.64$	139
6.1	Dynamics	139
6.1.1	Frequency Behavior and Auto-spectra	139
6.2	Time-averaged Behavior	142
6.2.1	Shear Layer Growth	142
6.2.2	Instantaneous Results	144
6.2.3	Time Averaged Results	145
7	Conclusions	157
7.1	Objectives	157

7.2	Numerical Methods	158
7.3	Simulation Physical Phenomena	160
7.4	Directions for Future Research	161
A	Von Neumann Stability Analysis	164
A.0.1	Convection Equation	165
A.0.2	Diffusion Equation	167
A.0.3	Convection-Diffusion Equation	169
	References	174

LIST OF FIGURES

1.1	CM-5 at NCSA, University of Illinois Urbana-Champaign.	8
1.2	Variation of computing speed with number of processing nodes for a fixed size problem.	11
1.3	Variation of computing speed as the number of grid points and the number of processing nodes are successively doubled.	11
1.4	Experimental test section	15
1.5	Two-dimensional computational domain schematic; physical 0.56x0.055 meters, grid 768x256.	16
2.1	Case I $M_c = 0.5$: The experiment velocity profile at 0.02 m and the simulation inlet boundary mean velocity profile at 0. m	24
2.2	Unsteady Boundary: Random Disturbance Effect on a Sinusoidal Unsteady Condition; a) Zero Degrees Disturbance, b) One Degree Disturbance, and c) Six Degrees Disturbance.	30
2.3	Rayleigh Equation Eigenfunctions at the Inlet for Case I, $M_c = 0.5$ Conditions; a) Axial Velocity m/s , b) Transverse Velocity m/s , c) Density kg/m_3 , and d) Pressure Pa	32
3.1	Amplification and Phase Error Behaviors of the MacCormack 2-4 Method applied to the convection model equation. Behaviors for two CFL numbers (λ) 2/3 and 1/4 are shown.	34
3.2	Interior, Boundary, and Ghost Cell Locations.	37
3.3	Wave number relation for Fourier transform of the fourth order central scheme	41
3.4	Ghost cell modeling past a change in slope of a sine function. The solid line and the squares are an exact sine curve. The two triangle points are extrapolated.	49
3.5	Density field exit plane with ghost cells. Flow direction is left to right. . . .	50

4.1	Rayleigh Equation Eigenfunctions for 25,000 Hz Disturbance at the Inlet for Case I $M_c = 0.5$ Conditions a) Axial Velocity m/s b) Transverse Velocity m/s c) Density kg/m^3 , b) and d) Pressure Pa	53
4.2	Total Mass Flux Unsteadiness $(\rho V)'$ at $X = 0.18$ m: a) FFT spectra and b) Auto-spectra.	54
4.3	Comparison of numerical shear layer growth rates, vorticity δ_ω , momentum 4θ . and boundary layer δ_{98}	56
4.4	Shear Layer Development Comparison for Single Frequency Excitations . .	57
4.5	Conservative Variable Density ρ (kg/m^3) a) Instantaneous Density, b) Time Averaged Density Field, and c) Cross Channel Density Profiles at $X = .12m$, $.20m$, $.28m$, and $.36m$	58
4.6	Conservative Variable Axial Mass Flux ρu (kg/sm^2) a) Instantaneous Mass Flux, b) Time Averaged Mass Flux Field, and c) Cross Channel Mass Flux Profiles at $X = .12m$, $.20m$, $.28m$, and $.36m$	59
4.7	Conservative Variable Transverse Mass Flux ρv (kg/sm^2) a) Instantaneous Mass Flux, b) Time Averaged Mass Flux Field, and c) Cross Channel Mass Flux Profiles at $X = .12m$, $.20m$, $.28m$, and $.36m$	60
4.8	Conservative Variable Total Energy ρe_t ($Joule/m^2$) a) Instantaneous Total Energy, b) Time Averaged Total Energy Field, and c) Cross Channel Total Energy Profiles at $X = .12m$, $.20m$, $.28m$, and $.36m$	61
4.9	Single Frequency 25 kHz Axial Mass Flux Flux Perturbation $\overline{(\rho u)'}'$: a) RMS Mass Flux Perturbation and b) Cross Channel Profiles at $X = .12m$, $.20m$, $.28m$, and $.36m$	63
4.10	Single Frequency 25 kHz Transverse Mass Flux Perturbation $\overline{(\rho v)'}'$: a) RMS Transverse Mass Flux Field and b) Cross Channel Profiles at $X = .12m$, $.20m$, $.28m$, and $.36m$	64
4.11	Single Frequency 25 kHz Time Averaged Reynolds Stress $\overline{\rho u'v'}$: a) Time-averaged Reynolds Stress Field, and b) Cross Channel Profiles at $X = .12m$, $.20m$, $.28m$, and $.36m$	65

4.12	RMS Perturbation Axial Growth Evolution for 25 kHz; Martens $\frac{(\rho u)'}{\rho u}$, Lockard PSE Normalized p' , and Single Frequency Excited Numerical Simulation p'/p_{mean} , Hudson $\frac{(\rho u)'}{\rho u}$	67
4.13	RMS Perturbation Growth Profile for 25 kHz at 0.28 m; Martens $\frac{(\rho u)'}{\rho u}$, Lockard PSE Normalized p' , Single Frequency Excited Numerical Simulation p'/p_{mean} , and Simulation $\frac{(\rho u)'}{\rho u}$	68
5.1	Unsteady Inlet Perturbation, $(\rho V)'$, Behavior: a) FFT Spectra and b) Auto-spectra.	72
5.2	FFT Spectra of the Total Mass Flux Unsteadiness $(\rho V)'$ at X = 0.18 m. . .	73
5.3	Auto-spectra of the Total Mass Flux Unsteadiness at X = 0.18 m: a) Simulation and b) Experimental.	74
5.4	Normalized Auto-spectra of the Total Mass Flux Unsteadiness at X = 0.18 m.	75
5.5	FFT Spectra of the Total Mass Flux Unsteadiness $(\rho V)'$ at X = 0.27 m. . .	76
5.6	Auto-spectra of the Total Mass Flux Unsteadiness at X = 0.27 m: a) Simulation and b) Experimental	78
5.7	Normalized Auto-spectra of the Total Mass Flux Unsteadiness at X = 0.27 m.	79
5.8	Comparison of numerical and experimental shear layer thicknesses, vorticity δ_ω , momentum 4θ , boundary layer δ_{98} , and experimentally determined vorticity.	80
5.9	Comparison of Numerical and Experimental Mean Velocity Profiles at X=0.44 m.	82
5.10	Normalized growth rates correlated with convective Mach number.	84
5.11	Instantaneous Descriptive Flow Parameters; a) Density Gradient Field, and b) Vorticity Field.	85
5.12	Instantaneous Density Field: a) Two-dimensional contour and b) Carpet plot.	89
5.13	Instantaneous Axial Mass Flux Field: a) Two-dimensional contour and b) Carpet plot.	90
5.14	Instantaneous Transverse Mass Flux Field: a) Two-dimensional contour and b) Carpet plot.	91
5.15	Close-up of the Instantaneous Transverse Mass Flux Field: a) Two-dimensional contour and b) Carpet plot.	92

5.16	Instantaneous Total Energy Flux Field: a) Two-dimensional contour and b) Carpet plot.	93
5.17	Conservative Variable Density ρ (kg/m^3) a) Instantaneous Density, b) Time Averaged Density Field, and c) Cross Channel Density Profiles at X = .12m, .20m, .28m, and .36m.	96
5.18	Conservative Variable Axial Mass Flux ρu (kg/sm^2) a) Instantaneous Mass Flux, b) Time Averaged Mass Flux Field, and c) Cross Channel Mass Flux Profiles at X = .12m, .20m, .28m, and .36m.	97
5.19	Conservative Variable Transverse Mass Flux ρv (kg/sm^2) a) Instantaneous Mass Flux, b) Time Averaged Mass Flux Field, and c) Cross Channel Mass Flux Profiles at X = .12m, .20m, .28m, and .36m.	98
5.20	Conservative Variable Total Energy Flux ρe_t ($Joule/m^2$) a) Instantaneous Total Energy, b) Time Averaged Total Energy Field, and c) Cross Channel Total Energy Profiles at X = .12m, .20m, .28m, and .36m.	99
5.21	Axial Variation of Numerical Time averaged Velocity Profiles	101
5.22	Comparison of Numerical and Experimental Mean Velocity Profiles; a) X=0.12 m, b) X=0.16 m, c) X=0.20 m d) X=0.24 m.	102
5.23	Comparison of Numerical and Experimental Mean Velocity Profiles; a) X=0.268 m, b) X=0.353 m, c) X=0.40 m d) X=0.44 m.	103
5.24	Numerical and experimental r.m.s. fluctuations $\frac{(\rho u)'_{rms}}{(\rho u)_{local}}$	105
5.25	Case I $M_c = 0.5$ Simulation and Experimental Auto-spectra at 0.18 m Location	106
5.26	Case I $M_c = 0.5$ RMS Mass Flux Perturbation $(\rho V)'$: a) Broadband Excited Simulation, b) Naturally Excited Experimental, c) 25 kHz Single Frequency Excited Simulation, and d) 25 kHz Single Frequency Excited Experiment.	109
5.27	Case I $M_c = 0.5$ Shear Layer Thickness Growth.	110
5.28	Case I $M_c = 0.5$ Axial Mass Flux Perturbation $\overline{(\rho u)'}'$: a) RMS Mass Flux Perturbation and b) Cross Channel Profiles at X = .12m, .20m, .28m, and .36m.	111
5.29	Case I $M_c = 0.5$ Transverse Mass Flux Perturbation $\overline{(\rho v)'}'$: a) RMS Transverse Mass Flux Field and b) Cross Channel Profiles at X = .12m, .20m, .28m, and .36m.	112

5.30	Case I $M_c = 0.5$ Time Averaged Reynolds Stress $\overline{\rho u'v'}$: a) Time averaged Reynolds Stress Field, and b) Cross Channel Profiles at $X = .12\text{m}$, $.20\text{m}$, $.28\text{m}$, and $.36\text{m}$	113
5.31	Shear Layer Velocity Field in Two Frames of Reference a) Convective Frame of Reference, b) Transverse Velocity Field v in Stationary frame of Reference.	116
5.32	Isentropic and Non-Isentropic Contributions to the Density Perturbations; a) Density perturbation from the Mean density field, b) Isentropic Pressure contribution, and c) Non-Isentropic processes contributions.	118
5.33	Three-dimensional Total Mass Flux Unsteadiness $(\rho V)'$ at $X = 0.30$ m: a) FFT spectra and b) auto-spectra	121
5.34	Three-dimensional Spanwise Mass Flux Unsteadiness $(\rho w)'$ at $X = 0.30$ m: a) FFT magnitude and b) auto-spectra	123
5.35	Comparison of three-dimensional shear layer growth rates, vorticity δ_ω , momentum 4θ , boundary layer δ_{98} , and experimentally determined vorticity thickness.	124
5.36	Three-dimensional normalized growth rates correlated with convective Mach number	125
5.37	Three-dimensional Instantaneous Descriptive Flow Parameters; a) Density Gradient Field, and b) Vorticity Field.	126
5.38	Conservative Variable Density ρ (kg/m^3) a) Instantaneous Density, b) Time Averaged Density Field, and c) Cross Channel Density Profiles at $X = .12\text{m}$, $.20\text{m}$, $.28\text{m}$, and $.36\text{m}$	128
5.39	Conservative Variable Axial Mass Flux ρu (kg/sm^2) a) Instantaneous Mass Flux, b) Time Averaged Mass Flux Field, and c) Cross Channel Mass Flux Profiles at $X = .12\text{m}$, $.20\text{m}$, $.28\text{m}$, and $.36\text{m}$	129
5.40	Conservative Variable Transverse Mass Flux ρv (kg/sm^2) a) Instantaneous Mass Flux, b) Time Averaged Mass Flux Field, and c) Cross Channel Mass Flux Profiles at $X = .12\text{m}$, $.20\text{m}$, $.28\text{m}$, and $.36\text{m}$	130
5.41	Conservative Variable Spanwise Mass Flux ρw (kg/sm^2) a) Instantaneous Mass Flux, b) Time Averaged Mass Flux Field, and c) Cross Channel Mass Flux Profiles at $X = .12\text{m}$, $.20\text{m}$, $.28\text{m}$, and $.36\text{m}$	131

5.42	Conservative Variable Total Energy Flux ρe_t (<i>Joule/m²</i>) a) Instantaneous Total Energy, b) Time Averaged Total Energy Field, and c) Cross Channel Total Energy Profiles at X = .12m, .20m, .28m, and .36m.	132
5.43	Comparison of Numerical and Experimental Mean Velocity Profiles; a) X=0.12 m, b) X=0.16 m, c) X=0.20 m d) X=0.24 m.	134
5.44	Comparison of Numerical and Experimental Mean Velocity Profiles; a) X=0.268 m, b) X=0.353 m.	135
5.45	Three-dimensional Case I $M_c = 0.5$ Time Averaged Reynolds Stress $\overline{\rho u'v'}$: a) Time averaged Reynolds Stress Field, and b) Cross Channel Profiles at X = .12m, .20m, .28m, and .36m.	137
6.1	Total Mass Flux Unsteadiness $(\rho V)'$ at X = 0.18 m: a) FFT spectra and b) Auto-spectra.	140
6.2	Total Mass Flux Unsteadiness $(\rho V)'$ at X = 0.27 m: a) FFT spectra and b) Auto-spectra.	141
6.3	Comparison of numerical and experimental shear layer growth rates, vorticity δ_ω , momentum 4θ , boundary layer δ_{98} , and experimentally determined vorticity.	143
6.4	Normalized growth rates correlated with convective Mach number, Case I and Case II.	144
6.5	Instantaneous Descriptive Flow Parameters; a) Density Gradient Field, and b) Vorticity Field.	145
6.6	Conservative Variable Density ρ (<i>kg/m³</i>) a) Instantaneous Density, b) Time Averaged Density Field, and c) Cross Channel Density Profiles at X = .12m, .20m, .28m, and .36m.	146
6.7	Conservative Variable Axial Mass Flux ρu (<i>kg/sm²</i>) a) Instantaneous Mass Flux, b) Time Averaged Mass Flux Field, and c) Cross Channel Mass Flux Profiles at X = .12m, .20m, .28m, and .36m.	147
6.8	Conservative Variable Transverse Mass Flux ρv (<i>kg/sm²</i>) a) Instantaneous Mass Flux, b) Time Averaged Mass Flux Field, and c) Cross Channel Mass Flux Profiles at X = .12m, .20m, .28m, and .36m.	149

6.9	Conservative Variable Total Energy ρe_t (<i>Joule/m²</i>) a) Instantaneous Total Energy, b) Time Averaged Total Energy Field, and c) Cross Channel Total Energy Profiles at X = .12m, .20m, .28m, and .36m.	150
6.10	Axial Variation of Numerical Time-averaged Velocity Profiles.	151
6.11	Case II $M_c = 0.64$ Axial Mass Flux Perturbation $\overline{(\rho u)'}'$: a) RMS Mass Flux Perturbation and b) Cross Channel Profiles at X = .12m, .20m, .28m, and .36m.	153
6.12	Case II $M_c = 0.64$ Transverse Mass Flux Perturbation $\overline{(\rho v)'}'$: a) RMS Transverse Mass Flux Field and b) Cross Channel Profiles at X = .12m, .20m, .28m, and .36m.	154
6.13	Case II $M_c = 0.64$ Time Averaged Reynolds Stress $\overline{\rho u'v'}$: a) Time-averaged Reynolds Stress Field, and b) Cross Channel Profiles at X = .12m, .20m, .28m, and .36m.	155
A.1	Amplification Factor of the Convection Equation, $\lambda = 2/3$ and $\lambda = 0.25$. . .	167
A.2	Amplification Factor of the Diffusion Equation, $r = 3/8$ and $r = 3/80$. . .	169
A.3	Diffusion versus Courant Relationship for the Convection-diffusion Equation Using the MacCormack 2-4 method.	171
A.4	Convection-Diffusion Amplification Factor for $\lambda = \frac{2}{3}, r = max$ and $r = \frac{3}{8}$. . .	172
A.5	Convection-Diffusion Amplification Factor for $\lambda = \frac{1}{4}, r = max$ and $r = \frac{max}{10}$. . .	172

LIST OF TABLES

1.1	Connection Machine Overview	9
1.2	Nominal Experimental Conditions	12
1.3	Simulation Inflow Conditions	14
3.1	Grid Resolved Frequencies	42
3.2	Free Slip and Wall Conditions: Cell Centered Boundary	45
4.1	Shear Layer Growth Rates for a Single Frequency 25 kHz	55
5.1	Shear Layer Growth Rates for Case I	81
5.2	Supplementary Parameters	83
5.3	Incompressible Growth Rates	83
5.4	Three-dimensional Shear Layer Growth Rates for Case I	124
6.1	Shear Layer Growth Rates for Case II	143

Acknowledgments

I extend my grateful appreciation for the provision of computational resources goes to the Numerical Aerodynamic Simulation (NAS) Program at NASA Ames and by the National Center for Supercomputing Applications (NCSA) at the University of Illinois, Urbana-Champaign. Thanks go to NASA Lewis for support of portions of this work under NASA grant NAG-3-1492.

I would like to thank my thesis advisors, Drs. Lyle Long and Philip Morris, for their contributions through insight, probing questions and invaluable guidance. Their contributions have made my doctoral program an excellent learning experience and a solid technical accomplishment. I would also like to thank those who have served as part of my doctoral committee; Drs. Dennis McLaughlin, Budugur Lakshminarayana, and Vigor Yang. Their interest and contributions have added significantly to the accomplishments achieved as part of this thesis.

Thanks go to several former and current graduate students; Dr. S. Martens, Dr. Long-Shin Lee and David Lockard, for their contributions in the form of discussions and data. Special thanks go to Steve Martens for his help in providing data for comparisons and to David Lockard for his providing eigenfunctions and linear theory results.

My most profound thanks go to my wife Gail, without whose exceeding love, patience, and unswerving support this effort could not have been undertaken or completed.

Finally, to the Most High God be all honor and glory for what He has accomplished in this work.

Iron sharpens iron,
So one man sharpens another.

Proverbs 27:17

Chapter 1

Introduction

1.1 Objectives and Overview

Compressible mixing layers have been a research topic with engineering and research importance for many years. They occur in a very broad spectrum of applications from the external aerodynamics of aircraft to the intense flow conditions of internal flows in propulsion and laser systems. During the last decade the oft cited application of shear layer research has been supersonic combustion/propulsion associated with scramjet missiles or vehicles such as the single-stage-to-orbit Aerospace Plane or the High Speed Civil Transport. Improvement of these systems is needed not only to reduce their size, cost and make them more efficient, but also to make them quieter. Achieving these improvements requires a better understanding of the basic mixing processes occurring in shear layers and that better understanding requires significant increases in the amount and resolution of fundamental flow variable data from within the shear layer. Numerical simulation of engineering problems is an emerging technology that holds great promise to provide the needed data.

The advancements in computing power of recent years are providing significant improvement in the ability of computational methods to provide fine grain solutions to engineering problems such as shear layer mixing mechanisms. Simulations provide a wealth of informational detail that is often difficult to obtain from contemporary experimental methods. As memory and visual data post-processing capabilities improve, simulations will provide greater detail to the researcher than can be practically collected from experiments. However, experimental methods provide the physical reality needed to validate and evaluate the computational methods.

This thesis is a computational part of ongoing research (Hackett [23], Kinzie [31], Kamvissis [29], Martens [41, 42]) at the Pennsylvania State University into the mixing of supersonic shear layers with convective Mach numbers in the low to moderate range. The focus of the present research has been the development of two- and three-dimensional

Euler software for the analysis of compressible mixing. The fundamental capability sought is the ability to model the steady and unsteady behavior of confined compressible shear layer mixing— at least to within the conventional guidelines for the resolution of important physical phenomena, such as 10 points per wave length.

The development of the software was accomplished on a CM-200a at Penn State, the Numerical Aerodynamic Simulation Program’s CM-5 at NASA Ames, and the National Center for Supercomputing Application’s CM-5 at the University of Illinois at Urbana-Champaign. The approach is guided by three principles: consistency with experimental data, consistency with analysis, and applicability to flow ranges of engineering interest. While comparisons between analytical and numerical results or experimental and numerical results are common practice, a growing number of researchers such as Mankbadi et al. [40] and Hayder [24] are including explicitly consistent comparisons between computational results and analysis. This consistency between computations, experiments and analysis relies on a common problem definition and the availability of resulting data. This thesis brings together numerical simulations, measurements by Martens’ [42], and analytical results from Lockard [44]; all for a common problem definition. The combination of experimental data, analytic stability information, and computational capability for a common set of flow conditions is improving our understanding of compressible shear layers.

1.2 Background

Research into the behavior of both incompressible and compressible mixing layers has spanned analytical, experimental and numerical efforts. Each type of research has contributed essential understanding to the knowledge base. Analytical methods of stability theory have given understanding of the basic character of the perturbations. Experimental efforts have quantified the basic mean and perturbation behaviors. Numerical methods have begun to provide close comparison with both analytical and experimental results. This opens a new way of study of mixing layers that can provide new information that is difficult or impossible to obtain by other means. Key papers that have contributed directly to this thesis topic are discussed below.

The early linear stability studies of compressible supersonic free shear layers were conducted by Lessen et al. [35, 36] and Blumen et al. [5]. They looked at the basic instabilities of

both two-dimensional and three-dimensional compressible mixing layers. Gropengiesser [20] investigated compressible mixing layers, changing to spatial stability theory and relaxing the iso-energetic restrictions of Lessen et al. [35]. Gropengiesser [20] investigated the effects of Mach number and temperature ratio under the assumptions of parallel mean flow and inviscid perturbations. Much more recently, Ragab and Wu [58] investigated linear instability waves in supersonic shear layers. They considered both inviscid and viscous disturbances. For Reynolds numbers > 1000 they found that shear layer growth rates approach those predicted by the inviscid stability equations. The only effect of viscosity they found was to slow down the growth of disturbances. They also investigated the effects of velocity and temperature ratio. The maximum growth rate of a compressible shear layer was found to depend on the velocity ratio $\lambda = (U_1 - U_2)/(U_1 + U_2)$ “in a complex manner.” They substantiated the correlation of compressibility by the convective Mach number of Bogdanoff [6] and Papamoschou and Roshko [53]. Non-parallel effects were found to be negligible for laminar mixing layers, and shear layer growth rates were found to follow the predictions of inviscid stability theory as the Reynolds number ($Re_y = \rho_1 U_1 \delta_x / \mu_1$) became large. Sandham and Reynolds [63] compared linear theory and direct numerical simulations of a time-developing mixing layer. They found directly proportional agreement between linear theory results and their simulation. The effects of density and velocity ratios on the growth rates were included. They also found that $M_c = 0.6$ was the dividing point below which the two-dimensional behavior was dominant and above which oblique three-dimensional waves became most amplified. In 1989 Jackson and Grosch [27] conducted an extensive study of the inviscid spatial stability of compressible mixing layers. They studied the effects of Mach number, temperature ratio, wave frequency and the direction of propagation. It was shown that there exists a critical Mach number above which there are two groups of unstable waves. One group has a fast phase speed and the second has a slow phase speed. Zhuang et al. [81] conducted an inviscid linear stability study similar to Ragab and Wu [58]; but, they introduced a new definition of convective Mach number using the phase velocity of the most unstable eigenvalue. They found “a nearly universal dependence of the normalized maximum amplification rate on the convective Mach number (theirs.)” The difference between their Mach number and that of Bogdanoff [6] and Papamoschou and Roshko [53] was the Mach number at which the normalized growth rate begins to level

off, being ≈ 0.6 for Papamoschou and Roshko [53] or ≈ 1 . for Zhuang et al. [81]. Jackson and Grosch [28] were able to derive a convective Mach number based on linear stability theory. Their definition of the convective Mach number $M_c = M(1 - \beta_u)/(1 + \sqrt{\beta_\gamma/\beta_\rho})$ is equal for a single species gas with $\beta_\gamma = 1$. Similar to the Zhuang definition, the normalized growth function levels off for $M_c > 1$. However, the Jackson and Grosch [28] definition for $M_c = 1$. was based on the physical condition at which the sonic speeds of the two streams are equal. Grosch and Jackson [21] extended their study of inviscid spatial stability to three-dimensional mixing layers. They developed a one-parameter family of curves that can give the growth rate for any given direction of mean flow and wave propagation direction. They also determined that for supersonic convective Mach numbers, certain combinations of cross-flow angle and propagation angle can double the growth rate. This body of work addresses the instability of free compressible shear layers, both subsonic and supersonic; but, it lacks the effect of walls.

The influence of confining walls on the instability modes of supersonic shear layers has been studied by a few researchers [73, 19, 69, 48]. The findings of Tam and Hu [73] show that the motion of the shear layer and the acoustic modes produce additional supersonic stability modes. Greenough et al. [19] showed that for a confined compressible mixing layer the effect of walls was to produce two general types of instabilities: confined Kelvin-Helmholtz modes and supersonic wall modes. The findings of Zhuang et al. [81] and Morris et al. [48] show that the growth rates for the Kelvin-Helmholtz modes are insensitive to the presence of walls. The subsonic convective Mach number modes are not materially influenced by the relative proximity of the wall. The Kelvin-Helmholtz mode is the fundamental instability mode observed in the experimental work used for comparison by this thesis.

Experimental efforts investigating the roll of large scale structures in the mixing process by researchers such as Winant and Browand [80] laid a foundation for the investigation of compressible shear layer growth. The experimental study of Brown and Roshko [7] generally begins historical reviews of compressible mixing layers research. Brown and Roshko [7] conducted a series of experiments investigating the effects of density ratio. They concluded that decreases in the shear layer growth rate were due to compressibility rather than density effects. Much later, Oster and Wygnanski [51] provided basic information about the rate at

which shear layers grow and their relationships to turbulence intensities, Reynolds stress, and the influence of forcing frequencies and their amplitudes.

Bogdanoff [6] developed the concept of correlating the mixing layer growth rate with the Mach number associated with the mean wave speed of the mixing layer's large scale structures. Papamoschou and Roshko [53] developed a similar definition of convective Mach number for the correlation of growth rates in compressible mixing layers. Compressible mixing layer growth rates collapse to a single curve when normalized by the growth rate that would have occurred if the flow was incompressible and the velocity and density ratios were unchanged. These early works only examined the effects of compressibility on growth rate and mean flow profiles. Samimy and Elliot [61, 12] have broadened the scope of the research to examine other parameters and correlations. They examined the use of alternative thickness parameters such as momentum thickness and found that it requires a linear transformation of the convective Mach number to collapse the data. Turbulence quantities such as intensities, shear stress and kinetic energy were found to decrease in level and lateral extent with increasing convective Mach number. Goebel and Dutton [16] found significantly different results. They did find that the normalized mixing layer growth rates decreased with increasing convective Mach number. They also found that transverse turbulence intensities and normalized Reynolds stress decreased with increasing convective Mach number. However, in contrast to the findings of others, Goebel and Dutton [16] found that the streamwise turbulence intensities and Reynolds stress remained constant with increasing convective Mach number. More recent work by other researchers [10, 4, 2] have shown more conventional findings including the streamwise turbulence intensities and Reynolds stress decreasing with increasing convective Mach number. Many issues remain in the research of compressible mixing layer growth such as the influence of inlet turbulence levels and some discussion of the existence of large scale structure at high Reynolds number. Some issues will be resolved as instrumentation techniques for supersonics shear layers improve. Other answers will come from the insight that can be gained from fine grained numerical simulations.

The early numerical investigations [38, 65] of mixing layers focused on the roll of vorticity in mixing layers and the entrainment between streams. Sandham and Reynolds [63] began looking at three-dimensional effects in the form of oblique waves and also included

the effect of compressibility. Chien et al. [8] conducted numerical simulations of unconfined inviscid spatially developing shear layers. They found the mean flow to be dominated by two-dimensional, inviscid effects and the r.m.s. fluctuating velocity and density profiles consistent with experimental results, except for the transverse velocity fluctuations, v' . They attributed the differences to three-dimensional effects. One possible contributor to the differences was their different inlet disturbance. All their inlet variables were held constant except the streamwise velocity which was perturbed sinusoidally. Their inlet conditions required numerical disturbances to begin the process of transport of energy between axes, a spatially slow process. Other researchers [75, 68] were beginning to move to Navier-Stokes solutions to explore the growth of Reynolds stress turbulence and three-dimensional effects. Farouk et al. [13] undertook an inviscid simulation of a confined supersonic shear layer. They investigated the effects of density ratio, pressure ratio and velocity ratio on mixing and the fundamental frequency of the mixing. Overall, differences in pressure between the two streams and the associated shocks were able to produce significant enhancements in mixing. Leep, Dutton and Burr [34] carried out an inviscid simulation of a temporally evolving, three-dimensional compressible mixing layer and arrived at results very similar to the prior work of Dutton et al. [16]. They found that compressibility primarily suppresses transverse turbulence intensity but that streamwise turbulence intensity remains relatively constant. Wilson et al. [79] conducted simulations of two-dimensional spatially developing mixing layers. They found that the location and type of vortex pairing is influenced significantly by the type of inlet forcing used to stimulate the shear layer. Enhanced mixing at discrete (fundamental and/or several sub-harmonics) produced vortex roll-ups at discrete locations followed by a space of reduced activity. Broad spectrum forcing derived from experimentally measured power spectra caused vortex pairing to occur over a region but not at fixed locations. The broad spectrum or more randomized inlet perturbations produced a more natural-like shear layer behavior. Recently Sarkar [67] took a detailed look at the mechanism causing the compressibility effect of reduced shear layer growth rate. He found that the compressibility effect was the reduced level of turbulence production and was not due to dilational effects. Oh and Loth [49] recently applied an adaptive unstructured grid method to inviscid simulations of the mean behavior of the velocity profile, turbulence intensities and Reynolds stress. Oh and Loth [49] compare their findings with experimental data.

Comparisons between numerical simulations, experimental data and analytical results guide each other to insure the development of an accurate understanding of the phenomena. As advanced computer systems allow better numerical simulations to be performed our understanding of the physical mechanisms of compressible mixing improve.

1.3 Parallel Computing

Parallel Computing is the current generation in the evolution of scientific supercomputing. Parallel computing paradigms range from simple parallel systems to massively parallel systems that have literally thousands of processors working in parallel. The simple parallel systems have multiple processors ranging in number from several to thousands of processors. Computers systems such as those made by Cray, Convex(SPP1000) and Meiko(CS-1) are typical of the not-so-simple simple parallel computers. These systems tend to follow conventional vector computing architecture. The massively parallel end of the advanced computer spectrum are machines such as the Intel Paragon, MasPar MP-2, Thinking Machines CM-2, CM-200 and CM-5, Kendall Square Research KSR-1, Cray Research T3D and nCUBE-2S. Each of these machines uses processors that number into the hundreds or thousands, all working in parallel. The extremely rapid pace of evolution and obsolescence in supercomputing research is best illustrated by the fact that three years ago these machines were the fastest available and seemed to be the best trend for the future. Now most of these machines are not in production. None is the fastest technology available nor is any one of them, as then envisioned, considered the trend of the future. The high cost of the massively parallel machines has directed the industry towards a more moderate approach using stackable units that employ tens to at most hundreds of processors. These new machines use a combination of improved chip technology and multiple processors to achieve megaflop rates that out perform all but the largest of the massively parallel systems [1].

The research of this thesis has been conducted on the massively parallel architectures of the Thinking Machines CM-200a and CM-5 machines. The CM-5 at the National Center for Supercomputing Applications (NCSA) program at the University of Illinois Urbana-Champaign is shown in Figure 1.1. Computing facilities at NAS and the National Center for Supercomputing Applications (NCSA) at the University of Illinois-Champaign were used



Figure 1.1. CM-5 at NCSA, University of Illinois Urbana-Champaign.

in this research. NAS had a 128 node CM-5 and NCSA has a 512 node CM-5. The CM-200a used for this research is the Aerospace/Computer Science machine at Penn State. The CM-200a was used for small scale code development and is capable of 1.2 Gflops peak speed. The 512 node CM-5 has a peak speed of 64 Gflops. The architecture and performance characteristics of these three machines are summarized in Table 1.1. The Connection Machines massive computing speed and data processing paradigm offer a significant opportunity to explore the use of fine grain computing in the solution of practical engineering problems. These advantages of speed and processing paradigm are discussed in greater detail below along with some simple illustrations of the performance and programming benefits.

Table 1.1. Connection Machine Overview

	PSU CM-200	NAS CM-5	NCSA CM-5
Architecture	massively parallel processor (MPP)		
Number of processors	64 Weitek processors	128 SPARC Cypres processors with 4 vector Units per processor (node)	512 SPARC Cypres processors with 4 Vector Units per processor (node)
Total memory	256 Mbytes (4 Mbytes per processor)	4 Gbytes (32 Mbytes per node)	16 Gbytes (32 Mbytes per node)
Total disk space	2 Gbytes	48 GB SDA (Scalable Disk Array)	130 GB SDA 2 Gbytes (Scalable Disk Array)
Clock speed/Processor cycle time	10 MHz	32 MHz	32 MHz
Peak performance	1200 Mflops (20 Mflops per node)	64 Gflops (128 Mflops per node)	256 Gflops (128 Mflops per node)
Software Environment			
Operating System	CMOST (based on SUNOS)		
Batch system	DQS	DJM (Distributed Job Manager)	
Programming Language	CM Fortran		

The Connection Machines, both the CM-200a and the CM-5, can be operated in a Single Instruction Multiple Data (SIMD) mode and primarily use the data parallel programming paradigm. Explicit algorithms such as the MacCormack 2-4 scheme work very well on data parallel machines since they use a single instruction at a time acting over the whole field or array. This is best illustrated in the array processing extensions of CM Fortran/Fortran 90/High Performance Fortran (HPF). In HPF, two NxM arrays A and B can be added element by element and assigned to a third NxM array C by simply writing $C = A + B$. Array constructs eliminate the cumbersome do loops of standard Fortran 77. One of the impressive features of the CM architecture is its nearly linear scalability between memory, solution speed and number of processing nodes. Doubling the number of grid points in a problem results in only an increase of about two in memory use and computation time. This is a significant development benefit.

The SIMD architecture of the Connection Machines and the data parallel paradigm are well matched to the explicit MacCormack algorithm being used here to solve the unsteady shear layer mixing problem. The very high floating point operation (flop) rate enables this flow field to be solved within an acceptable time frame. The grid used for this shear layer calculation is 786 by 256 or 196,608 grid points. To run a long enough time history to get a 512 point FFT time series requires about 51200 time steps using a CFL of 0.25. The 51200 time steps takes 4.3 hours cpu time on 128 nodes (processors) of the NCSA CM-5. Figure 1.2 shows how this problem scales in run time between different numbers of nodes. The problem memory size is best matched to 32 processors but scaling is nearly linear to 128 nodes. The linear scaling of the CM-5 architecture makes changing the problem size very acceptable in terms of time and cost. The problem can be doubled in size (number of grid points) and run on twice the number of processors and hold execution time per time-step nearly constant. The results from successively doubling the problem size and number of processors are given in Figure 1.3. These results show the scaling characteristics of the massively parallel machines. They also provide compute times that grow with N, the number of grid nodes, rather than the N^2 growth common with more conventional vector systems. Order N scaling characteristics alone do not govern the size or types of problems that engineers and scientist may attempt to solve, but the softer size barrier takes a lot of the headaches out of making the problem slightly larger.

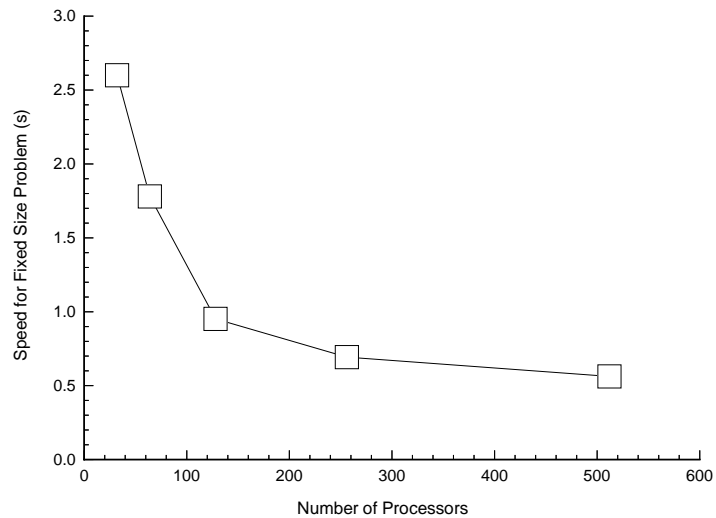


Figure 1.2. Variation of computing speed with number of processing nodes for a fixed size problem.

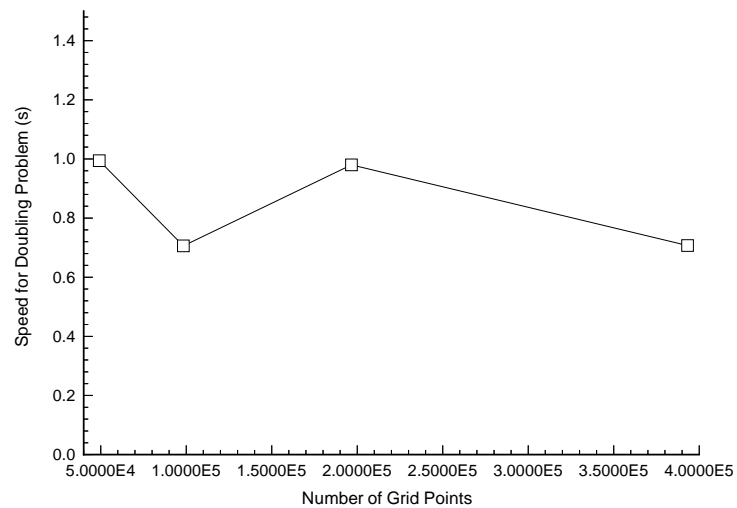


Figure 1.3. Variation of computing speed as the number of grid points and the number of processing nodes are successively doubled.

Table 1.2. Nominal Experimental Conditions

Parameter	High Speed	Low Speed
Case I	Convective Mach Number $M_c=0.5$	
Mach	3.	1.2
T_{tot} (K)	293.	293.
P_{tot} (Pa)	42663.	2864.
U velocity(m/s)	614.	360.
V velocity(m/s)	0.	0.
Case II	Convective Mach Number $M_c = 0.64$	
Mach	4.	1.2
T_{tot} (K)	293.	293.
P_{tot} (Pa)	102658.	3019.
U velocity(m/s)	670.	370.
V velocity(m/s)	0.	0.

1.4 The Simulation

The numerical simulation research that is presented in this thesis draws its simulation flow conditions from the experimental work of Martens [42]. Martens investigated two basic cases of confined compressible supersonic shear layers looking at the causes of mixing. A summary of the nominal flow conditions for the experiments are given in Table 1.2. The experimental conditions have Reynolds numbers that range from 6600 to 9500, based on the shear layer thickness (0.002 m) as the length dimension. At Reynolds numbers greater than 1000, inviscid effects dominate the flow. At these Reynolds numbers the shear layer is initially laminar at the Case I and II conditions. The laminar flow permits the investigation of shear layer growth mechanisms without the complication of turbulence. The growth mechanisms that produce large scale structures in these experimental shear layers are Kelvin-Helmholtz instabilities. One of the goals for this simulation was to be able to match the experimental results with a minimum number of adjustable constants and ad hoc assumptions.

The experimental works of Martens et al. [42, 43] and McLaughlin et al. [46] explore the structure of large scale instabilities in supersonic shear layers. The large scale structures present in the flow at low-to-moderate Reynolds number conditions are characterized as Kelvin-Helmholtz instabilities. Martens uses a sub-atmospheric test facility to generate

low-to-moderate Reynolds number flows with Mach numbers up to 4.0. The experimental conditions allowed the experimenter to investigate the influence of convective Mach number while operation at differing pressures allowed the Reynolds number to be varied. Case I, with a high speed Mach number of 3, has a convective Mach number of 0.5 and a most unstable frequency for the shear layer at about 25 kHz. Laminar stability theory predicts the most unstable frequencies for the two cases to occur in the mid to high 20 kHz range. The experimental data were collected using a combination of static pressure taps, a five-hole Pitot probe, hot-wire anemometers and schlieren photography. A comprehensive presentation of Martens' data is given in reference Martens [42] and unless specifically noted it will be the source for all references to experimental results.

Numerical simulations were made at both of Martens' Case I and Case II conditions. Static conditions for the field variables were derived from experiment total conditions and recorded stream Mach numbers. Other conditions such as the unsteady inlet conditions were developed as part of this research and are discussed in detail below. The mean inlet primitive variables along with several other properties are given in Table 1.3.

The experimental test section has stream wise, transverse and span wise dimensions of 0.75 m, 0.055 m and 0.125 m respectively. A schematic of the experimental test facility is shown in Figure 1.4. The adjustable top and bottom walls diverge slightly to negate the effect of boundary layer growth. The geometry and size of the test section were reduced and idealized for the simulation. A constant cross-section was assumed to simplify the numerical simulation. The computational domain was reduced to 0.5625 m by 0.055 m in the streamwise and transverse directions for the two-dimensional computations. Figure 1.5 shows a schematic of the two-dimensional computational domain. The three-dimensional domain added the full duct width of .12 m, bounded by hard parallel walls. The length was also reduced to 0.4 m to conserve the computational size of the problem. Most of the experimental data was recorded upstream of the 0.4 m position and both the numerical and experimental results show that as the flow approaches the 0.4 m position the shear layer becomes turbulent and is significantly influenced by the walls. Effort was made to minimize the impact of compromises between experimental detail and simulation practicality. A key accomplishment was being able to place the flow splitter at the inlet plane of the computational domain. No extra inlet region for flow maturation (virtual origin) was needed. At

Table 1.3. Simulation Inflow Conditions

Flow Variable	High Speed	Low Speed
Case I	Convective Mach Number $M_c = 0.5$	
Mach	2.98	1.19
T_{tot} (K)	293.	293.
P_{tot} (Pa)	42663.	2864.3
R_{tot} (Kg/ m^3)	0.5081	0.0341
U velocity(m/s)	613.0	359.9
V velocity(m/s)	0.	0.
T_s (K)	105.5	228.0
P_s (Pa)	1196.7	1196.7
R_s (Kg/ m^3)	0.0396	0.0183
Acoustic C(m/s)	205.7	302.4
μ (Kg*m/s)	7.3177E-6	1.4838E-5
E_t (Joule)	263575.	228318.
Unit Rey	3315489.	444166.
Case II	Convective Mach Number $M_c = 0.64$	
Mach	4.03	1.23
T_{tot} (K)	293.	293.
P_{tot} (Pa)	102658.	3018.9
R_{tot} (Kg/ m^3)	1.222	0.03595
U velocity(m/s)	669.0	369.4
V velocity(m/s)	0.	0.
T_s (K)	68.7	224.9
P_s (Pa)	649.6	649.6
R_s (Kg/ m^3)	0.03299	0.010076
Acoustic C(m/s)	166.	300.
μ (Kg*m/s)	4.6351E-6	1.46726E-5
E_t (Joule)	273080.	229620.
Unit Rey	4761464.	253729.
Physical Domain		
Length(m)	0.5625	
Height(m)	0.0550	
Width(m)	0.125	

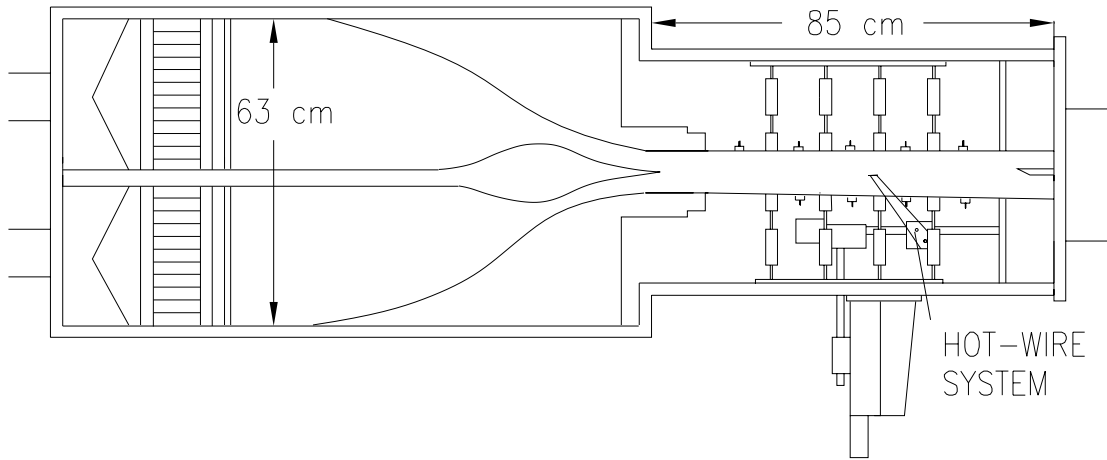


Figure 1.4. Experimental test section

the inlet the axial velocity profile was approximated with a hyperbolic tangent function. Velocity profile data at the inlet plane was not sufficiently detailed nor was the available grid adequate for resolution of boundary layer like wakes. The very thin initial thickness of the shear layer aided in achieving acceptable results with the hyperbolic tangent profile assumption.

The grid for the two-dimensional simulation was selected by first finding the axial spacing required to resolve the shear layers' most unstable frequency. Ten points per wave length for the fundamental frequency instability were required. The grid spacing was then modified to give a point count that was a multiple of 32. The multiple of 32 requirement provided needed computer memory matching to obtain the best computational speeds. The transverse grid spacing was selected based upon the ability to resolve the shear layer linear stability eigenfunctions at the fundamental frequency. This spacing was also adjusted to a multiple of 32. The final two-dimensional grid has 768 axial by 256 transverse points. The grid for the three-dimensional simulation was found by a similar process and yielded a system of 256 axial, 128 transverse and 160 lateral points. The use of such a fine grid is made possible through the use of the large memory and high speed of massively parallel computing technology. The computations were performed in the physical domain to facilitate comparison with experiment.

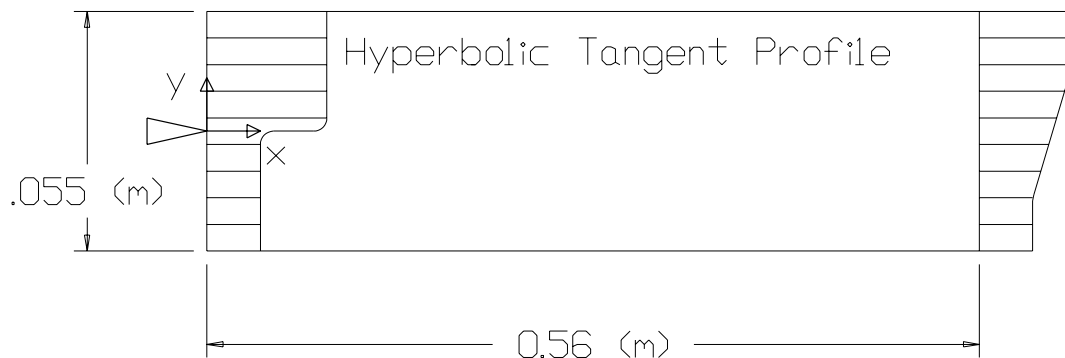


Figure 1.5. Two-dimensional computational domain schematic; physical 0.56x0.055 meters, grid 768x256.

1.5 Scope and Outline

The chapters that follow present in detail the significant contributions that have been made by this work. Six principal contributions have been made by this work: 1) the development of a modified Jameson damping based on density rather than the pressure, 2) the development of an extrapolation method that yields realistic bounded results while letting shock-like gradients pass through the boundary, 3) the development of an unsteady inlet disturbance method that produces realistic near-field behavior, 4) for a single physical set of flow conditions comparison of results from experimental data, numerical simulation and analytical laminar stability theory, and finally 5) a detail stability analysis of the stability limits for the MacCormack 2-4 scheme including the diffusion terms. The fine grain numerical simulations provide much finer detail than can typically be collected by experiments if for no other reason than cost. The numerical results also represent the unperturbed flow field which has not been intruded upon by instrumentation. A brief description of these contributions is given below followed by in depth discussion in later sections of the thesis.

Early computer runs identified the need for artificial viscosity to dampen errors that were building up during long run times and causing the code to fail at unpredictable times. The primary region of failure was along the shear layer and a relatively strong damping was

required to maintain stability. The conventional Jameson's artificial viscosity has the desired feature of adding low order damping only where needed but was found to be ineffective in the nearly uniform pressure field. The Jameson method was modified to use a dynamic coefficient based on the density gradient. The modified Jameson method has been found to be equally effective for conventional problems such as the Riemann problem.

The MacCormack 2-4 method can not solve for the solution directly over the entire domain. The one-sided stencils of the predictor-corrector algorithm do not integrate the solution variables at the first two or last two grid points in the domain. They must be found from some other method. A third order extrapolation that is commonly used with the method gave unbounded values when the high gradients of large rolling vortices passed through the boundary. An alternative scheme was developed that gives third order and higher extrapolations. The method provides smooth, bounded extrapolated values, except when shock-like gradients are passing through the boundary.

Numerical shear layer calculations have been found to fall into two classes, first those that use very low disturbances and only compute laminar flows and, second, those that use a virtual origin to match numerical results to experimental data. Virtual origins are used to allow the numerical field to develop an unsteadiness typical of real flows. An inlet disturbance method based on the homogeneous turbulence behavior of shear layers has proven to be very effective at letting the computational inlet and the experimental inlet to be coplanar. Excellent comparison with experimental results was obtained. The new inlet method produces realistic results at disturbance magnitudes consistent with those found from experiments.

The research presented in this thesis brings together the numerical results presented herein, experimental work from Martens [42] and analytical results from Lockard [37] to provide a three way comparison on a single problem. The three way comparison helps insure validity of results by requiring agreement across the different methods. The cross-comparison also provides expanded perspectives from which to attack the remaining issues.

Finally, in the original publication on the MacCormack 2-4 scheme, Gottlieb and Turkel [18] presented a stability analysis for the convection equation giving the amplification factor equation and the associated CFL number limit. They also suggested a process for adding the diffusion terms to the finite difference scheme and stated, without detail, a

diffusion number limit for the scheme. An independent von Neumann analysis was conducted for both the convection equation and the convection-diffusion equation. The high order of the method results in very complicated amplification factor equations, the forms of which are very sensitive to the implementation process. The results replicate the Gottlieb and Turkel analysis for the convection equation but find a small difference in the diffusion number limit. Also the interrelationship between the CFL and diffusion number was found.

The unique contributions and comparisons of this thesis research are discussed in greater detail in subsequent sections. Chapter 2, the mathematical formulation section, provides a discussion of the various governing equations and their supporting theories, assumptions and physical principals. The methods and techniques for implementing these governing equations are discussed in Chapter 3, numerical formulation. Included in this section are discussions of the practical considerations for implementing the various algorithms and procedures. Chapter 4 presents the single frequency simulations that examine Case I conditions as stimulated by the time dependent eigenfunction profiles generated by the Rayleigh Equation. Chapter 5 presents the shear layer simulation results for Case I $M_c = 0.5$ conditions and a full range of steady and unsteady results for each conservative variable and selected physical parameters. Chapter 5 also includes a discussion of the results of a three-dimensional simulation of Case I conditions and discusses the differences from the two dimensional results. Chapter 6 gives the simulation results for the Case II $M_c = 0.64$ conditions. Comparisons are made with the Case I results to examine the influence of convective Mach number. The final chapter, Chapter 7, draws a number of conclusions about the accomplishments that have been made and makes recommendations for future work. An appendix provides a detailed von Neumann analysis of the MacCormack 2-4 scheme.

Chapter 2

Mathematical Formulation

The mathematical representations of fluid motion are founded in the expression of the governing conservation laws for mass, momentum, and energy. Various flow conditions influence the formulation of the conservation laws into a set of governing equations. The supersonic speeds and the large relative Mach number of the shear layer streams require the conservative formulation of the governing equations to correctly compute the speed and intensities of possible discontinuities. The non-dimensional Mach numbers show the degree to which inertia forces dominate over compressibility effects. Since the Mach numbers encountered are of $O(1)$ compressibility effects are important and must be included. Compressibility effects couple mass and energy through the primitive variable density. Similarly, the non-dimensional Reynolds number shows the relative magnitude of inertia forces to viscous forces. The Reynolds numbers for the simulated shear layers range from approximately 6000 to 10000, and show that the inertia forces dominate over the viscous forces by several orders of magnitude. The final set of flow equations are obtained by deleting viscous terms and the addition of one additional requirement, no heat conduction. The governing flow equations now consist of the conservation form of the conservation of mass, momentum, and energy laws for inviscid flow with no heat conduction. The resulting set of equations are first order and hyperbolic in time and are commonly referred to as the Euler equations. In the strictest sense the Euler equations are just the inviscid momentum equations but the newer broader definition is used in this thesis. The Euler equations provide accurate numerical simulation of flows where dynamic effects dominate. The boundary conditions that guide the solution are based upon the conventional method of characteristics used to determine the number of physical conditions required at each boundary.

2.1 Governing Equations

The Euler equations along with two equations of state are needed to solve for the shear layers dynamic behavior. The time-dependent Euler equations in conservation form for the

conservative variables form a system of first-order, non-linear partial differential equations that are hyperbolic in time. Expressing the Euler equations in vector form we obtain the following.

$$\frac{\partial \vec{Q}}{\partial t} + \frac{\partial \vec{E}}{\partial x} + \frac{\partial \vec{F}}{\partial y} + \frac{\partial \vec{G}}{\partial z} = 0 \quad (2.1)$$

The column vector \vec{Q} contains the conservative variables and the vectors \vec{E} , \vec{F} , and \vec{G} contain the conserved fluxes. A rectilinear grid system is used for the simulations allowing the governing equations to be written in Cartesian coordinates. The Cartesian components of \vec{Q} are

$$\vec{Q} = \left\{ \begin{array}{c} \rho \\ \rho u \\ \rho v \\ \rho w \\ \rho e_t \end{array} \right\} \quad (2.2)$$

and the flux vectors are defined by equations

$$\vec{E} = \left\{ \begin{array}{c} \rho u \\ \rho u^2 + p \\ \rho uv \\ \rho uw \\ (\rho e_t + p)u \end{array} \right\} \quad (2.3)$$

$$\vec{F} = \left\{ \begin{array}{c} \rho v \\ \rho vu \\ \rho v^2 + p \\ \rho vw \\ (\rho e_t + p)v \end{array} \right\} \quad (2.4)$$

$$\vec{G} = \left\{ \begin{array}{c} \rho w \\ \rho w u \\ \rho w v \\ \rho w^2 + p \\ (\rho e_t + p)w \end{array} \right\} \quad (2.5)$$

The above set of equations assemble into five of the seven governing equations needed for three-dimensional flow. To close this system of fluid dynamic equations, two equations of state are needed that give the relationships between the thermodynamic variables. The seven unknown primitive variables that satisfy these equations are density (ρ), the axial, transverse, and spanwise velocity components ($u, v,$ and w , respectively), pressure (p), temperature (T), and internal energy (e). The total energy term e_t used in the governing equations is defined by $e_t = e + \frac{1}{2}(u^2 + v^2 + w^2)$. Equations 2.6 and 2.7 show both general and common forms of perfect gas equations of state. Equation 2.6 is for a calorically perfect gas with the assumption that the specific heat at constant volume C_v is a constant. Equation 2.7 presents the perfect gas equation of state.

$$e = e(\rho, T) = C_v T = \frac{p}{(\gamma - 1)\rho} \quad (2.6)$$

$$p = p(\rho, T) = \rho R T \quad (2.7)$$

2.2 Boundary Conditions

Unsteady boundary conditions have largely been developed in fields such as turbulence and acoustics that are concerned with waves moving through the boundary. Work in unsteady fluid dynamics areas such as turbulence simulation has produced inflow boundary methods based on linear theory eigenfunctions. Outflow boundary treatments are typified by extrapolations or radiation methods. Radiation methods allow small amplitude waves to propagate out of a domain without producing reflected waves. Large amplitude waves, especially shocks, generally cause these methods to fail.

Research in unsteady inlet boundary conditions has grown as numerical simulation of turbulence has become more practical. Rogallo and Moin [59] discuss some of the earlier methods such as the “frozen turbulence” approximation, irrotational free stream, the forcing of continuity, and stress-free boundary conditions ($v_n = 0$ and $\frac{\partial u_t}{\partial x_n} = 0$). These approaches were many of the common methods in use at that time for turbulent inflow, outflow and wall boundary conditions. Subsequent research by investigators [57, 13, 76, 63, 64, 78, 39, 60] has used either the full complex eigenfunctions or the real part of eigenfunctions to provide the unsteady behavior around the inlet mean profile. Numerous simplified versions are commonly used; such as the addition of perturbations to only the axial velocity [38] or requiring perturbations of select boundary variables to be zero [78, 8]. The most common approach has been to employ the form of the real part of the eigenfunction as an amplitude profile for a sinusoidal series, with each term driven at a different frequency. Typically only the most unstable frequency and two or three sub-harmonic frequencies are used [64, 78, 60, 39]. Several researchers [8, 39, 49] have used FFT’s from experimental data to model the specific frequency spectra of an experiment. The models derived from experimental data typically contain from nine to 13 frequencies. Moin [47] found that inflow disturbances based on the fundamental and several sub-harmonic frequencies resulted in equilibrium turbulence characteristics within the distance convected in 0.3 eddy turnover time. Alternative methods include the use of directly computed turbulence through extended inflow regions or other ad hoc methods such as periodic inflow-outflow conditions or the direct addition of a scaled random number. The purpose of these methods has been to introduce unsteady behavior that mimics both time-averaged and dynamic behaviors of real flows correctly.

The accuracy with which a simulation reproduces real flow behavior depends on how closely the boundary conditions mimic the behavior of the physical variables. The approach taken in this work has been to develop a simple disturbance form that uses physically based coefficients and has a minimum of ad hoc constants. The inflow boundary conditions are divided into their steady and unsteady parts. The steady boundary conditions are unchanged from those that have historically been used for steady computational fluid mechanics problem. The unsteady perturbations build upon knowledge from linear stability theory eigenfunctions but use only a single sinusoidal term driven by a single frequency. A random phase is added to the perturbation to give a white noise characteristic. For the outflow

boundary an extrapolation method has been developed that tolerates shock-like gradients moving through the boundary.

2.2.1 Steady Boundary Conditions

The steady boundary conditions used for this simulation are the mean variable profiles at the inflow plane and hard reflecting insulated surface conditions for the channel walls. The primitive variables are fully specified at the inflow plane due to the totally supersonic inflow conditions. The mean profiles of the primitive variables at the inflow plane are based upon an assumed hyperbolic velocity profile and isentropic fluid mechanics. The boundary conditions at the outflow boundary are determined from the interior conditions since the flow generally remains supersonic. An exception to the general outflow boundary conditions occurs when a localized cell of subsonic flow develops. The subsonic cell is treated as a convecting cell that is only influenced by the immediately surrounding gas. Reflected cell boundary conditions are used at the solid walls to ensure that the only physical boundary condition, vanishing normal velocity, is imposed.

The Inflow Boundary

Accurate definition of the shear layer's physical behavior at an inflow is typically made difficult by poor quality and limited quantity of experimental data from the inflow plane. The strong gradients and severe flow conditions make the inflow region a difficult area to describe accurately for both experimental and numerical investigators. Experimental data from Martens as close as 0.02 m to the inflow plane significantly improves the estimation of the initial shear layer thickness and velocity profile shape and perturbation level. Martens' experiment was designed as a balanced pressure shear layer to give a uniform static pressure field. The nominal Mach numbers and equal static pressure field data along with the known total conditions of each stream, are used to determine the remaining variables. The simulation conditions for both cases are given in Table 1.3. The remaining unknowns are less well defined information such as the velocity profile shape and the shear layer thickness.

In Figure 2.1, Martens' data for Case I conditions at 0.02 m show that the shear layer was extremely thin. Based on the velocity profile at this axial position, the experimental shear layer was estimated to be 0.002 m thick. The inlet velocity profile used for the inlet

boundary condition is also plotted in Figure 2.1 for comparison. Two questions arose for this simulation. For a very thin shear layer at supersonic speeds is the velocity profile a primary contributor to the shear layer behavior? And, what is the impact of the grid system's ability to resolve the profile? Other investigators [64] have shown that for incompressible flow, the shape of the velocity profile influences the asymmetry and non-linearity of the mixing process. The complex shape of a boundary layer generated wake could not be resolved adequately by the desired grid system but the hyperbolic tangent profile could be resolved. A poorly resolved wake was explored briefly for the very thin shear layer but no discernible differences from the hyperbolic profile were found. Therefore, a hyperbolic tangent profile was used as the mean shape of the axial velocity. Thicknesses of 0.008, 0.005 and 0.002 m were investigated numerically. The smallest thickness, 0.002 m, was selected as giving the most satisfactory comparison with the near inflow experimental data.

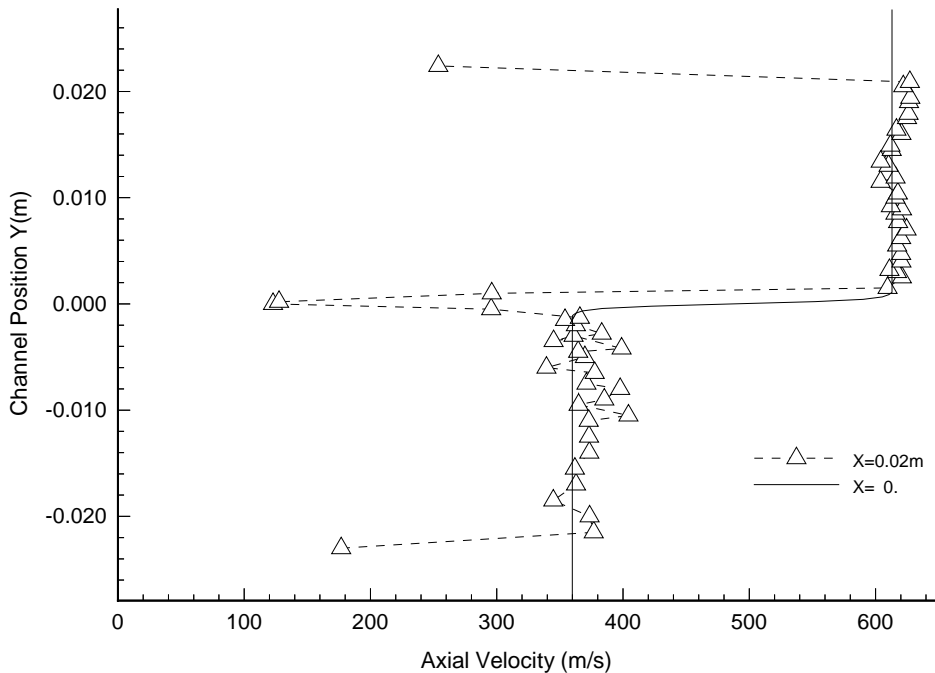


Figure 2.1. Case I $M_c = 0.5$: The experiment velocity profile at 0.02 m and the simulation inlet boundary mean velocity profile at 0. m

At the inflow the two streams were joined by specifying the mean axial velocity profile u and a uniform static pressure p . The hyperbolic profile used for the mean axial velocity had the form

$$u = \left(\frac{u_1 + u_2}{2} \right) + \left(\frac{u_1 - u_2}{2} \right) \tanh \left(\frac{2.65 * y}{\delta/2} \right) \quad (2.8)$$

where u_1 and u_2 are the high speed and low speed streams respectively. The parameter y is the transverse distance from the splitter and δ is the inlet shear layer thickness (0.002 m). The mean transverse velocity v was set to zero across the inflow plane. With the velocity profiles defined and the pressure specified the temperature and density profiles were determined to complete the inflow conditions. The temperature profile for each stream was calculated from the known total temperature and velocity profile using the isentropic relation. The inflow conditions were completed using the perfect gas equation of state to find the density profile. At the walls a free-slip condition was assumed.

The Outflow Boundary

At supersonic outflow conditions no flow information is transmitted into the domain from downstream events. Therefore, the supersonic outflow plane conditions were calculated as part of the interior domain. The shear layer conditions produce vortices that have enough circulation to produce occasional pockets of subsonic flow that move through the boundary. The outflow treatment of the boundary was modified to test for subsonic cells and to provide the necessary physical boundary condition. The subsonic pockets of flow have Mach numbers as low as ≈ 0.9 in the low speed stream. From visual observations of the solution contours, the subsonic regions had only a small influence on surrounding gas. The one-dimensional characteristic equations were added to treat the subsonic regions. Application of the one-dimensional characteristic equations assumed that the transverse velocity behavior was unchanged by the boundary as the gas convected through it. The constant static pressure condition typically used for time averaged subsonic outflows was not appropriate. While the time averaged static pressure was nearly uniform, local peaks and depressions in static pressure traveled with each vortex. The constant value boundary condition artificially distorted the solution as the local pressure variations moved through

the boundary. The static pressure from the previous solution time step was used to give the most realistic outflow conditions. No experimental data was available as far down stream as the exit plane but numerical tests showed the subsonic effect to be very local and transient. The one-dimensional treatment provided an adequate measure of subsonic influence into the domain without contributing a large computational expense.

Wall

The solid walls that confine the flow were treated as ideal reflecting adiabatic walls. Characteristic analysis at the wall boundary yielded only a single positive eigenvalue that required a physical boundary condition. The single physical wall boundary condition required was a vanishing normal velocity, $v_n = 0$. Implementation of the wall condition was based on the concept of reflected cells [25, 50]. The flow variables at reflection cells were defined so that all normal fluxes vanished at the wall.

2.2.2 Unsteady Boundary Conditions

Development of “natural” inflow conditions has not received a lot of attention to date. Researchers have used a broad array of concepts to introduce unsteadiness from numerical truncation error to small perturbations added to a mean flow variable. The small perturbation methods took on forms from planar pulsating of the inflow velocity to more complicated disturbances driven by series of sinusoidal functions. Many of these disturbance techniques were explored as part of this research but none were able to overcome the need for a flow maturation region. The use of a maturation region requires shifting the numerical results some artificial distance to form a virtual origin. Comparisons are then made between the shifted computational results and experimental data. None of the methods found in the literature produced a realistic mimicking of the inflow flow behavior such that a virtual origin was not required to show close comparison with experimental data. By combining ideas and data from stability theory and turbulence research a method was developed that yields good comparisons with experimental data and uses only simple inflow specifications.

Use of the eigenfunction profiles for the perturbation of inflow variables produced Euler simulations with results very similar to linear theory. However, eigenfunctions are of limited usefulness for two reasons: 1) they are based upon an assumed known mean

flow field and 2) their complex number functions are difficult to relate to physical inflow data. However, the use of the eigenfunctions caused the magnitude, phase, and drive characteristics of the velocity components, the pressure, and the density disturbances to all be examined. The basic drive characteristic of each perturbation was chosen to be a single sinusoid. The magnitude and shape of the u and v velocity disturbances were derived from subsonic plane mixing experiments of Plesniak and Johnston [54]. To approximate the shape of the velocity profiles a normalized Gaussian distribution was assumed. The Gaussian was normalized by its peak magnitude and the $\pm 2\sigma$ width was matched to the shear layer thickness. The disturbance magnitude then became a coefficient to the Gaussian profile. The axial perturbation, $\Delta U_{disturb}$, was specified to be a few tenths (0.3 – 0.4) of a percent of the high speed stream inflow velocity. The transverse velocity perturbation was specified by an additional coefficient that gave its relative magnitude to the axial perturbation. The Δv_{factor} was set at 0.7 (70%) based on data from Plesniak and Johnston [54]. A constant phase difference of 90° between the axial and transverse disturbances was added by using cosine and sine functions respectively to drive the perturbations. The basic unsteady velocity equations now has the form

$$u = u_{mean} + \Delta U_{disturb} \cdot Gaussian \cdot \cos(\omega_{drive} \cdot t) \quad (2.9)$$

$$v = \Delta v_{factor} \cdot \Delta U_{disturb} \cdot Gaussian \cdot \sin(\omega_{drive} \cdot t) \quad (2.10)$$

The exact relationships between the pressure and density are unknown; therefore, simplifying assumptions were made. The pressure perturbations were limited in magnitude to the levels produced by the maximum velocity disturbance levels based on incompressible flow. The Bernoulli equation was used to determine the magnitude, frequency and phase of the pressure perturbation relative to the unsteady velocity components. The expansion of both shear layer streams to a common pressure level provided the constant mean pressure across the inlet. The pressure mean field and perturbations yielded the following unsteady pressure equation

$$p = p_{mean} + \Delta p_{disturb} \cdot Gaussian \cdot \sin(-2\omega_{drive} \cdot t) \quad (2.11)$$

To preserve consistency and boundedness in the fluctuating inflow variables, the mean total energy profile was assumed to be constant. The unsteady density was then solved for using the total energy equation.

$$\rho = \frac{p}{(\gamma - 1)((e_t)_{mean} - \frac{1}{2}(u^2 + v^2))} \quad (2.12)$$

This complex process allows inflow disturbances to be defined in terms of conventional experimental data, mean profiles and perturbation amplitudes. It also maintains consistency between the thermodynamic variables and maintains them within physically realistic bounds. The boundary variables now have a sinusoidal unsteadiness. The unsteadiness could now be thought of as the disturbance amplitude of very small coherent turbulence eddies rolling past the boundary point. At this point the disturbance was similar to methods used by many turbulence and shear layer researchers who added sinusoidal disturbances at the most unstable frequencies and several of its harmonics. The inflow disturbance lacked the randomness of scales seen in small scale turbulence. The randomness seen in natural flows was contributed by adding a random phase disturbance.

Random Disturbance

Randomization of the sinusoidal disturbances was still needed to produce a natural white noise disturbance behavior. The random walk concept was used by Sandham and Reynolds [64] to add unsteadiness to the inflow physical variables. A random walk process produces a definable drift in the mean value of the randomized variable. Consider a point that moves along a line in one-dimensional space. The point moves along the line by means of successive jumps to the left and to the right. For any given jump it has a probability p that the jump will be to the right and a probability $1 - p$ that the jump will be to the left. If successive jumps are independent, the point will move along the line at a speed dependent on the size of each Δx . This basic scheme can be elaborated on in a variety of ways such as varying Δx at each step. The method of implementation had to consider that the phase behavior of the inflow variables was being controlled by sine and cosine functions. A randomized phase disturbance was developed from a mean speed or drift and a randomized disturbance to that mean speed. The mean speed or drift was defined by a

frequency multiplied by the solution time variable. The randomized phase disturbance was designed as a phase step size multiplied by a random variable that ranged from zero to one. The random phase equation had the following form

$$\phi = \phi + \text{sign}(\Delta\phi_{\text{disturbance}}, \text{random}), \quad -1 \leq \text{random} \leq 1. \quad (2.13)$$

By adding the phase parameter, ϕ , to accumulate random size increments at each time step, the unsteadiness now has a complex random nature to drive the sinusoidal variation. The final disturbance equation for each inflow variable has the generic form

$$\psi = \psi_{\text{mean}} + \psi_{\text{disturbance}} \cdot \cos(\omega_{\text{drift}} \cdot t + \phi) \quad (2.14)$$

The magnitude of the $\Delta\phi_{\text{disturbance}}$ has an important effect on the final disturbance time history. The magnitude of the phase increment controls the effective frequencies introduced into the solution. Very large phase increments produced very choppy behavior of the disturbance and very small increments produced insufficient choppiness to mask the basic driving frequency. Phase increments in the range between 3 and 6 degrees were found to be most effective. The influence on the disturbance signal is shown in Figure 2.2 for zero, one and six degrees of disturbance respectively. Six degrees of disturbance was used throughout this research. It successfully mimicked the white noise behavior of small scale turbulence and masked the basic driving frequency of the disturbance functions.

A final but key issue in implementing unsteady boundary conditions is physical consistency. For high energy flows such as simulated in this work, randomly assigned small percentage changes in all the physical variables can eventually lead to an unstable solution. From early simulation runs it was discovered that energy and density are closely coupled in the solution. As a consequence, consistency was forced between density and energy. Pressure and both velocity components were randomly disturbed about their mean profiles; but, density was computed from the disturbed variables and the mean total energy profile. A limit on the pressure variation was found using Bernoulli's equation to determine the maximum change in static pressure that would be caused by the peak velocity disturbances. This procedure was found to be very effective in ensuring that disturbed variables maintained values within certain finite limits and that the energy, and consequently density,

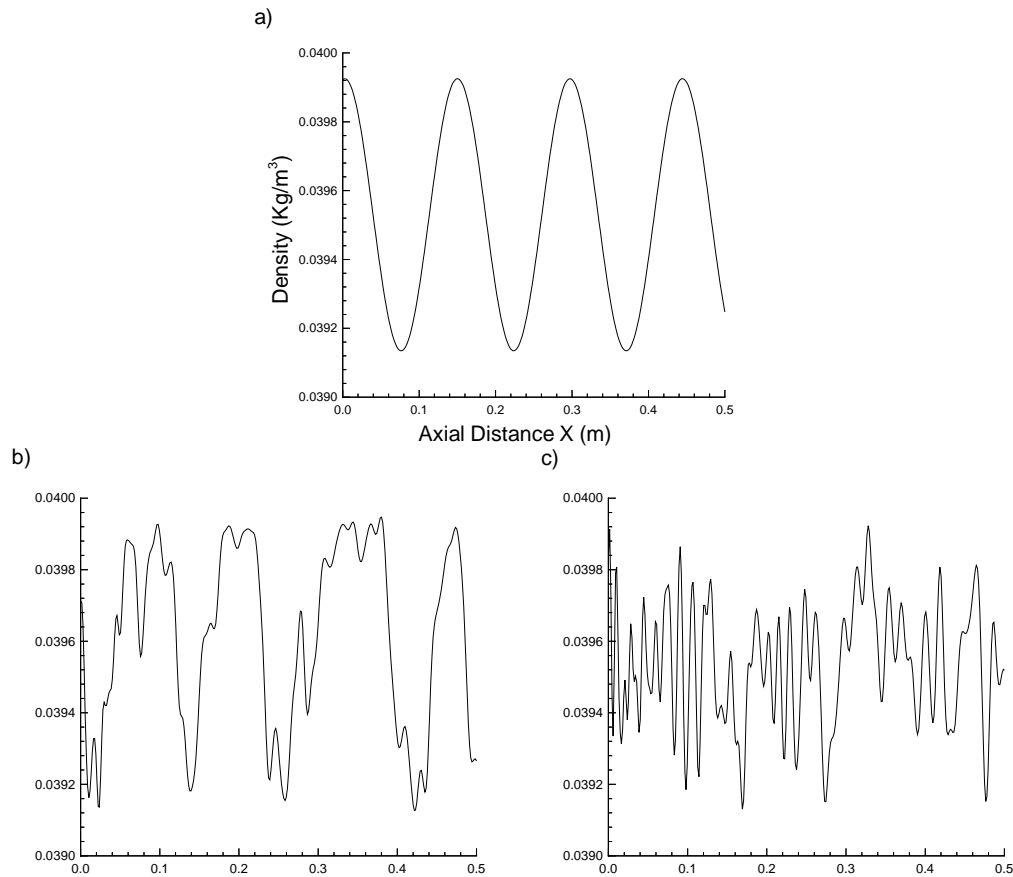


Figure 2.2. Unsteady Boundary: Random Disturbance Effect on a Sinusoidal Unsteady Condition; a) Zero Degrees Disturbance, b) One Degree Disturbance, and c) Six Degrees Disturbance.

remained bounded. Use of disturbance equations with randomization produced realistic results and successfully eliminated the use of a virtual origin for obtaining close comparisons with experimental data.

2.2.3 Linear Theory Eigenfunctions

Simulations of the shear layer for single frequency excitation were developed to examine the code's basic ability to reproduce dynamic behavior correctly. Linear instability theory has been used for many years to predict the behavior of shear layers due to small amplitude disturbances. Consequently linear theory provided an excellent source of the

perturbation functions and the disturbance behavior for comparison with numerical simulations. The shear layer mean velocity field was computed using the unsteady inlet conditions and was provided as input to a solution of the Rayleigh perturbation equation. The Rayleigh equation was solved to find the eigenfunctions. The eigenfunction form is shown by Equation 2.15.

$$\phi = e^{-\alpha_I x} \left[\hat{\phi}_r \cos(\alpha_r x - \omega t) - \hat{\phi}_I \sin(\alpha_r x - \omega t) \right] \quad (2.15)$$

The eigenfunctions are a complete description of the primitive variable's behavior for a single frequency. They provide a precise description across the entire inflow; and, they are thermodynamically consistent. At the inflow plane the stream-wise dependency x drops out and the inflow eigenfunction boundary conditions become

$$\phi = \hat{\phi}_r \cos(-\omega t) - \hat{\phi}_I \sin(-\omega t) \quad (2.16)$$

A complete set of eigenfunctions at the inflow plane for Case I conditions are shown in Figure 2.3. The eigenfunctions and the analytical results used for comparison were provided by Lockard [37].

The governing equations, the steady, the unsteady, and the eigenfunction boundary conditions all form the basis of the numerical simulations that were conducted. The ability of these equations to correctly simulate the shear layer is influenced strongly by their numerical implementation. The next chapter discusses the numerical methods used to transform the equations into computer solvable finite difference equations. The methods used influence everything from the frequencies that can be resolved to the accuracy to which they can be resolved, the stability of the solution process and the speed at which the solution can be computed.

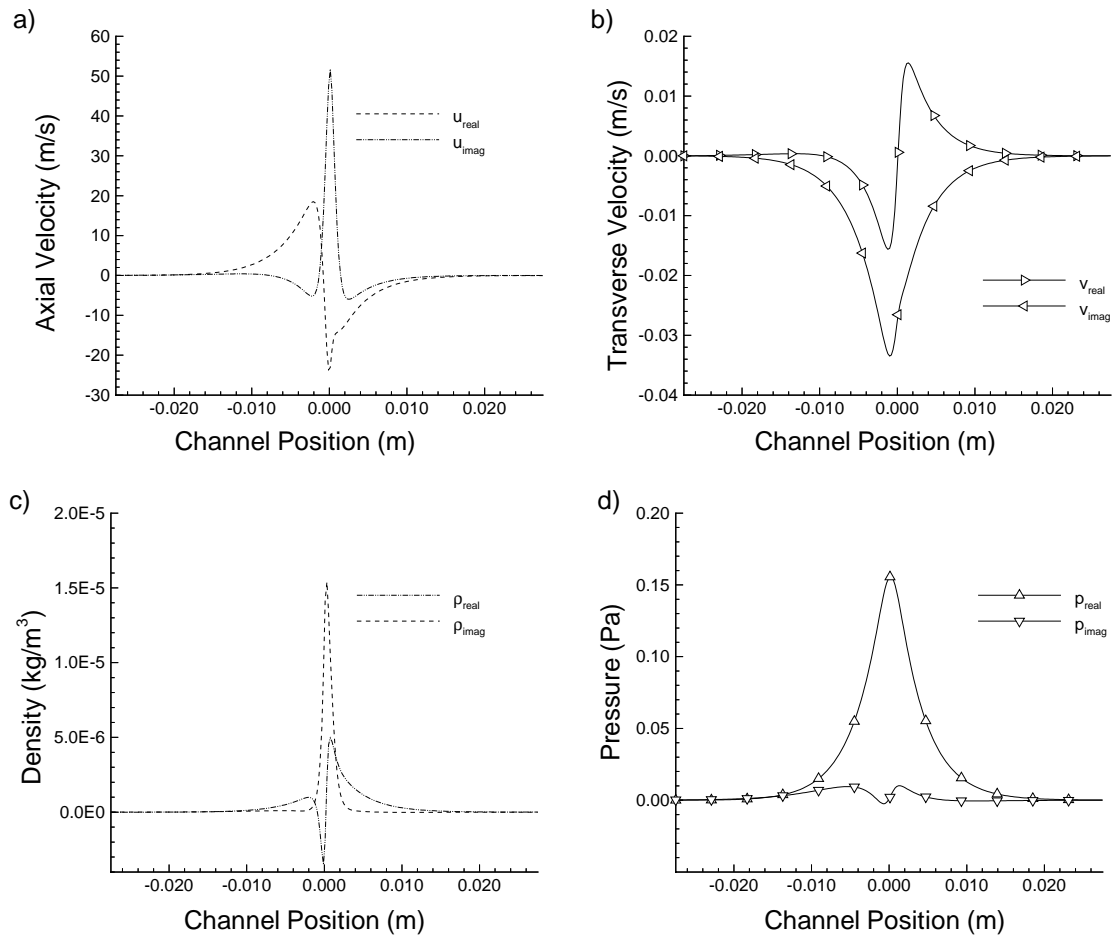


Figure 2.3. Rayleigh Equation Eigenfunctions at the Inlet for Case I, $M_c = 0.5$ Conditions; a) Axial Velocity m/s , b) Transverse Velocity m/s , c) Density kg/m_3 , and d) Pressure Pa .

Chapter 3

Numerical Formulation

The time-dependent Euler equations are well matched to the MacCormack two-step numerical scheme used to integrate the governing equations. For this simulation the inlet was treated as fully supersonic; the outlet was treated as a mix of supersonic and subsonic flow; and the walls were treated as parallel hard reflecting surfaces. In the experimental flow there are subsonic regions in each boundary layer and in the immediate wake of the splitter plate. For the Euler simulations presented in this thesis, the boundary layers do not exist and the splitter wake was assumed to yield a hyperbolic tangent profile immediately downstream of the splitter. A Cartesian grid system was used.

3.1 MacCormack 2-4 Method

The MacCormack 2-4 method has been used by many researchers investigating shear flows. The higher-order accuracy of the fourth-order derivative in space is needed to resolve the nonlinear behavior of the flow accurately, especially if turbulence quantities are to be resolved. The MacCormack 2-4 scheme was developed by Gottlieb and Turkel [18]. The method is a predictor-corrector scheme that is second-order in time and fourth-order in space. Gottlieb and Turkel investigated the von Neumann stability limits for this method using the convection and the diffusion model equations. For the convection equation the stability is achieved for CFL numbers of $2/3$ or less. They also determined the diffusion coefficient limit of $3/8$ for the diffusion equation. The von Neumann stability analysis for both equations is presented in detail in Appendix A. The potential application of the method to the Navier-Stokes equations was examined by development of the von Neumann analysis of the convection-diffusion model equation. The analysis found a cell Reynolds number type of relationship between the CFL and diffusion coefficient limit equations. The limit was supported in practice when to attempts compute viscous solutions would remain stable for only a relatively small number of time steps. Detailed von Neumann stability analysis of the convection-diffusion equation is presented in Appendix A.

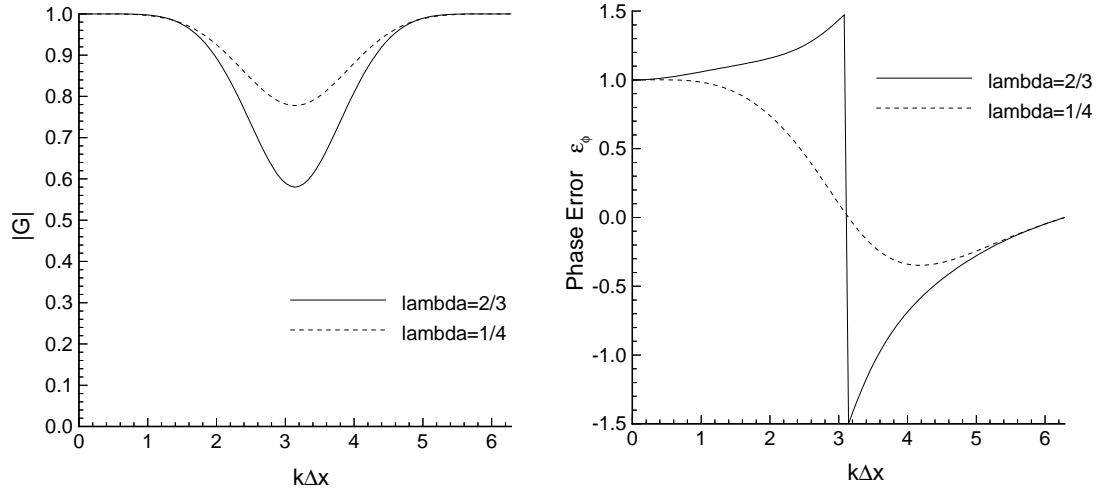


Figure 3.1. Amplification and Phase Error Behaviors of the MacCormack 2-4 Method applied to the convection model equation. Behaviors for two CFL numbers (λ) $2/3$ and $1/4$ are shown.

The amplification and phase error behaviors of the MacCormack 2-4 method as applied to the convection equation are shown in Figure 3.1. The figure shows that both the amplification factor damping and the phase error improve as the CFL number is reduced from $2/3$ to $1/4$. THE CFL number of 0.25 has less damping and less phase error, especially for the lower wave numbers. The phase error also changes from a leading error to a lagging error. The most accurate wave representation occurs when the amplification damping and phase error are within acceptably small limits. Based on this analysis, waves that are represented by a $k\Delta x$ of 0.8 or less are considered accurately resolved.

In their analysis of the method Gottlieb and Turkel [18] make the statement that the method becomes time accurate at CFL numbers less than $1/4$. This is based on the magnitude of the time error approaching the same magnitude as the spatial error. One-dimensional simulations of acoustic waves were conducted to examine the predicted wave speeds for a range of CFL numbers from $2/3$ to $1/4$. The tests demonstrated that acoustic wave speeds are not predicted accurately until the CFL numbers approaches 0.25 . Based on the results of these tests and the von Neumann analysis, all the simulations conducted in this research used a CFL number of 0.25 .

Application of the MacCormack 2-4 method begins with the hyperbolic form of the Euler equations. The Euler equations in two dimensions take the form

$$\frac{\partial Q}{\partial t} + \frac{\partial E}{\partial x} + \frac{\partial F}{\partial y} = 0 \quad (3.1)$$

where Q is the conservative variable vector written $Q = (\rho, \rho u, \rho v, \rho e)^T$ and E and F are the mass, momentum, and energy flux vectors. In 1963 Strang [71, 72] developed the concept used by MacCormack's method of representing the multidimensional difference operator as a product of one-dimensional operators. The split operator method developed by Strang was for linear systems. However, Gottlieb [17] later demonstrated that the method was also valid for the non-linear case. Similar to the second-order MacCormack scheme, the MacCormack 2-4 method can be time split into separate spatial operators. The time-split form improves stability and increases the time-step limit. Time-splitting gives the following operator form

$$Q_{i,j}^{n+4} = L_x^+(\Delta t_x)L_y^+(\Delta t_y)L_y^-(\Delta t_y)L_x^-(\Delta t_x)Q_{i,j}^n \quad (3.2)$$

where $L_x(\Delta t_x)$ and $L_y(\Delta t_y)$ are one-dimensional time-split operator sequences. The “+” and “-” superscripts denote the forms of the operator in which the embedded predictor-corrector sequences alternate between forward-backward and backward-forward sequencing, respectively. Strang [70] also established the requirement that the operators must be applied in a symmetric sequence to maintain the order of accuracy. To avoid biasing errors, each spatial operator is alternated between a forward-backward and backward-forward sequence of predictor-corrector applications. Each operator includes a double sequence of the basic predictor-corrector stencil. The result of a complete integration cycle, which includes both L^+ and L^- in each direction, is the advancement of the solution four complete Δt time steps. Each one-dimensional predictor-corrector operator is implemented in a four-step, time-split sequence that is illustrated by the following equations.

$$Q_j^{n+1/2} = Q_j^n - \frac{\Delta t}{6\Delta x}(-7E_j^n + 8E_{j+1}^n - E_{j+2}^n) \quad j = 1, \dots, N - 2. \quad (3.3)$$

$$Q_j^{n+1} = \frac{1}{2}[Q_j^{n+1/2} + Q_j^n] - \frac{\Delta t}{12\Delta x}(7E_j^{n+1/2} - 8E_{j-1}^{n+1/2} + E_{j-2}^{n+1/2}) \quad j = 3, \dots, N. \quad (3.4)$$

$$Q_j^{n+3/2} = Q_j^{n+1} - \frac{\Delta t}{6\Delta x}(7E_j^{n+1} - 8E_{j-1}^{n+1} + E_{j-2}^{n+1}) \quad j = 1, \dots, N - 2. \quad (3.5)$$

$$Q_j^{n+2} = \frac{1}{2}[Q_j^{n+3/2} + Q_j^n] - \frac{\Delta t}{12\Delta x}(-7E_j^{n+3/2} + 8E_{j+1}^{n+3/2} - E_{j+2}^{n+3/2}) \quad j = 3, \dots, N. \quad (3.6)$$

Each predictor or corrector operator can not directly compute either the first or last two grid points in each direction because of the one-sided stencils used. The alternating forward-backward and backward-forward sequence of application increases the number of specially coded boundary treatments needed to compute all the possible alternatives. Some authors [77, 3] have incorporated their extrapolation schemes into the predictor and corrector equations. However, coding and computing efficiencies were gained by separating the directly computable interior solution and the extrapolated ghost cell regions $j \leq 2$ or $j \geq N - 2$. One corner of the grid system with two ghost cell borders is illustrated in Figure 3.2. During integration the basic predictor or corrector operators are used to integrate the non-linear Euler equations over their complete $N - 2$ domain. The solution for the remaining two rows of points ($i = 1, 2$ or $N - 1, N$) are found using an alternative method. That alternative method is a combination of boundary conditions and extrapolation. The interior grid locations $j = 3$ or $j = N - 2$ are treated with the appropriate boundary condition at each operator application. The interior solution and boundary conditions are then extrapolated to the ghost cells. The continual boundary updates keep the interior and boundary solutions in close synchronization with each time-split operator as it steps across two time steps. The boundary conditions and the ghost cell treatment are key elements in how successfully the unsteady boundary conditions are transmitted into the simulation. They are discussed below in subsequent sections.

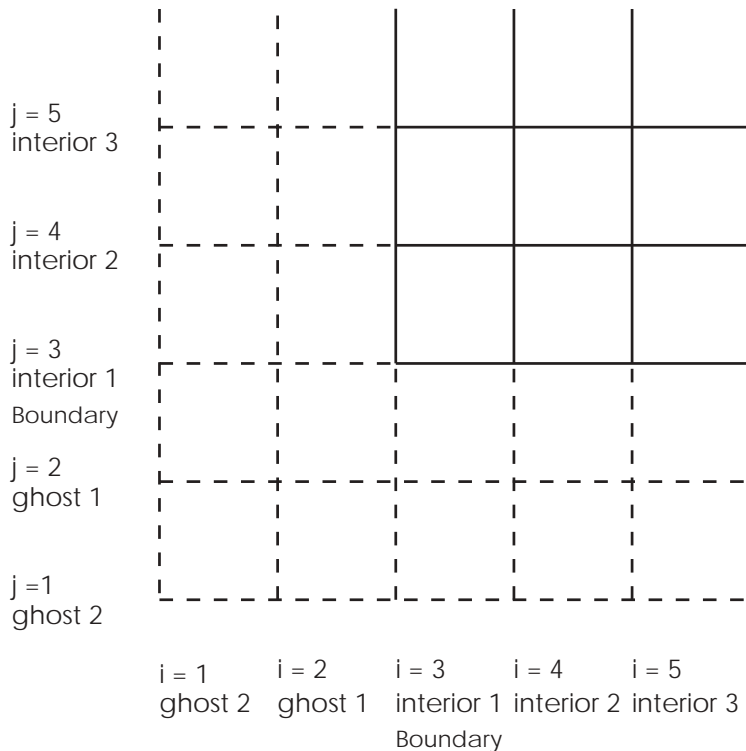


Figure 3.2. Interior, Boundary, and Ghost Cell Locations.

3.2 Artificial Viscosity

3.2.1 Modified Jameson

As the shear layer solution progresses in time, strong dispersion effects occur and grow at the shear layer interface. The addition of artificial viscosity is a common method used to dampen strong dispersion effects and unstable growth. The static pressure field in the shear layer is nominally constant across both high and low speed streams; but, the temperature and density both changed significantly. The density difference between the low to high Mach number streams is a factor of approximately two. This strong density change causes the split MacCormack operator L_y to see a shock-like increase in the conservative variables density and total energy. The modified form of Jameson's artificial viscosity damps the non-physical dispersion errors that occur. The Jameson type of artificial viscosity was chosen due to its selective application of second or fourth order damping to the flux terms. The basic form of the method is given by

$$E^{AV} = E - \epsilon^{(2)} \frac{\partial U}{\partial x} + \epsilon^{(4)} \frac{\partial^3 U}{\partial x^3} \quad (3.7)$$

The magnitudes of the computed coefficients $\epsilon^{(2)}$ and $\epsilon^{(4)}$ determine the amount of second and fourth order damping, respectively. The standard form of Jameson artificial viscosity uses a pressure gradient switch to add second order damping in regions of large discontinuities. However, the pressure based switch is ineffective in the nearly uniform pressure field of the shear layer. The pressure terms of coefficient $\epsilon^{(2)}$ were directly replaced with the density variable. The modified switch was tested in simulations of the Riemann shock tube problem. It demonstrated nearly identical behavior to the pressure based switch. The density based switch is shown in Equation 3.8. The fourth order damping coefficient did not require any modification or variable changes.

$$\epsilon_i^{(2)} = \alpha_2 (|u| + c)_i \frac{|\rho_{i+1} - 2\rho_i + \rho_{i-1}|}{\rho_{i+1} + 2\rho_i + \rho_{i-1}} \quad (3.8)$$

and

$$\epsilon_i^{(4)} = \max[0, \alpha_4 (|u| + c)_i - \epsilon_i^{(2)}] \quad (3.9)$$

The recommended constants α_2 and α_4 remain unchanged from the values 0.24 and 1/256, given in Hirsch [25]. Slight performance gains can be achieved by tuning the constants.

Application of the density switch to the shear layer problem was very effective. The modified Jameson method effectively stabilized the shear layer solution. Startup from the estimate of the initial flow field is the only situation that occasionally required high levels of damping. To avoid frequent changing the constants α_2 and α_4 , an additional method of damping by Sankar was added during startup calculations.

3.2.2 High Order Sankar Damping

Sankar [66] introduced a filter for aeroacoustics applications that was explored as a competing method to Jameson artificial damping. Sankar has demonstrated the method's ability to dampen very high frequency non-physical oscillations. The filter provides a high order damping by adding an explicit term to each conservative flux term that is an average

of the local fourth-order gradient in each of the dimensional directions. The filter has the form

$$D = -\epsilon [q_{i+2,j} - 4q_{i+1,j} + 12q_{i,j} - 4q_{i-1,j} + q_{i-2,j} + q_{i,j+2} - 4q_{i,j+1} - 4q_{i,j-1} + q_{i,j-2}] \quad (3.10)$$

where ϵ is a user-supplied coefficient. Sankar suggested ϵ be on the order of $(1/32)$. With the suggested coefficient, Sankar's filter has a powerful influence on the solution. The intent of the Euler solutions was to run with as little dissipation as needed to make the numerical scheme stable. Consequently, Sankar's filter was only used when start-up disturbances were present.

3.3 Grid

The grid system used for the numerical simulations was developed by examining five issues: 1) the ability to resolve the axial length of the instability wave, 2) the ability to resolve the shear layer velocity profile, 3) the ability to resolve acoustic frequencies in the two streams, 4) the maintenance of acceptable cell aspect ratios and 5) the consideration of computer memory capacity. The ability to resolve a wave was first assessed by determining the number of points required by the numerical scheme to resolve a wave. From the stability analysis presented in the previous chapter, The MacCormack method can accurately resolve waves for which the grid system provides about 8 points per wave. A second method of assessing the ability of a numerical scheme to accurately resolve a wave is by examining the methods degree preservation of the wave's dispersion relation. Tam and Webb [74] developed a method for evaluating the ability of a finite difference equation accurately compute a wave. The key steps of the method begin with the finite difference equation written in a general form as

$$\frac{\partial f}{\partial x}(x) \cong \frac{1}{\Delta x} \sum_{j=-N}^M a_j f(x + j\Delta x) \quad (3.11)$$

where the a_j 's are the coefficients of the difference scheme. Applying a Fourier transform to both sides yields

$$i\bar{\kappa}\tilde{f} \cong \left(\frac{1}{\Delta x} \sum_{j=-N}^M a_j e^{i\kappa j \Delta x} \right) \tilde{f} \quad (3.12)$$

Comparing the two sides yields a relationship for the wave number of the Fourier transform of the finite difference equation 3.11. The final form is given by

$$\bar{\kappa} \cong \left(\frac{-i}{\Delta x} \sum_{j=-N}^M a_j e^{i\kappa j \Delta x} \right) \quad (3.13)$$

Figure 3.3 shows Equation 3.13 plotted for the fourth order central scheme. For the linear wave equation used for von Neumann stability analysis, the MacCormack 2-4 method is equivalent to a fourth order central scheme. The fourth order central scheme is accepted here as being representative of the MacCormack 2-4 scheme. Figure 3.3 shows the close comparison between the fourth order central scheme and the ideal up to about $0.8 \kappa \Delta x$ or approximately 8 points per wave. Ten points per wave were chosen to provide a working margin in development of the simulation grid.

The critical-path sequence for the grid development was inflow velocity profile resolution, computer memory capacity, and the resolved acoustic frequency. The grid system for the two-dimensional simulation provided the greatest spatial resolution over the computational domain. The three-dimensional simulations required compromises in both the physical domain and the frequencies that could be resolved. The reduced resolution of the instability and acoustic waves had a profound impact on both the dynamic and time-averaged results. To help understand the influence of wave resolution on the simulation results, initial estimates were made of the resolved frequencies based upon wave lengths of ten grid spaces.

For each set of simulation conditions the Kelvin-Helmholtz most unstable frequency, and the acoustic frequencies of both the high and low speed streams were estimated. Table 3.1 present the estimated resolved frequencies for each of the three simulations. The lowest upper boundary of acoustic frequency that could be resolved was considered the limiting wave for each simulation. As shown in Table 3.1 for Case I, 2-D $M_c = 0.5$, frequencies of 27888 Hz and below could be computed accurately. Extending the case to three-dimensions reduced the limiting acoustic frequency to 6373 Hz. It also reduced the resolved instability

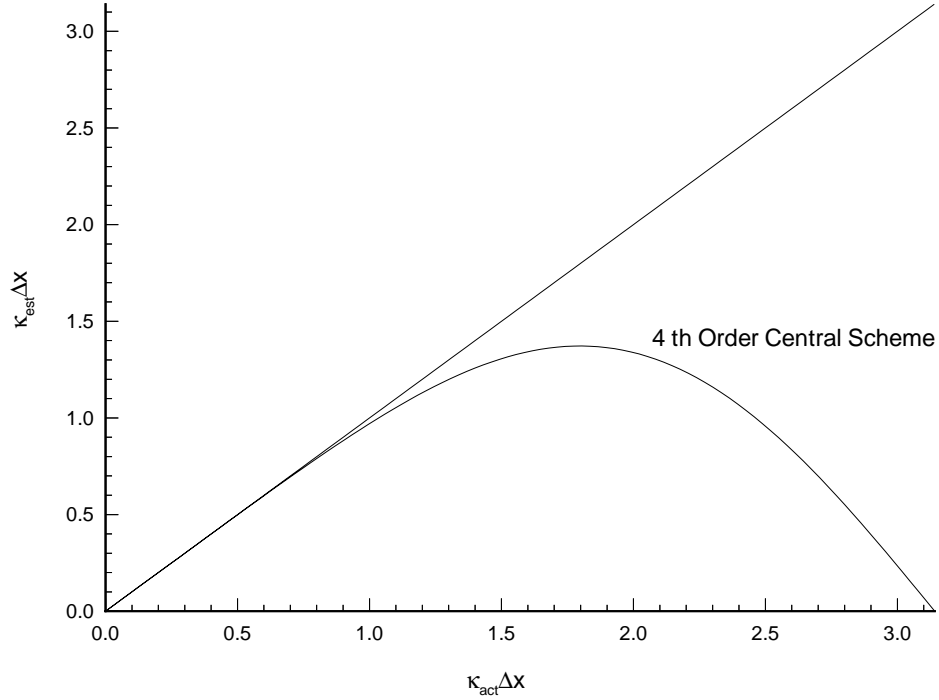


Figure 3.3. Wave number relation for Fourier transform of the fourth order central scheme

wave to less than the expected most unstable frequency. The last question of grid resolution was the question of how close to turbulence dissipation scales could be resolved with the fine grain grid.

The lower limit of the grid's ability to resolve large scale motions was examined by finding the local Kolmogorov scales at the inlet and shear layer growth saturation locations (for 2-D at $x = 0$, and $\approx 0.3m$). The experimental conditions and the local shear layer thickness were used to compute a local Reynolds number. The ratio of the Kolmogorov scale length η to the large scale length l was determined from

$$\frac{\eta}{l} = Rey^{-\frac{3}{4}} \quad (3.14)$$

The local length scales used were $l_{inlet} = 0.002 m$ and $l_{saturation} = 0.02 m$. The computed Kolmogorov scales in both the axial and transverse directions were approximately two

Table 3.1. Grid Resolved Frequencies

	Kelvin-Helmholtz Instability	High Speed Stream Acoustic	Low Speed Stream Acoustic
Case I, 2-D $M_c = 0.5$	28 points @ 25 kHz	27,888 kHz	41,060 kHz
Case I, 3-D $M_c = 0.5$	6 points @ 25 kHz	6,373 kHz	9,384 kHz
Case II, 2-D $M_c = 0.64$	11 points @ 30 kHz	22,546 kHz	40,747 kHz

orders of magnitude $O(10^2)$ smaller than the shear layer local thickness scales at both axial locations. The fine grid resolution controls not only the scale of the waves that could be resolved but also the basic programs memory requirements and overall speed.

For the two-dimensional simulations the final grid provided nine points across the inflow velocity profile. The 768 length by 256 height grid yielded a cell aspect ratio of 3.5 and required 389 Mbytes of memory to run on the 256 node CM-5 at NCSA. The computed domain physical size was 0.5625 m in length and 0.055 m in height. The compute time was 1.6×10^{-6} seconds per grid point per solution time step. The 256 node CM-5 has a theoretical peak speed of 32 Gigaflops per second. The Euler code ran at 1.3 Gigaflops per second, or 4% of peak. The numerous variables and physical parameters that were collected pushed the code memory requirement to approximately 2000 bytes per grid point.

The physical domain for the three-dimensional case was reduced to 0.40 m in length, 0.055 m in height and 0.12 m in width. The grid for the length, height and width of the three-dimensional simulations was 256 by 128 by 160, respectively, for a total of 5,242,880 points. This grid provided five points across the inflow velocity profile. The 256 length by 128 height grid maintained the a cell aspect ratio at the two dimensional value of 3.5. The number of stored variables and physical parameters was reduced dropping the memory requirement to 1108 bytes per grid point and 5.6 Gigabytes overall. The compute time was 1.03×10^{-6} seconds per grid point per solution time step. The three-dimensional simulations ran at 1.6 Gigaflops per second, or 5% of peak. For both the two- and three-dimensional simulations the computation of the boundary conditions was the most significant limitation to the speed at which the code ran.

3.4 Boundary Conditions

The experimental problem being solved is predominately supersonic at both the inlet and outlet. When only computing the Euler equations, the inlet was treated as fully supersonic; and, the inflow physical variables were all specified. Supersonic flow conditions at the outlet were calculated directly as part of the interior solution. However, subsonic cells did occur due to the exiting vortices. The flow in these vortices was usually near sonic conditions with a rotational velocity that was slow compared to the convective velocity. The resulting subsonic flow was treated with one-dimensional characteristics. This procedure proved to be practical due to the infrequent occurrence of subsonic cells and their high convection rate. The confining walls were treated as hard reflecting adiabatic walls with slip velocity conditions.

3.4.1 Unsteady Inflow

The basic development of the unsteady inflow conditions was given in the discussion of the mathematical formulation of the inflow conditions. The remaining issues are how to introduce the unsteadiness without introducing a dominant single frequency and how to ensure that the perturbation is accepted into the interior solution.

Unsteadiness must be introduced into the inflow boundary conditions in a reliable way and yet produce a purely random disturbance. In order not to introduce a single driving frequency into the solution, a frequency selection process was developed which yielded a higher frequency than that which can be resolved by the grid. The excitation frequency ω_{shear} was found by dividing the shear layer mean acoustic speed by twice the shear layer thickness. The resulting drive frequency for the Case I shear layer was 63750 Hz. The random walk phase ϕ was added to the unsteady equations to produce the white noise behavior in the perturbations. The final unsteady inflow boundary conditions are given by the following pseudo-code

$$\omega_{shear} = 2\pi \left(\frac{(c_1 + c_2)}{2} \right) \frac{1}{2\delta} \quad (3.15)$$

$$\phi = \phi + \Delta_{walk} * \text{sign}\left(\frac{\pi}{180}, \text{random}\right) \quad \text{where} \quad -1. < \text{random} < +1. \quad (3.16)$$

$$p = p_{mean} + G(y) * \Delta P_{max} * \sin(-2\omega_{shear} * \text{time} + \phi) \quad (3.17)$$

$$u = u_{mean} + G(y) * \Delta U_{max} * \cos(-\omega_{shear} * \text{time} + \phi) \quad (3.18)$$

$$v = G(y) * V_{factor} * \Delta U_{max} * \sin(-\omega_{shear} * \text{time} + \phi) \quad (3.19)$$

$$\rho = \frac{p}{(\gamma - 1) * (e_{tbc} - .5 * (u^2 + v^2))} \quad (3.20)$$

The final issue for the inflow was how to set the ghost cell values such that the prescribed boundary behavior is accepted by the interior scheme. Unsteady inflow conditions severely tax the central difference algorithm's ability to accept the behavior of a rapidly varying variable into the domain. A key contributor to transmission of the boundary condition into the domain is the smoothness of the derivatives. A conventional zero derivative extrapolation method occasionally resulted in a nearly discontinuous change in the solution variable at the ghost cell. Simulations that used this technique had difficulty transmitting the perturbation into the interior domain. Time averaged data showed significant fall-off in the r.m.s. amplitude of the perturbation at the first few grid points in the interior domain. The magnitude of the fall-off showed the interior algorithm's difficulty in accepting both the rapid variation of the boundary value and a non-smooth derivative. The ghost cell extrapolation method discussed in a following section provides a smooth, damped variable behavior. The smooth behavior of the variable and its derivatives greatly reduced the magnitude of disturbance needed to stimulate the flow. Inflow disturbance amplitudes used for the simulation were reduced from several percent of the mean field variable to several tenths of a percent. The reduced values are consistent with levels estimated from experimental data.

Table 3.2. Free Slip and Wall Conditions: Cell Centered Boundary

Density and Pressure (int1 = boundary point)
$\rho_{g1} = \rho_{int2}$
$\rho_{g2} = \rho_{int3}$
$p_{g1} = p_{int2}$
$p_{g2} = p_{int3}$
$\rho_{int1}, t_{int1}, p_{int1}$ <i>calculated</i>
Tangential velocity
u_{wall} <i>calculated</i>
$u_{g1} = u_{int2}$
$u_{g2} = u_{int3}$
Normal velocity
$v_{int1} = 0$
$v_{g1} = -v_{int2}$
$v_{g2} = -v_{int3}$

3.4.2 Wall Conditions

The bounding walls in this simulation are treated as hard reflecting adiabatic surfaces. Symmetry conditions were used to provide wall boundary conditions. Symmetry conditions can be used for boundaries for which the boundary conditions can be expressed as symmetric or antisymmetric reflections of the interior solution. The adiabatic reflecting walls of this simulation are an ideal example. Setting the wall boundary conditions involved setting the ghost cells to symmetric or asymmetric values of interior conditions. The symmetry conditions are equivalent to the zero gradient condition, (i.e. $\frac{\partial p}{\partial n} = 0$) and were used for the physical variables density, and pressure or temperature. The tangential velocity u was also set with symmetry conditions while the condition of zero normal velocity was set using anti-symmetry conditions. The wall boundary conditions and the ghost cell values are given in Table 3.2.

3.4.3 Outflow Conditions

The outflow conditions for the shear layer are predominantly supersonic. Since the supersonic flow characteristics all point out of the domain, the exit boundary conditions

were computed directly as part of the interior solution. The backward stencil used for the MacCormack scheme's predictor-corrector sweeps leaves the last two cells un-computed; and, they must be extrapolated. The extrapolation method developed as part of this research was used to determine the ghost cell values. The extrapolation method is discussed in the following section.

The outflow conditions for the shear layer were not always totally supersonic. Occasionally one of the large vortex structures had sufficient strength to cause the total velocity magnitude in part of the core to drop below sonic conditions. The result was a pocket of fluid advecting axially with a Mach number between .9 and 1.0. The size of the pocket was occasionally not small in relation to the size of the duct; being up to approximately 35% of the channel height. In addition, the pressure at the center of the vortices varied significantly from the mean static level. The subsonic boundary treatment had to provide downstream influence without significantly distorting the vortex pressure field to allow rapid convection of the cell out of the domain and not distort the surrounding supersonic field. The solution was to locally apply the one-dimensional outflow characteristic equations where the flow was subsonic and use the local pressure at the immediately preceding time step as the boundary condition. This small Δp was used to provide the subsonic boundary correction into u and ρ . The transverse velocity was assumed constant. This simple procedure provided the small subsonic influence into the solution.

3.4.4 Ghost Cell Determination

The MacCormack 2-4 method lends itself readily to the treatment of the two outside grid locations of a domain as ghost cells. The one-sided operators of the stencil can not compute the outside cells directly. Therefore, some form of approximation had to be used to obtain their value. The supersonic outflow found in a confined shear layer problem can be treated by classic extrapolations in time or space. Second-order methods have commonly used first or second-order spatial or temporal derivative formulas to determine extrapolated values. While these methods may work, they introduce an ad hoc assumption, (i.e. $\frac{\partial f}{\partial x} = 0$) into the solution. This assumption has little justification other than that it has provided acceptable results. Turkel et al. [77, 3] extended this type of extrapolation to employing higher order derivatives for higher order finite difference schemes. These zero

derivative assumptions can introduce unbounded variable behavior into the solution. The errors propagate into the interior domain solution because of the width of the interior stencil and can cause significant change in the interior solution. The use of improved boundary approximations became especially important as the gradients moving through the boundary were occasionally very large. Some variables could change by a factor of more than two within only several grid spaces.

Some researchers [30] investigating numerical methods have asserted the importance of having the order-of-accuracy of boundary conditions one order-of-accuracy less than the interior scheme. The one-order reduction of accuracy provides improved solution stability at the boundary through artificial viscosity damping. This has been found to improve the stability of high order methods at the boundaries, while minimizing inaccuracies introduced into the interior solution. The approach taken for this work is to model the boundary derivatives and use the resulting stencils to obtain spatial extrapolations to update the ghost cells.

A new extrapolation stencil was developed from the known derivative of the boundary variable. The first derivative of flow variable, f , at the boundary was computed using only interior points. Next the first derivative central difference was set equal to this known derivative. The central difference stencil provides the single unknown at the ghost cell location. The depth of the ghost cell that was reached depended on the width of the central stencil that was used. Conceptually this approach is given by the equation

$$\frac{\partial f}{\partial x} |_{backward} = \frac{\partial f}{\partial x} |_{central} \quad (3.21)$$

Determination of the interior derivative and the ghost cell calculation can be combined into a single stencil. Use of second order accurate difference equations for both the backward and central stencils yielded a single equation for the first ghost cell beyond the boundary. In difference form Equation 3.21 becomes

$$\frac{3f_i - 4f_{i-1} + f_{i-2}}{2\Delta x} = \frac{f_{i+1} - f_{i-1}}{2\Delta x} \quad (3.22)$$

that can be solved for f_{i+1} to give

$$f_{i+1} = 3f_i - 3f_{i-1} + f_{i-2} \quad (3.23)$$

Taylor-series expansions about point i were substituted into the stencil to find the actual partial differential equation being solved. The modified equation solved by stencil Equation 3.23 has the following form

$$\frac{\partial^3 f}{\partial x^3}|_i - \frac{1}{2} \frac{\partial^4 f}{\partial x^4}|_i (\Delta x) + \frac{1}{4} \frac{\partial^5 f}{\partial x^5}|_i (\Delta x)^2 - \dots = 0 \quad (3.24)$$

The modified equation shows the stencil solves the PDE of the third order derivative at i being equal to zero. The advantages of this method are that 1) the stencil is centered on the boundary cell for which all the flow conditions are known, and 2) no assumptions about the value of the flow variables or their derivatives were required to derive the stencil.

The second ghost cell value can be determined in a similar manner by use of either the first or second derivative. Use of the first derivative required the substitution of a high-order central difference stencil to obtain a term at $i+2$. The extrapolation equation for the second ghost cell value is given by

$$f_{i+2} = 8f_{i+1} - 18f_i + 16f_{i-1} - 5f_{i-2} \quad (3.25)$$

This extrapolation formula has a modified equation that also yields a PDE of the third order derivative at i being equal to zero. The PDE has the form:

$$\frac{\partial^3 f}{\partial x^3}|_i - \frac{3}{4} \frac{\partial^4 f}{\partial x^4}|_i (\Delta x) + \frac{\partial^5 f}{\partial x^5}|_i (\Delta x)^2 - \dots = 0 \quad (3.26)$$

The second derivative formulation of the extrapolation equation caused the stencil width to grow to six terms and yielded the following

$$f_{i+2} = 16f_{i+1} - 54f_i + 76f_{i-1} - 49f_{i-2} + 12f_{i-3} \quad (3.27)$$

The modified equation for this stencil yields a PDE with the fourth order derivative at i being equal to zero. The modified equation has the form

$$\frac{\partial^4 f}{\partial x^4}|_i - \frac{12}{11} \frac{\partial^5 f}{\partial x^5}|_i (\Delta x) + \frac{47}{66} \frac{\partial^6 f}{\partial x^6}|_i (\Delta x)^2 - \dots = 0 \quad (3.28)$$

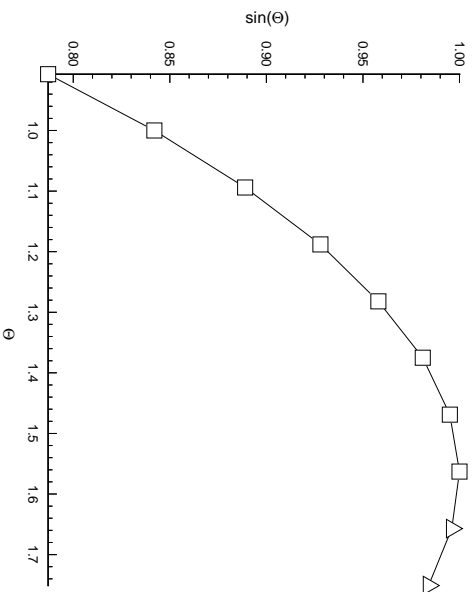


Figure 3.4. Ghost cell modeling past a change in slope of a sine function. The solid line and the squares are an exact sine curve. The two triangle points are extrapolated.

The stencils developed here, Equations 3.23, 3.25, and 3.27, have several key properties that cause them to yield excellent modeling of variables at the extrapolated positions. First, no ad hoc assumptions about the value of the variable or its derivatives were introduced. Second, all three stencils have simple, clean modified equation PDEs based on third-order or higher derivatives. Third, stability is added through artificial damping associated with the first-order accurate approximations. Fourth, extrapolated values are forced to give derivatives at the boundary that are consistent with the interior solution. And fifth, all three stencils are based upon the same boundary point, i . The composite effect is that the solution field at and around the ghost cells is smooth and consistent.

The combination of Equations 3.23 and 3.25 were used for this simulation. They provided excellent outflow behavior, even when severe gradients and large scale structures moved through the boundary. Figure 3.4 shows the ability of this approach to follow a change in the slope of a function smoothly. The smooth curve of a sine function is plotted with a solid line. Square symbols mark the positions of exact calculated points. The two triangle symbols on the right are extrapolated values. Figure 3.5 illustrates the smoothness of the density solution field for a vortex moving through the exit and ghost cell planes. Each identifiable block in the figure represents one grid cell. The last two cells on the right are the extrapolated ghost cells.

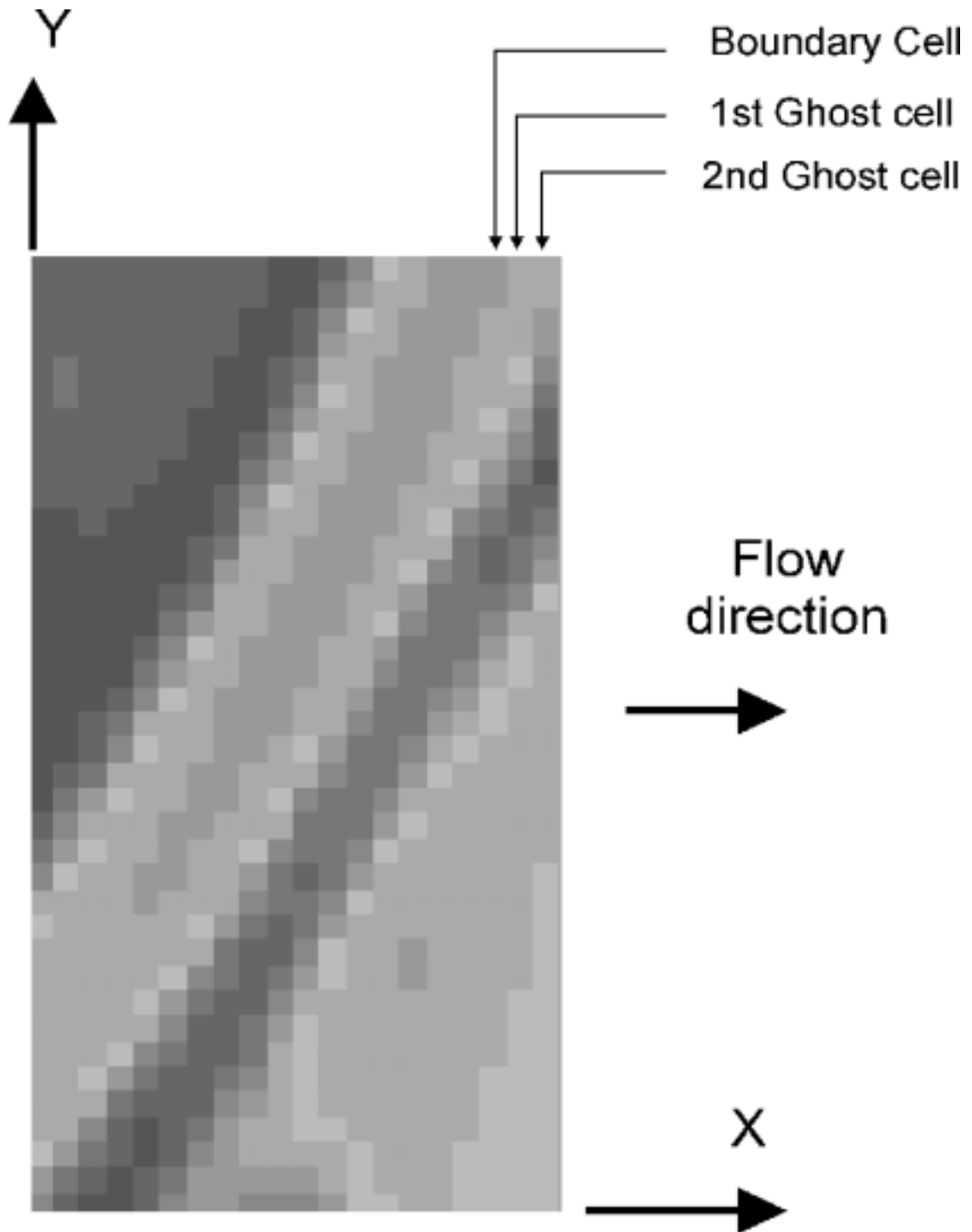


Figure 3.5. Density field exit plane with ghost cells. Flow direction is left to right.

Completion of the extrapolation method completes the numerical development of the code. The next step in the development process is the simulation of single frequency driven shear layers. The following chapter discusses a series of simulations of the $M_c = 0.5$ Case I shear layer under single frequency excitation. The single frequency simulations provided insight into the behavior of the shear layer in response to a dominant single frequency. The insight gained has also helped in understanding the observed behaviors into broad frequency excited simulations.

Chapter 4

Shear Layer Single Frequency Excitation

Linear stability theory is a proven method to determine the motion of small amplitude perturbations in a steady or mean flow field. As such it provides a reliable method with which to compare both numerical and experimental research. Linear theory solutions have been used by numerical simulation researchers [40, 39] as a check on the basic capability of their simulation codes. Linear theory results have been used in several ways in this research; first, to provide first order behavior in the development of the inflow perturbation method, second to establish the frequency resolving capturing capability of the code, and third to improve understanding of the contribution to the overall solution made by single frequency waves. This chapter presents Euler simulations of a shear layer at the nominal Case I conditions under single frequency eigenfunction excitation.

4.1 Dynamics

The eigenfunctions used to provide inlet excitation were developed by Lockard based upon Martens experimental mean velocity profiles at Case I nominal conditions. Only the inlet excitation method differentiates these single frequency simulations from the broad spectrum excitations results presented in Chapter 5. A complete set of linear theory eigenfunctions for the Rayleigh equation were used to provide a thermodynamically consistent set of inflow conditions for the supersonic inlet. The eigenfunctions for a 0.002 m shear layer thickness at 25,000 Hz are displayed in Figure 4.1.

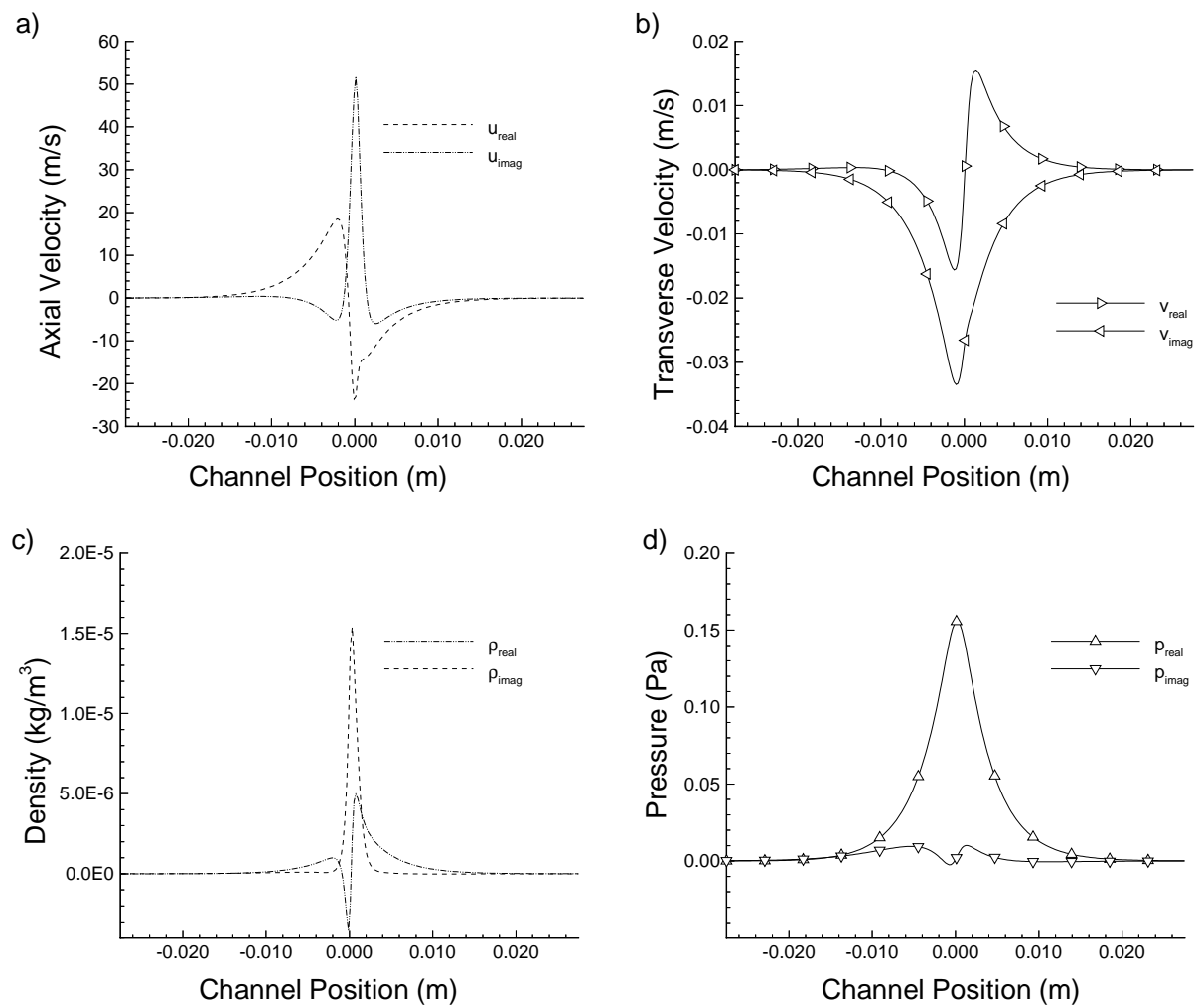


Figure 4.1. Rayleigh Equation Eigenfunctions for 25,000 Hz Disturbance at the Inlet for Case I $M_c = 0.5$ Conditions a) Axial Velocity m/s b) Transverse Velocity m/s c) Density kg/m^3 , b) and d) Pressure Pa .

4.1.1 Frequency Behavior and Auto-spectra

Time histories of the total mass flux unsteadiness $(\rho V)'$ were recorded to allow examination of the frequency simulation behavior of the shear layer. Figure 4.2 presents the discrete FFT spectra and its auto-spectra. The transverse width of the eigenfunction profiles and the Euler equation admittance of multiple frequencies result in a frequency spectra and auto-spectra with finite width at the 0.18 m downstream position.

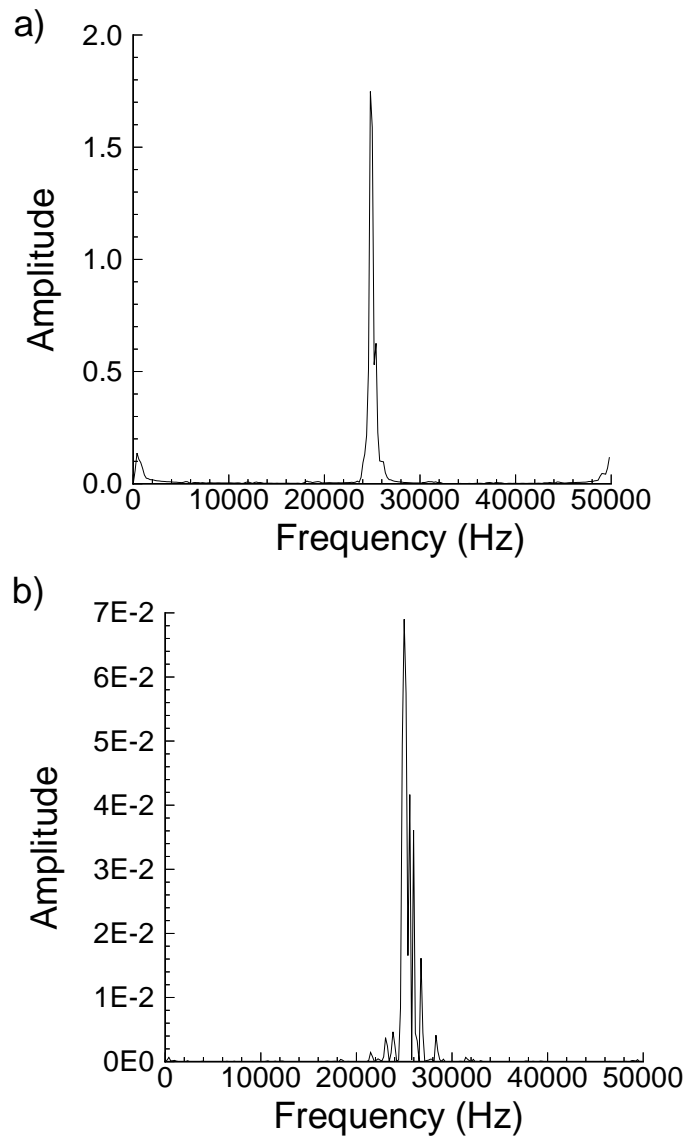


Figure 4.2. Total Mass Flux Unsteadiness $(\rho V)'$ at $X = 0.18$ m: a) FFT spectra and b) Auto-spectra.

4.2 Time-averaged Behavior

4.2.1 Shear Layer Growth

Linear theory predicts that a single frequency shear layer growth will begin with slowly, followed by a period of rapid growth until a maximum is reached after which the shear layer thickness decreases to some constant level. The shear layer growth profiles, δ_{98} boundary layer, δ_ω vorticity and 4θ momentum, are displayed in Figure 4.3. The linear theory sequence of the disturbance growth and decay is shown by the boundary layer and vorticity thicknesses. The growth rate in the rapid growth region are given in Table 4.1. These rates are lower than those found for the broad frequency or “natural” simulations. Other simulation researchers, such as Lu and Wu [39] who have used single frequency and eigenfunction based inlet excitation, have found similar growth rates, albeit for a much higher range ($1.05 \leq M_c \leq 1.77$) of convective Mach number. The constant turbulent growth rate in the region between 0.1 to 0.18 m axial distance are approximately 60% of the “natural” values. The cause of the differences is not understood at this time.

Table 4.1. Shear Layer Growth Rates for a Single Frequency 25 kHz

Growth Type	$\frac{d\delta}{dx}$
δ_{98} (Boundary Layer)	.0493
δ_ω (Vorticity)	.0415
4θ (Momentum)	.0415

4.2.2 Instantaneous Results

Conventional Two-dimensional Plot Observations

The shear layer growth for four single frequency excitation cases is shown in Figure 4.4. From linear theory lower frequencies are expected to have longer laminar periods followed by rapid transition to larger scale vortices. The density gradient show clearly the smooth inlet region, the transition to single well formed vortices, followed by a loss of distinct definition and shape. The lack of vortex pairing in any single frequency behavior suggests that different frequency disturbances traveling at different wave speeds are a primary mechanism in vortex paring.

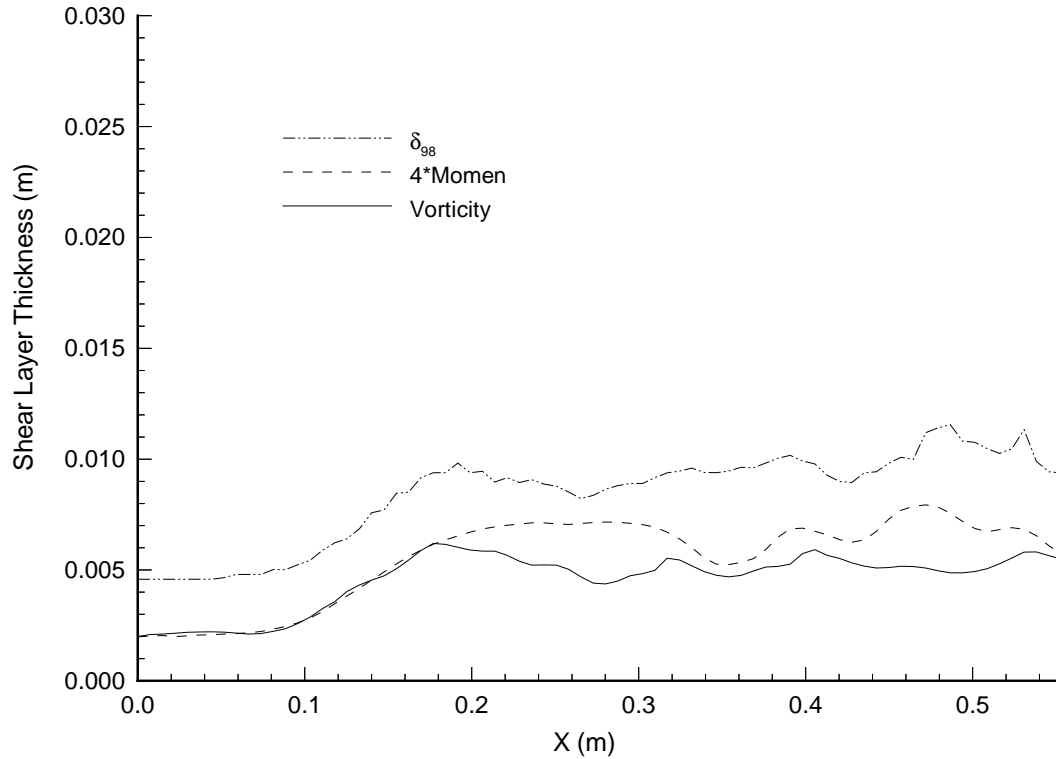


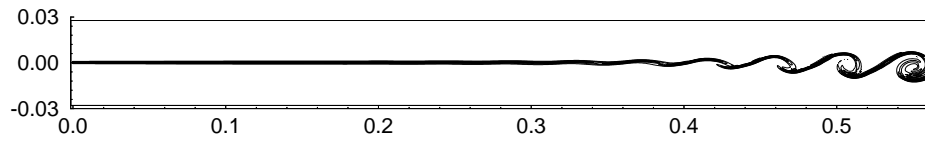
Figure 4.3. Comparison of numerical shear layer growth rates, vorticity δ_ω , momentum 4θ , and boundary layer δ_{98} .

4.2.3 Time Averaged Results

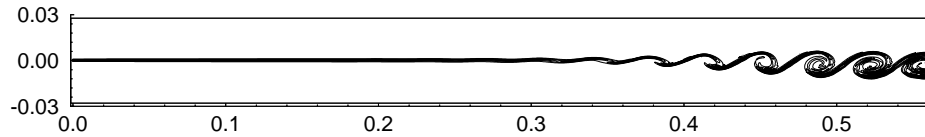
Instantaneous to Time-Averaged Comparison

The time-averaged conservative variable fields are plotted for comparison with the instantaneous fields in Figures 4.5, 4.6, 4.7, and 4.8. The 25,000 Hz excitation case was chosen because it is closest to the Case I most unstable frequency. The density field contours shown in Figure 4.5 illustrate two key points for confined mixing layers. First, the shear layer involvement with the wall begins early, for this frequency in the 0.2 to 0.3 m distance. Second, in contrast to the broad spectra excitation simulation, the time averaged field is not smooth and monotonic like a hyperbolic tangent profile in the transverse direction. And

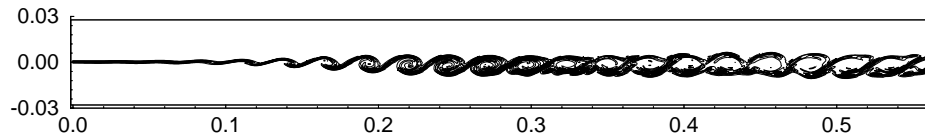
a) Density Gradient Field: 12,000 Hz Single Frequency



b) Density Gradient Field: 15,000 Hz Single Frequency



c) Density Gradient Field: 20,000 Hz Single Frequency



d) Density Gradient Field: 25,000 Hz Single Frequency

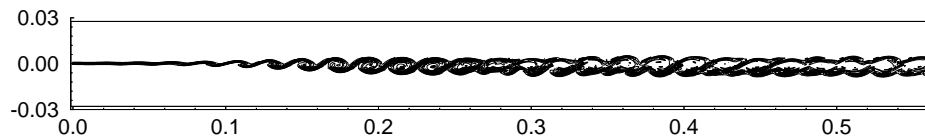


Figure 4.4. Shear Layer Development Comparison for Single Frequency Excitations

finally, the individual vortices capture pockets or wells of low density fluid that convect with the vortex. The vortex becomes a protecting mechanism that appears to actually reduce mixing. The time averaged effect is seen clearly in the cross channel profile at $X = .28m$ position.

The growth, peak and then decay process is best seen in Figure 4.7. Down stream of the initial peak the shear layer transverse mass flux diffuses. The shear layer also acts as a barrier to Mach wave disturbances trapping them in the high speed stream.

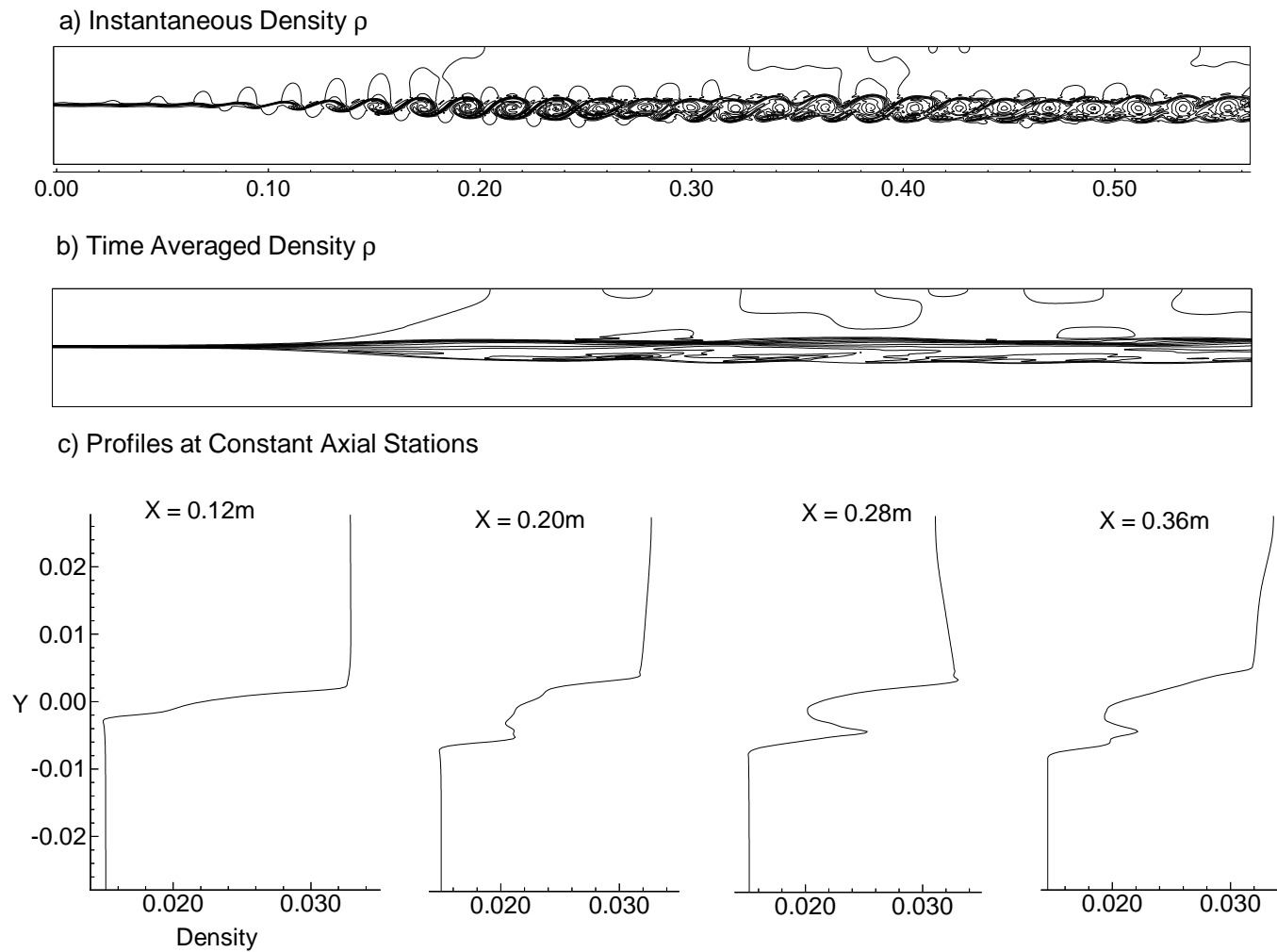


Figure 4.5. Conservative Variable Density ρ (kg/m^3) a) Instantaneous Density, b) Time Averaged Density Field, and c) Cross Channel Density Profiles at $X = .12m, .20m, .28m,$ and $.36m$.

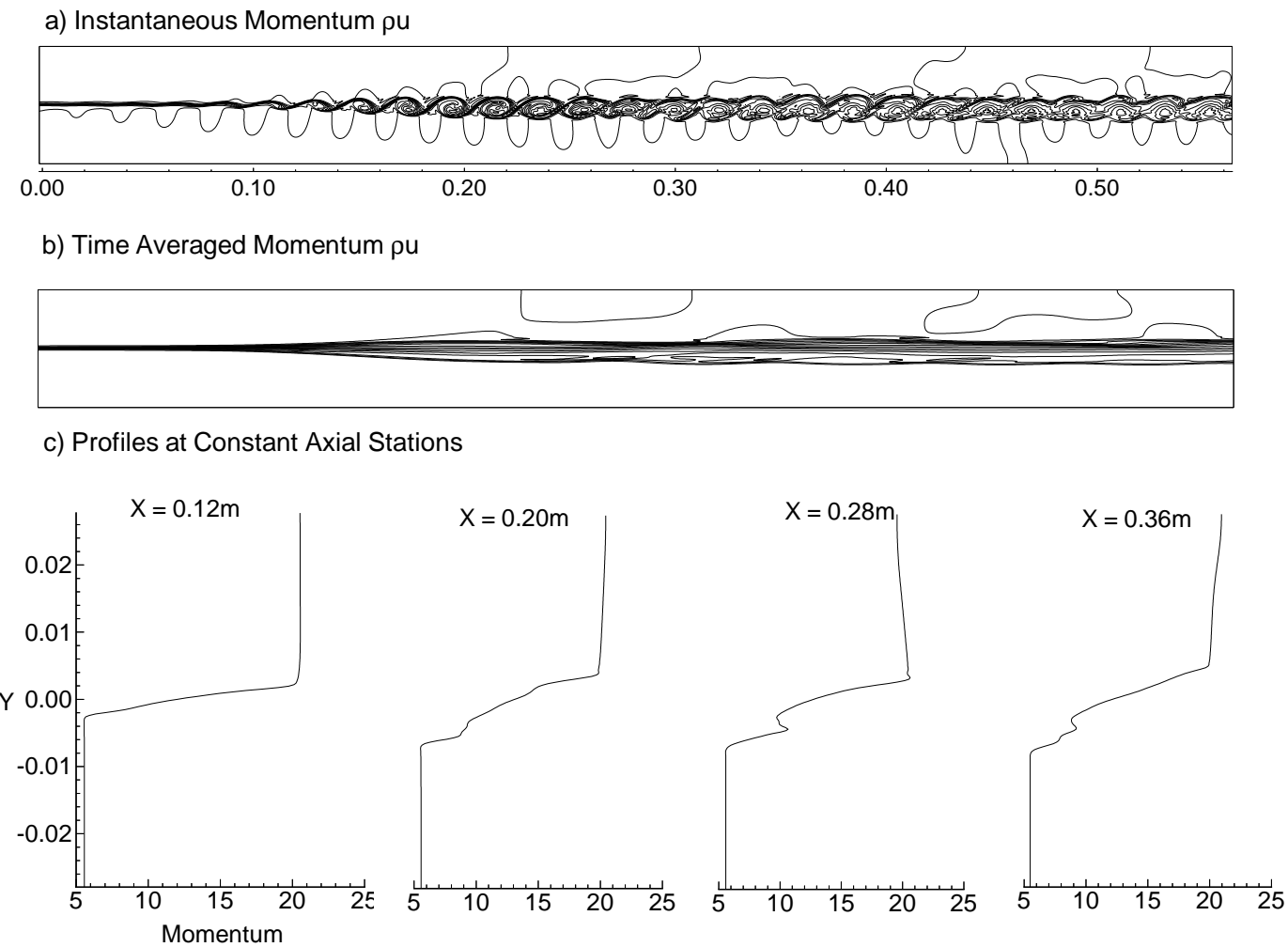


Figure 4.6. Conservative Variable Axial Mass Flux ρu (kg/sm^2) a) Instantaneous Mass Flux, b) Time Averaged Mass Flux Field, and c) Cross Channel Mass Flux Profiles at $X = .12m, .20m, .28m,$ and $.36m$.

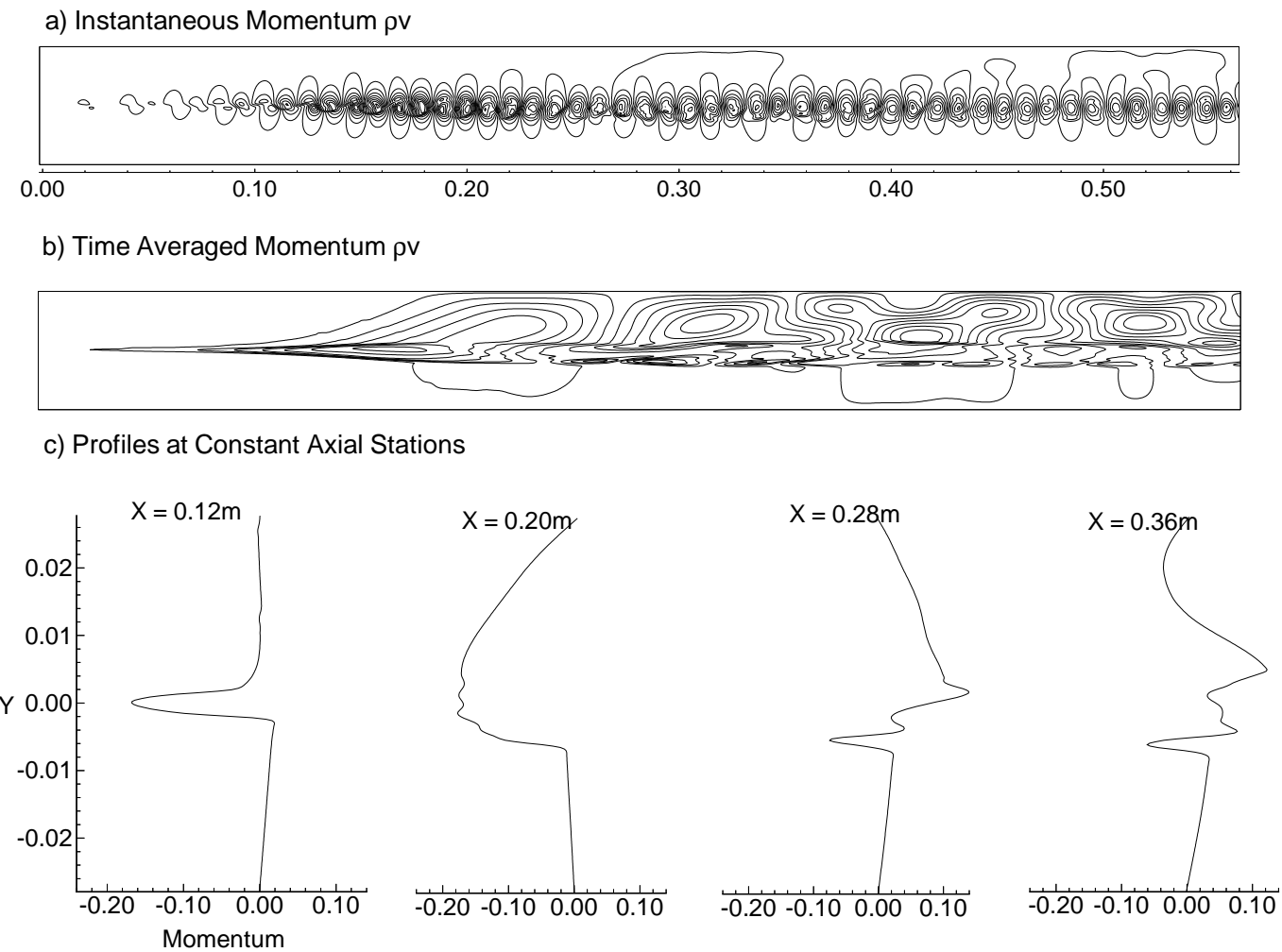


Figure 4.7. Conservative Variable Transverse Mass Flux ρv (kg/sm^2) a) Instantaneous Mass Flux, b) Time Averaged Mass Flux Field, and c) Cross Channel Mass Flux Profiles at $X = .12m, .20m, .28m,$ and $.36m$.

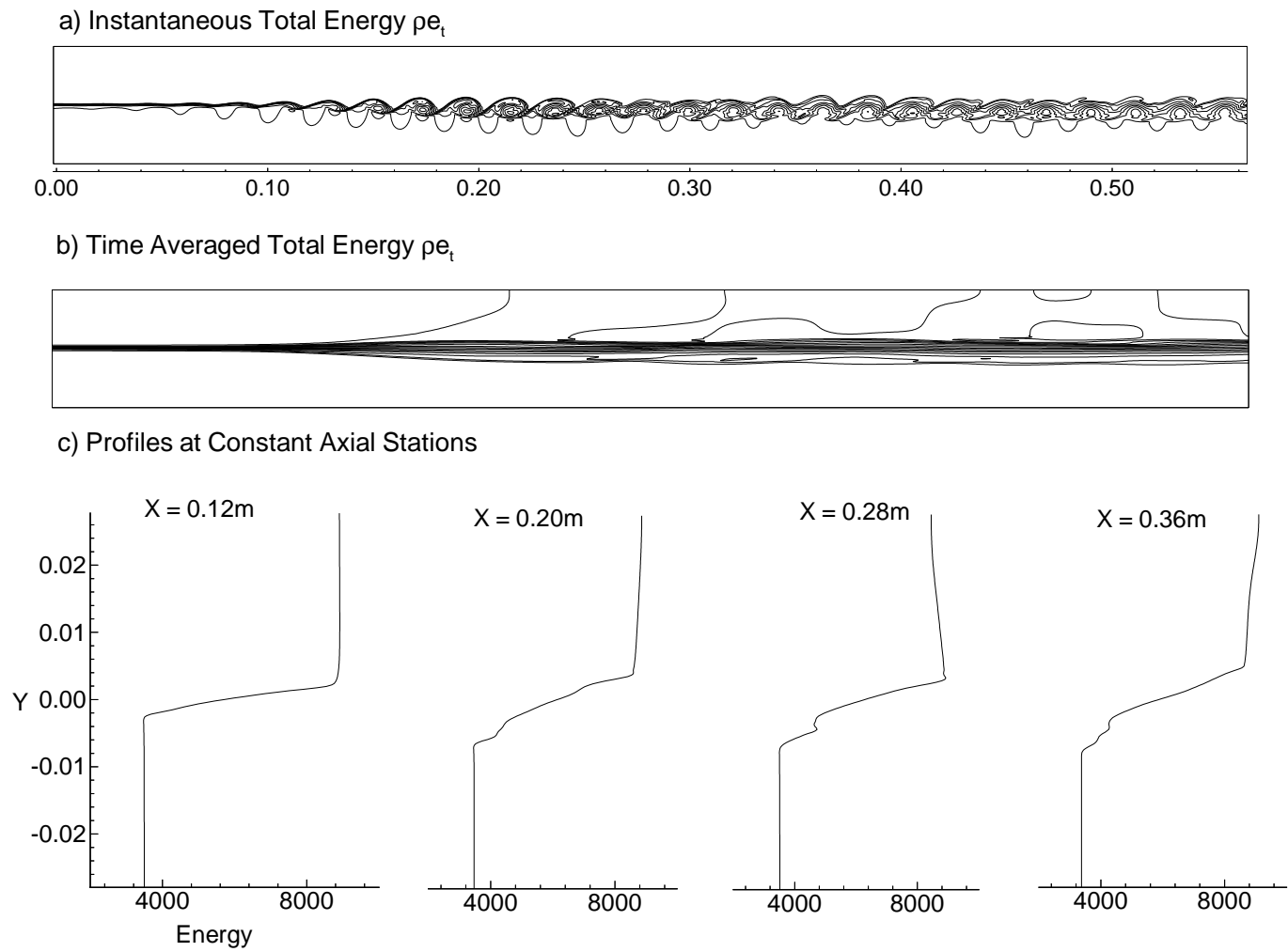


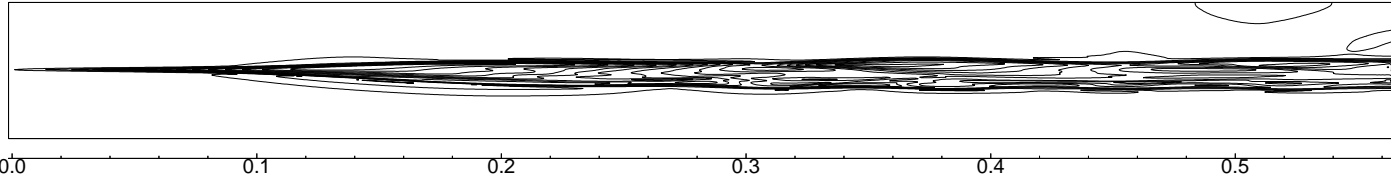
Figure 4.8. Conservative Variable Total Energy ρe_t ($Joule/m^2$) a) Instantaneous Total Energy, b) Time Averaged Total Energy Field, and c) Cross Channel Total Energy Profiles at $X = .12m, .20m, .28m,$ and $.36m$.

Time Averaged Fluctuating Quantities

The mass flux fluctuation and Reynolds stress fields provide some insight into the behavior of the shear layer. They also provide possible explanations for conflicting behaviors observed by researchers. In Figure 4.9, cross-channel profiles of the axial mass flux perturbation or turbulence intensity $(\rho u)'$ show the commonly observed skewed and double peaked profiles at axial positions $X = 0.20$ and $0.36m$ respectively. The broad frequency or “naturally” excited simulations produce cross-channel profiles of the skewed shape. Double peaked profiles have only been observed from data fields which were not time-average mature or were single frequency excited. Since most experimental data is expected to be time-averaged stable, the presence of double peaked behavior suggests the possible presence of a strong single frequency behavior.

The Reynolds stress contour field shows the turbulence mixing peaking very early in the region of rapid shear layer thickness growth. Beyond this region the Reynolds stress dissipates quickly. Growth in the Reynolds stress appears to lead the occurrence of rapid shear layer growth. In the downstream region where the Reynolds stress is very weak the shear layer thickness is nearly constant.

a) Momentum Perturbation: $\rho u'$



b) Profiles at Constant Axial Stations

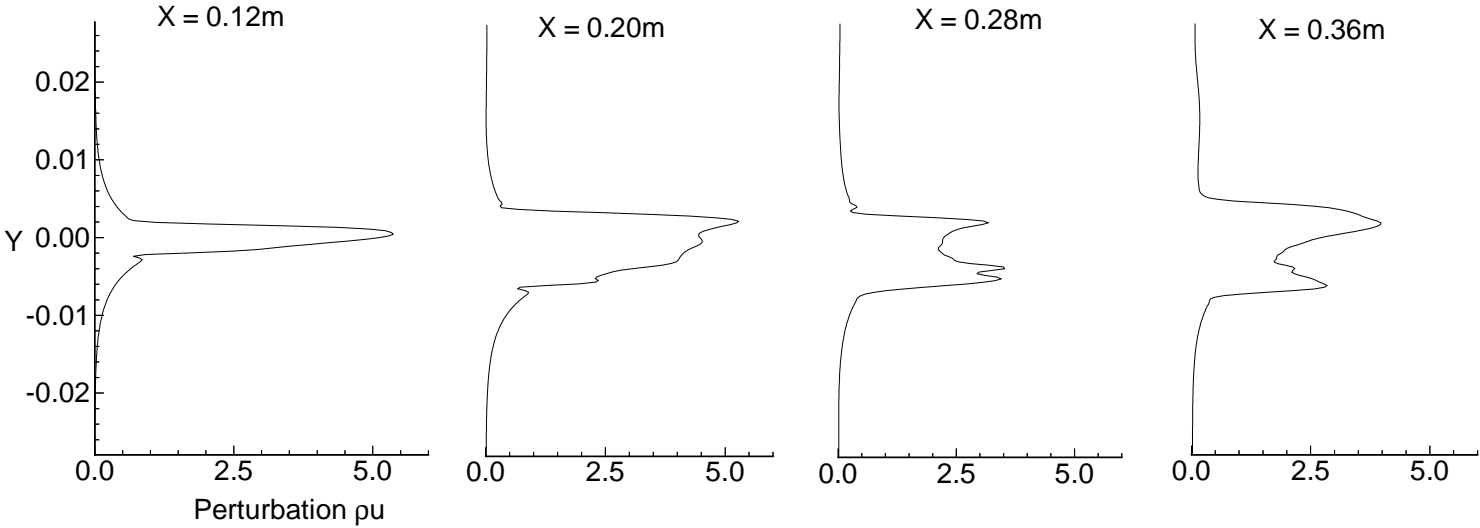
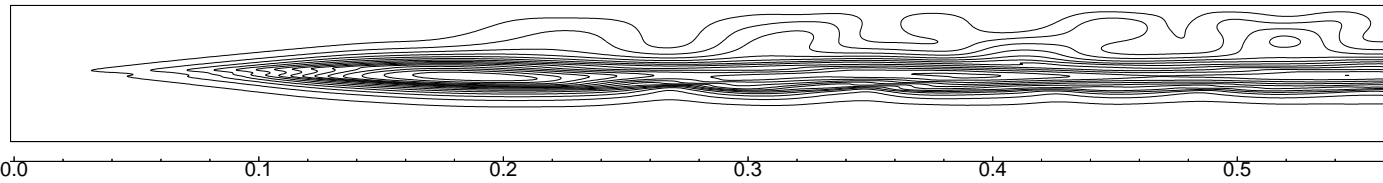


Figure 4.9. Single Frequency 25 kHz Axial Mass Flux Flux Perturbation $\overline{(\rho u)'}'$: a) RMS Mass Flux Perturbation and b) Cross Channel Profiles at $X = .12\text{m}$, $.20\text{m}$, $.28\text{m}$, and $.36\text{m}$.

a) Momentum Perturbation: $\rho v'$



b) Profiles at Constant Axial Stations

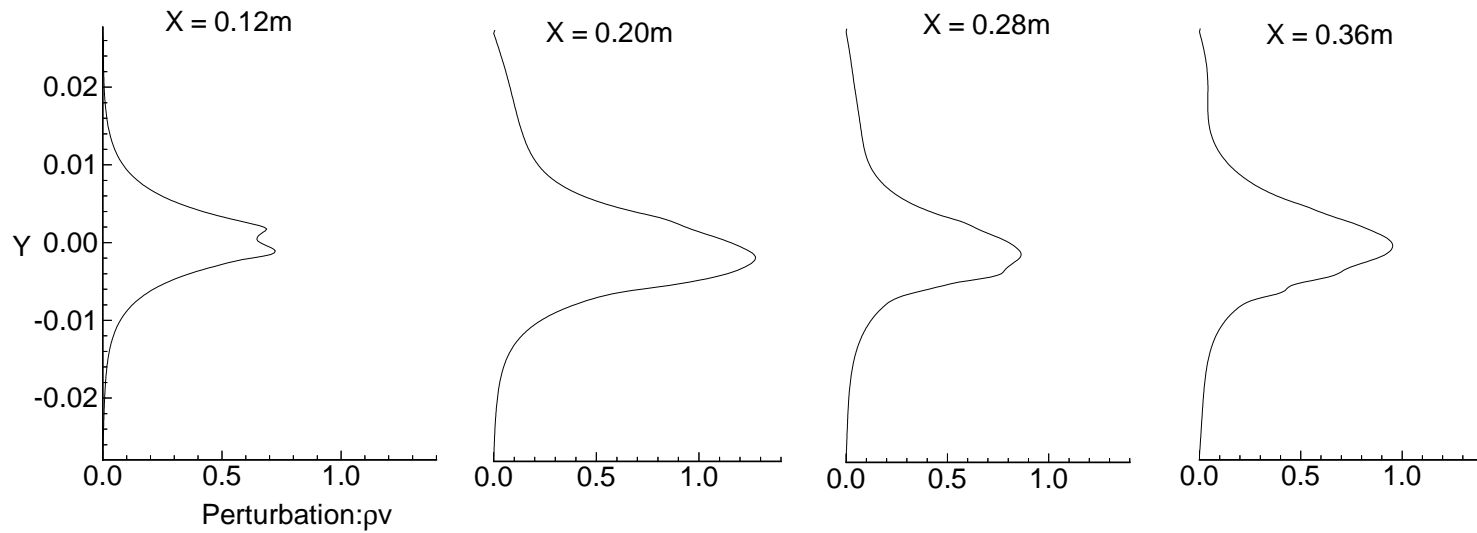
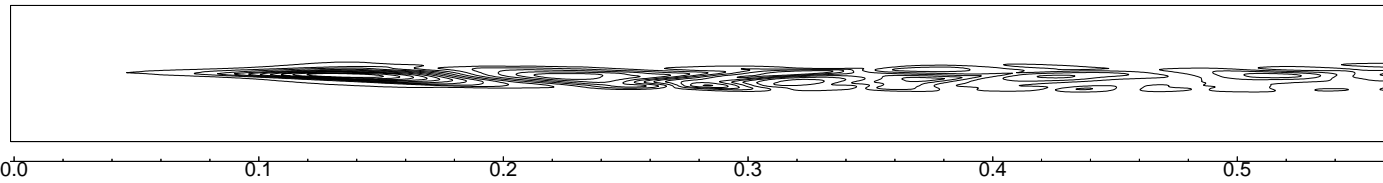


Figure 4.10. Single Frequency 25 kHz Transverse Mass Flux Perturbation $\overline{(\rho v)'}'$: a) RMS Transverse Mass Flux Field and b) Cross Channel Profiles at X = .12m, .20m, .28m, and .36m.

a) Time Averaged Reynolds Stress: $(\rho u v)'$



b) Profiles at Constant Axial Stations

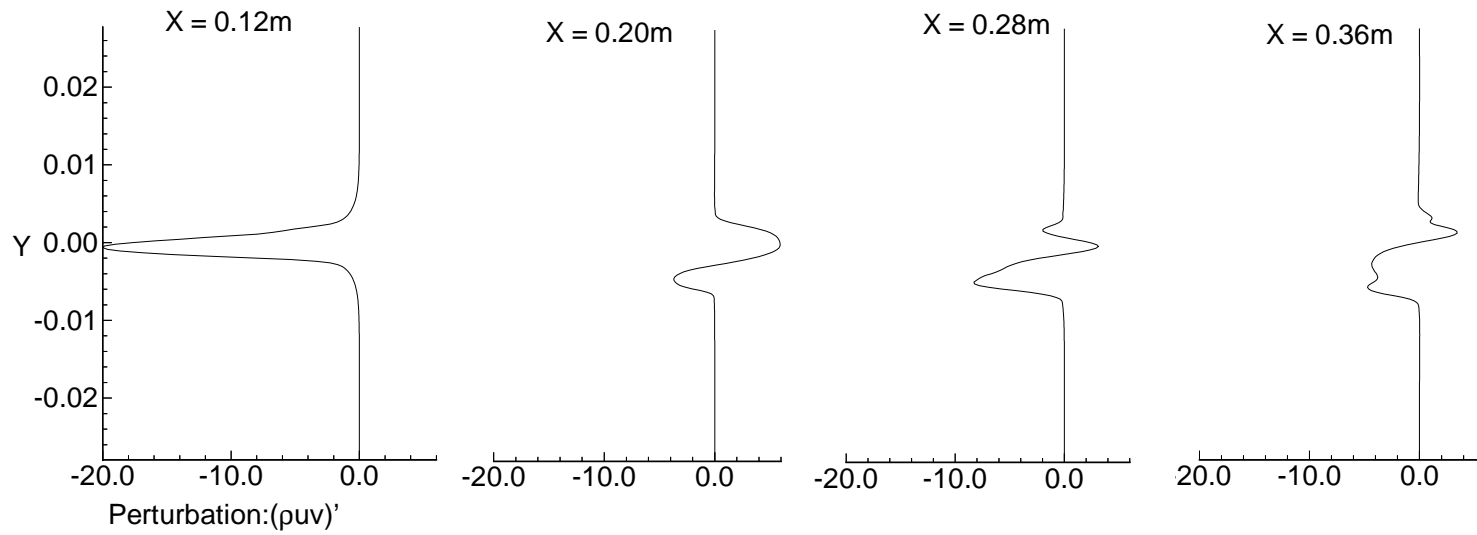


Figure 4.11. Single Frequency 25 kHz Time Averaged Reynolds Stress $\overline{\rho u'v'}$: a) Time-averaged Reynolds Stress Field, and b) Cross Channel Profiles at $X = .12\text{m}$, $.20\text{m}$, $.28\text{m}$, and $.36\text{m}$.

Comparison with Parabolized Stability Equation Results

Case I conditions were excited using eigenfunction profiles for 25000 Hz at the inlet boundary. The axial growth profile and the cross channel growth profile of the r.m.s pressure perturbation were compared to the experimental and Parabolized Stability Equation (PSE) results presented by Martens et al. [44]. In Martens et al. [44] Martens' experimental results were narrow bandpass filtered to yield the axial profile of the r.m.s. mass flux perturbation for a 25,000 Hz wave. The filtered profile was compared with the r.m.s. pressure perturbation profile produced by Lockard using the stability theory PSE method. The Parabolized Stability Equation (PSE) results are based on a curve fit of the experimental mean flow field. The PSE theory produces eigenfunction results for the selected frequency.

Figure 4.12 displays the filtered experimental growth profile of the axial normalized mass flux perturbation, the PSE growth profile for p' normalized to match the experimental profile's magnitude, and the simulation p'/p_{mean} and the normalized mass flux perturbation profiles produced by the single frequency eigenfunction excitation. The PSE and filtered experimental results show agreement as to the axial location of the peak disturbance. The PSE results are, of course, based upon the full frequency range experimental mean profile. The 25000 Hz eigenfunction excited shear layer simulation computes both the single frequency mean profile and the perturbation field. The simulation shows the pressure perturbation peaks 0.06 m before the experimental results. The difference could be attributed to two possible sources, 1) the influence of broad frequency content of the experimental flow on the mean profile and 2) simulation error in computing the shear layer mean field. The differences in the peak perturbation magnitudes are attributed to the excitation magnitudes in the experimental flow and the simulation. The mass flux perturbation of the simulation shows a continuing rise through several peaks. This mass flux behavior is in agreement with the PSE mass flux results [44]. The cause of the variation from the experimental profile of Martens is not known.

The cross channel profiles were compared at the 0.28 m axial location, see Figure 4.13. The profiles show generally good agreement. In this figure 0.004 m has been added to the simulation profile, shifting it towards the high speed stream. The shift amount of 0.004 m was determined based upon the velocity profile comparisons shown in Figures 5.22 and 5.23. The simulation and PSE pressure profiles compare well in shape. The difference

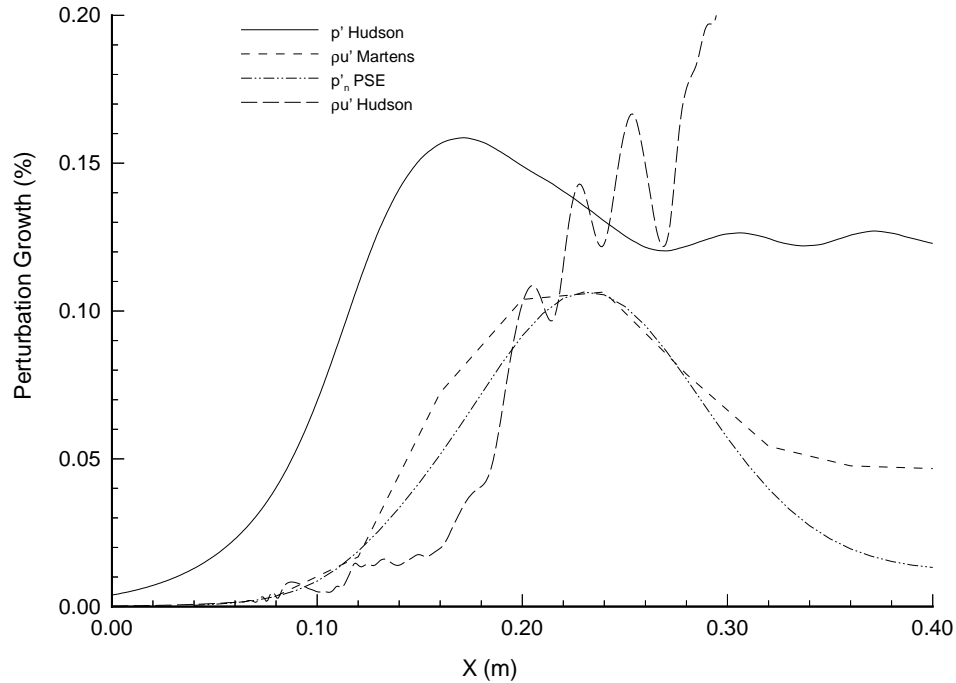


Figure 4.12. RMS Perturbation Axial Growth Evolution for 25 kHz; Martens $\frac{(\rho u)'}{\rho u}$, Lockard PSE Normalized p' , and Single Frequency Excited Numerical Simulation p'/p_{mean} , Hudson $\frac{(\rho u)'}{\rho u}$.

in magnitude is attributed to the simulations excitation strength. The mass flux profile does not compare well in shape due to the dominant single frequency behavior of the simulation. The magnitude difference is due to the elevated perturbation levels of the simulations at frequencies near the dominant disturbance frequency.

Single frequency simulation of the Case I shear layer conditions has produced results that compare well with stability theory and experimental results, within explainable differences. A more thorough discussion of the cause for the differences shown by the mass flux perturbation are presented in the next chapter. Closer comparisons would require far greater precision in the coordination of flow conditions for each of the three research methods in order to produce exact comparisons. The comparisons establish, for this research, a consistency between the differing research methods.

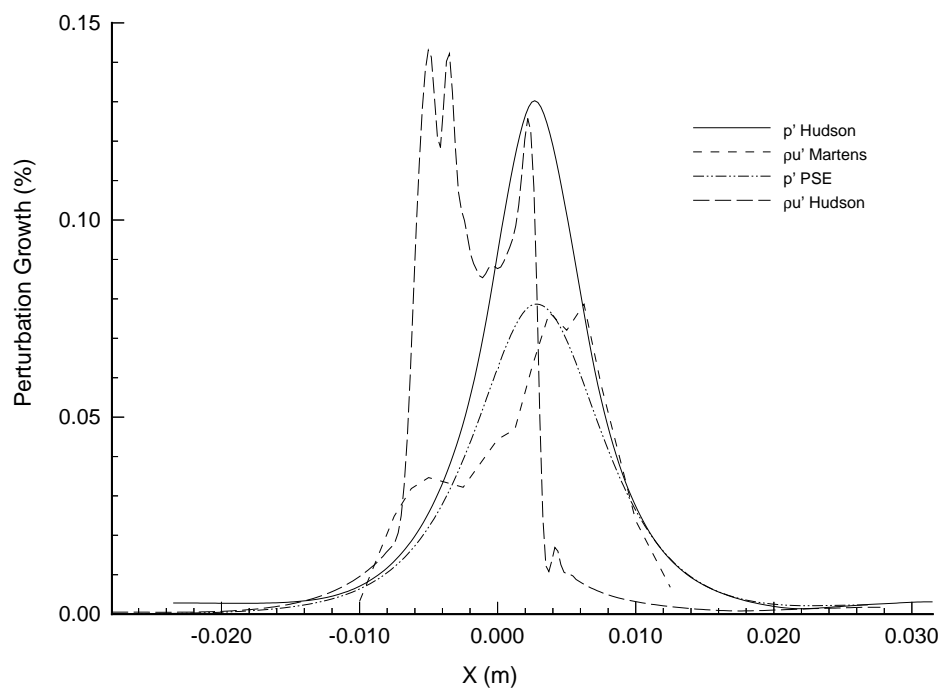


Figure 4.13. RMS Perturbation Growth Profile for 25 kHz at 0.28 m; Martens $\frac{(\rho u)'}{\rho u}$, Lockard PSE Normalized p' , Single Frequency Excited Numerical Simulation p'/p_{mean} , and Simulation $\frac{(\rho u)'}{\rho u}$.

Chapter 5

Shear Layer Simulation Case I: $M_c = 0.5$

The results of the numerical simulation of Case I conditions at a convective Mach number of 0.5 are presented and compared to Martens' experimental results. Issues addressed begin with the effectiveness of unsteady inflow boundary conditions in providing a "natural" inflow condition. The ability of the simulation to produce realistic dynamic behavior in terms of frequency spectrum and associated auto-spectra and their comparison with experimental results are assessed. The growth rate of the shear layer is discussed and numerical rates are compared with experimental values. Possible sources of any differences are addressed. The instantaneous solution of conservative solution variables are presented in two and three-dimensional forms to aid in gaining insight into the flow's and/or simulations behavior. Time-averaged data are presented in contour plots of the solution domain and cross-sectional profiles for examining the steady behavior of the solution. The mean velocity profiles are plotted against Martens velocity profile data at six axial locations. Time-averaged mass flux fluctuations and Reynolds stress are compared with experiment. The effect of normalization on profile shape and peak magnitude are discussed. The capabilities of the simulation as well as points of deviation from the experiment are discussed. The ability of the simulation to model dynamic growth of the shear layer is examined by comparison between analytical results from Martens and Lockard et al. [44] and a single frequency eigenfunction forced solution. The simulation was solved in physical units and all data are in the MKS system unless otherwise noted.

5.1 Dynamics

Frequency spectra analysis has historically been used as a basic tool in the investigation of shear layer behavior [80, 51, 62]. Early work by Oster and Wygnanski [51] investigated the frequency behavior of shear layers in both natural or unforced and forced layers. They investigated a variety of effects such as the influence of excitation on mixing layer growth rates and the cascade of frequency (energy) with spatial evolution of a mixing

layer. They found that small amplitude excitations of negligible energy cause increased growth rates; but, at large amplitudes the flow resonates with the frequency of the excitation. The amplitude at which an excitation frequency begins to force resonance in the shear layer is of critical importance to a numerical simulation. Physical flow variables do not have the steadiness of numerical constants and therefore inlet boundary conditions must be perturbed. They must be perturbed in such a way as to mimic the real variable behavior and avoid any excitation resonance. A few researchers have begun to use frequency spectra in the analysis of numerical simulations [13, 79]. Oster and Wygnanski also showed the basic cascade of energy from high frequencies to lower frequencies as the shear layer evolves spatially. These basic behaviors remain consistent until three-dimensional effects start to become dominant [62]. Of the two flow conditions simulated, Case I conditions fall in the two-dimensional region but Case II conditions are at the lower edge of where the shear layer begins to develop three-dimensional effects. Numerical simulations must be able to reproduce these behaviors accurately.

The ability of the simulation to reproduce the dynamic behavior of the experimental conditions accurately was examined by sampling the mass flux and analyzing the frequency spectrum and auto-spectra of the data. Martens used the method of Kistler [32] and Ko et. al [33] to determine the fluctuation calibration of his hot-wire. The calibration equation was expressed as

$$\frac{e'}{\overline{E}} = A_m \frac{(\rho u)'}{\overline{\rho u}} - A_T \frac{T_0'}{\overline{T_0}} \quad (5.1)$$

where $A_m = \left[\frac{\overline{\rho u}}{E} \frac{\partial \overline{E}}{\partial \overline{\rho u}} \right]$ for $\overline{T_0}$, and T_{wall} constant and $A_T = - \left[\frac{\overline{T_0}}{E} \frac{\partial \overline{E}}{\partial \overline{T_0}} \right]$ for ρu and T_{wall} constant. The second term was dropped as immaterial based on the work of Ko et. al [33], who found that total temperature variations less than 3%. Martens determined the coefficient A_m of the first term from hot-wire calibrations in an atmospheric jet. The final total mass flux equation used by Martens was given by

$$m' = \frac{1}{A_m} \frac{e'}{\overline{E}} = \frac{(\rho u)'}{\overline{\rho u}} \quad (5.2)$$

The experimental time history data was collected with a hot-wire probe that measured the mass flux of the air stream normal to the hot wire not just the axial component. The

total mass flux for both the experiment and the simulation are defined as the local (ρV) , where $V = \sqrt{u^2 + v^2}$. The total mass flux histories were recorded at the inlet and two axial locations 0.18 m and 0.27 m.

5.1.1 Frequency Behavior and Auto-spectra

Inlet Conditions

The total mass flux at the inflow boundary was sampled to investigate the ability of the unsteady boundary conditions to produce a white noise stimulation to the flow. The frequency spectra of the total mass flux perturbation $(\rho V)' = (\rho V) - \overline{(\rho V)}$ produced at the inlet is shown in Figure 5.1. The spectra is fairly uniform in magnitude across the range of frequencies of interest. The frequency spectra were determined from the discrete Fourier transform of the total mass flux time history. Martens made “informal” estimates of the power spectral density in the shear layer by taking the modulus-squared of the discrete Fourier transform, i.e. the auto-spectra of the total mass flux perturbation time history [55]. The auto-spectra of the inlet signal shows that the power is evenly distributed across the frequency regime. The design intent in the development of the inlet perturbation method was to avoid the addition of power into the flow at the fundamental frequency or any of its subharmonics. As desired, the power distribution of inflow unsteadiness is roughly uniform and does not have any unusually large spikes in the range of interest. The benefit of this inflow excitation method is its relative simplicity and simple ties with experimental data.

Downstream Behavior

The unsteady behavior produced by the inflow conditions compared well with experimental results, both qualitatively and quantitatively. The anticipated shape of the frequency spectra was a roughly bell shaped curve with the peak at the most unstable frequency for the local shear layer thickness. The shear layer simulation produced the anticipated frequency spectra profile in both shape and frequency peak location, as shown in Figure 5.2. The broad peak of the FFT spectra is centered in the high 20 kHz range, in agreement with the estimated most unstable frequency of 27 kHz for the 0.18 m downstream location.

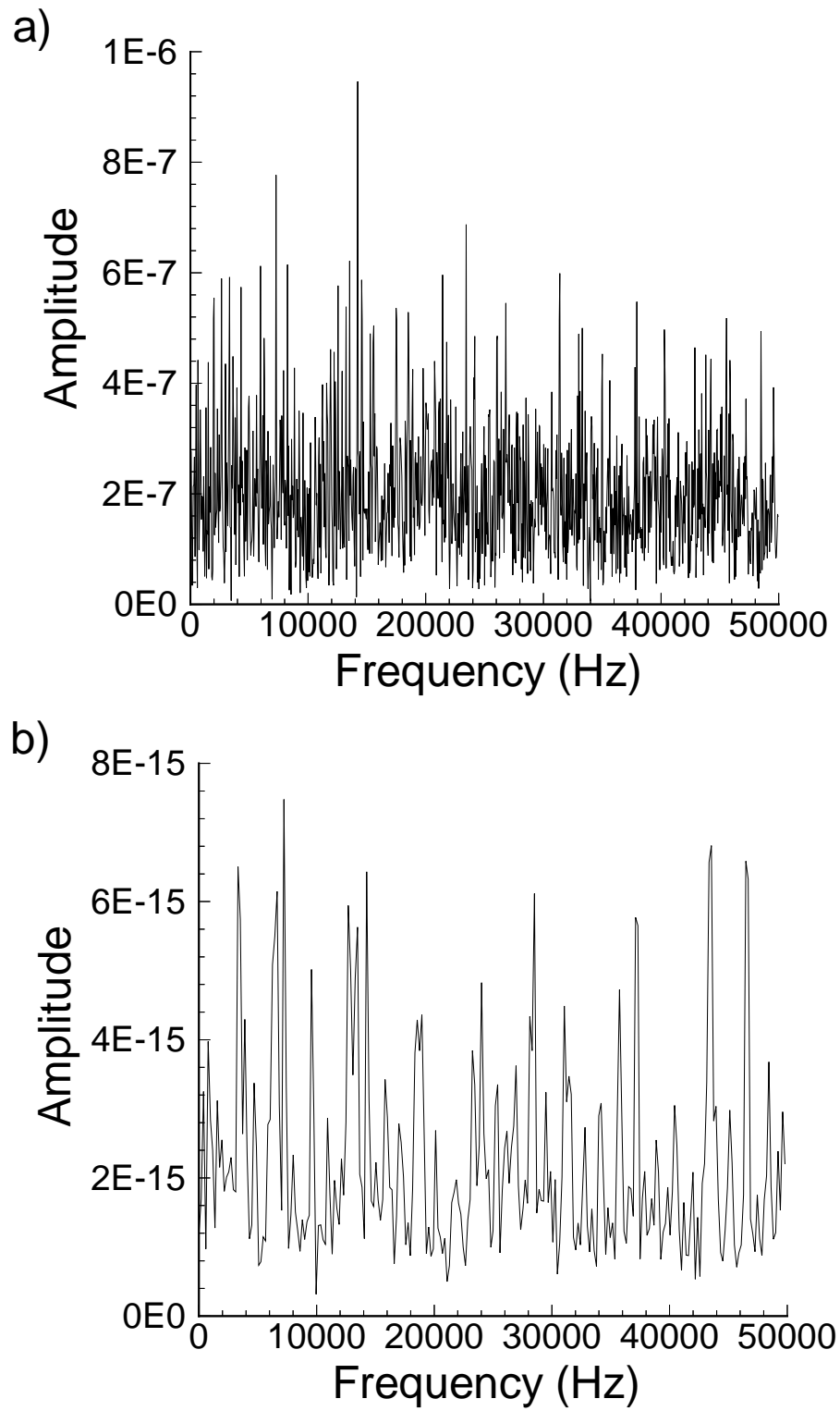


Figure 5.1. Unsteady Inlet Perturbation, $(\rho V)'$, Behavior: a) FFT Spectra and b) Auto-spectra.

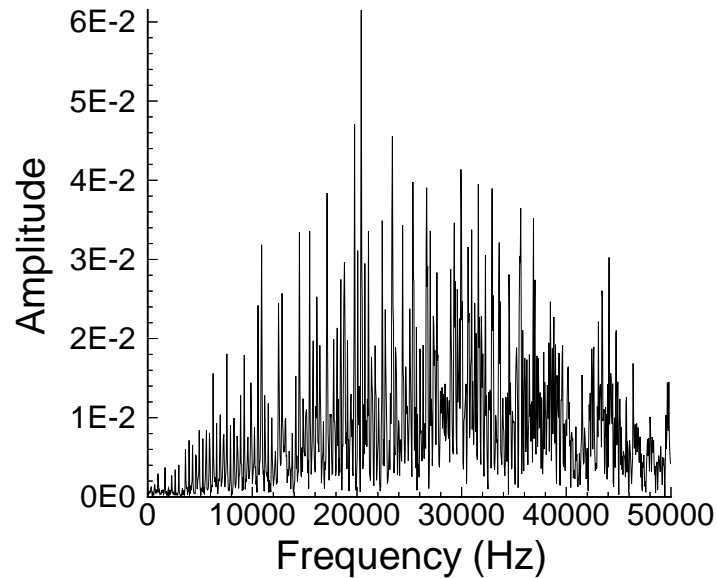


Figure 5.2. FFT Spectra of the Total Mass Flux Unsteadiness $(\rho V)'$ at $X = 0.18$ m.

The power spectra density of the shear layer unsteadiness is given approximately by the auto-spectra of the Fourier transform spectra. Figure 5.3 presents the auto-spectra of the simulation and experiment at the 0.18 m location. The key comparison is that both auto-spectra show that the peak total mass flux perturbation energy is at the most unstable frequency of approximately 27 kHz. The large magnitude difference between the two auto-spectra corresponds to an FFT magnitude (wave amplitude) ratio of about eight. The cause of the magnitude difference has not been determined but several possible contributing factors are as follows; 1) the magnitude of the inlet excitation of the simulation, 2) the lack of viscous damping by the Euler damping and 3) the use of atmospheric “calibration” of the hot-wire for an experiment at 1200 Pa pressure and 100° K temperature. The relative magnitude of these effects are unknown. Another contributor to the peak magnitude difference between the two auto-spectra is the number of data points averaged into each curve. The experimental work is based on an essentially unlimited amount of data while the simulation auto-spectra is based on only 2048 data points. An increased number of data points would average out high peaks moving the auto-spectra closer to its stationary average profile.

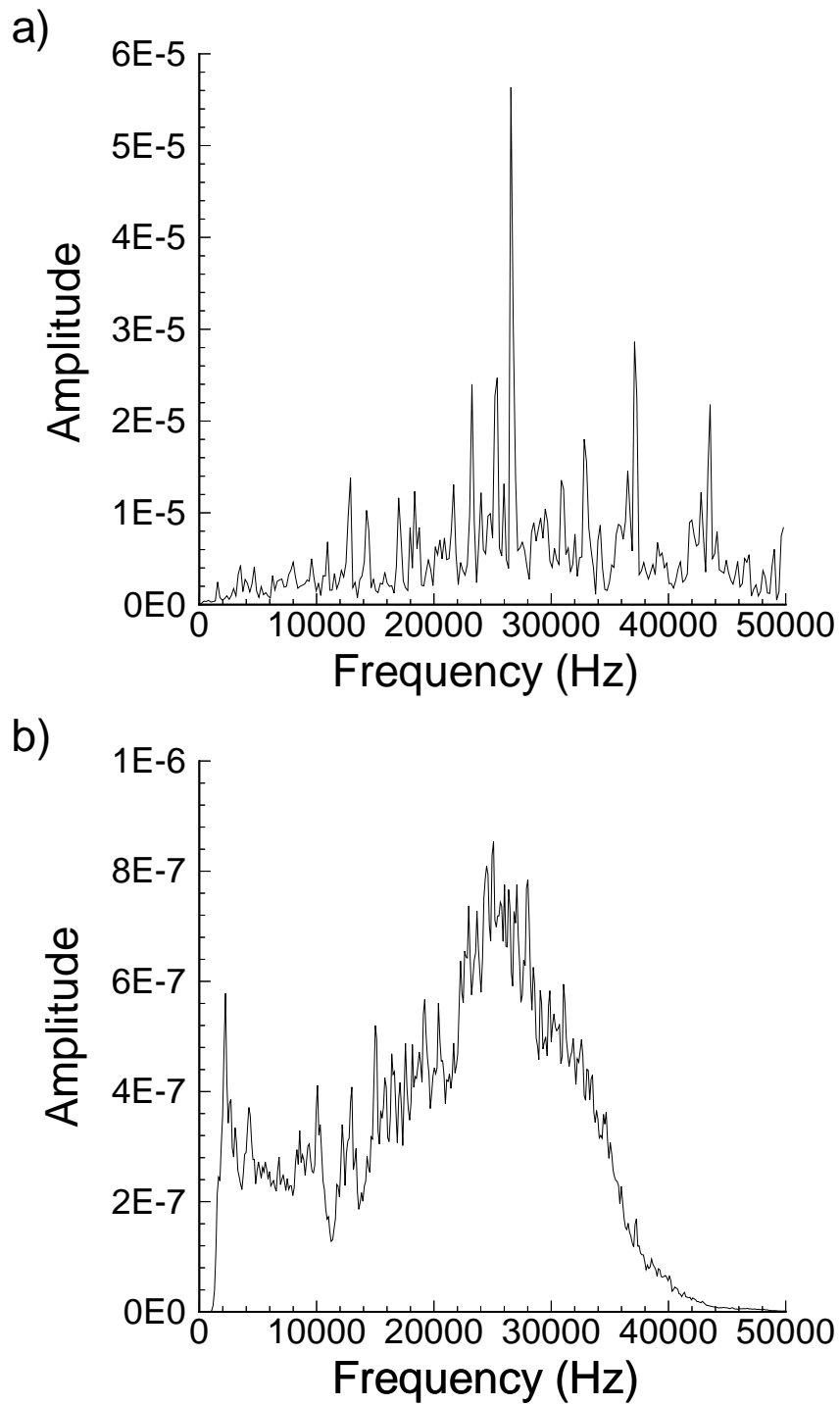


Figure 5.3. Auto-spectra of the Total Mass Flux Unsteadiness at $X = 0.18$ m: a) Simulation and b) Experimental.

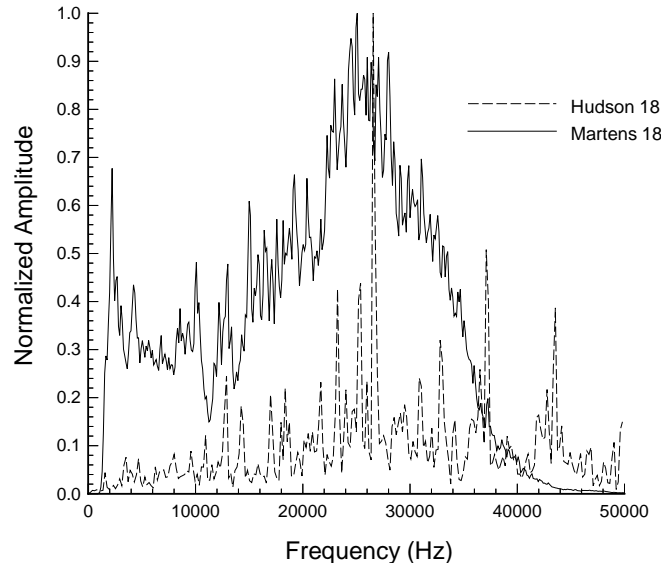


Figure 5.4. Normalized Auto-spectra of the Total Mass Flux Unsteadiness at $X = 0.18$ m.

Normalized versions of both auto-spectra are plotted in Figure 5.4 to allow closer comparison of the power spectra. Again, the simulation agrees with the experiment by showing the peak power magnitude occurs at the most unstable frequency of the shear layer. The simulation does show more energy at very high frequencies above 36 kHz than the experiment. Since viscous dissipation has its greatest effect at the small scales of high frequencies, the lack of viscosity in the solution is considered the most probable cause. The experimental auto-spectra shows high levels of energy at low frequencies below 10 kHz. High energy levels at unexpectedly low frequencies are typically attributable to facility or instrumentation vibrations. However, the precise cause of high energy levels at low frequencies has not been determined. Overall, the FFT and auto-spectra profiles show the ability of the Euler simulation to predict the shear layer dynamic behavior. The shape of the FFT spectra suggests that the power spectral density profile can also be predicted with larger data sets from simulations.

The simulation shows equally good results at the 0.27 m downstream location. The FFT spectra in Figure 5.5 shows the cascade to lower frequencies. The shear layer grows thicker due to increasing spatial oscillations with axial distance and at some point vortex

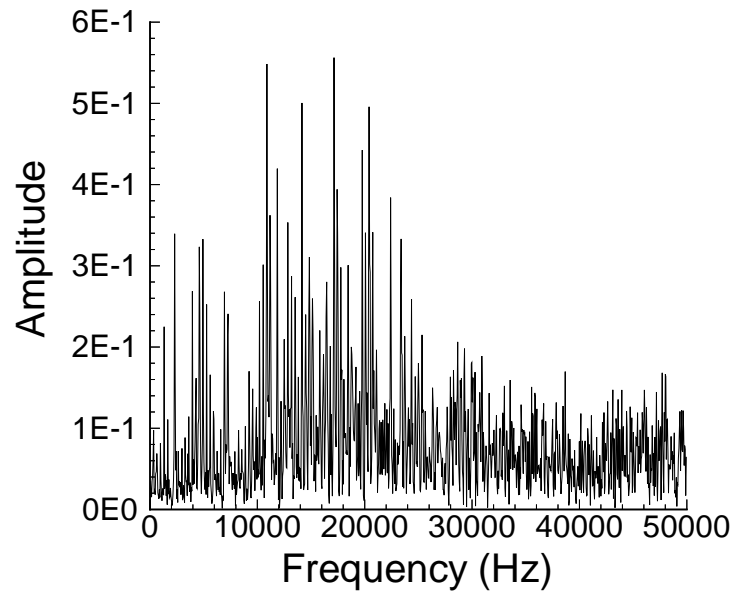


Figure 5.5. FFT Spectra of the Total Mass Flux Unsteadiness $(\rho V)'$ at $X = 0.27$ m.

pairing begins. Both of these mechanisms, spatial oscillation growth and vortex pairing, cause the structures to decrease in frequency. The peak frequencies are predicted correctly at the local most unstable frequency of about 14 kHz. At this downstream location the cascade of energy is producing more large amplitude waves in the low frequency range below 10 kHz.

Figure 5.6 presents the auto-spectra of the simulation and experiment at the 0.27 m location. Both auto-spectra show equal shifts to lower frequencies. The simulation shows a peak energy at the anticipated 14 kHz most unstable frequency. Similar to the comparison at the .18 m location, the experimental auto-spectra shows a slightly lower frequency for the peak energy of about 12 kHz. Observance of high energy at low frequencies as seen at the .18 m location is obscured by the normal cascade of energy into that frequency range. The simulation auto-spectra shows nearly a two order of magnitude growth from the .18 m location. This growth is consistent with the factor of ten change in magnitude of the peak FFT spectra. Based on the experimental auto-spectra data, the experimental FFT peaks grew by only a factor of two. The difference in the peak growth rates are contributed to by the unresolved high frequencies waves and to a lesser extent the absence of viscous

damping. The unresolved high frequency waves contribute to power redistribution in the fluid through non-linear interactions. The normalized auto-spectra are plotted together in Figure 5.7. The figures show that the method correctly predicts the energy cascade trend and identifies the local frequency of the dominant large scale behavior but fails to predict the broader distribution of power.

The FFT and auto-spectra results from the inlet and two downstream locations have demonstrated a good capability of this Euler simulation to predict the shear layer dynamic behavior. The inlet excitation successfully introduces a white noise excitation to the shear layer. The resulting flow field reproduces the Kelvin-Helmholtz instability behavior of the shear layer. The FFT spectra and the auto-spectra demonstrate the ability to predict the most unstable frequencies along the shear layer and to reproduce realistic frequency spectra. The primary limitation of the method was its inability to predict the diffuse power spectrum of the experimental results. The simulation frequency spectra and auto-spectra were calculated from a sample base of 2048 points. The fine grid inviscid simulation produced a good simulation of the dynamic behavior of the supersonic shear layer.

5.2 Instantaneous and Time-averaged Behavior

5.2.1 Shear Layer Growth

As discussed previously, the effect of confinement on the Kelvin-Helmholtz instabilities of the shear layer should be minimal. Therefore, conventional free shear layer thickness and growth rate methods should apply. There is a multitude of definitions and methods of determining the thickness of shear layers and their attendant growth rates. The most common definitions for shear layer thickness are the visual, the Pitot or velocity, vorticity and momentum thicknesses. The visual thickness is the shear layer thickness as measured by observation methods such as schlieren photography. The Pitot thickness, δ_{pit} , is the width of the Pitot pressure profile from 5% to 95% of the difference of the free-stream values. The vorticity thickness is defined by the equation

$$\delta_\omega = \frac{\Delta U}{\left(\frac{\partial U}{\partial y}\right)_{max}} \quad (5.3)$$

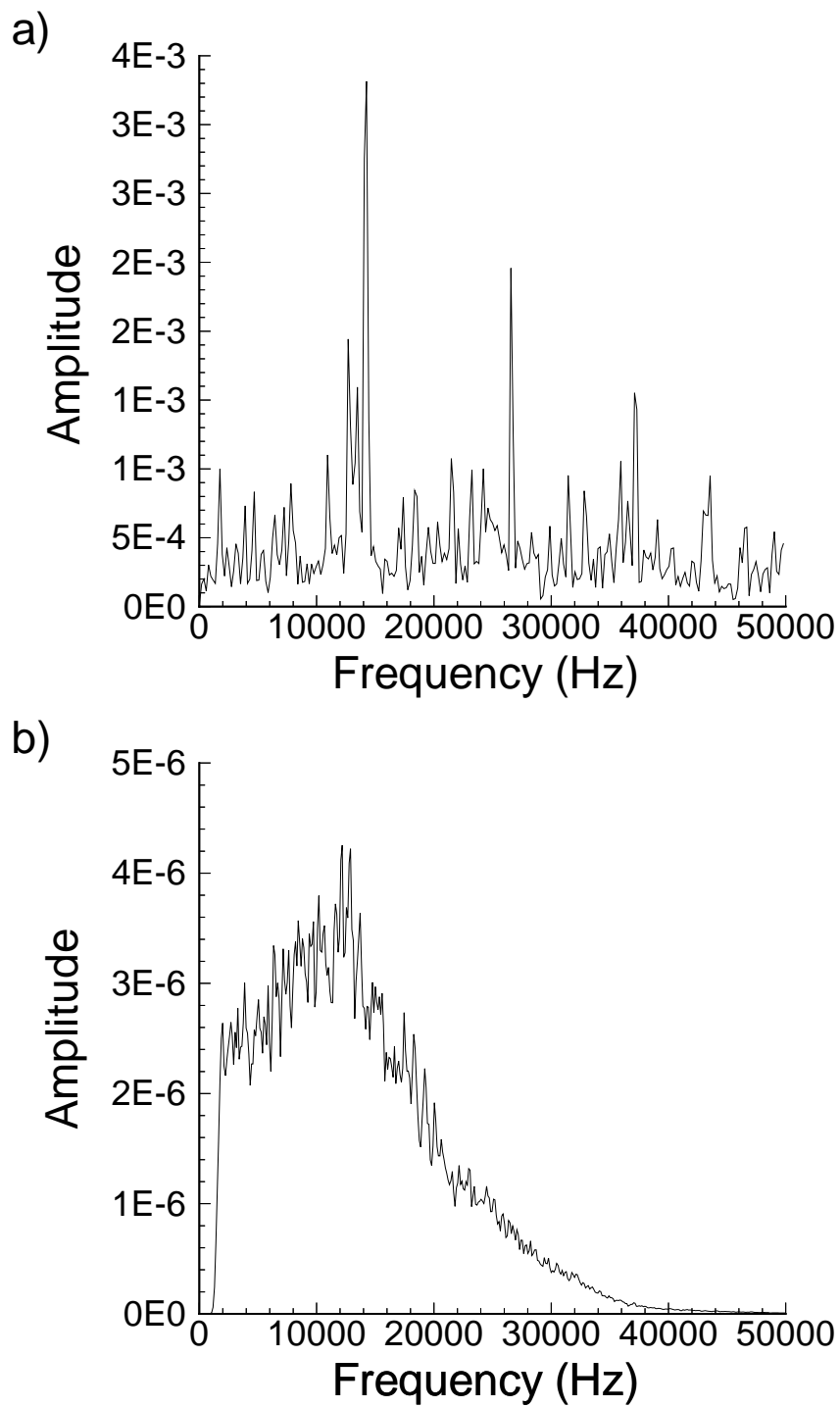


Figure 5.6. Auto-spectra of the Total Mass Flux Unsteadiness at $X = 0.27$ m: a) Simulation and b) Experimental

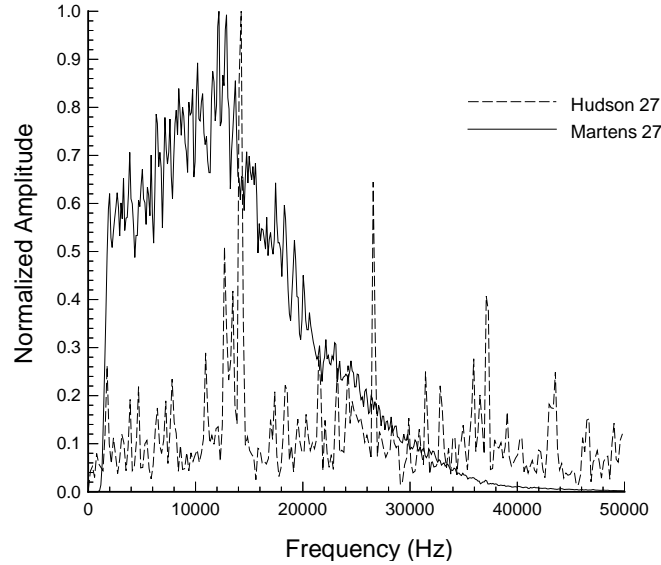


Figure 5.7. Normalized Auto-spectra of the Total Mass Flux Unsteadiness at $X = 0.27$ m.

The vorticity thickness determined from Equation 5.3 is very sensitive to the maximum slope of the shear layer. The numerical vorticity thickness was computed directly from the time averaged variables. The experimental vorticity thicknesses were determined by a graphical method [45]. The momentum thickness is computed based on the compressible definition

$$\theta = \int_{-H/2}^{+H/2} \frac{\rho}{\rho_1} \left(\frac{(U_1 - u(y))(u(y) - U_2)}{(U_1 - U_2)^2} \right) dy \quad (5.4)$$

An additional definition, δ_{98} , was also compared to the experimental data. The δ_{98} thickness is similar to a velocity thickness and was determined much like a boundary layer thickness. A similar boundary layer thickness parameter has been used by Clemens and Mungal [10] to correlate visual thicknesses from schlieren photographs. The thickness is defined by the following equations

$$U_{lower} = U_2 + 0.01\Delta U \quad (5.5)$$

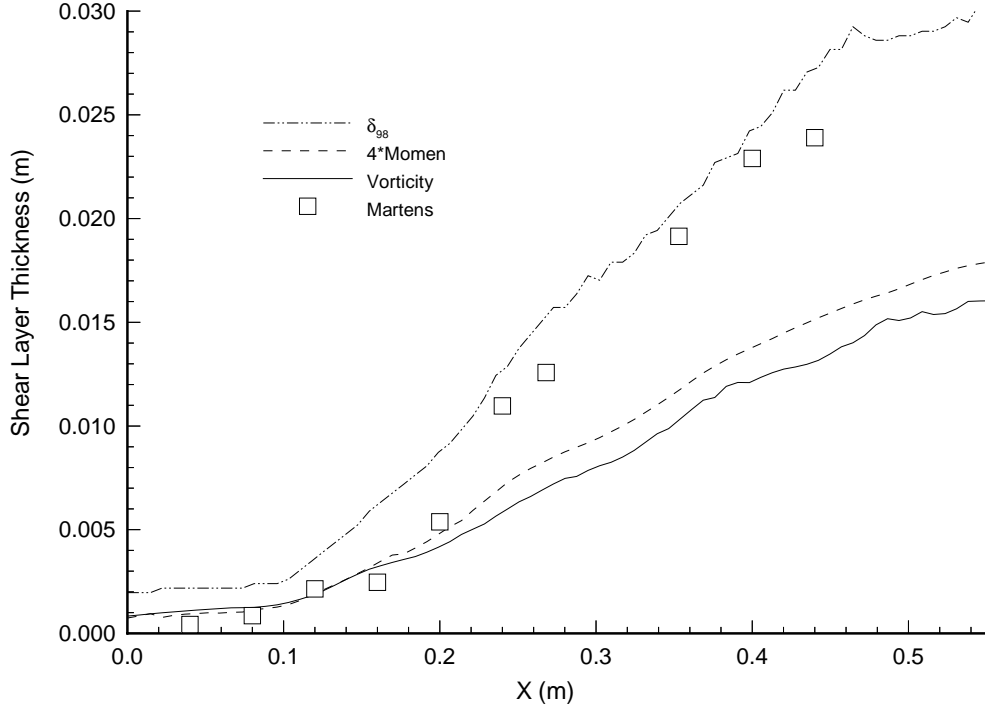


Figure 5.8. Comparison of numerical and experimental shear layer thicknesses, vorticity δ_ω , momentum 4θ , boundary layer δ_{98} , and experimentally determined vorticity.

$$U_{upper} = U_1 - 0.01\Delta U \quad (5.6)$$

$$\delta_{98} = y(U_{upper}) - y(U_{lower}) \quad (5.7)$$

Three shear layer thickness measurements, δ_{98} , vorticity and momentum thickness, were compared to the experimental vorticity thickness growth. Figure 5.8 shows the growth of the shear layer with streamwise distance as measured by these various parameters.

The three thickness measures computed from the numerical simulation bound the experimental growth profile. The δ_{98} method provides the best comparison with the results of Martens' graphical method, nearly falling on top of the experimental data. Since the

Table 5.1. Shear Layer Growth Rates for Case I

Growth Type	$d\delta/dx$
δ_{98} (Boundary Layer)	.075
δ_ω (Vorticity)	.042
4θ (Momentum)	.035
δ_ω (Experimental)	.0765

experimental profiles are Pitot data, the associated thicknesses may be more appropriately classified as Pitot thicknesses. For a hyperbolic tangent velocity profile the vorticity and momentum thicknesses are related by $\delta_\omega = 4\theta$. The factor of four relationship between vorticity to momentum holds well for this confined shear layer. The thickness growth profiles behave in accordance with free shear layer behavior. Two distinct regions of growth exist, a region of very slow laminar growth and then a period of very rapid turbulent growth. Growth rate comparisons in the laminar region are not meaningful due to the large initial shear layer definition and poor velocity profile resolution of the numerical simulation. Even the point of transition is highly dependent upon the degree to which the inflow boundary conditions stimulate realistic downstream behavior. The scatter in the experimental data makes a precise statement of the transition point difficult. Martens used 0.16 m compared to the very precise simulation transition point of 0.10 m. The turbulent growth region produced a constant growth rate that extends out to about the 0.4 m position. Beyond this position the shear layer becomes significantly influenced by the wall boundary layers. The simulation results do not show the wall influence due to lack of boundary layers in the inviscid calculation.

The growth rates for the different methods are given in Table 5.1. The experimental growth rate reported here was computed independently. As can be seen, the simulation growth rate δ_{98} is nearly identical to the experimental vorticity growth rate. One source of the difference between the experimental and numerical vorticity thicknesses is the shape of the velocity profile. Figure 5.9 shows the numerical and experimental profiles at the 0.44 m location. At this location the time averaged velocity profiles are affected by the loss associated with the unresolved waves and the lack diffusion effects due to the absence of viscosity in the simulation. The relative importance of each factor can not be assessed with the data available.

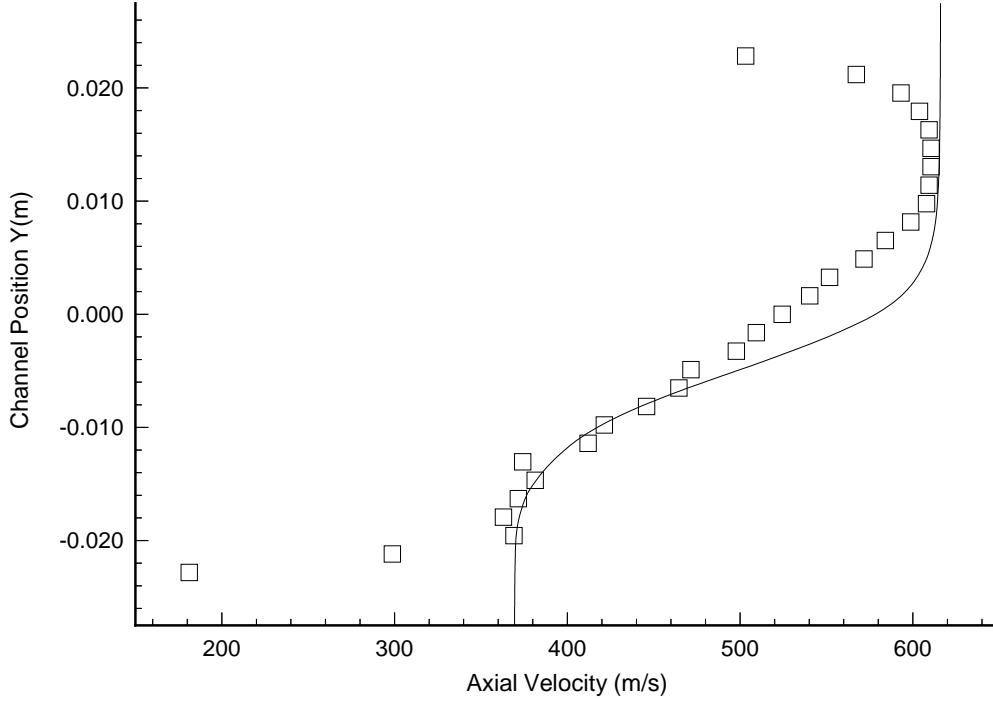


Figure 5.9. Comparison of Numerical and Experimental Mean Velocity Profiles at X=0.44 m.

Shear layer growth rate data are correlated with the convective Mach number by the method of Bogdanoff and Papamoschou & Roshko [6, 53]. The convective Mach number is calculated using the definition of Papamoschou [52]

$$M_c = \frac{U_1 - U_2}{c_1 + c_2} \quad (5.8)$$

The growth rates are typically normalized by the incompressible growth rates as determined by the equation of Papamoschou and Roshko.

$$\frac{\partial \delta}{\partial x} = C_\delta \cdot \frac{(1-r)(1+s^{\frac{1}{2}})}{(1+rs^{\frac{1}{2}})} \quad (5.9)$$

where $r = \frac{U_2}{U_1}$ and $s = \frac{\rho_2}{\rho_1}$ and C_δ is a constant, dependent on the type of thickness used. The supplementary physical parameters needed to correlate the growth rates and that help

define the convecting instability waves are given in Table 5.2. The incompressible growth rate constants and resulting incompressible growth rates for both flow Cases I and II are given in Table 5.3.

Table 5.2. Supplementary Parameters

Flow Conditions (Units MKS)	Case I	Case II
Shear Layer		
Convective Mn	0.50	0.64
Convective Vel	510.5	562.4
Difference Rey	1636.1	2547.7
Velocity ratio	0.59	0.55
Density ratio	0.46	0.31

Table 5.3. Incompressible Growth Rates

Thickness Type	Thickness Coefficient	Incompressible Growth Rate	
		Case I	Case II
δ_ω [39]	.085	.0418	.0476
δ_{Pitot} [7]	.181	.0889	.1014
δ_{vis} [11]	.17	.0835	.0952
δ_{Pitot} [11]	.14	.0688	.0784

The normalized δ_{98} growth rate is plotted with the experimental growth rate along with data from other researchers in Figure 5.10. The Pitot growth-rate coefficient by Brown and Roshko [7], $C_\delta = 0.181$ was used for normalization by Martens and has been used to normalize δ_{98} in this thesis. The results marked “Martens” were calculated from his Case I and Case II, $Re_y(40,000/cm)$ growth profiles. The data scatter of the experimental results can yield differing results based upon the precise method used to compute the growth. The normalized growth rates based on the results given in Table 5.1 are nearly identical. The high degree of scatter in this plot suggests that improvements are needed in the growth rate definition or that the convective Mach number may only be a first order factor in the data correlation. The correlation function of Ragab and Wu [58] is included in Figure 5.10 to show the expected correlation behavior.

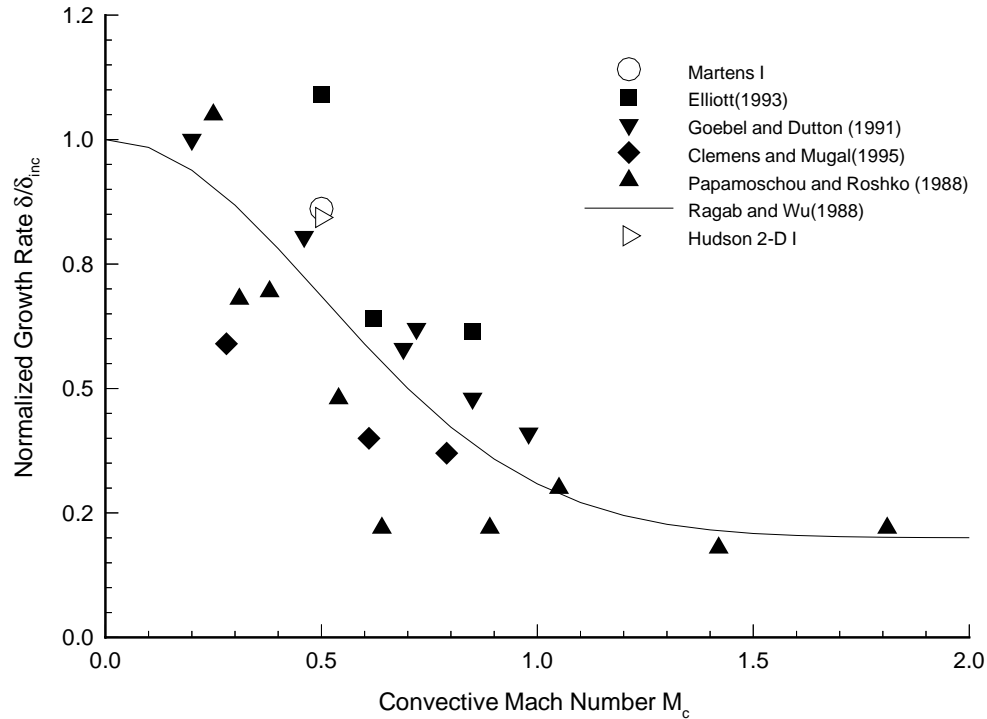


Figure 5.10. Normalized growth rates correlated with convective Mach number.

5.2.2 Instantaneous Results

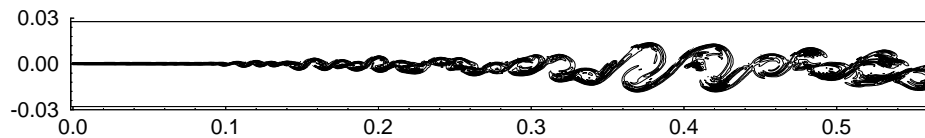
Conventional Two-dimensional Plot Observations

To obtain the correct time-averaged behavior, such as the growth rate, carries with it at least the assumption that the dynamic behavior is being simulated correctly. The density-gradient method of Quirk [56] and the vorticity field are useful parameters to begin the examination of the flows' dynamic behavior. Figure 5.11 shows the Kelvin-Helmholtz instability growth as the shear layer develops downstream. The modeled portion of the duct has an aspect ratio of approximately 10 to 1 and is shown in correct proportion. The density gradient field, Figures 5.11 a), gives a schlieren-like visual image of the vortex sheet and shows vortex pairing and shape distortion. Unsteady structure begins appearing by 0.1 meter with a vortex pair “peanut” being clearly visible by about 0.24 m. From the 0.3 m

position the vortices begin to flatten along the shear layer. The physical size of the vortices in the shear layer begin to fill the duct height which impacts the flow behavior significantly beyond the of 0.4 m location. Beyond the 0.4 m position, the now stretched vortices distort as they try to rotate further. Vortex roll-up pairing is the basic pairing mechanism at subsonic speeds; while a second mode, slapping, was also observed in simulations by Oh and Loth [49]. The slapping mode consists of vortices traveling at different speeds and merging upon collision. Oh and Loth state that the slapping mode becomes the predominate merging process at higher convective Mach numbers.

The role of large scale structures in the shear layer mixing process for high unit Reynolds number flows has been questioned by some experimenters. Goebel and Dutton [16] conducted a series of experiments for shear layers at unit Reynolds numbers at 7.7×10^6 and higher. They found only weak evidence for large scale structures and that only at the lowest unit Reynolds number conditions. However, Clemens and Mungal [11] suggest that the difference in results may be due to the differences in the schlieren visualization techniques used. The numerical simulation literature reviewed consistently showed the presence of large scale structures. The unit Reynolds numbers for Case I and Case II conditions are 3.3×10^6 and 4.8×10^6 respectively. Both Case I and Case II show the fundamental mixing mechanism to be the large scale structures.

a) Density Gradient Field



b) Vorticity

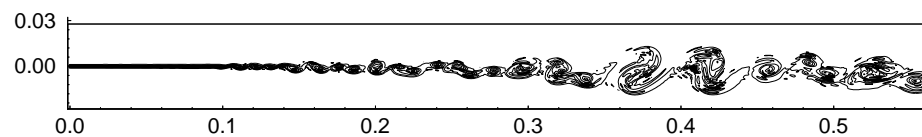


Figure 5.11. Instantaneous Descriptive Flow Parameters; a) Density Gradient Field, and b) Vorticity Field.

The vorticity field displayed in Figure 5.11 shows a strong line of vortices as they move along the shear layer. This line of vortices has been credited with being the cause of the axial mass fluctuations taking on twin peak profile across the shear layer. Oh and Loth [49] have attributed the twin peak structure to the strength of coherency in the large scale structures. They suggest that as the shear layer loses coherency the shear layer loses the twin peak form and transitions to a single peak profile. The possible causes of the twin peak behavior are discussed in more detail later when the velocity profiles are examined in carpet plot form.

Pseudo-3d Examination

The advanced graphics capabilities available today are significant analysis tools in the development of advanced simulation software. They can change our perspective on physical problems. The conservative solution variables were plotted in 2-D gray-scale contours and orthographic projections of pseudo 3-d or carpet plots. The carpet portion of Figure 5.12 adds a physical feel to the high density areas that build up on the upstream side of each vortex. The figures show that the numerical scheme handles the 2.16 density ratio at the inlet very well. But, as the vortex street moves down stream thin strands of the high speed high density fluid are convected into the low speed stream. These thin ribbons of high density fluid can quickly exceed reasonable levels, showing possible sources of severe numerical error. The combination of strong gradients and the need for artificial damping lead to some adjustment of the damping coefficients. The pseudo-3d plots aid in overcoming data glut by quickly showing features which may not be readily spotted from the conventional contour plot. The time needed to determine the correct levels of damping was greatly aided by the ability to easily see spikes in a variable's behavior. The other conservative variables did not exhibit the type of severe spike behavior present in the density field.

The confined flow plots contribute a degree of physical feeling to the flows involvement with the wall. Conventional line contours of density, such as given in Figure 5.18, show involvement with the wall as early as $x \approx .2m$. The pseudo-3d figure gives a better physical feel. Wave like fluctuations in density along the walls were first described as "strange waves" by Papamoschou [52]. Papamoschou observed wall-to-wall banding in schlieren photographs of compressible shear layers in a two-stream supersonic wind tunnel. He hypothesized

that these waves were caused by interaction with the test section walls and the supersonic shear layer structure. He added that the lack of observed waves for cases having subsonic convective Mach number supported the hypothesis that they were related to supersonic waves in the flow. He also observed that these strange waves were relatively stationary. Subsequent researchers, Lu and Wu [39], conducted numerical simulations of supersonic convective Mach number shear flows. Based on their findings, they state explicitly that the strange waves exist only for supersonic wall mode flows, i.e. flows for which the convective Mach number is supersonic. However, results from this simulation show that similar banded structures are present for subsonic convective Mach number flows. The banding appears as broad plane waves of compression and expansion. The strength of the waves is directly related to the degree of interaction with the walls. These strange waves can be seen in the pseudo-3d plot Figure 5.12. The dark line at the edge of the high density stream should be straight along the entire length of the domain, indicating constant density. However, the density at the edge or wall is seen to take on a wavy behavior. Unlike Papamoschou's suggestion of the waves being stationary, these waves move with the vortices. The results of this simulation suggest that the waves are not supersonic wall-mode related. They are more likely the result of fundamental Kelvin-Helmholtz mode vortices interacting with test section walls. Observance of the strange waves appears to be comparable to the problem of schlieren observation of large scale structures in mixing layers.

The axial mass flux field displayed in Figure 5.13 reveals several vortex pair "peanuts" at several axial positions. The presence of pairing at numerous locations axially is due to a broad spectrum of frequencies present in the flow. As pointed out by Wilson and Demuren [79] excitation by a single frequency will produce pairing at a fixed axial position.

The transverse mass flux field displays the unique structure of this conservative variable in Figure 5.14. Coupled positive and negative peaks in the mass flux field are associated with individual vortices of the shear layer. The locations of the vortices are clearly visible and the magnitude of the peaks shows the relative vortex strength. The vorticity field displayed in Figure 5.11. A closeup view in Figure 5.15 shows that some positive areas have two peaks. The cause of this multiple peak behavior is not known at this time. Similar structures exist in the negative mass flux areas. The presence of twin peak structures of varying size and shape as well as single peak structures suggests that this local behavior

may not, and indeed does not, show up in the time-averaged r.m.s. mass fluctuation profiles of this simulation.

The instantaneous total energy field shows a comparably quiet flow of energy from the high speed stream into the low speed stream. Dark centers in each vortex show a process of low energy fluid being engulfed by the high energy stream. The apparent persistence of the dark cores in the vortices suggest that mixing within the vortex structure may be a limiting factor for processes such as fuel mixing and related combustion.

The pseudo-3d figures contribute to an understanding of the instantaneous variable fields by adding a dimension of magnitude that is more difficult to obtain with conventional contour plots. Each new perspective or form of the data contributes to a more complete understanding of what the data has to tell us. Comparisons between the instantaneous variables and their time-averaged fields helps the researcher understand how the instantaneous flow structures produce the mean behavior.

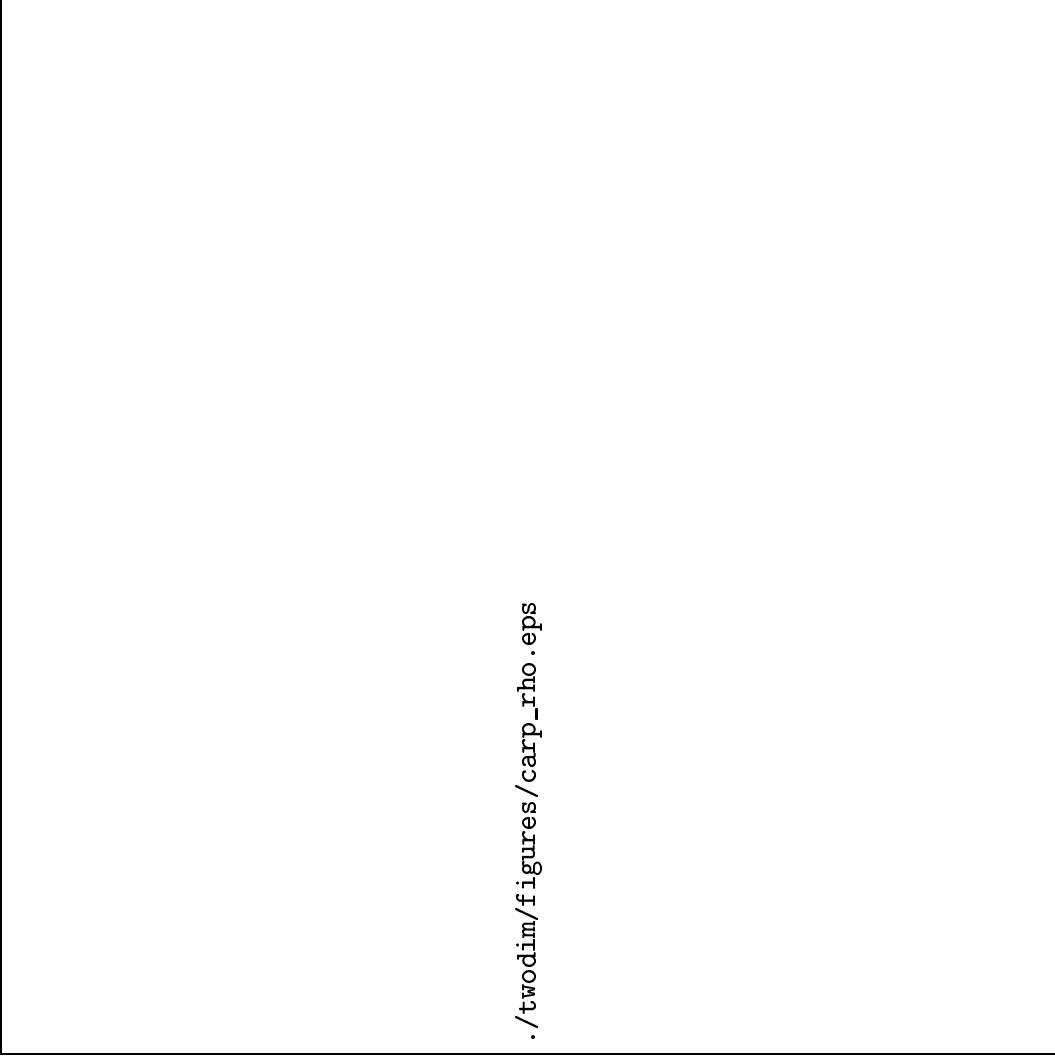


Figure 5.12. Instantaneous Density Field: a) Two-dimensional contour and b) Carpet plot.

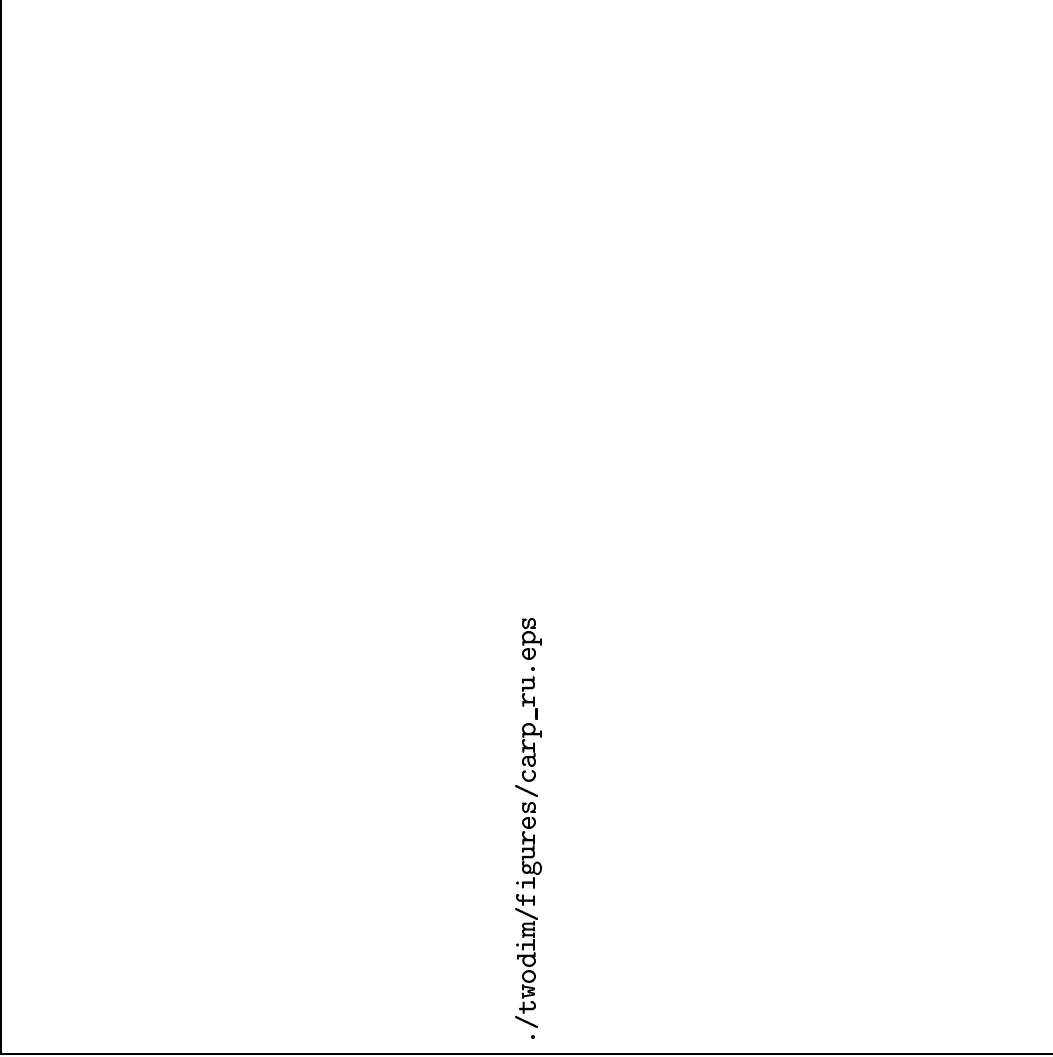
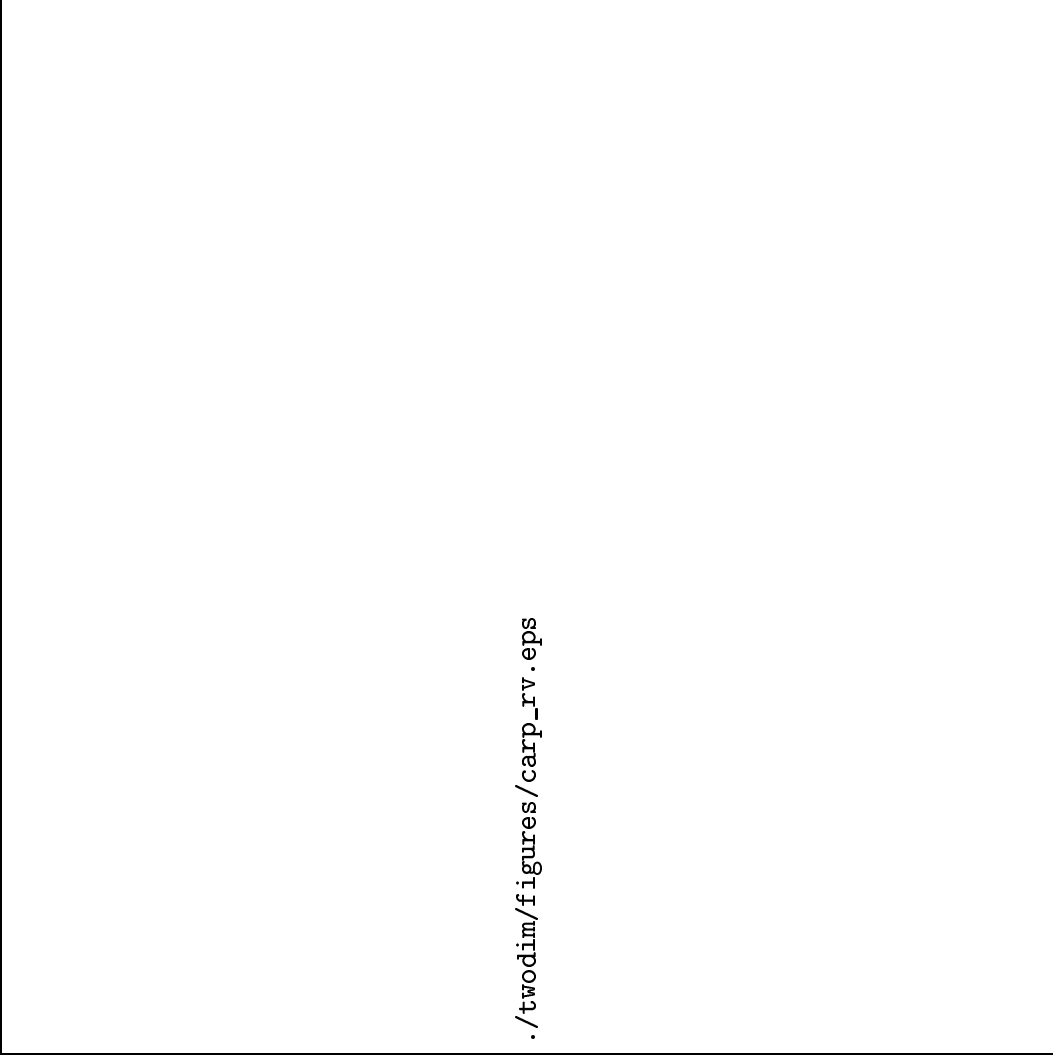


Figure 5.13. Instantaneous Axial Mass Flux Field: a) Two-dimensional contour and b) Carpet plot.



./twodim/figures/carp_rv.eps

Figure 5.14. Instantaneous Transverse Mass Flux Field: a) Two-dimensional contour and b) Carpet plot.

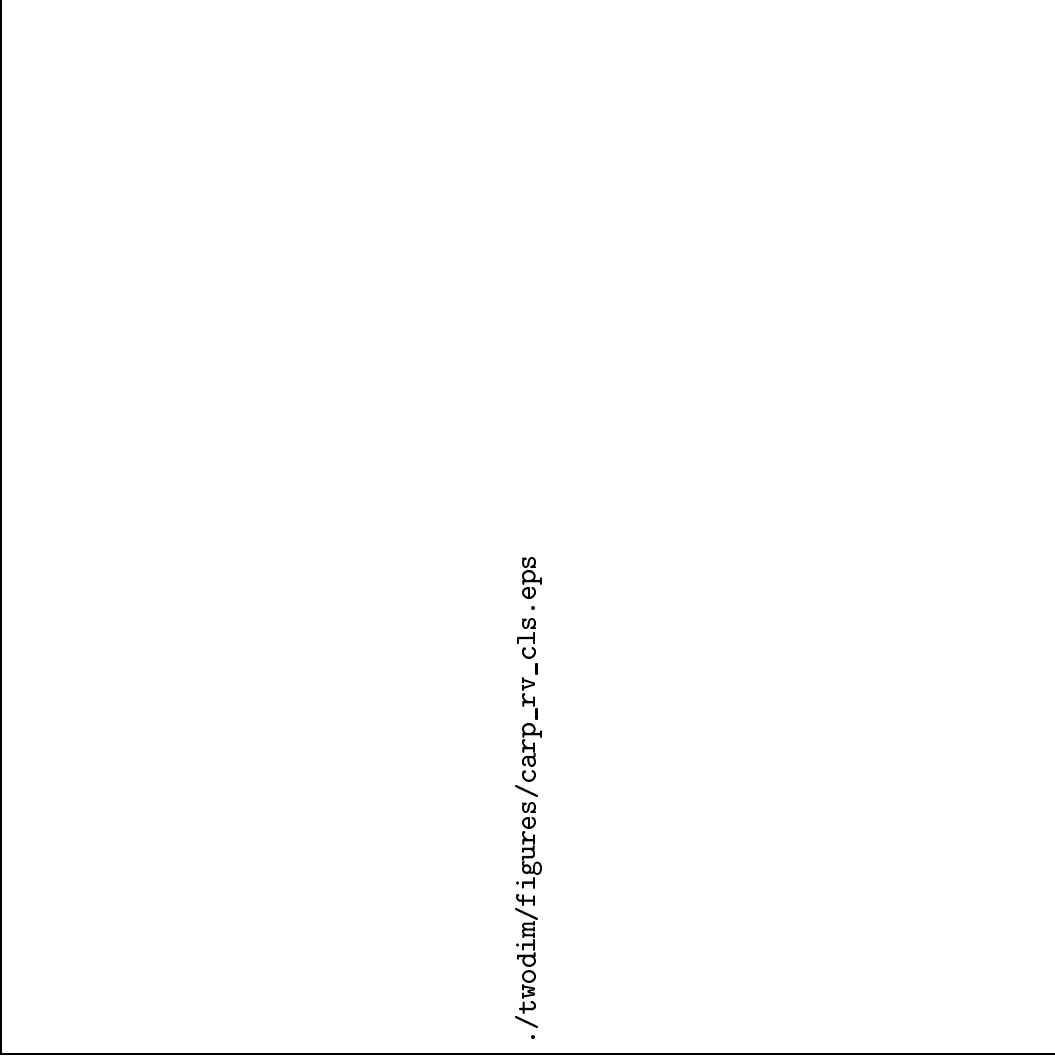
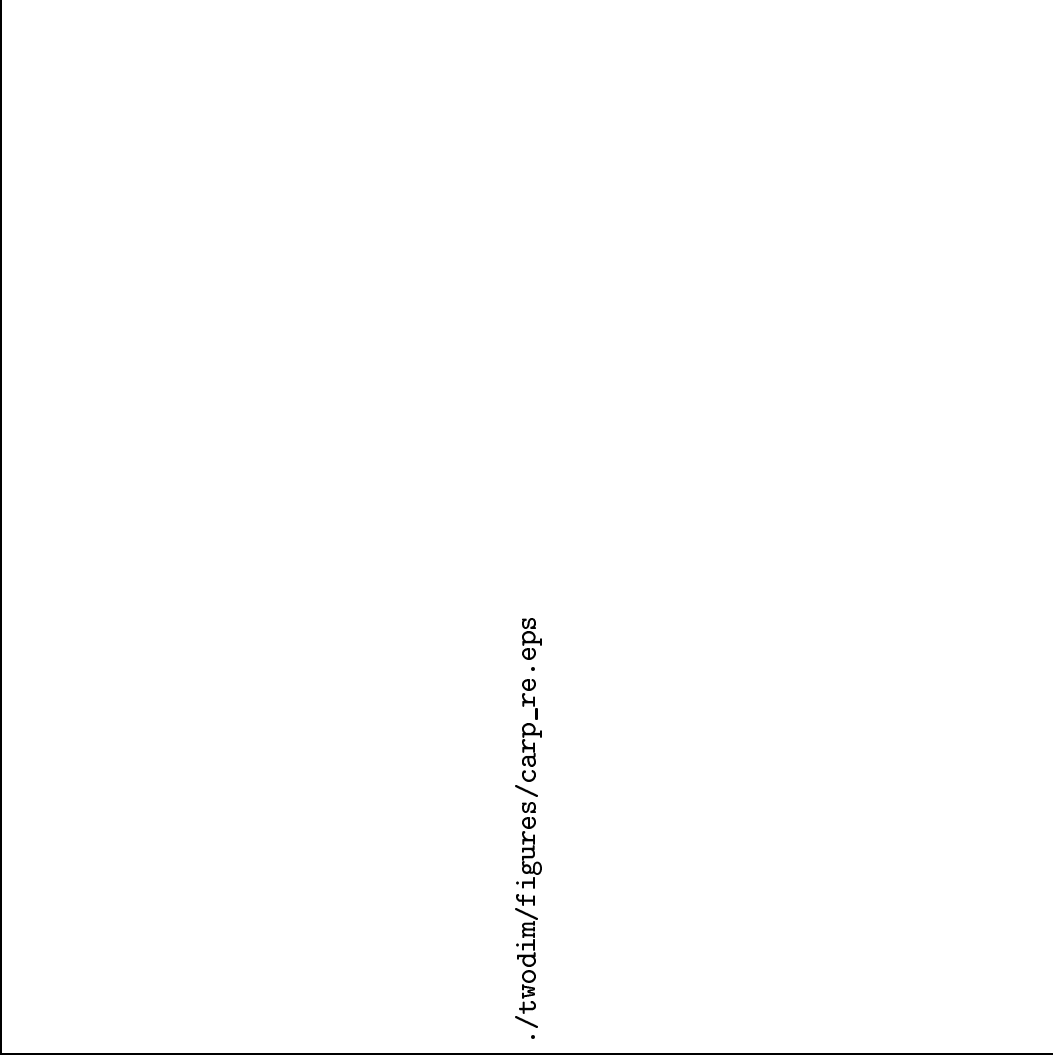


Figure 5.15. Close-up of the Instantaneous Transverse Mass Flux Field: a) Two-dimensional contour and b) Carpet plot.



./twodim/figures/carp_re.eps

Figure 5.16. Instantaneous Total Energy Flux Field: a) Two-dimensional contour and b) Carpet plot.

5.2.3 Time Averaged Results

Instantaneous to Time Averaged Comparison

Conventional time averaged data has given global measures of shear layer performance such as the various growth rates discussed previously. By examination of the time averaged field of a variable and comparing it with the instantaneous field insight can be gained as to the causal behavior. The ability to make such comparisons is unique to numerical simulations. The contour plots of the conservative variables' instantaneous and time averaged fields along with the cross-section line plots of the time averaged data are displayed in Figures 5.17, 5.18, 5.19, and 5.20. The time averaged density field shows occasional points along the streamwise development where slight but sudden spreading of the contour lines occur. More notable are the bumps in the cross channel profiles. These bumps are the time averaged effects of high density ribbons that vortices draw into the low density stream; see also Figure 5.12. The density profiles given in other numerical simulations [8, 64] as well as experimental results by Brown and Roshko [7] show nearly identical behavior. The axial mass flux fields, Figure 5.18, show a much smoother profile indicating the velocity contribution dominates the conservative mass flux variable. The comparison of transverse mass flux provides the greatest amount of information about how time averaged or stationary structures interact with the instantaneous field, Figure 5.19. Early disturbance growth is shown to produce Mach waves at a fixed position in the time averaged field. The Mach waves are most readily observed in the Transverse mass flux field but can be found in the data of all the variables. The relatively small magnitude of the Mach wave disturbances makes their observations difficult for the other variables. The Mach waves move out from the shear layer, reflect from the walls then hit and excite the shear layer at the 0.15 m location. Subsequent wall reflections of the Mach wave system produce multiple peaks or islands of high transverse mass flux along the axial direction. The energy captured by the confining walls is fed back into the shear layer growth by periodic stimulation of vortex growth. However, this effect is weak as evidenced by the negligible effect shown on the growth rate profile of Figure 5.8. The predominately negative sign of the mass flux indicates a net flow of mass from the high density stream into the low density stream. The total energy profiles of Figure 5.20 show smooth behavior similar to the axial mass flux

fields. Two notable differences are the thinner time averaged shear layer thickness and less distinct vortex structures in the instantaneous contours. The vortices are less well defined on the low energy side of the shear layer. Finally the energy profiles across the shear layer are very smooth indicating a smooth cascade of energy from one stream to the other.

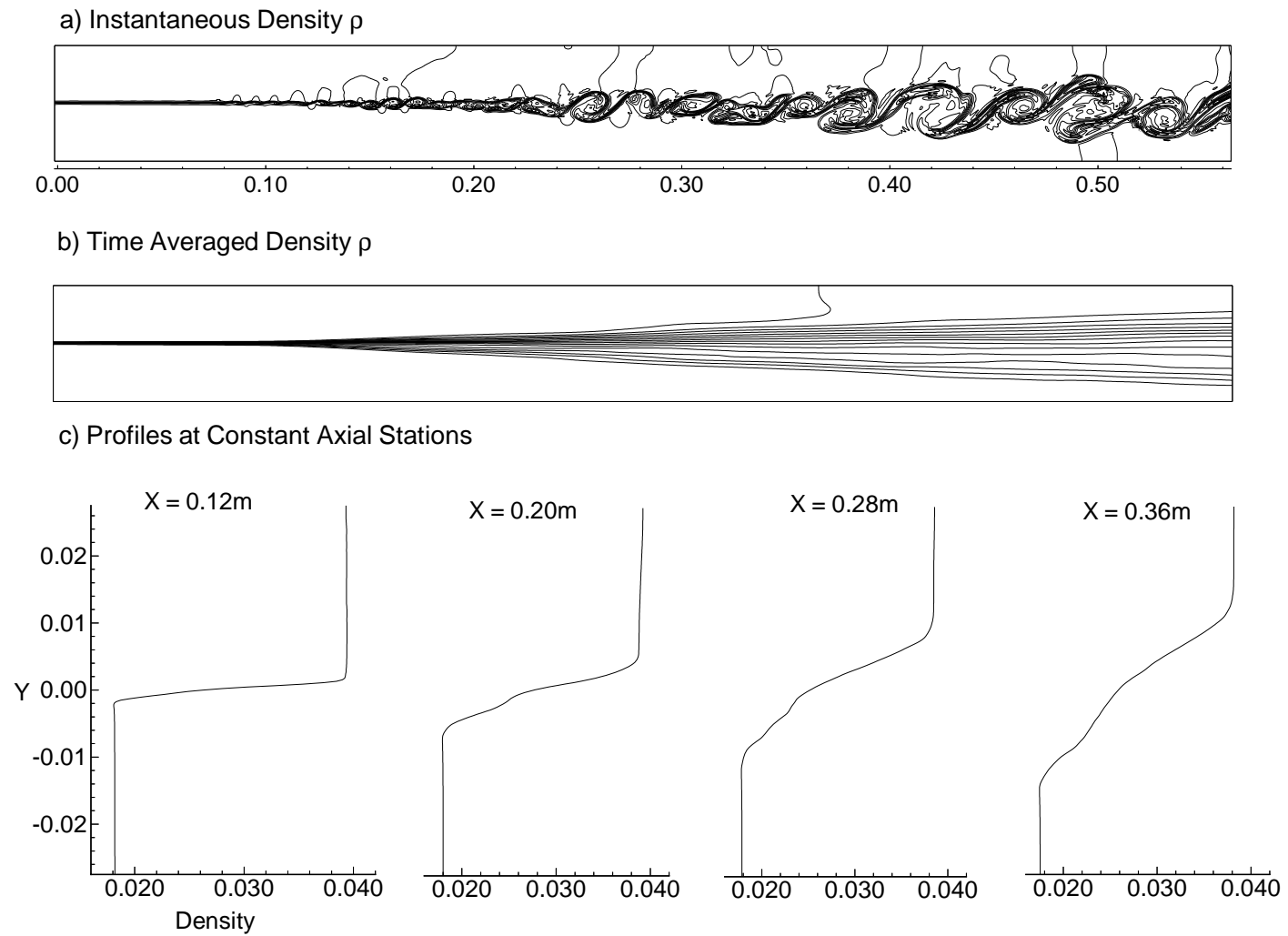


Figure 5.17. Conservative Variable Density ρ (kg/m^3) a) Instantaneous Density, b) Time Averaged Density Field, and c) Cross Channel Density Profiles at $X = .12\text{m}$, $.20\text{m}$, $.28\text{m}$, and $.36\text{m}$.

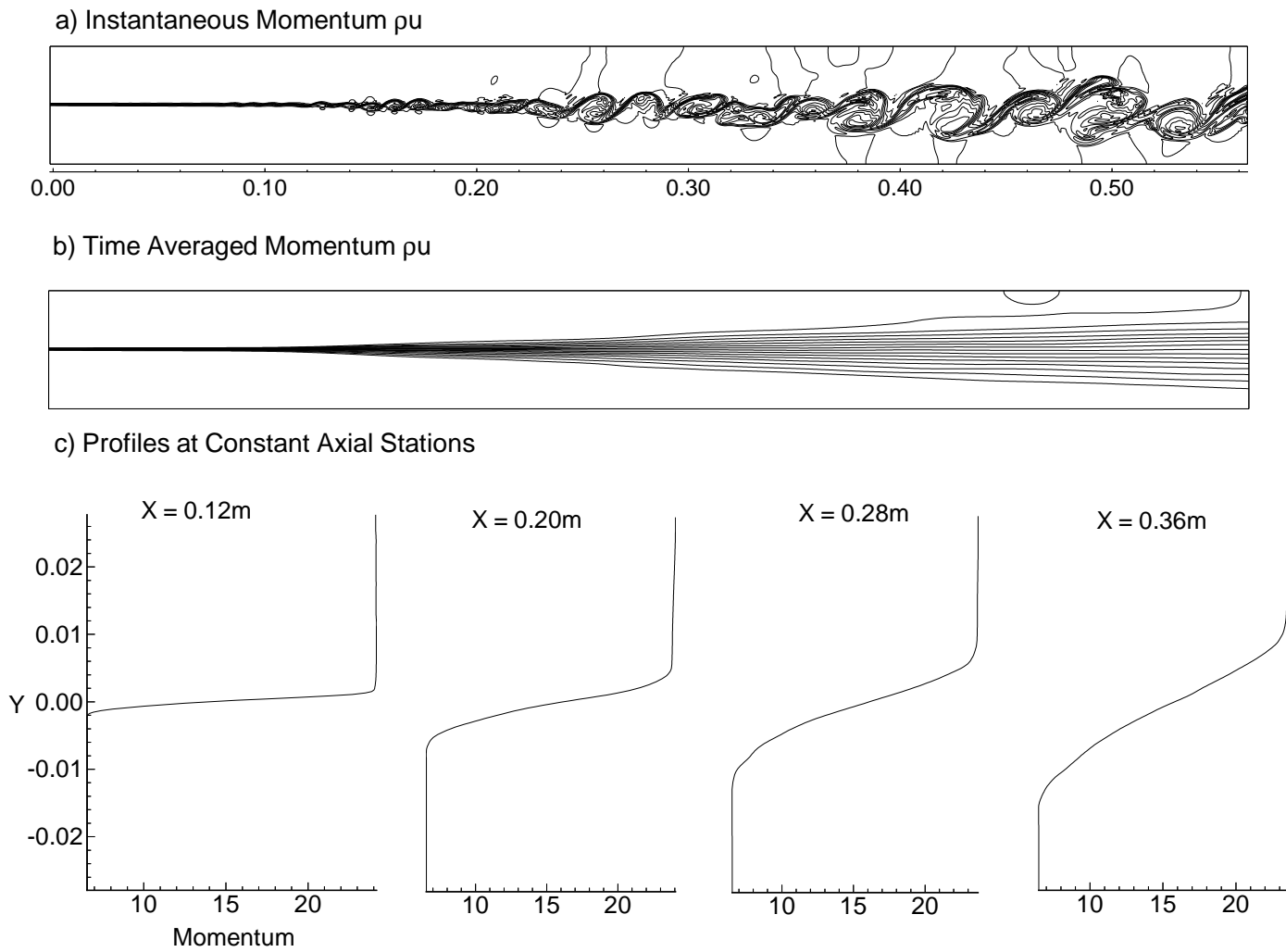


Figure 5.18. Conservative Variable Axial Mass Flux ρu (kg/sm^2) a) Instantaneous Mass Flux, b) Time Averaged Mass Flux Field, and c) Cross Channel Mass Flux Profiles at $X = .12m, .20m, .28m,$ and $.36m$.

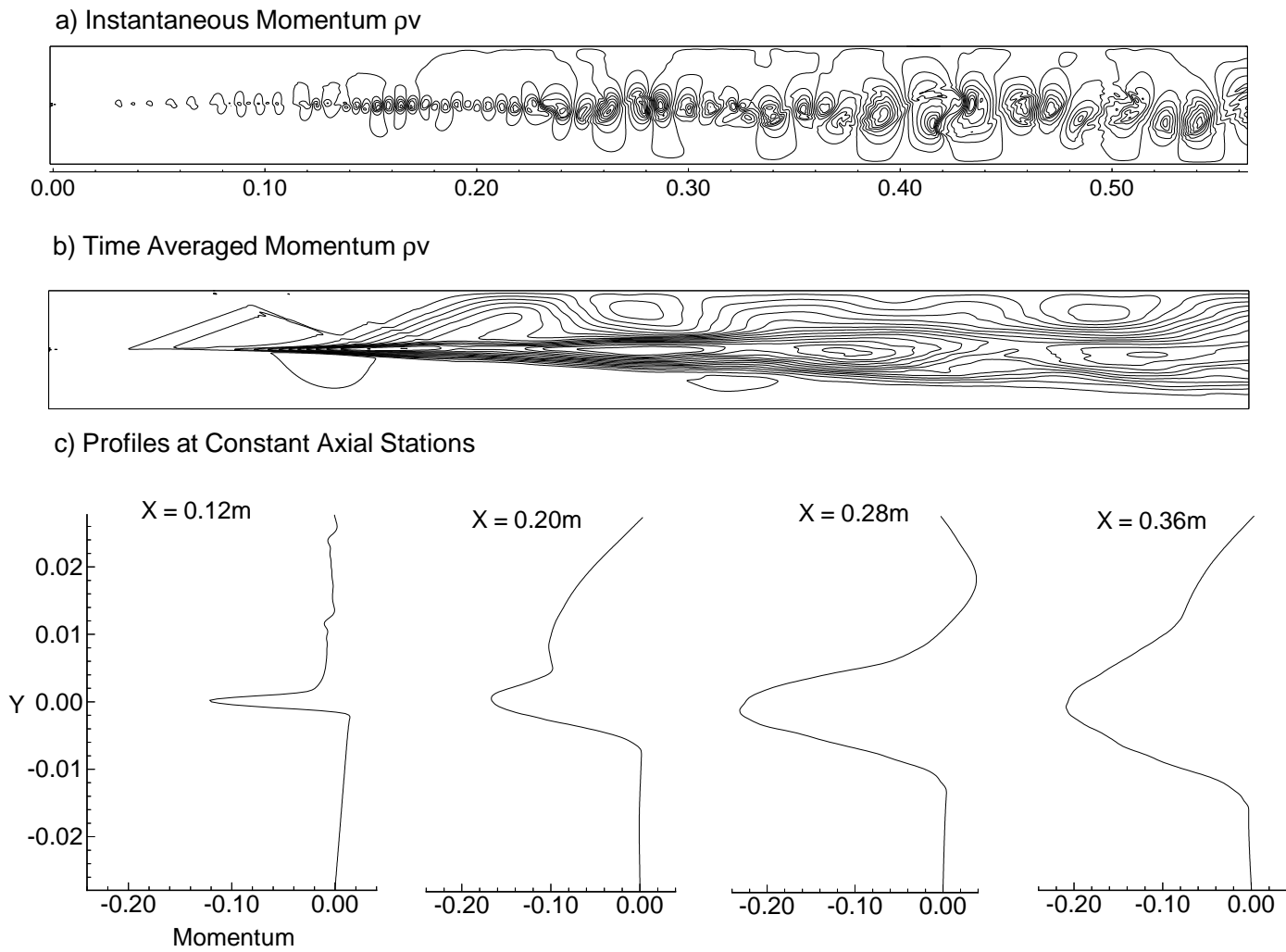


Figure 5.19. Conservative Variable Transverse Mass Flux ρv (kg/sm^2) a) Instantaneous Mass Flux, b) Time Averaged Mass Flux Field, and c) Cross Channel Mass Flux Profiles at $X = .12m$, $.20m$, $.28m$, and $.36m$.

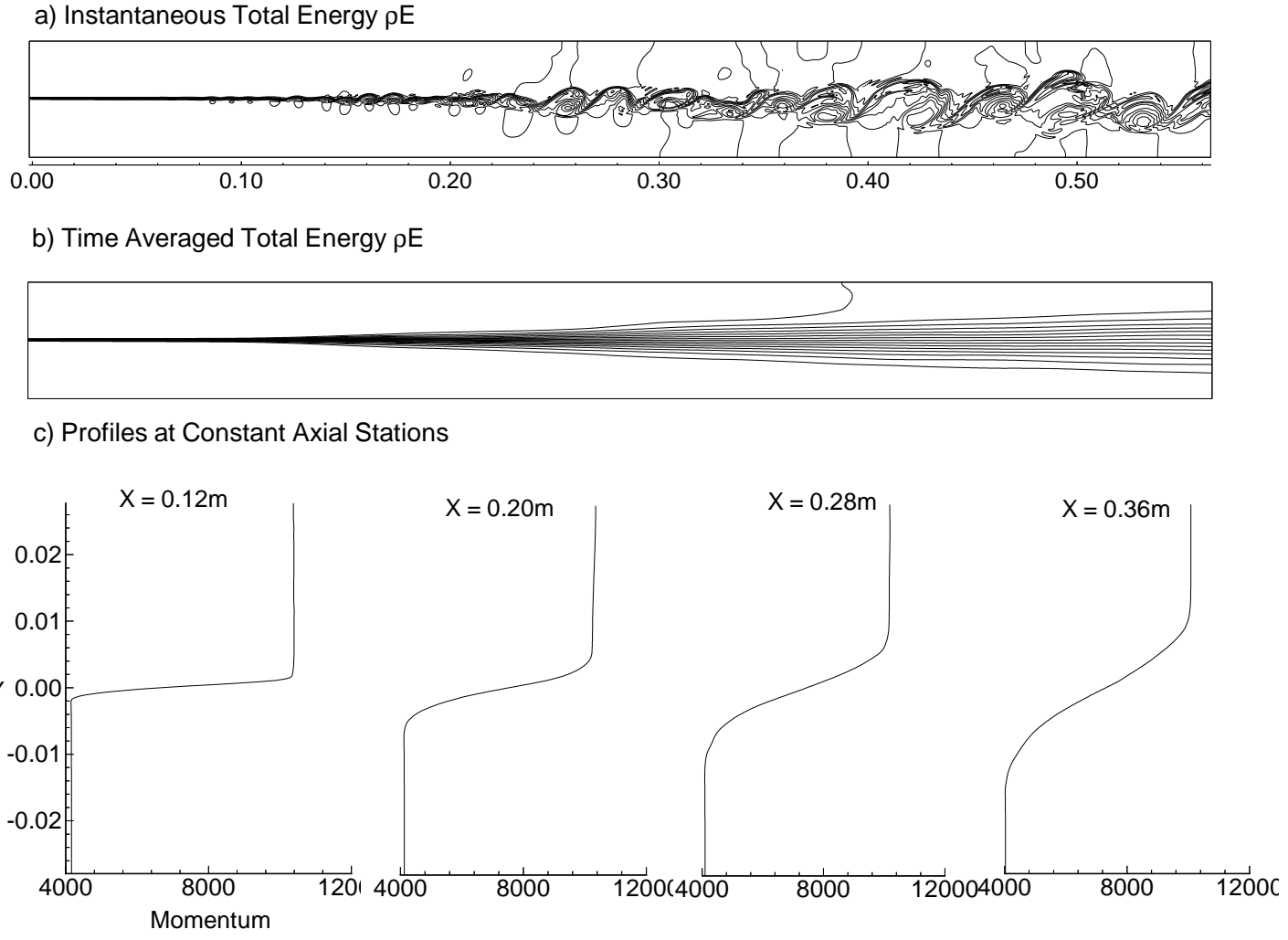


Figure 5.20. Conservative Variable Total Energy Flux ρe_t ($Joule/m^2$) a) Instantaneous Total Energy, b) Time Averaged Total Energy Field, and c) Cross Channel Total Energy Profiles at $X = .12m, .20m, .28m,$ and $.36m$.

Comparisons between instantaneous fields of the conservative variables and the time averaged fields have led to several new observations about shear layers. First, density appears to be an accommodating factor in the transfer of energy from one stream to the other. Second, shear layer confinement does cause energy feed back into the shear layer and the stimulation of vorticity. Finally, the significance of the feed back energy to the shear layer growth rates can not be assessed without more direct investigation.

Time Averaged Comparison With Experiment

Computed shear layer results have been compared to the experimental results with overall good agreement. The results compare well with the experimental data without the need for a virtual origin shift. The inlet treatment yields an inflow disturbance that produces down stream behavior that compares well with the experimental data.

Of the numerous inlet perturbation parameters, the ghost cell treatment and the addition of v' perturbation were found to be the most influential in causing the shear layer to grow at the experimental rate. The ghost cell treatment ensured the smooth gradient behavior of the inlet boundary variables. The v' perturbation was set at a magnitude of $0.7u'$ with the phase at 90° to u' . The v' perturbation conditions were based upon plane mixing layer experiments [54].

The experimental data at the 0.12 m position show the presence of a strong splitter plate wake. The effect of the splitter plate wake profile on the shear layer and its growth has not been well explored. Some early research [64] has shown that for subsonic shear layers the inlet wake shape significantly affects the symmetry of the shear layer growth and yet most numerical simulations continue to use the hyperbolic tangent profile successfully.

The spreading of the shear layer is shown in Figure 5.21 by a plot of the velocity profiles at eight axial locations. The high speed (energy and density, also) stream is shown spreading into the low speed stream. The locations were chosen to show the progression of the shear layer growth at positions where experimental data were available. Figures 5.22 and 5.23 present comparisons between computed mean velocity \bar{u} , shown by the solid line, and experimental mean velocity profiles from Pitot probe data, shown by the symbols. The data and computed profiles are “as given” and have not been adjusted to correct for inaccuracies in the experimental shear layer’s position or the inlet hyperbolic profile placement.

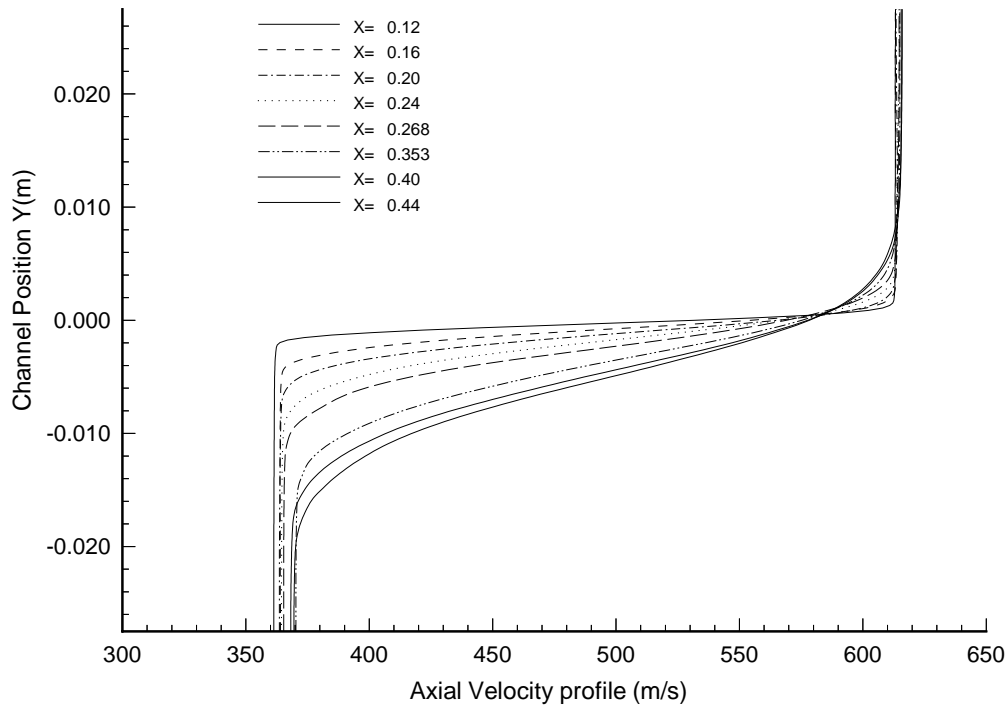


Figure 5.21. Axial Variation of Numerical Time averaged Velocity Profiles

The profiles compare closely over most of the length for which data are available. The comparisons of the shear layer thickness and maximum gradient of the velocity between experiment and simulation deteriorate beginning at the 0.35 m location. The lack of diffusion from viscosity in the simulation is believed to be the primary cause of the persistent steep velocity gradient across the shear layer. As the downstream distance grows the shear layer becomes influenced by the walls. Figure 5.23 shows that the wall boundary layers begin to merge with the shear layer at 0.44 m distance.

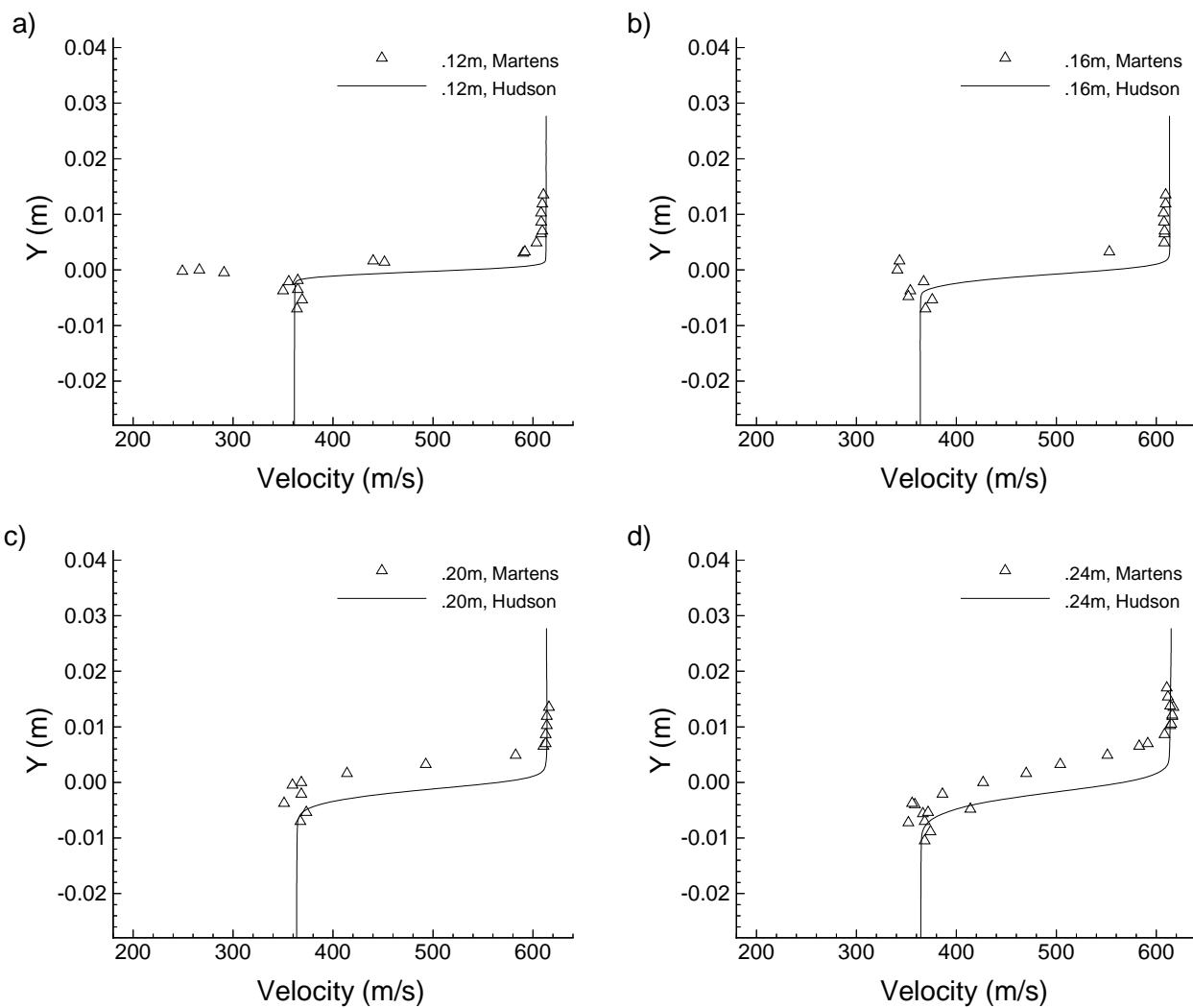


Figure 5.22. Comparison of Numerical and Experimental Mean Velocity Profiles; a) X=0.12 m, b) X=0.16 m, c) X=0.20 m d) X=0.24 m.

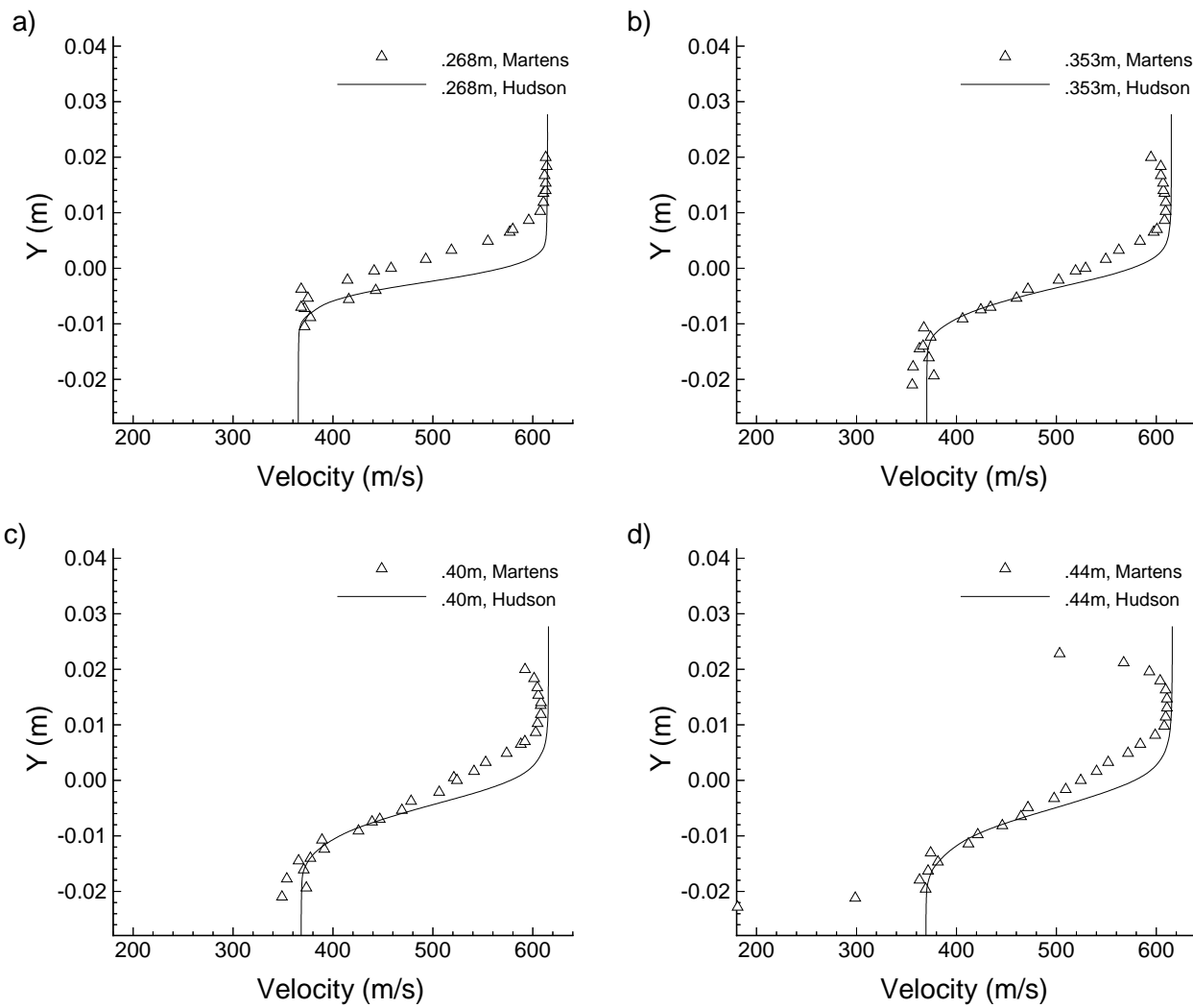


Figure 5.23. Comparison of Numerical and Experimental Mean Velocity Profiles; a) X=0.268 m, b) X=0.353 m, c) X=0.40 m d) X=0.44 m.

The comparisons that have been made between the simulation results and the experimental data have been good but not perfect. The time-averaged velocity profiles, and the shear layer thickness growth compare well to a point but the comparisons do not give a lot of insight as to the source of the differences. The auto-spectra of the simulation show the power in the unsteady mass flux fluctuations are confined to narrow frequency bands. The auto-spectra of the experimental data show a much lower levels of power that are distributed over a much broader range of frequencies. The comparison suggests that the differences may be based in the simulation of the fluctuating behavior.

Fluctuating Quantities

The simulation results have compared well with most of the experimental data for both dynamic and time averaged data. Four-way comparisons between the broadly excited and the single frequency excited results of both simulation and experiment were also conducted. The fluctuating behavior of the flow was examined by comparison of Martens' mass-velocity fluctuation data with the equivalent simulation quantities. Large differences were found between the experimental and simulation profiles of the mass-velocity fluctuations. The dynamic comparisons, in particular the auto-spectra comparisons, have suggested that the differences are related to the ability of the simulation to predict the distribution of power over an increasing range of frequencies. The impact on the shear layer thickness growth appears to be significant. Additional study will be necessary to establish the precise cause of the simulations confining of energy in a narrow bandwidth of frequencies. The final part of the study of the fluctuating quantities looked at the axial mass flux rms fluctuations, transverse mass flux fluctuations, and the Reynolds stress fields. These fields have similar behaviors to turbulence intensity results being reported by other researchers. Examination of the fields has suggested possible explanations for conflicting trends being reported.

Martens' rms mass-velocity fluctuations are defined by Martens as $(\rho u)_{rms}^l / \overline{(\rho u)}_{local}$. The experimental parameter and the simulation parameter are compared at four axial locations. The results are shown in Figure 5.24. The profiles show significant differences between the experimental results and the simulation values. Three types of differences are observed; first, is the large difference in the peak magnitudes, second the general shape of the profiles, and third the difference in trends of the peak magnitudes with axial distance.

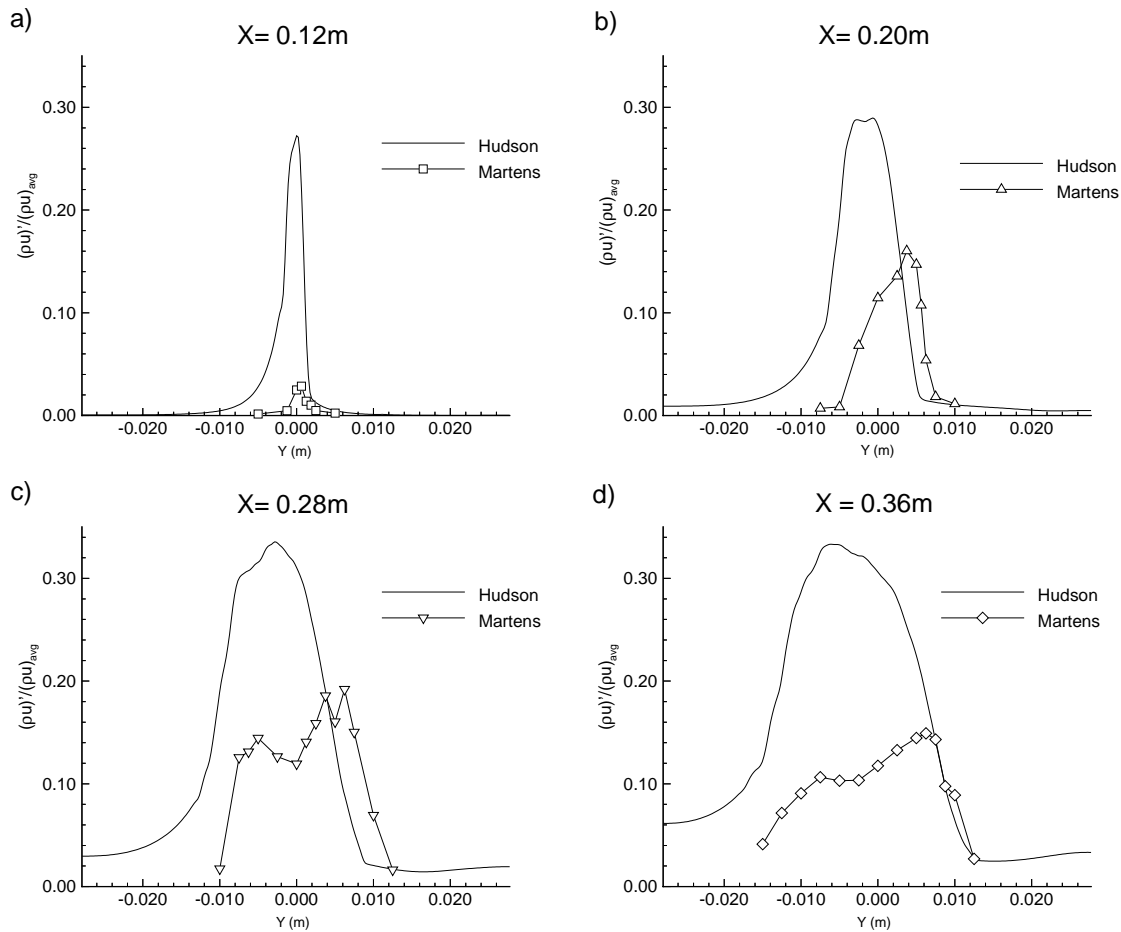


Figure 5.24. Numerical and experimental r.m.s. fluctuations $\frac{(\rho u)'}{(\rho u)_{local}}$.

The precise causes of the differences are not known but several observations point to some possible explanations.

The large differences in the peak magnitudes of simulation and experiment data may be due to two possible causes 1) over excitation of the inlet and 2) the focus of unsteady power in a narrow frequency range. During development of the simulation attention was focused on the effect of the inlet perturbation magnitude on the growth of the shear layer thickness and not so much on the magnitude of the subsequent fluctuation fields. The inlet disturbance magnitudes are on the order of a few 10ths of a percent of the variable's local value, nearly an order of magnitude less than the fluctuation levels shown in Figure 5.24.

Consequently, a direct connection between the inlet disturbance and the downstream fluctuation levels is not considered the primary cause. Examination of the second potential cause focuses on the narrow frequency range in which most of the simulation's unsteady power is contained.

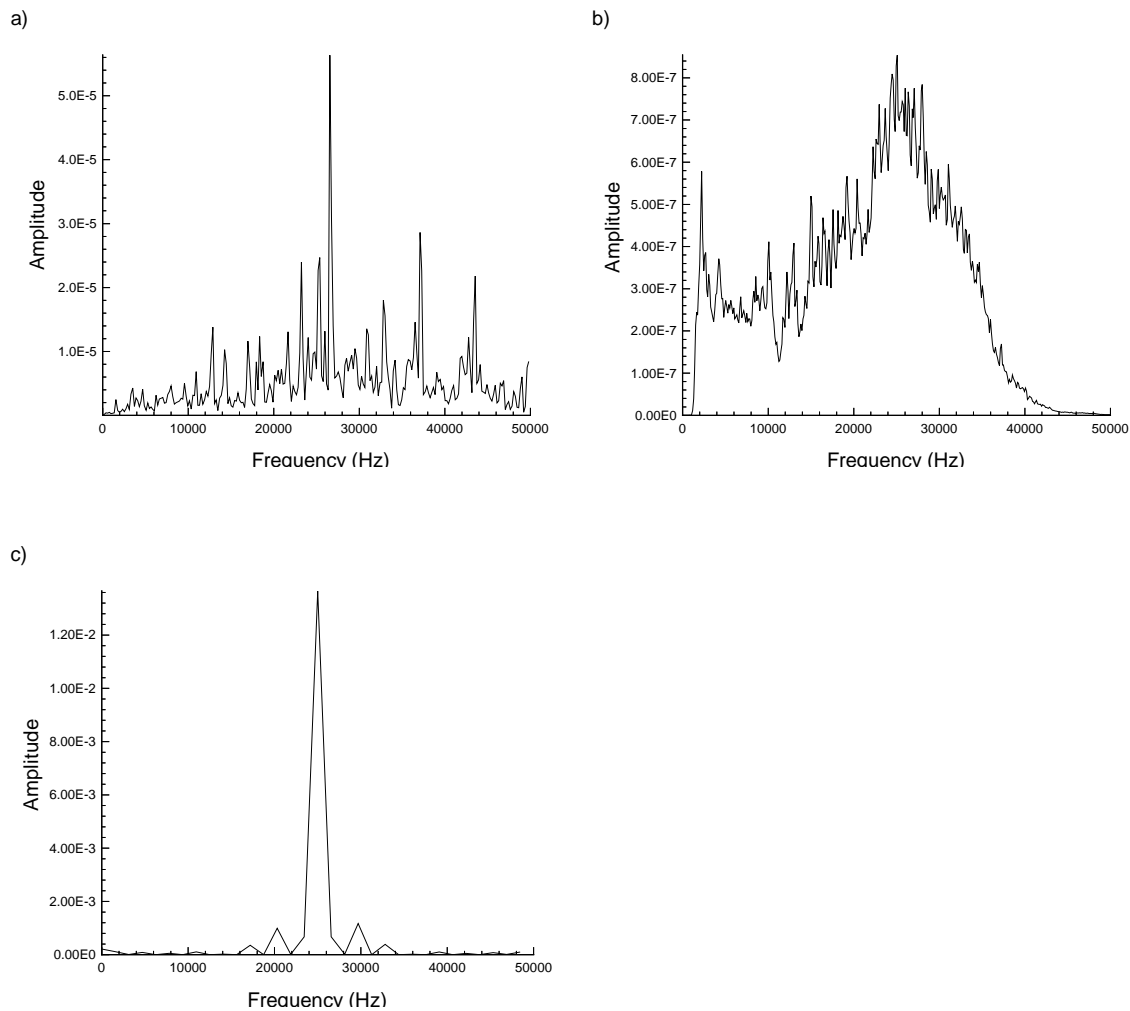


Figure 5.25. Case I $M_c = 0.5$ Simulation and Experimental Auto-spectra at 0.18 m Location: a) Broadband Excited Simulation, b) Naturally Excited Experiment, c) 25 kHz Single Frequency Excited Simulation, and d) 25 kHz Single Frequency Excited Experiment.

The four-way comparison of the auto-spectra are shown in Figure 5.25. The broadband, and single frequency excited simulations as well as the single frequency excite experimental data show concentrations of power in very narrow frequency bands centered at the locally dominant frequency. The naturally excited experimental auto-spectra has a much

broader frequency distribution of power. The peak amplitude of power is also several orders of magnitude smaller than the peaks shown for the simulations and the single frequency excited experimental case. The peak power levels were also evident in the rms mass-flux perturbations.

The several key observations can be made from the four-way comparisons of the rms mass-flux perturbations. The first observation is the significantly higher peak magnitudes of the three data sets exhibiting power concentration near the dominant frequency. The observation of the higher peak magnitudes for the first three data sets shows agreement with the auto-spectra grouping of these three data cases. In contrast, the twin peaked profiles in the single frequency excited simulation and experiment and in the naturally excited experiment show a similarity in these three processes that is different from the perturbation magnitude issue. Another compare and contrast type observation is made for the two simulation cases and the two experimental cases. The simulation cases have very different shaped perturbation profiles and yet have auto-spectra that are visually very similar. Again, in contrast, the experimental cases have visually very similar perturbation profiles while their auto-spectra are very different. The final observation is the very narrow and nearly constant shear layer thickness with axial distance for the single frequency excited simulation. All of the questions raised by these observations point back to the desire to understand the mechanisms that influence the shear layer growth.

The shear layer thickness growths for the four cases are compared in Figure 5.27. From Figure 5.27, similarity is seen in the growth behavior for three cases that have narrow power bands. And yet the simulations have obvious similarities such as the transition point for the laminar to turbulent growth. The experimental growth profiles also have similar shapes in their rapid growth region. These growth profiles suggest the narrow concentration of perturbation power may be the key to enhanced shear layer mixing. The perturbation and Reynolds stress fields, when viewed as contour fields, also provide insight as to factors that influence research findings from both numerical and experimental research.

Finally, the mass flux perturbations and Reynolds stress fields are displayed in Figure 5.28, Figure 5.29 and Figure 5.30. The mass flux perturbations $(\rho u)'$ and $(\rho v)'$ fields have contour fields that resemble turbulence intensity fields. Study of these fields will contribute to our understanding of the shear layer behavior and maybe of the associated

turbulence fields. The axial mass flux perturbation grows to a maximum and then holds a constant contour shape and magnitude. The transverse mass flux perturbation has a similar growth pattern; it grows quickly until about $X = 0.28 m$ and then remains approximately constant throughout the remaining length of the duct. By comparing the rms perturbation and time averaged fields of the transverse mass flux variable two very different behaviors are observed. The time averaged field of Figure 5.19 shows a strong interaction with the walls. The impact of the wall interaction is much smaller on the rms perturbations shown in Figure 5.29. The Reynolds stress $\rho u'v'$ shows a repeating process of growth and decaying very similar to the time averaged transverse mass flux field contours. The growth and decay process occurs several times within the length of the computational domain. Several conclusions can be drawn from all the observed behaviors as to their different causes.

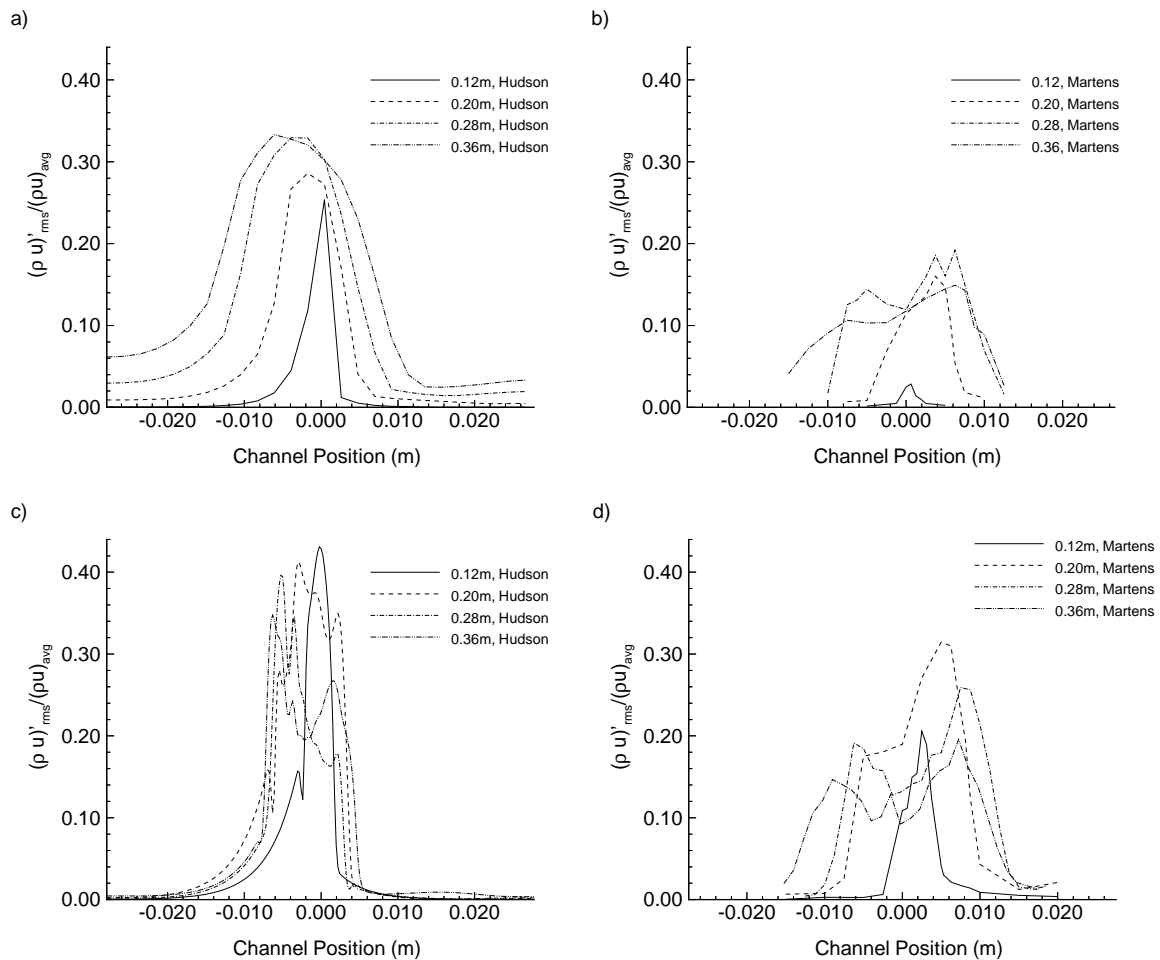


Figure 5.26. Case I $M_c = 0.5$ RMS Mass Flux Perturbation $(\rho V)'$: a) Broadband Excited Simulation, b) Naturally Excited Experimental, c) 25 kHz Single Frequency Excited Simulation, and d) 25 kHz Single Frequency Excited Experiment.

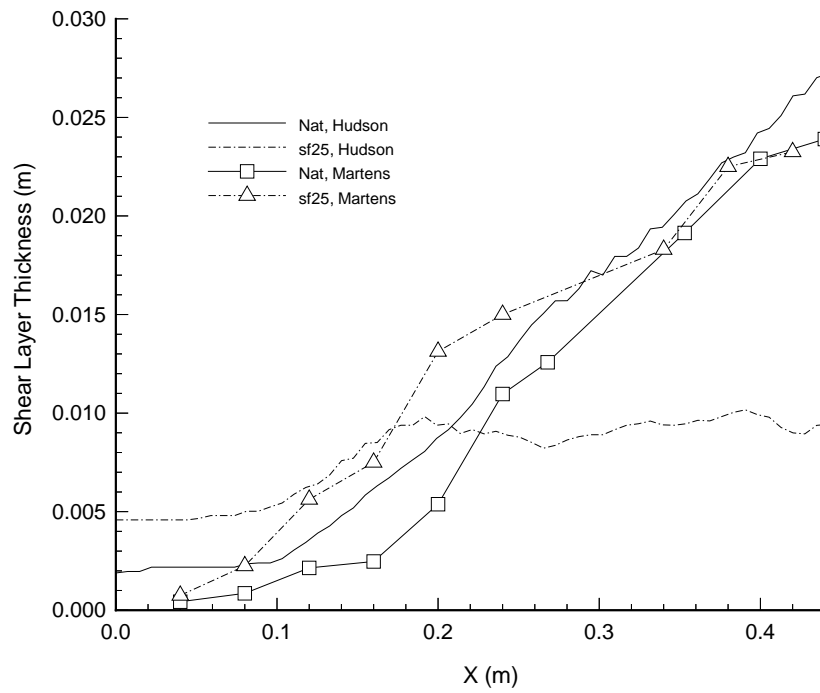
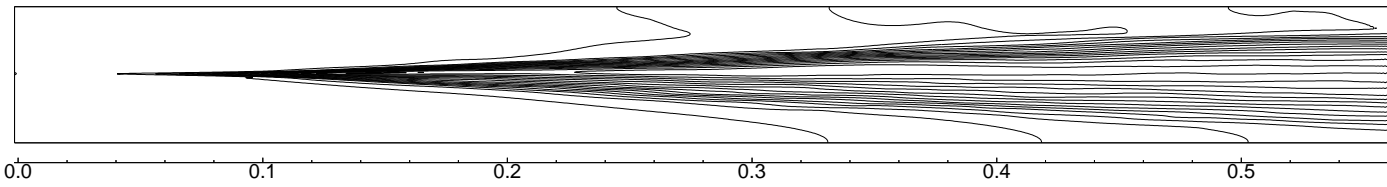


Figure 5.27. Case I $M_c = 0.5$ Shear Layer Thickness Growth.

a) RMS Momentum Perturbation: $(\rho u)'$



b) Profiles at Constant Axial Stations

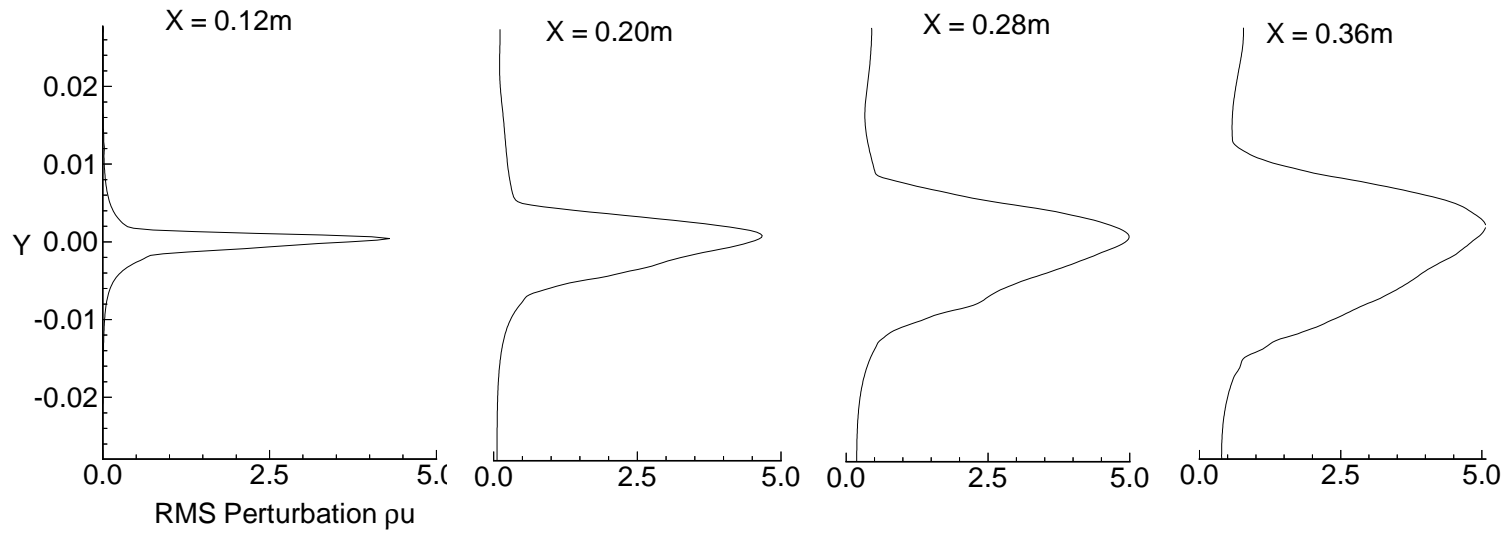
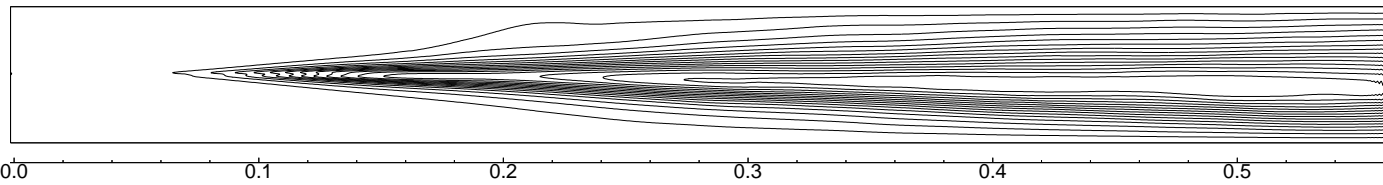


Figure 5.28. Case I $M_c = 0.5$ Axial Mass Flux Perturbation $\overline{(\rho u)'}'$: a) RMS Mass Flux Perturbation and b) Cross Channel Profiles at $X = .12\text{m}$, $.20\text{m}$, $.28\text{m}$, and $.36\text{m}$.

a) RMS Momentum Perturbation: $(\rho v)'$



b) Profiles at Constant Axial Stations

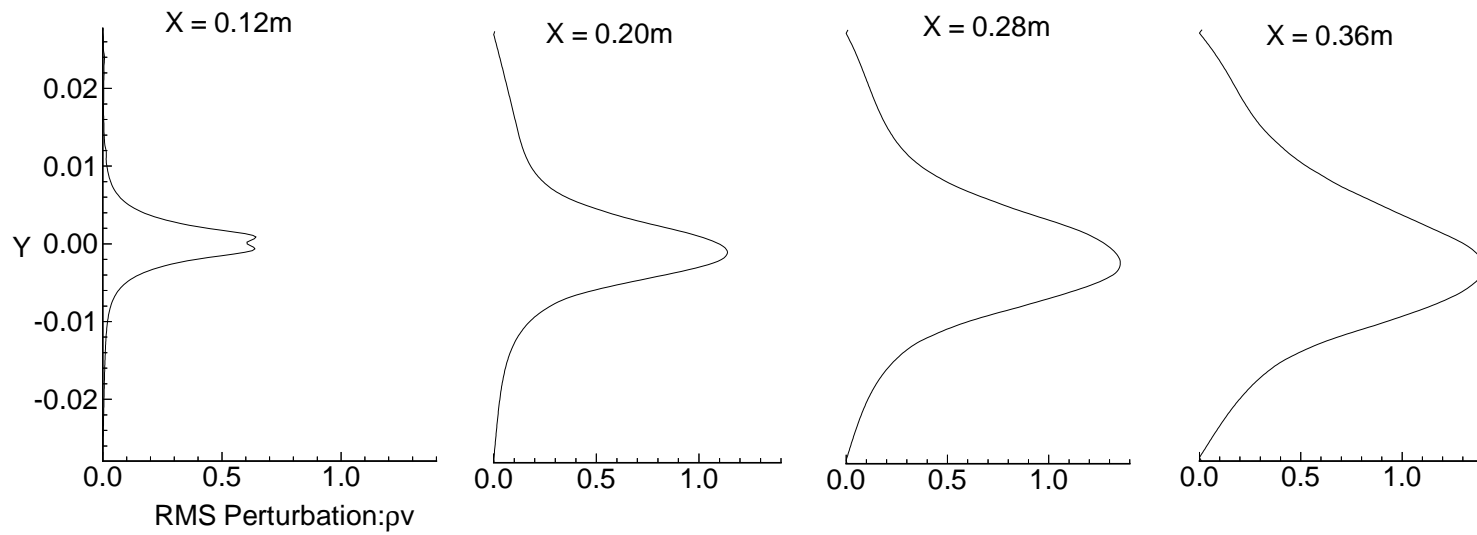
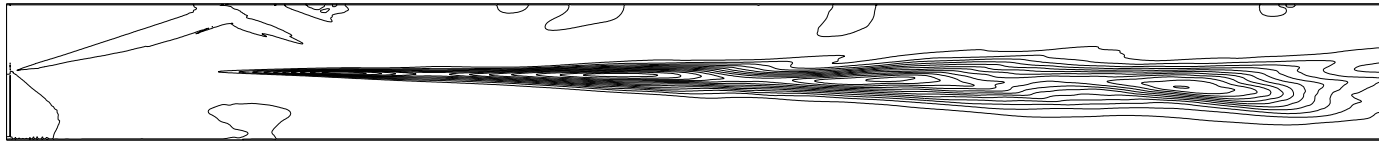


Figure 5.29. Case I $M_c = 0.5$ Transverse Mass Flux Perturbation $\overline{(\rho v)'}'$: a) RMS Transverse Mass Flux Field and b) Cross Channel Profiles at $X = .12m, .20m, .28m,$ and $.36m$.

a) Time Averaged Reynolds Stress: $\rho u'v'$



b) Profiles at Constant Axial Stations

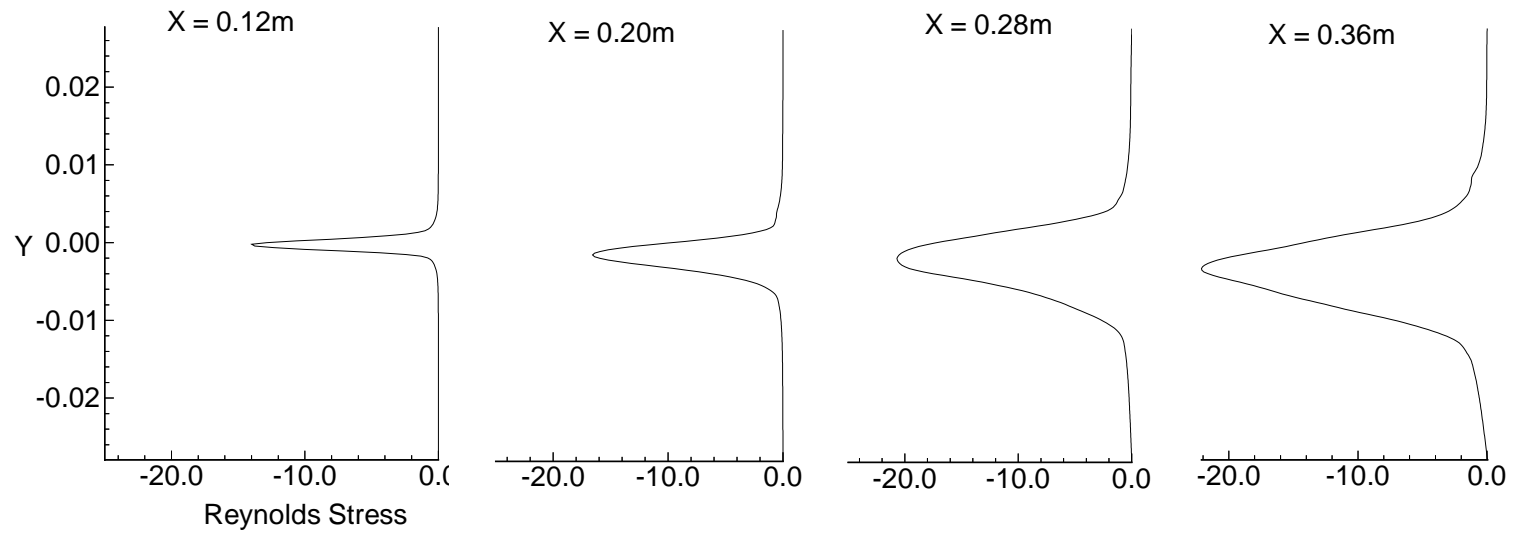


Figure 5.30. Case I $M_c = 0.5$ Time Averaged Reynolds Stress $\overline{\rho u'v'}$: a) Time averaged Reynolds Stress Field, and b) Cross Channel Profiles at $X = .12m, .20m, .28m,$ and $.36m$.

The observations made from the perturbation behaviors seem to concentrate into three general conclusions. First the wave resolution in the research domain is critical the quality of the data. The natural fluids of experiments admit waves down to extremely small wave lengths. This admittance is key in providing the small scales necessary for non-linear interactions to distribute power over a broad range of frequencies. The redistribution of energy by high admittance also allows small scale behavior to cloud single behavior. The second conclusion is that the power and associated perturbation magnitude are the key factors in the early onset of high/early turbulent growth rates. The final observation is that the domain of the simulation or experiment significantly contribute to the flow field and the associated finding from data obtained. Hard reflecting and confining walls can and do add energy back into the shear layer, affecting the growth. Special insights can also be obtain from simulations that are impossible to obtain experimentally. The two investigations of the next section provide such insights; flow behavior as seen from a convecting frame of reference and the location of entropy generation in the shear layer.

5.2.4 Special Topics

Direct simulations of fluid processes have many advantages over conventional experimental data collections. The advantages generally stem from the ability to capture the complete set of conservative variables throughout the simulation domain. In addition, the ability to record various forms, such as instantaneous, time-averaged and perturbation forms, allow the flow behavior to be investigated from many different perspectives including different frames of reference. Two investigations were conducted to look at the flow behavior to obtain information that is not possible with today's experimental capabilities. The first investigation compares the flow behavior in small section of the shear layer as seen from a stationary and a moving frame of reference. The second investigation looks at the contribution of non-isentropic processes to the overall density perturbation in the shear layer.

Convecting Large Scale Structures

Papamoschou discussed in several of his publications [53, 52] an idealization of compressible shear layers in the reference frame of the large scale structures. The hypothesis

specified that, in a frame of reference moving at the convective velocity of the instability wave, a saddle type of stagnation point occurs between adjacent vortices. Earlier work in which, Bogdanoff [6] and Papamoschou [53] had developed a relationship between the convective Mach numbers of each stream, Mc_1 and Mc_2 . The isentropic model they developed yielded a relationship between the convective Mach number of the two streams, $Mc_1 = \sqrt{\gamma_1/\gamma_2} Mc_2$, where γ is the specific heat ratio. The convective Mach number relation was obtained by requiring equality of total pressures of the two streams in the convective frame. The equity of pressures occurs at the stagnation point between large scale structures in the convective frame of reference. Since experimental illustration is difficult, the concept is illustrated here with a vector plot of a large scale structure in the convective frame of reference ($u - U_c$) and the same large scale structure as seen from the stationary reference frame by viewing the transverse velocity field v . Figure 5.31 shows the large scale structure of the compressible shear layer in both convecting and stationary frames of reference. The flow structures appears to conform to the original hypothesis reasonably well.

Isentropic and Non-Isentropic Density Perturbations

Inviscid flow without heat sources or conduction, as governed by the Euler equations, describes isentropic flow in the absence of discontinuities. However, the Euler equations do admit entropy producing discontinuities such as vortex streets, contact surfaces and shocks in supersonic flows. The vortex street and large density gradients are the primary sources of entropy production in the shear layer simulation. The instantaneous density perturbations about the mean field were investigated to identify the relative contributions of isentropic and non-isentropic processes.

The investigation begins with the standard decomposition of the density and pressure variables into their time averaged and perturbation parts. The density perturbation is thus expressed as $\rho' = \rho - \bar{\rho}$. A second equation for the perturbation of density and pressure can be found beginning with the equation for entropy change from a reference state

$$s - s_A = c_v \ln \left(\frac{p/p_a}{(\rho/\rho_A)^\gamma} \right) \quad (5.10)$$

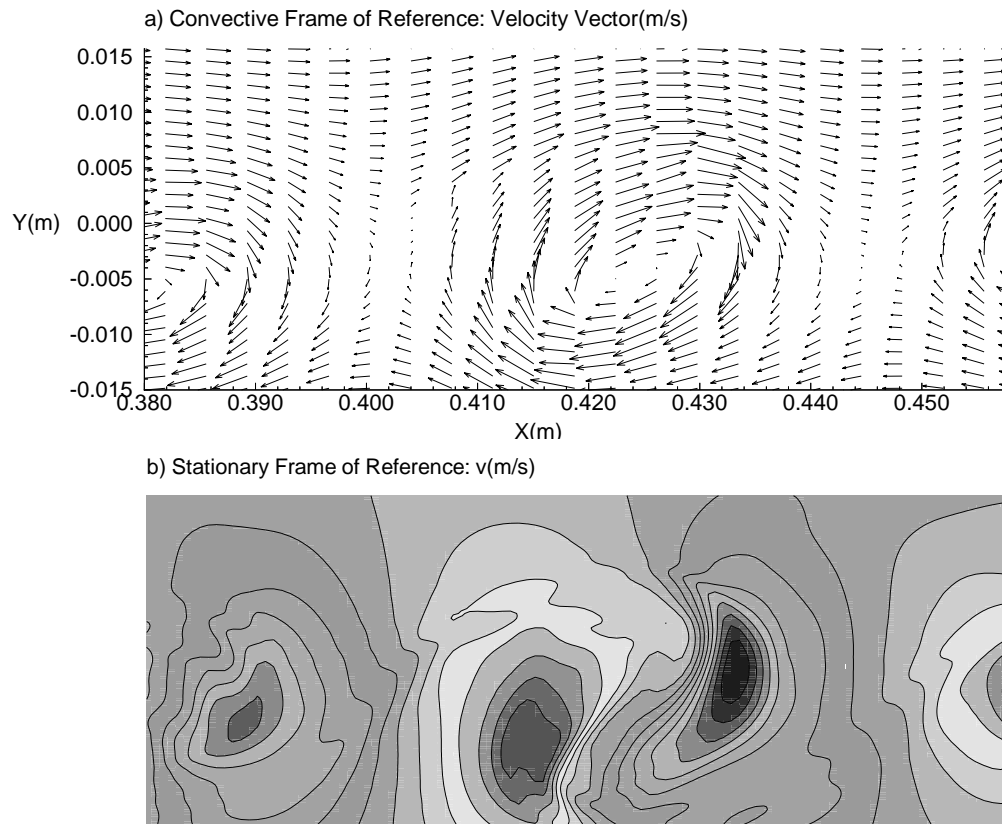


Figure 5.31. Shear Layer Velocity Field in Two Frames of Reference a) Convective Frame of Reference, b) Transverse Velocity Field v in Stationary frame of Reference.

By differentiating and expressing the differentials in prime notation yields

$$\rho' = \frac{p'}{c^2} - \left(\frac{\rho}{c_p} \right) s' \quad (5.11)$$

The first term on the right hand side of Equation 5.11 is the reversible or isentropic contribution to the density perturbation. The non-isentropic density contribution was found from the difference between the computed density and pressure contributions. Contour plots of the density perturbation, pressure contribution and the entropy contribution fields are shown in Figure 5.32. The isentropic contributions by the pressure perturbations are shown as a minor contributor to the overall density perturbations. The vorticity is the dominant contributor. Three additional non-isentropic processes can contribute to the contours of Figure 5.32 c). Crocco's form of the equations of motion give by

$$\frac{\partial \vec{v}}{\partial t} - (\vec{v} \times \vec{\zeta}) = T \vec{\nabla} s - \vec{\nabla} H \quad (5.12)$$

shows possible contributions from the velocity change with time, the vorticity $\vec{\zeta}$, and the gradient of the total enthalpy H. The gradient of the total enthalpy does not contribute for these simulations since the total enthalpy of the streams are equal. The change of velocity with time contributes to the cross-channel gradient of entropy as does the difference in entropy between the two streams at the inlet. Both the velocity change and the initial entropy difference contribute as the mean density and velocity fields develop with downstream distance. The ratio of entropy levels of the two streams at the inlet is approximately three.

The processes that generate entropy change in the shear layer are same processes that define the shear layer behavior. For Case I conditions both the fluid dynamic behavior and the entropy generation processes are two-dimensional. Three-dimensional processes become important and contribute significantly to the shear layer behavior and the generation of entropy as the convective Mach number increases beyond 0.6. The three-dimensional simulation results discussed in the next section only confirm the dominant two-dimensional nature at Case I flow conditions. The key difference between Case I conditions and Case II conditions is the slightly three-dimensional behavior expected at the higher convective Mach number of $M_c = 0.64$. The three-dimensional behavior of the Case II shear layer is sufficiently small that the two-dimensional simulation can yield a good prediction of

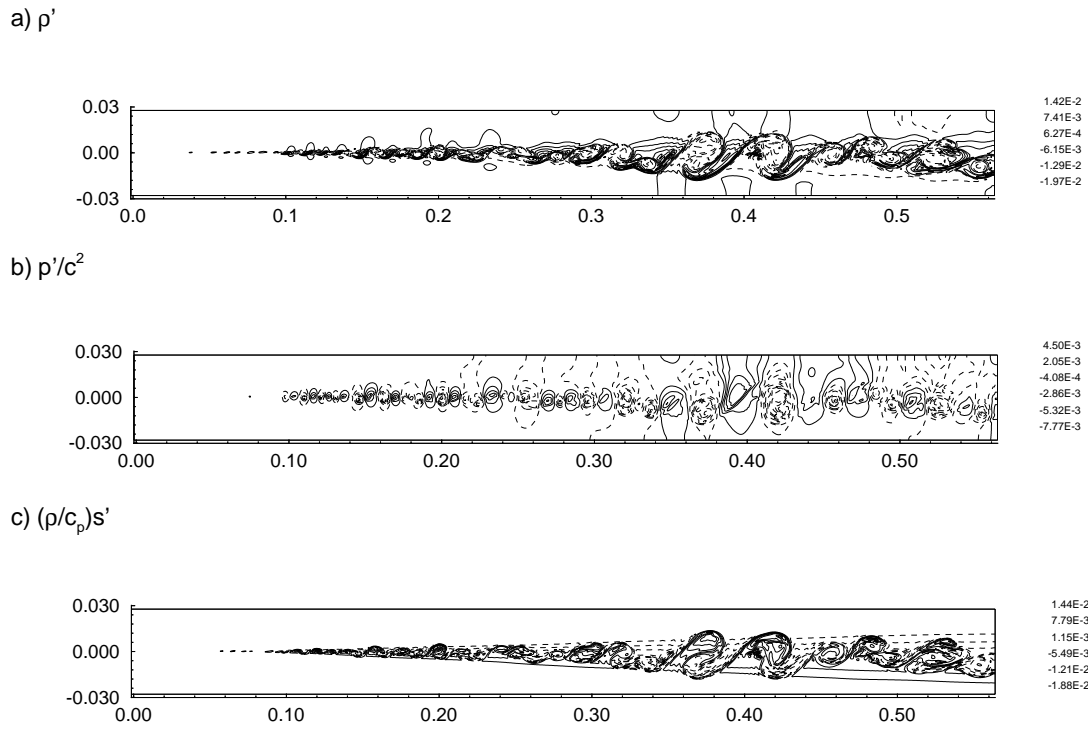


Figure 5.32. Isentropic and Non-Isentropic Contributions to the Density Perturbations; a) Density perturbation from the Mean density field, b) Isentropic Pressure contribution, and c) Non-Isentropic processes contributions.

the shear layer's behavior. Consequently the non-isentropic processes and their relative contributions to the shear layer are approximately the same for these Case I conditions and the Case II conditions that are discussed in the next chapter.

5.3 Three-dimensional Simulation of Case I

The Case I shear layer behavior at $M_c = 0.5$ is generally considered two-dimensional but some aspects of the flow such as turbulence are known three-dimensional phenomena. In addition, oblique Kelvin-Helmholtz waves are known to begin appearing at convective Mach numbers above 0.5. The Case I shear layer was computed using a three-dimensional simulation to examine the ability to predict the shear layers behavior on what in three-dimensions is now a coarse grid. The results were compared to the two-dimensional results to compare accuracy and to look for early signs of three-dimensional behavior. The basic finding is that the loss in grid resolution destroyed the ability to quantitatively predict even mean behaviors. Although quantitative accuracy was lost trends appeared to remain consistent with the two-dimensional results. No three-dimensional effects were observed but then no reliable 3-D results were expected given the general loss of accuracy that occurred. The most notable differences affecting how the simulations were performed are the number of grid points, the resulting wave resolution level and the relative time history of the data. These differences all contribute directly to the accuracy that is achievable in the simulation.

The rapidly growing ability to compute large numerical simulations is forcing the improvement of our understanding of accuracy in numerical simulations. Accuracy is no longer just grid independence for the mean flow behavior. Accuracy now includes the ability to predict the dynamic behavior of the fluid and the transmission of waves, both magnitude and phase behavior. The ability to resolve waves in the two-dimensional and three-dimensional simulations of this thesis is shown in Table 3.1. Redistribution of the grid to span the experimental domain resulted in large reductions in the resolved frequencies. To obtain accurate resolution of waves to the highest possible frequencies the simulation of Case I conditions was extended to a three-dimensional computation using the largest possible grid. The grid was expanded within limitations of maintaining cell aspect ratios and multiples of 2^N in each matrix dimension. The final grid filled 87% or 6.5 Gigabytes of the largest partition (256 nodes) of the NCSA CM-5 that provided sufficient available run time.

The role of parallel processing becomes acutely apparent for the three-dimensional system. The two- and three-dimensional grids contain 196,608 points versus 5,242,880

points; a ratio of almost 1 to 27. The associated computing speeds were 1.6×10^{-6} seconds per point per solution time step and 1.03×10^{-6} seconds per grid point per solution time step, for the two-dimensional and three-dimensional codes respectively. This 36% improvement in speed per grid point only reduced the computation time to 17 times larger than the two-dimensional simulations. The time duration of the three-dimensional simulation runs were necessarily reduced. The effects of the resolution loss by extending the simulation to three-dimensions are shown in both the dynamic and time-averaged results.

5.3.1 Dynamics

Frequency Behavior and Auto-spectra

Frequency spectral analysis was used to look for any shift in frequency behavior due to the change to a three-dimensional simulation. As with the two-dimensional simulation the time history of the total mass flux was recorded at a down stream location. In addition, the spanwise mass flux ρw was recorded to detect the presence of spanwise waves that might indict the presence of oblique Kelvin-Helmholtz waves. The inlet excitation levels for u' and v' were adjusted to give the same white noise behavior and energy levels that were used in the two dimensional simulations. Overall the amount of energy in the inlet perturbations increased by the amount of energy added by the w' perturbation.

The frequency spectra and auto-spectra for the two- and three-dimensional simulations and the experiment all compare well. The simulations correctly predict the energy spectrum peak at 14 kHz, which is in good agreement with the experimental results. The three-dimensional simulation frequency spectra and auto-spectra at the 0.30 m axial position are shown in Figure 5.33. Study of the frequency spectra and auto-spectra show that the two- and three-dimensional codes do a good job of predicting the major frequencies present such as the local Kelvin-Helmholtz instability frequency. The three-dimensional simulation does predict the cascade of energy but not the distribution energy across the frequency range of interest. The simulation FFTs and auto-spectra shown here are based upon a data sample of 128 points.

The frequency spectra and auto-spectra of the spanwise mass flux was also analyzed in order to identify any organized spanwise frequencies that might be developing and taking energy from the shear layer growth process. The spanwise frequency spectra and auto-spectra

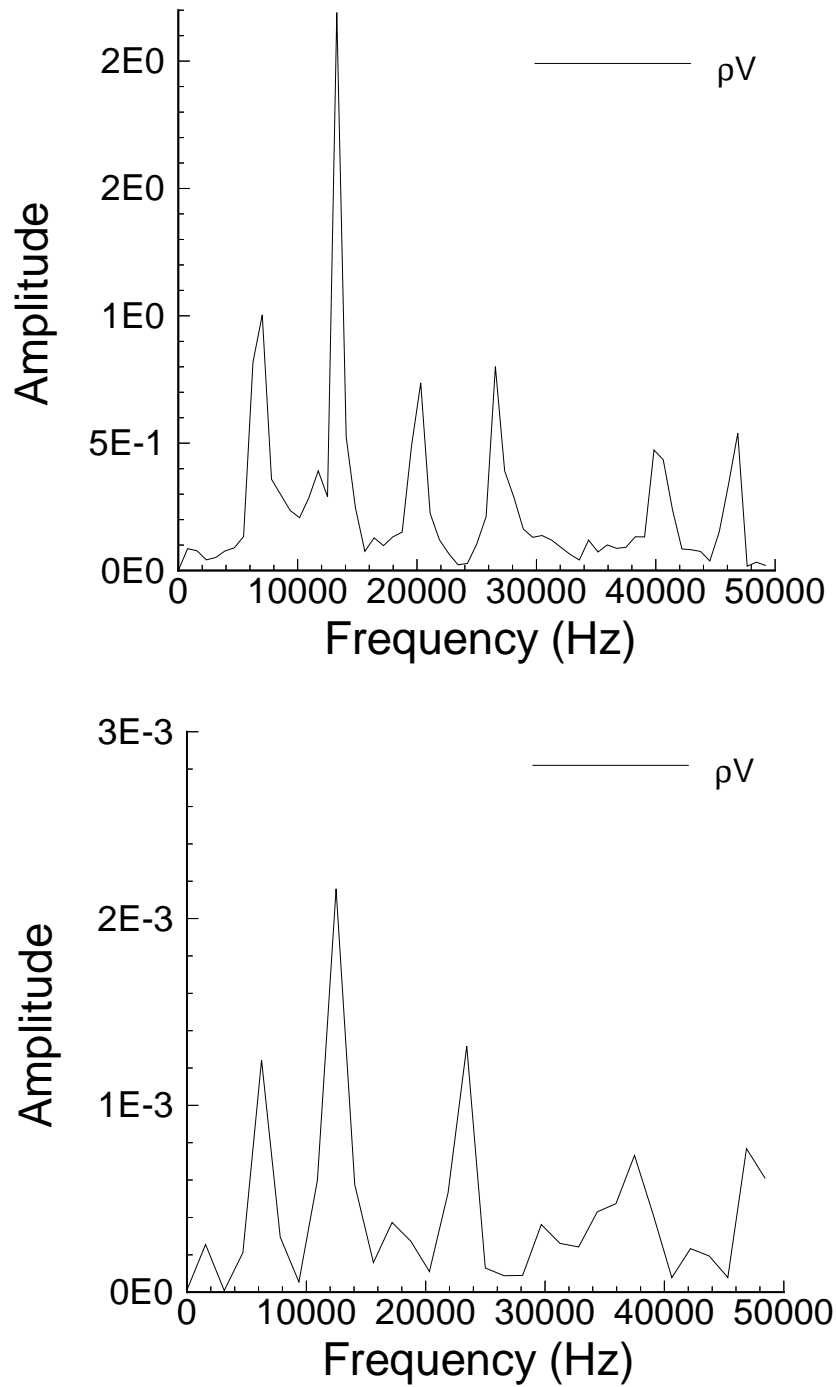


Figure 5.33. Three-dimensional Total Mass Flux Unsteadiness $(\rho V)'$ at $X = 0.30$ m: a) FFT spectra and b) auto-spectra

at the 0.30 m position show no frequency preferences and only negligible power levels as can be seen in Figure 5.34. Overall the analysis did not detect any three-dimensional effects at Case I conditions. The lack of any preferred frequency behavior does not necessarily mean that the spanwise mass flux does not play a role in shear layer development. One can speculate that the $(\rho w)'$ mass flux provides an energy sink mechanism to the shear layer, uniformly absorbing energy from small scale turbulence. The time-averaged field would remain at or near zero and no preferred frequencies would be observed until reaching some threshold indicator, such as $M_c = 0.6$.

5.3.2 Instantaneous and Time-averaged Behavior

Shear Layer Growth

The three shear layer thickness measurements, δ_{98} , vorticity and momentum thickness, were again compared to the experimental vorticity thickness growth. The three-dimensional simulation shows a delayed transition to the turbulent growth rates when compared to the experimental data and the two-dimensional simulation. The three-dimensional simulation predictions in Figure 5.35 show the growth profiles with more gradual transitions to turbulent growth rates. The delayed transitions depict a 0.06 m lag in onset of the turbulent growth region. The delayed transition is believed to be due to the much coarser resolution of the shear layer near the inlet. The transition to turbulent growth is more gradual than in the two-dimensional profiles; but, the final growth rates are actually slightly higher. The ability of the simulation to predict a transition from laminar to turbulent growth suggests a basically sound simulation mechanism. Accurate simulation of the disturbance growth in both the laminar and turbulent regions may depend upon a critical ratio of disturbance amplitude to grid spacing.

While the three thickness measures computed from the numerical simulation do not bound the experimental growth profile, their growth rates do. The δ_{98} method provides the highest growth rate, about 15% higher than the experimental rate. The vorticity and momentum thicknesses follow closely together at a lower rate than the experimental value but much closer than predicted in the two-dimensional simulation. The computed values for the three types of growth rates are given in Table 5.4 along with the restated experimental growth rate.

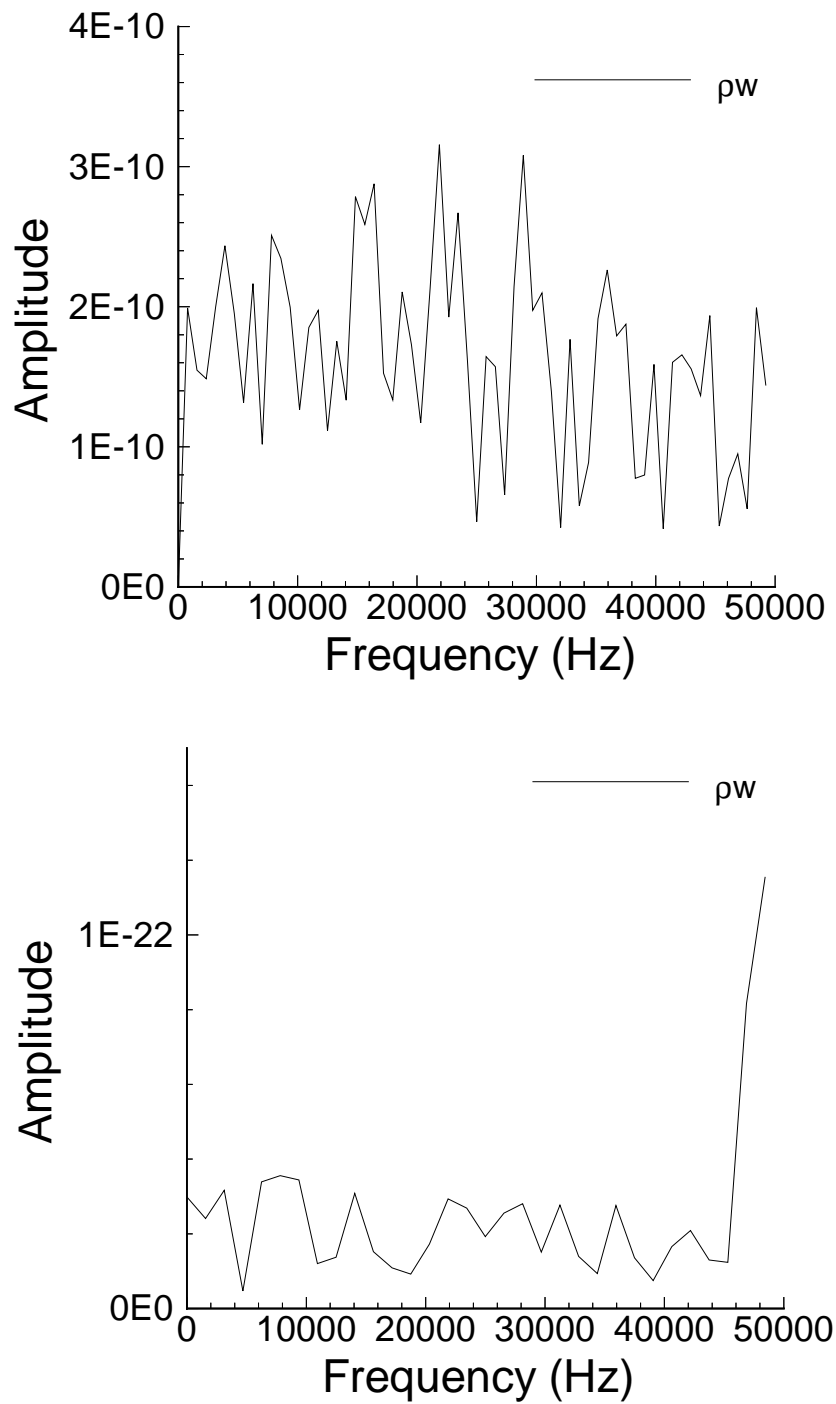


Figure 5.34. Three-dimensional Spanwise Mass Flux Unsteadiness $(\rho w)'$ at $X = 0.30$ m: a) FFT magnitude and b) auto-spectra

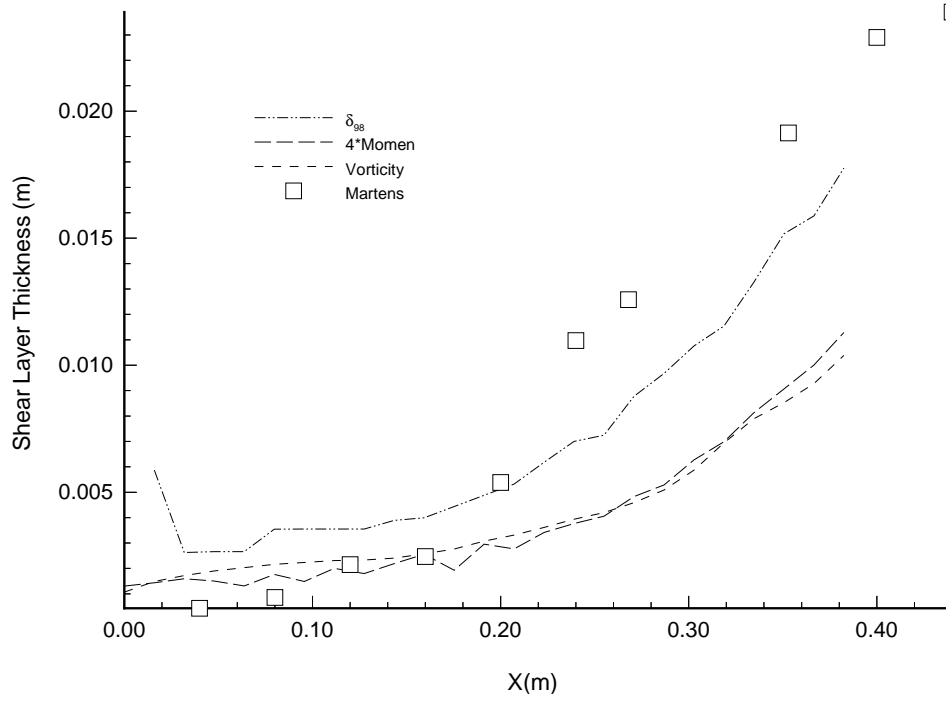


Figure 5.35. Comparison of three-dimensional shear layer growth rates, vorticity δ_ω , momentum 4θ , boundary layer δ_{98} , and experimentally determined vorticity thickness.

Table 5.4. Three-dimensional Shear Layer Growth Rates for Case I

Growth Type	$d\delta/dx$
δ_{98} (Boundary Layer)	.0878
δ_ω (Vorticity)	.0629
4θ (Momentum)	.0566
δ_ω (Experimental)	.0765

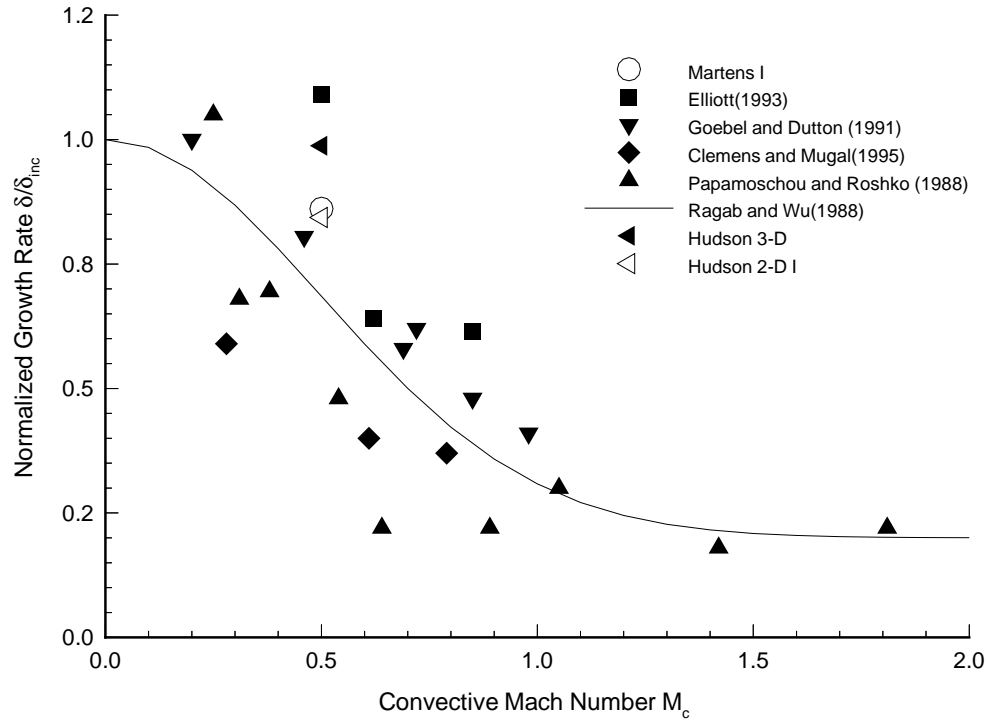


Figure 5.36. Three-dimensional normalized growth rates correlated with convective Mach number

The normalized δ_{98} growth rate for the three-dimensional simulation has been added to the normalized growth rate plot in Figure 5.36. The causes for reduced accuracy of the predicted growth rate are attributed to the reduced grid resolution of the shear layer and the smaller region of linear growth from which to determine the rate.

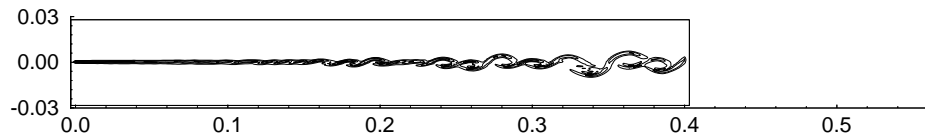
Instantaneous Results

Conventional Two-dimensional Plot Observations

The descriptive parameters density gradient and vorticity are shown in Figure 5.37 at the same scale as used for the two-dimensional simulation plots of Figure 5.11. The density gradient and vorticity plots show that the same basic flow structures, such as vortex roll up, are present in both simulations. Comparing just the 0. to 0.4 m portions of the figures from

the two simulations show that the shear layers are visually very similar. The most defined differences are the diminished presence of the vortices in the 0.1 m region. This diminished presence is directly attributed to reduced grid resolution in the early shear layer region.

a) Density Gradient Field for 3D Solution



b) Vorticity for 3D Solution

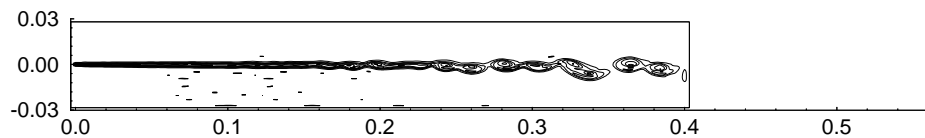


Figure 5.37. Three-dimensional Instantaneous Descriptive Flow Parameters; a) Density Gradient Field, and b) Vorticity Field.

Time Averaged Results

Instantaneous to Time Averaged Comparison

The plots of the instantaneous and time averaged conservative variables for both simulations were examined for differences. Both simulations were found to show all of the same basic features. Key differences between the plots are the evidences of reduced early coherence and diminished mass flux transfer into the low speed stream. The density profiles of Figure 5.38 show the ‘bump’ in the density profile near the edge of the low speed stream but the three-dimensional simulation does not show the early coherence in the shear layer that is evident in Figure 5.17 of the two dimensional simulation. The most pronounced difference in the axial mass flux profiles is the significantly reduced spreading of the shear layer profile. The transverse mass flux plots provide the most new information. The delayed shear layer growth provides a longer inlet region where the Mach wave behavior can be observed. The three-dimensional simulation plots show two events of Mach waves exciting vortices in the shear layer. The second large Mach wave to shear layer interaction

appears to trip or stimulate the shear layer into its rapid growth region. This interaction appears to be a major shear layer growth or excitation mechanism. This interaction also raises important questions about; the differences between confined and unconfined shear layers, and their growth mechanisms, and about how they are experimentally investigated. The two dimensionality of the Case I flow conditions are substantiated by Figure 5.41, the spanwise mass flux ρw . With no spanwise driving mechanism, the initial inlet excitation quickly disappears. The total energy plots show the reduced cascade of energy into the low speed stream. Examination of the contour plots of the conservative field variables, both instantaneous and time averaged, and cross-sectional plots of the time averaged plots have emphasized the two dimensional nature of the Case I conditions. The comparisons have also identified the significant contribution of reflected Mach wave energy to the growth of confined shear layers.

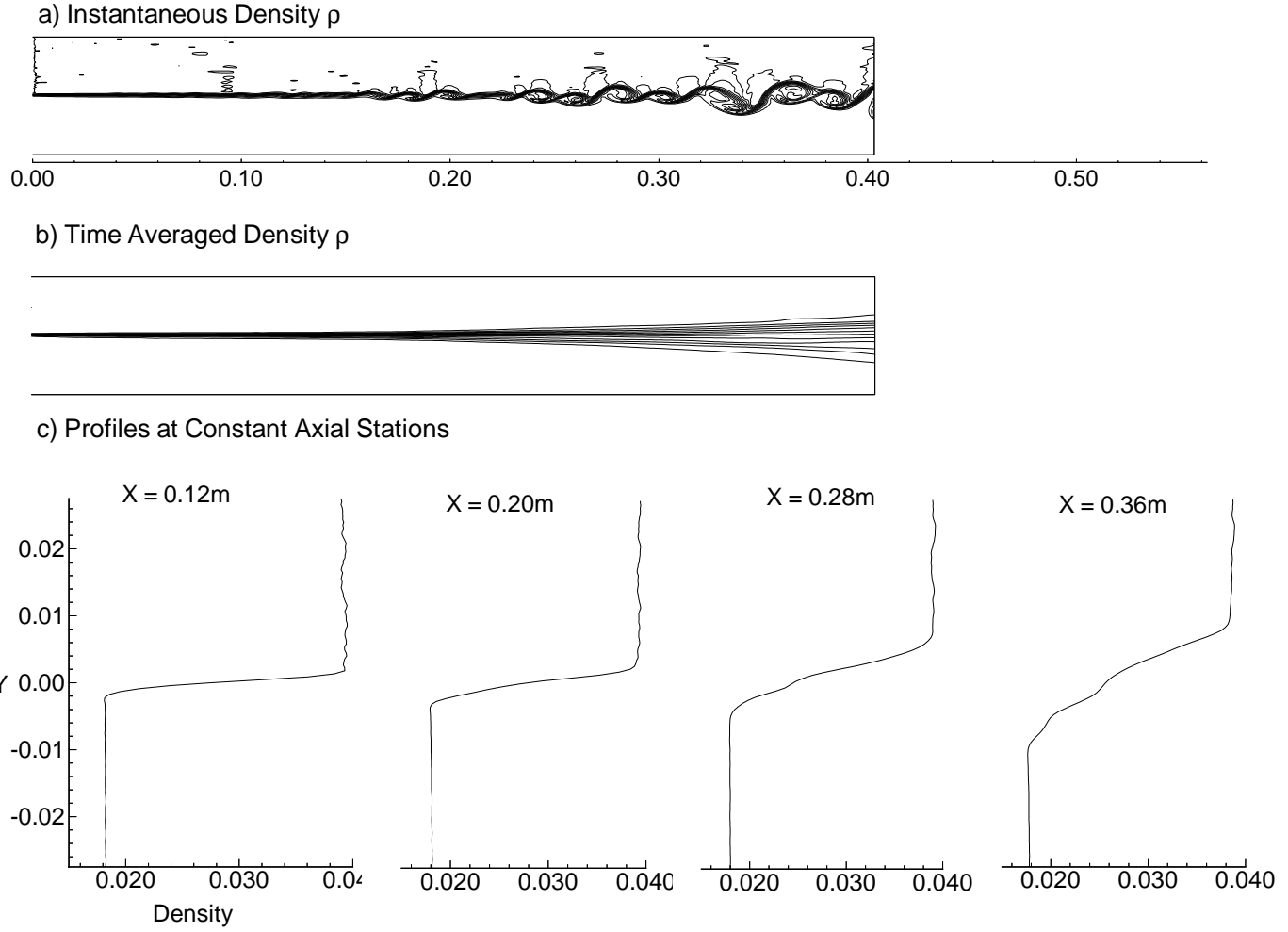


Figure 5.38. Conservative Variable Density ρ (kg/m^3) a) Instantaneous Density, b) Time Averaged Density Field, and c) Cross Channel Density Profiles at X = .12m, .20m, .28m, and .36m.

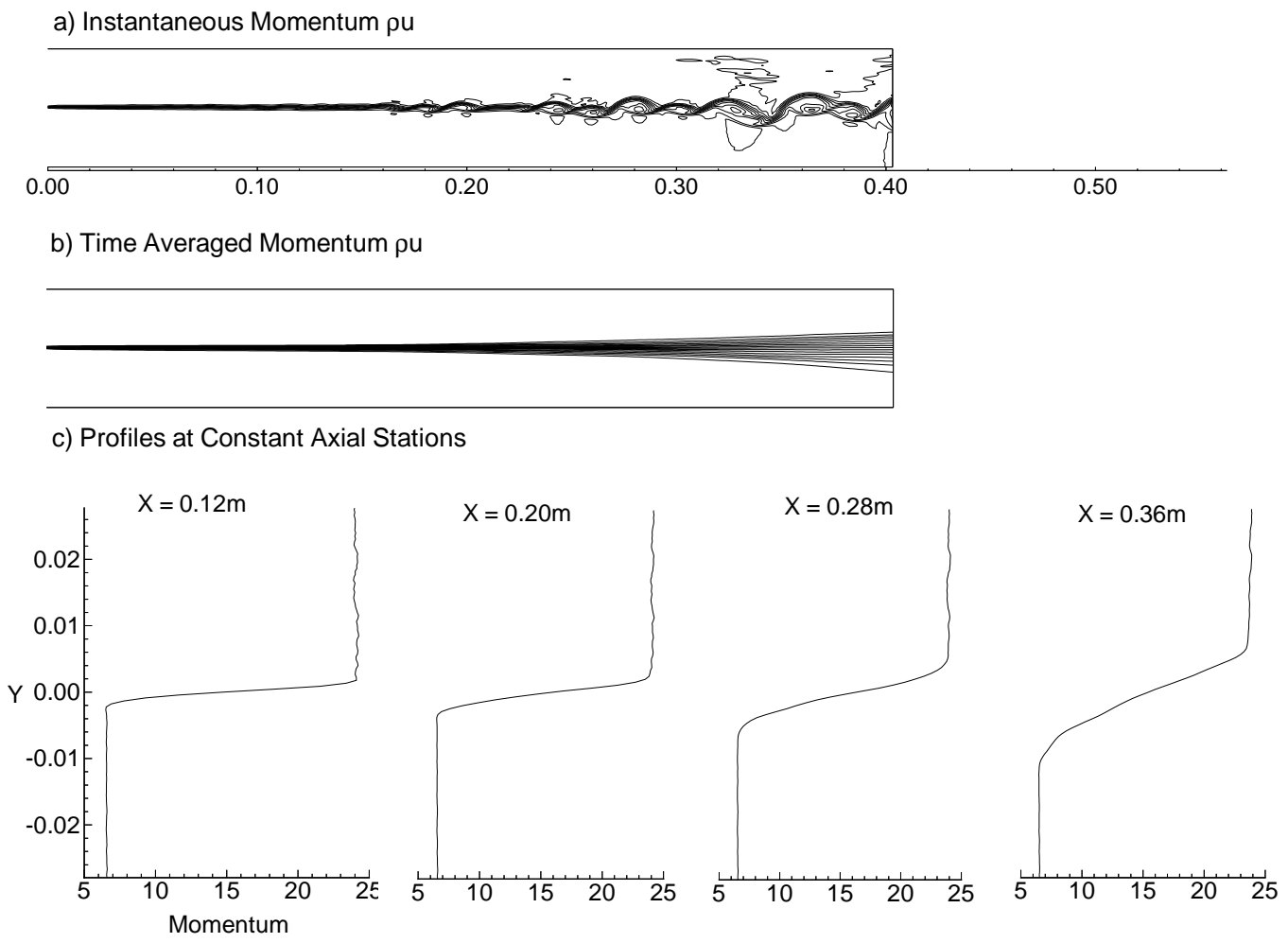


Figure 5.39. Conservative Variable Axial Mass Flux ρu (kg/sm^2) a) Instantaneous Mass Flux, b) Time Averaged Mass Flux Field, and c) Cross Channel Mass Flux Profiles at $X = .12m, .20m, .28m,$ and $.36m$.

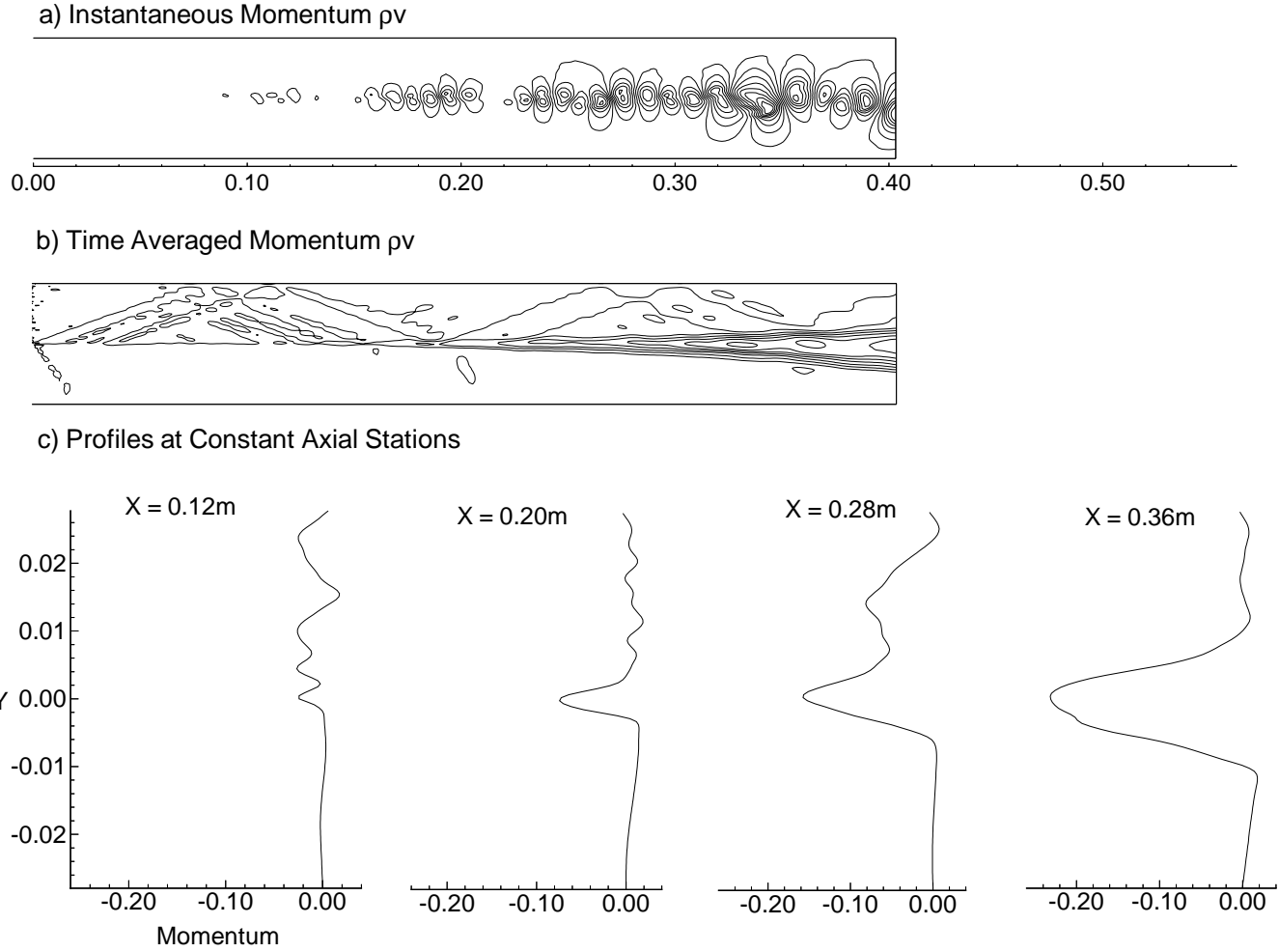


Figure 5.40. Conservative Variable Transverse Mass Flux ρv (kg/sm^2) a) Instantaneous Mass Flux, b) Time Averaged Mass Flux Field, and c) Cross Channel Mass Flux Profiles at $X = .12m, .20m, .28m,$ and $.36m$.

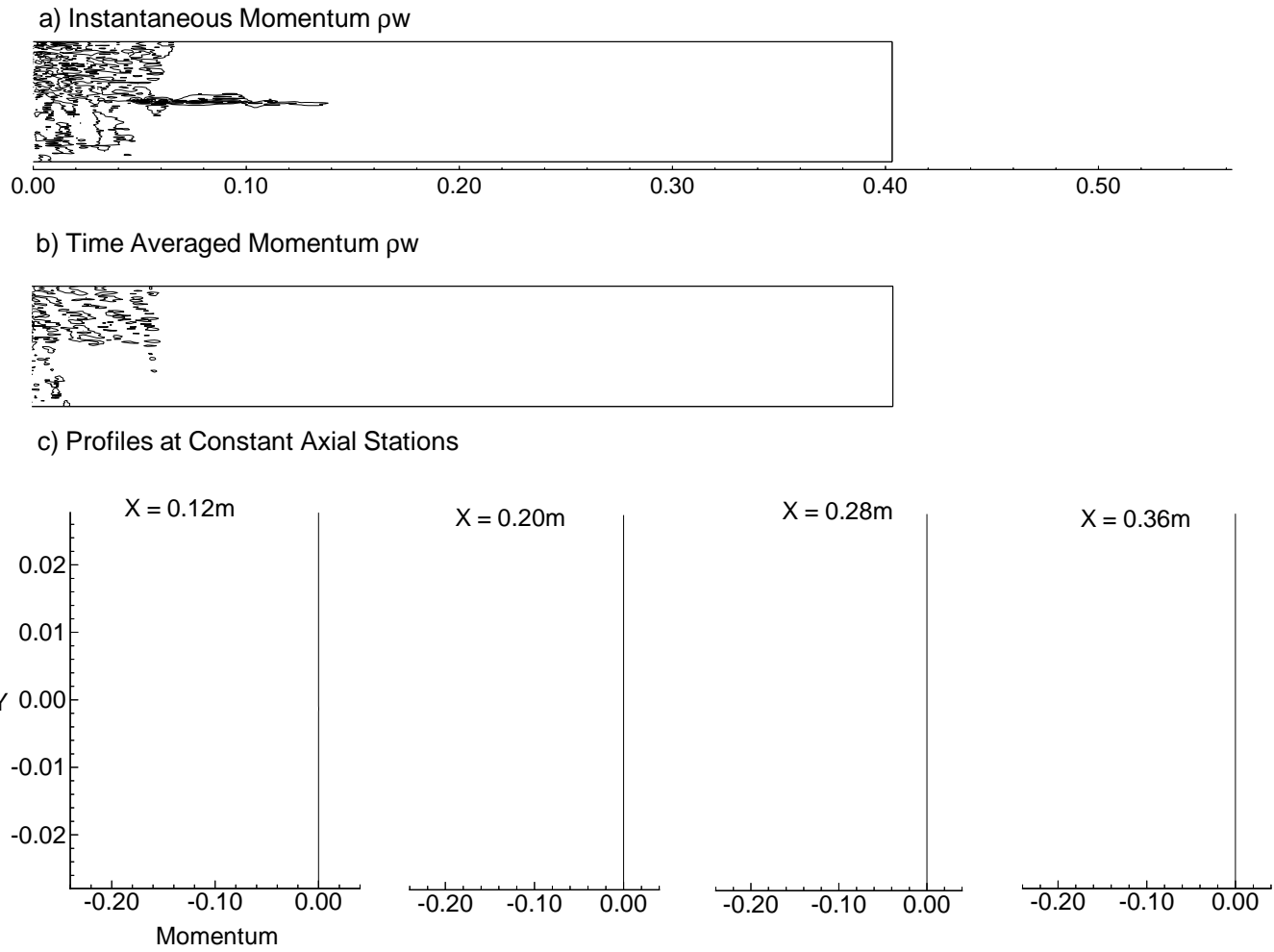


Figure 5.41. Conservative Variable Spanwise Mass Flux ρw (kg/sm^2) a) Instantaneous Mass Flux, b) Time Averaged Mass Flux Field, and c) Cross Channel Mass Flux Profiles at $X = .12m, .20m, .28m,$ and $.36m$.

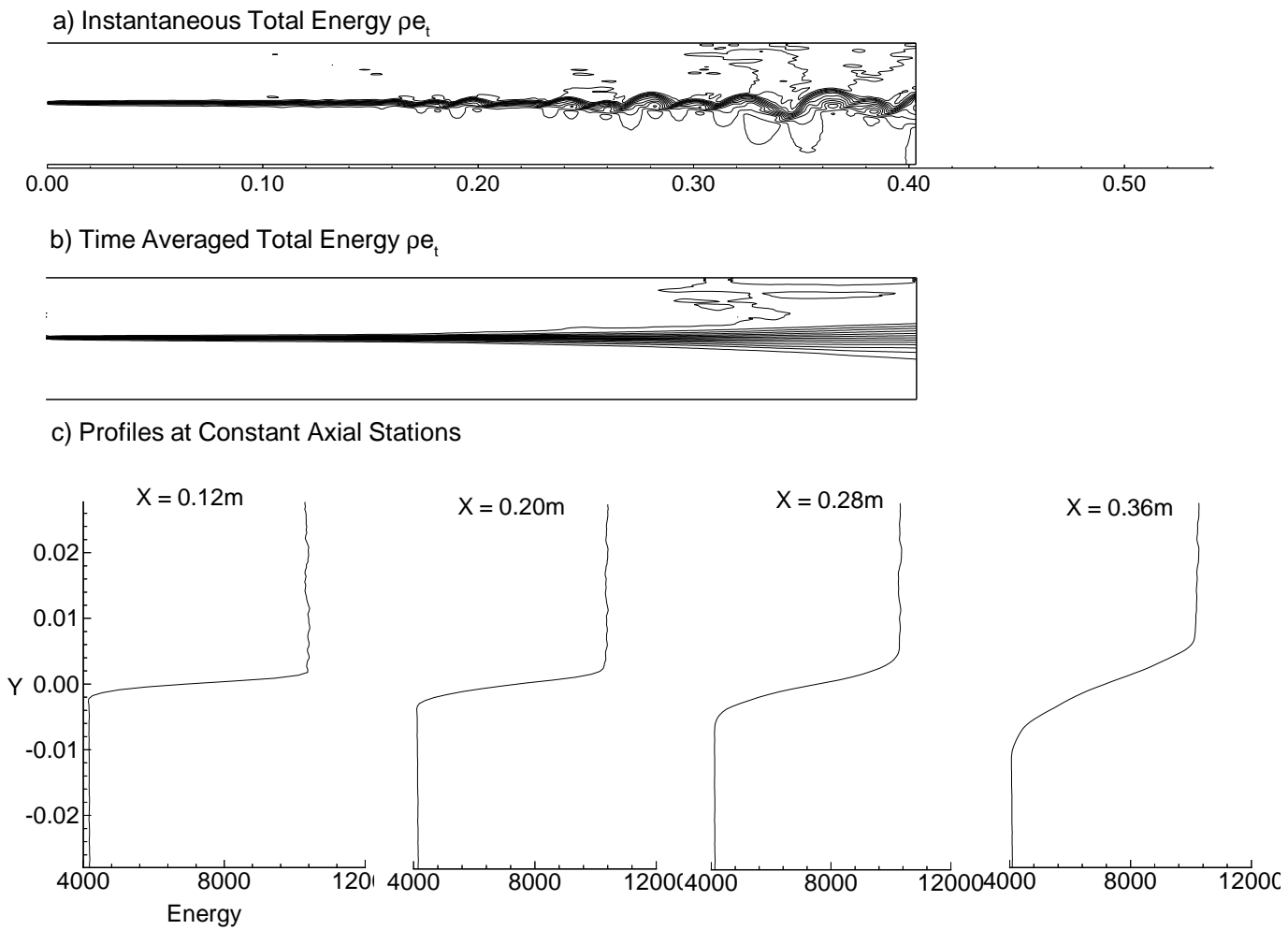


Figure 5.42. Conservative Variable Total Energy Flux ρe_t ($Joule/m^2$) a) Instantaneous Total Energy, b) Time Averaged Total Energy Field, and c) Cross Channel Total Energy Profiles at X = .12m, .20m, .28m, and .36m.

Time Averaged Comparison With Experiment

The computed shear layer velocity profiles were compared with Martens' velocity profiles. A virtual origin shift of 0.06 m was applied to the simulation profiles for comparison with Martens' velocity profiles. The shift of 0.06 m was taken from the growth rate profiles discussed earlier in this chapter. Comparison was not as good as for the two-dimensional simulation. Significant conclusions are difficult to draw from comparisons of the very thin laminar shear layer region. The slight differences noticed are attributed to grid differences. However, two observations can be made about the simulation profiles at the end of the domain, i.e. at about 0.4 m of the simulation domain. The shear layer profile has a slightly steeper profile and the edges of the profile are noticeably sharper. One contribution to these differences is that the solution is not as mature as the two-dimensional simulation and therefore the corners are just not rounded from a long running time average. Overall the three-dimensional simulation velocity profiles do not compare as well with the experimental data as does the two-dimensional data.

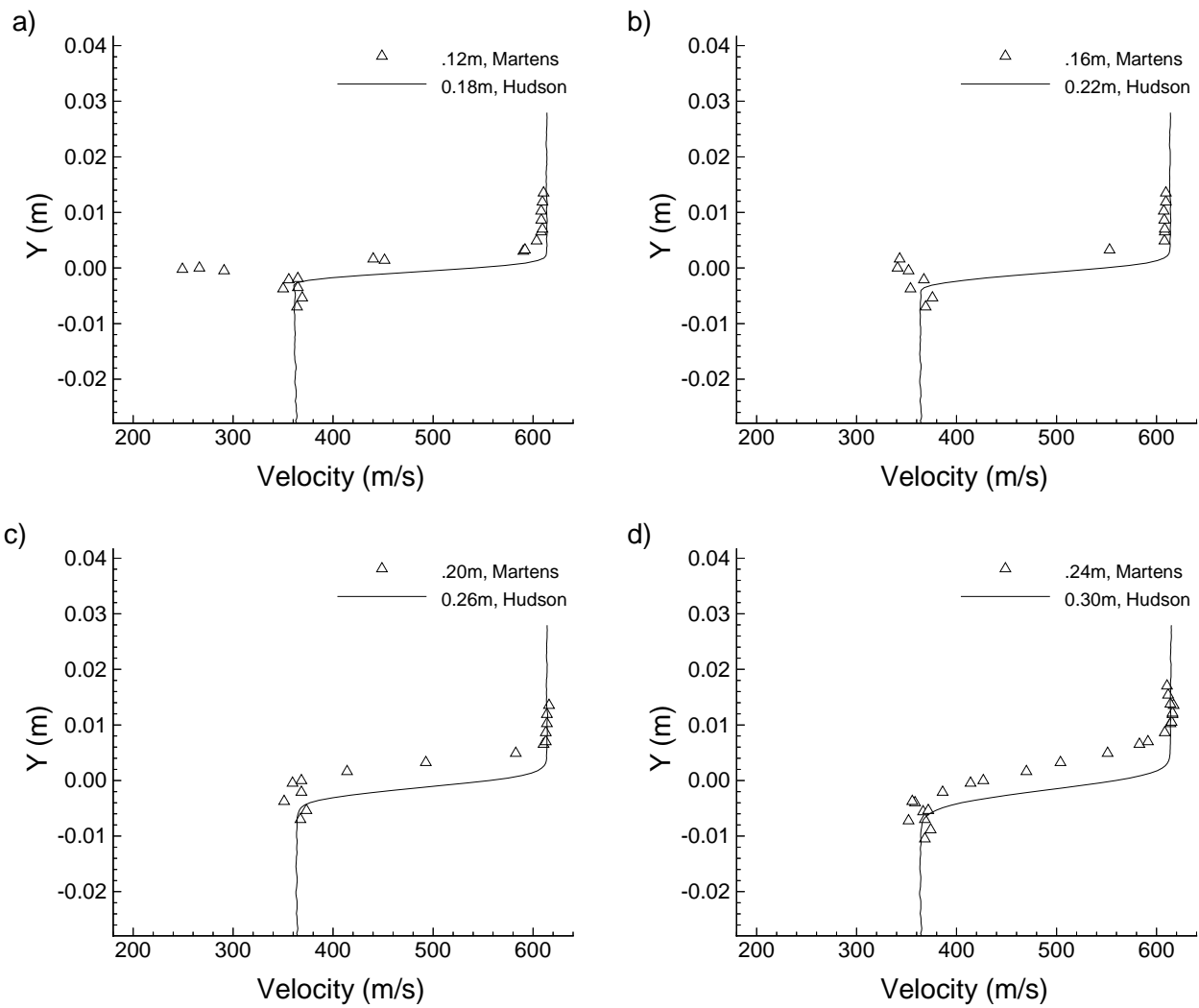


Figure 5.43. Comparison of Numerical and Experimental Mean Velocity Profiles; a) X=0.12 m, b) X=0.16 m, c) X=0.20 m d) X=0.24 m.

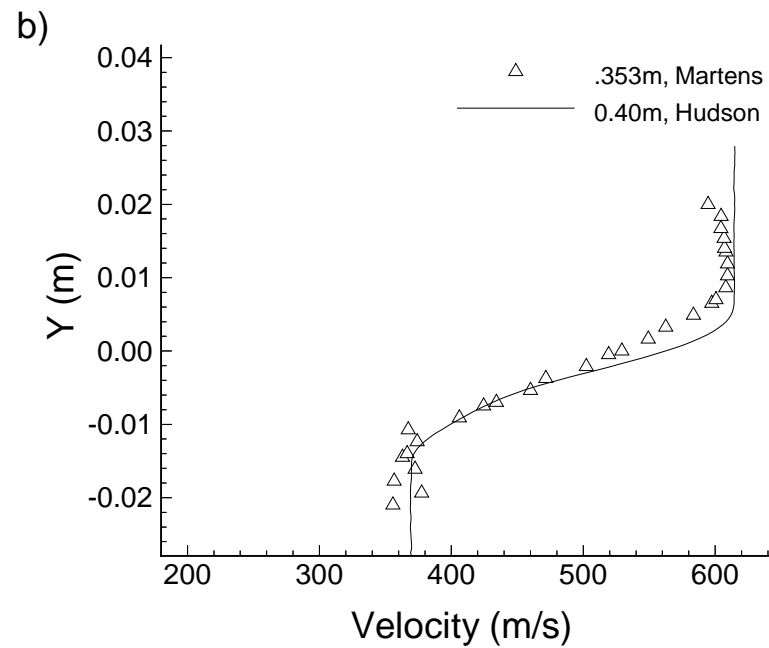
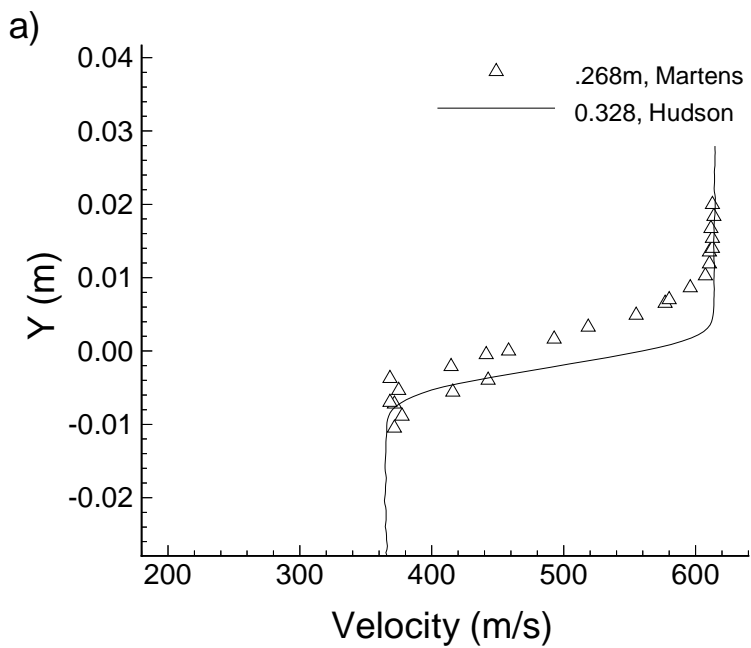


Figure 5.44. Comparison of Numerical and Experimental Mean Velocity Profiles; a) $X=0.268$ m, b) $X=0.353$ m.

Time Averaged Reynolds Stress

The time averaged Reynolds Stress field provides useful insight into the shear layer turbulence field. Figure 5.45 shows that the primary source of disturbances in the shear layer is the Mach wave system of the high speed stream. The Mach wave amplitudes are of $O(1)$ nearly to the point that turbulent growth begins. The two-dimensional simulation does not show the Mach waves to be as significant contributors to the Reynolds stress field. Improvements to the simulation need to be made to assess the precise contribution of the Mach waves to the Reynolds stress field and the shear layer growth mechanism.

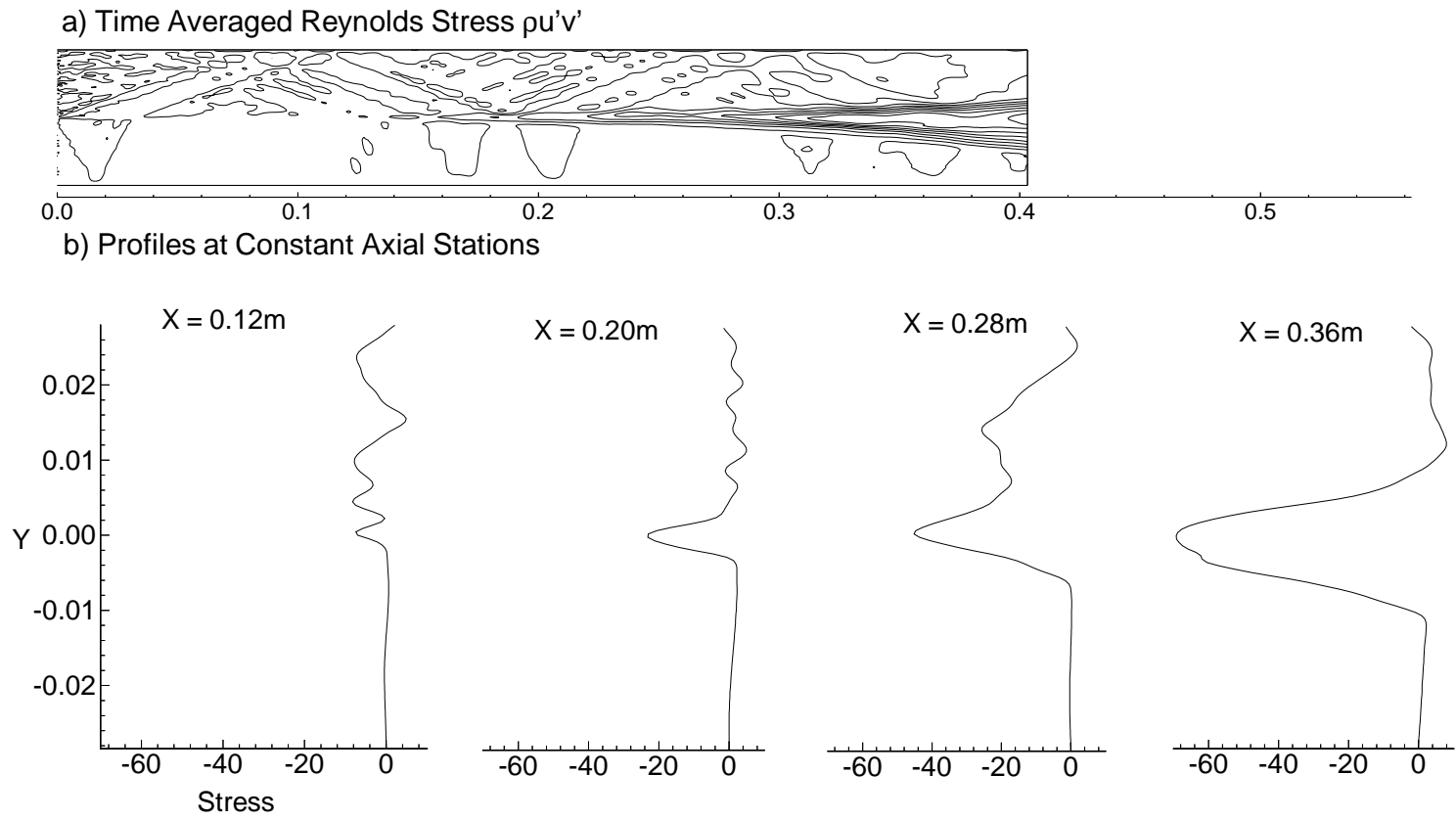


Figure 5.45. Three-dimensional Case I $M_c = 0.5$ Time Averaged Reynolds Stress $\overline{\rho u'v'}$: a) Time averaged Reynolds Stress Field, and b) Cross Channel Profiles at $X = .12\text{m}$, $.20\text{m}$, $.28\text{m}$, and $.36\text{m}$.

Overall the three-dimensional simulation showed little payoff for the greatly increased computational costs. The three-dimensional simulation did contain all the flow features seen in the two-dimensional simulation such as laminar and turbulent shear layer growth regions, vortex combinations, qualitative consistency from two-dimensions to three-dimensions of the perturbation quantities such as the Reynolds stress. Unfortunately, as reported by Ferziger [14] in his paper discussing error in numerical solutions, simulations are known to be able to predict trends even in the presence of major quantitative error. In the area of dynamic behavior the three-dimensional solution was able to predict dominant wave frequencies even if only marginally resolved. Quantitative comparisons such as the shear layer velocity profiles required the use of an artificial offset or virtual origin to provide agreement with the experimental data that only rates as acceptable. Three-dimensional simulations remain challenge for problems that have the large physical domains the size used in this simulation; and that require accurate resolution of the high frequency level that were also needed. In contrast, two-dimensional simulations hold an excellent capability to predict quantitatively the dynamic and steady shear layer behaviors, as long as the dominant phenomena remains two-dimensional. The following chapter presents the results of a two-dimensional shear layer simulation under the slightly three-dimensional flow conditions of Case II.

Chapter 6

Shear Layer Simulation Case II: $M_c = 0.64$

Compressible shear layers begin to show three-dimensional effects when the convective Mach number is greater than approximately 0.6 to 0.62. Martens' second experimental case and the present, second simulation were conducted at a convective Mach number of 0.64. At $M_c = 0.64$ the effects should be small and limited to the generation of weak spanwise waves. Data comparison for Case II is limited since only a small amount of experimental data is available. The basic flow conditions for Case II were reported earlier in Table 1.3. The high and low speed Mach numbers are 4.0 and 1.23 respectively. The inflow shear layer thickness was set to 0.002 m, the same thickness used for Case I. The fundamental frequency was expected to be higher and shear layer growth was expected to be smaller due to increased compressibility effects. Expected behaviors were predicted along with some enhanced interaction between Mach waves and the shear layer.

6.1 Dynamics

6.1.1 Frequency Behavior and Auto-spectra

The simulation predicts the delayed growth in the shear layer correctly at the higher convective Mach number. The dynamic effect of the delay is a higher frequency spectra at a given distance from the splitter plate as compared to the Case I results. The FFT spectra and auto-spectra are shown in Figure 6.1. The peak frequency and power levels occur in the 40 kHz range as compared to 28 kHz for Case I. The inlet disturbance algorithm yielded a driving frequency of 63,512 Hz, slightly lower than for Case I but still beyond the fully resolved frequency of grid and numerical systems. The frequency and energy cascade due to shear layer thickness growth can be seen in Figure 6.2.

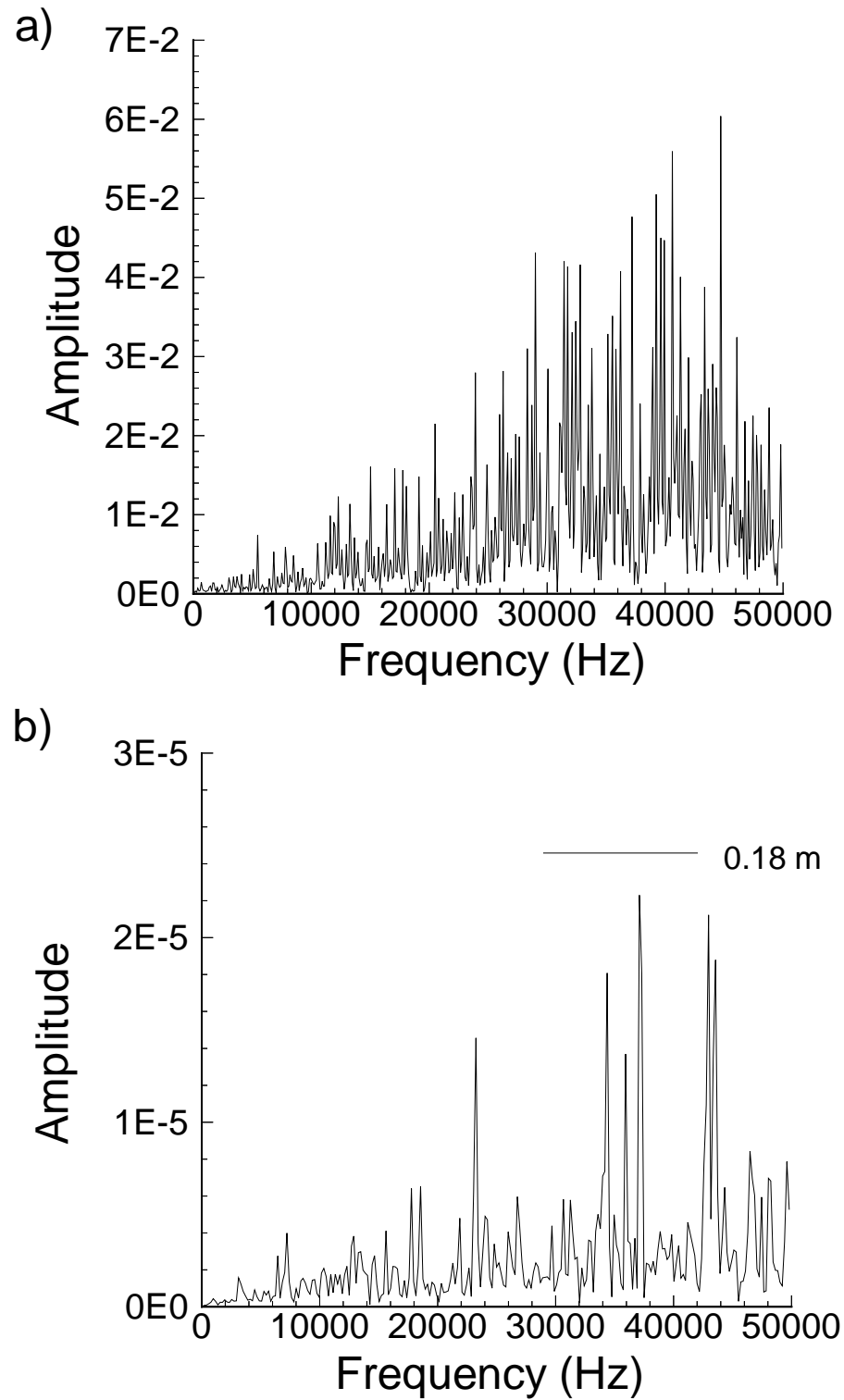


Figure 6.1. Total Mass Flux Unsteadiness (ρV)' at $X = 0.18$ m: a) FFT spectra and b) Auto-spectra.

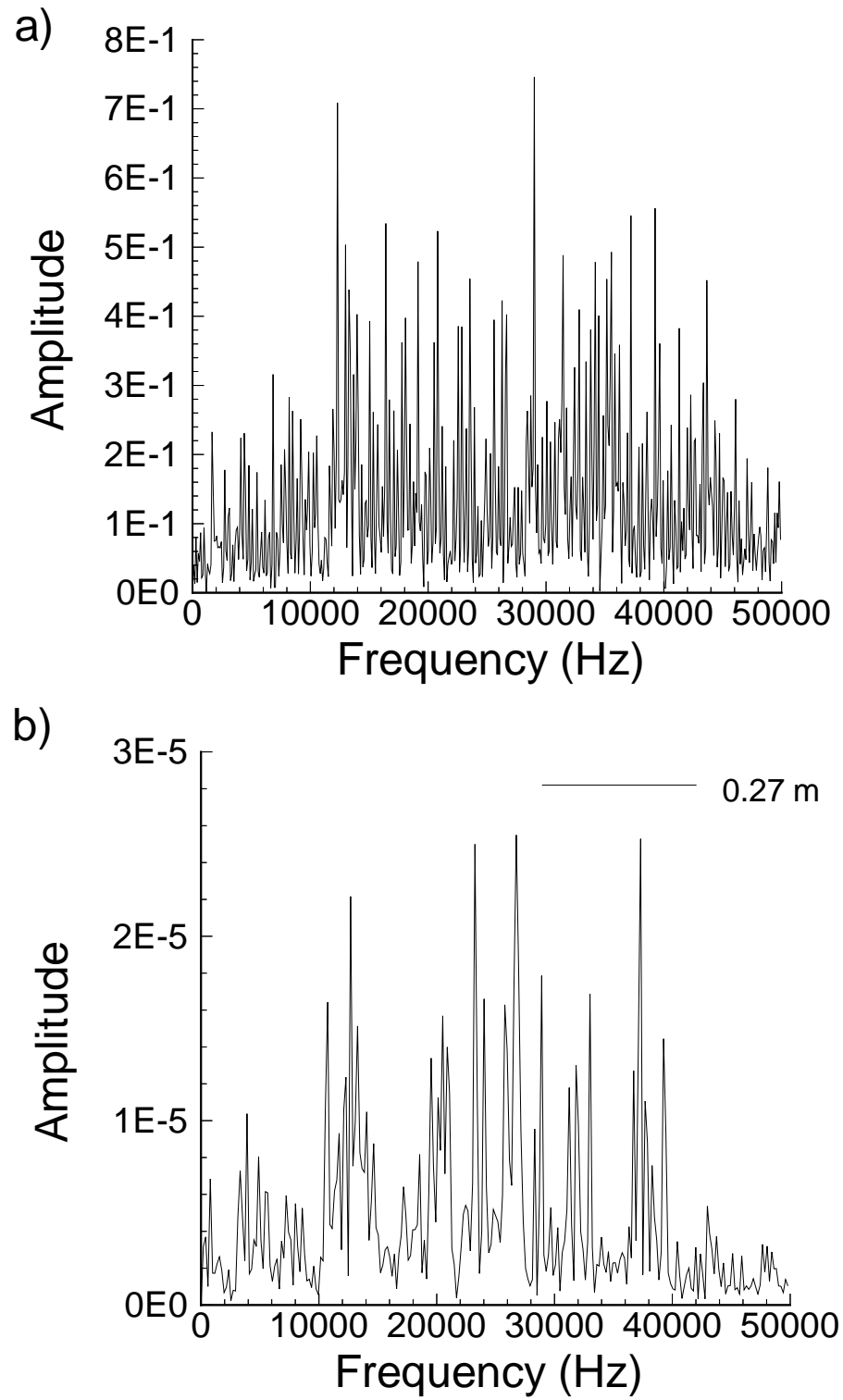


Figure 6.2. Total Mass Flux Unsteadiness $(\rho V)'$ at $X = 0.27$ m: a) FFT spectra and b) Auto-spectra.

6.2 Time-averaged Behavior

6.2.1 Shear Layer Growth

The shear layer growth profiles for the three methods, δ_{98} , momentum and vorticity are compared to the experimental vorticity thickness in Figure 6.3. Straight lines have been added to each growth profile to aid in examining the profiles. The early part of the shear layer has the classic low growth-high growth characteristics. The growth rates in the low growth region are again not compared to laminar growth rates due to the artificially large simulation initial thickness. The turbulent high growth rates were computed and are given in Table 6.1. Interestingly the δ_{98} thickness and momentum thicknesses show decreases in growth rates of 13% and 18% respectively, as compared to Case I conditions. The computed vorticity thickness remained essentially constant. The behavior of the experimental data made determining its the correct growth rate difficult. Several estimates ranged from .031 to .047 based on a straight line through the data point at .24 m and one of the several downstream data points. The largest growth rate computed from the experimental data was .047 which is approximately equal to the vorticity thickness growth rate of 0.043 for the simulation. The relative change in the reported experimental data from the Case I growth rate of 0.0765 to a Case II growth rate of 0.043 was much larger than expected. The maximum growth rates, 0.047 for the experiment and 0.065 for the simulation, were normalized with the incompressible growth rate of 0.1014 and compared to other normalized growth rate data in Figure 6.4. The results marked “Martens” were calculated from his Case I and Case II, $Re_{\nu}(40,000/cm)$ growth profiles. The simulation results compare favorably with the normalized growth rate function of Ragab and Wu. The experimental results fall within the normal data scatter. The second surge in the shear layer thickness profiles for the simulation is of particular interest, because of the added mixing that accompanies the added thickness. It will be shown later that the second surge corresponds to interaction between the shear layer and standing Mach waves in the solution.

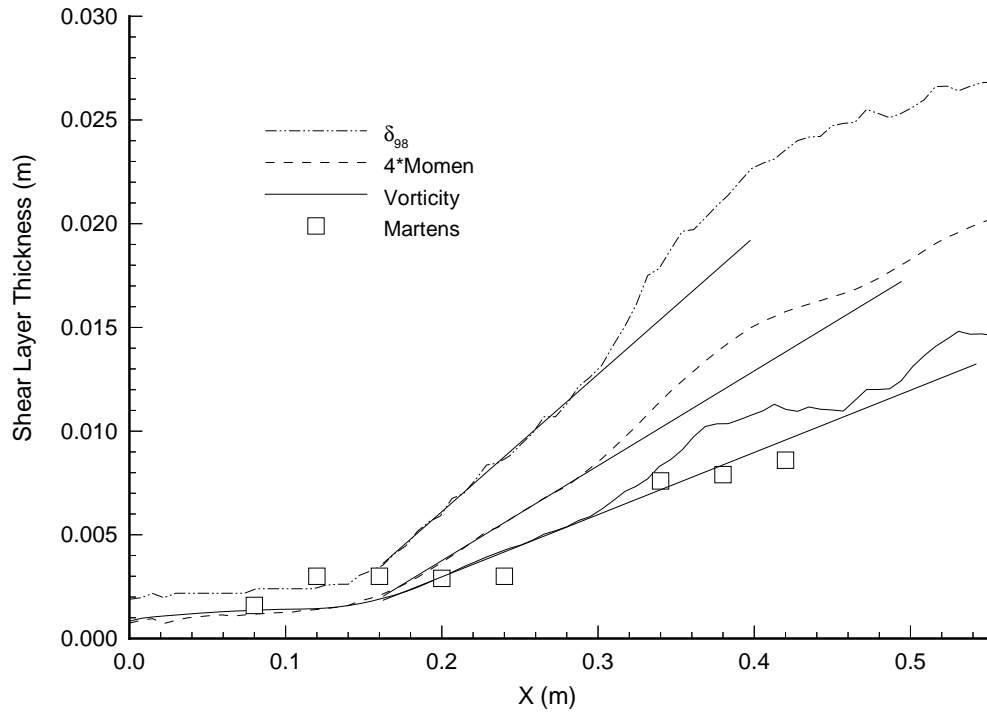


Figure 6.3. Comparison of numerical and experimental shear layer growth rates, vorticity δ_ω , momentum 4θ , boundary layer δ_{98} , and experimentally determined vorticity.

Table 6.1. Shear Layer Growth Rates for Case II

Growth Type	$d\delta/dx$
δ_{98} (Boundary Layer)	.065
δ_ω (Vorticity)	.043
4θ (Momentum)	.0288
δ_ω (Experimental)	.031

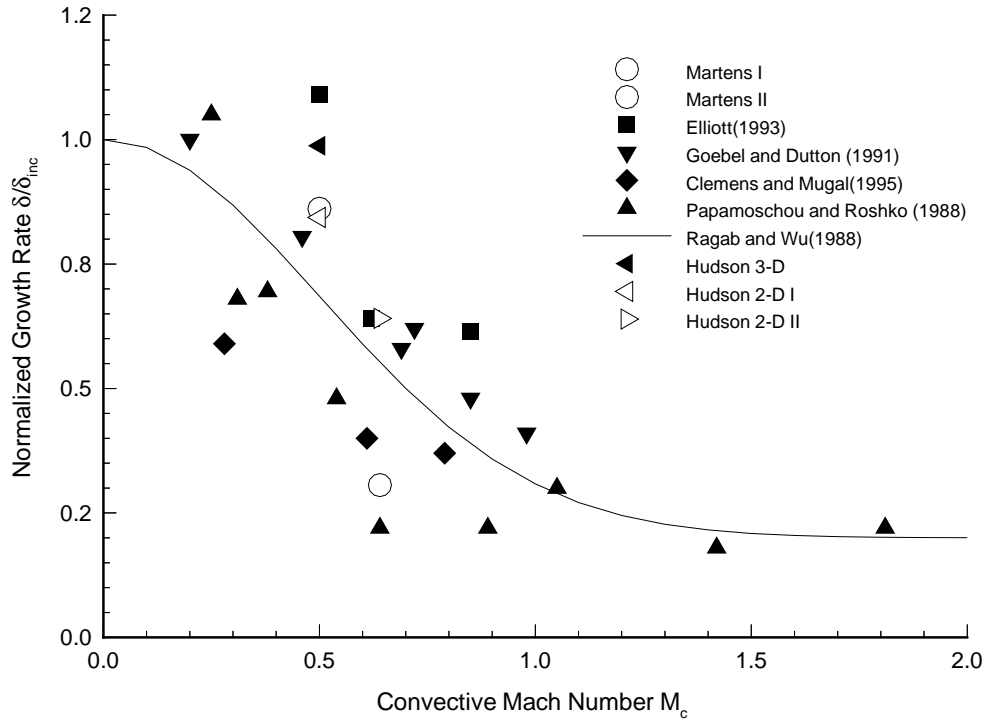


Figure 6.4. Normalized growth rates correlated with convective Mach number, Case I and Case II.

6.2.2 Instantaneous Results

Conventional Two-dimensional Plot Observations

Examination of the density gradient field and the vorticity field in Figure 6.5 shows a much subdued shear layer when compared to the Case I conditions. As discussed before, the expected results of a higher convective Mach number are decreased mixing and growth. The point at which shear layer oscillation becomes noticeable occurs at about 0.15 m axial distance, 0.05 m later than the $M_c = 0.5$ shear layer. Despite the delayed growth, the shear layer displays all the behaviors of the Case I conditions such as vortex roll ups, etc. In these figures we see the cause and effects of the bulge in the shear layer thickness profiles. Notice that the vortices in the region between 0.3 and 0.4 m axial distance have an unusually uniform size.

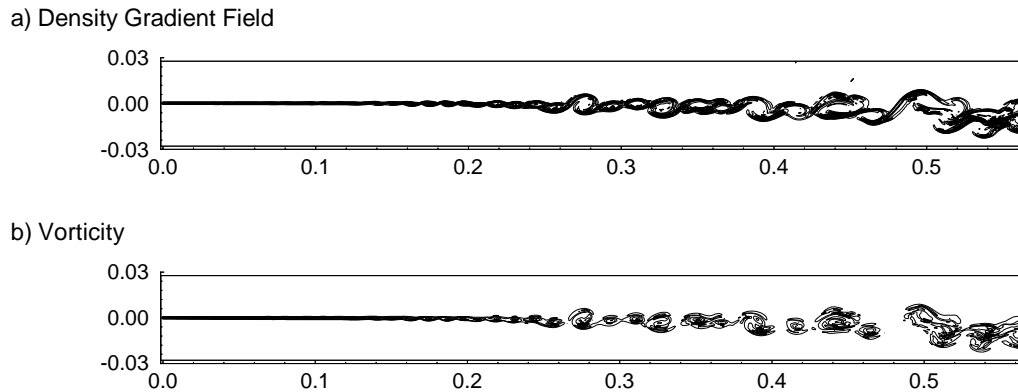


Figure 6.5. Instantaneous Descriptive Flow Parameters; a) Density Gradient Field, and b) Vorticity Field.

6.2.3 Time Averaged Results

Instantaneous to Time-Averaged Comparison

Examination of the field behavior of the conservative variables contributes greatly to our understanding of the flow and also provokes many questions. The time-averaged density field shown in Figure 6.6 shows a very smooth contour field with a few notable features. But, the sudden spreading between two contour lines beginning at the 0.4 m axial position provokes the question of, what is the cause? In the instantaneous field complex vortex combinations can be seen in the region from 0.4 m through the exit plane. The complex structures result from what Oh and Loth [49] described as “slapping” combination. The “slapping” combination process occurs when vortices collide due to their moving at different velocities. The spreading of the contour lines is due to the vortex combination and the associated sudden movement of high density fluid into the low speed stream. The slapping combination process does not produce any observable effects in the time-averaged mass flux field of Figure 6.7. The axial mass flux figures show very few unique features; although they do show the first stationary Mach waves in the high speed steam and the beginning of the “strange wave” region where the shear layer motion begins to influence the shear streams completely across the channel significantly.

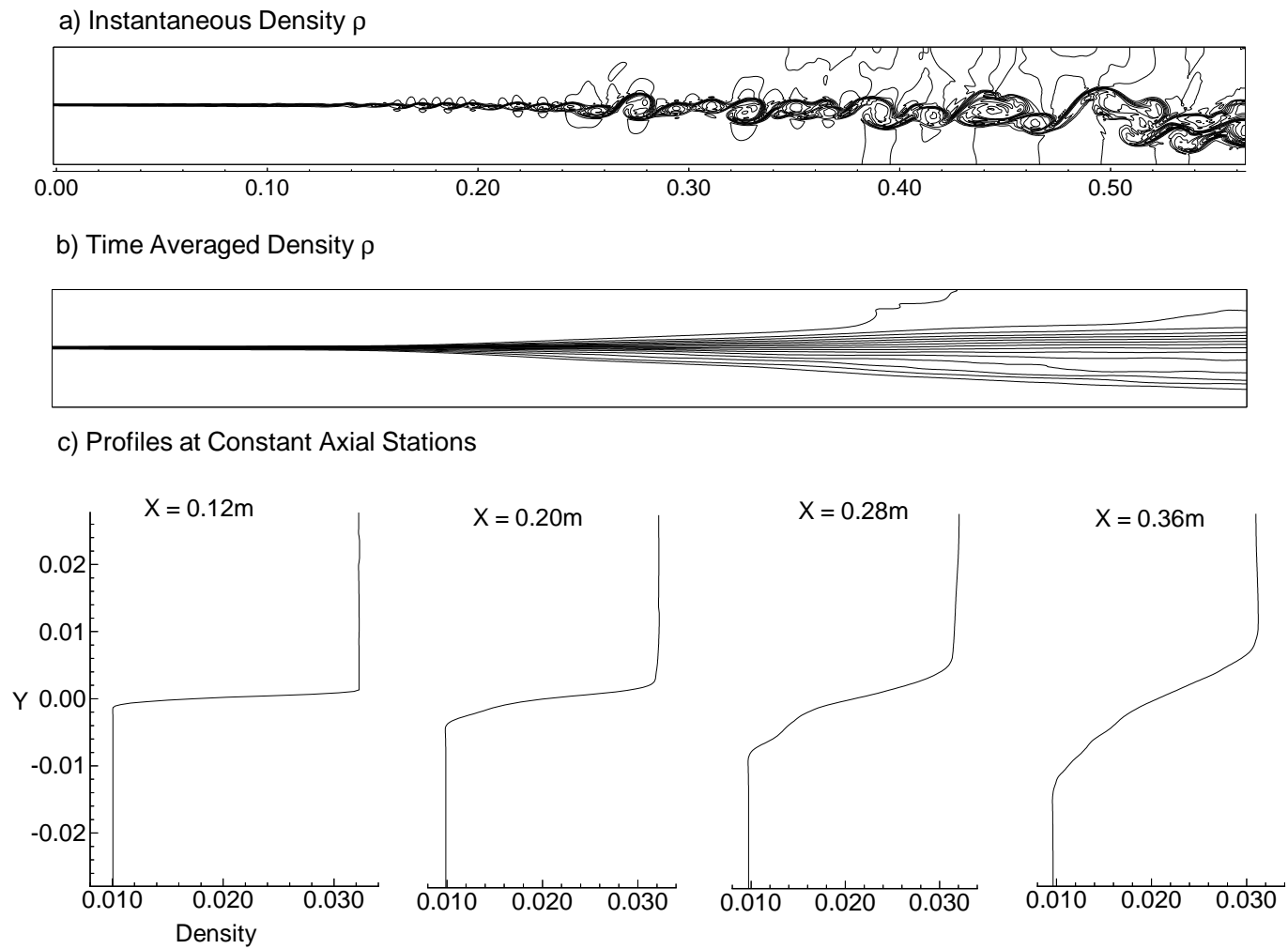


Figure 6.6. Conservative Variable Density ρ (kg/m^3) a) Instantaneous Density, b) Time Averaged Density Field, and c) Cross Channel Density Profiles at $X = .12m, .20m, .28m,$ and $.36m$.

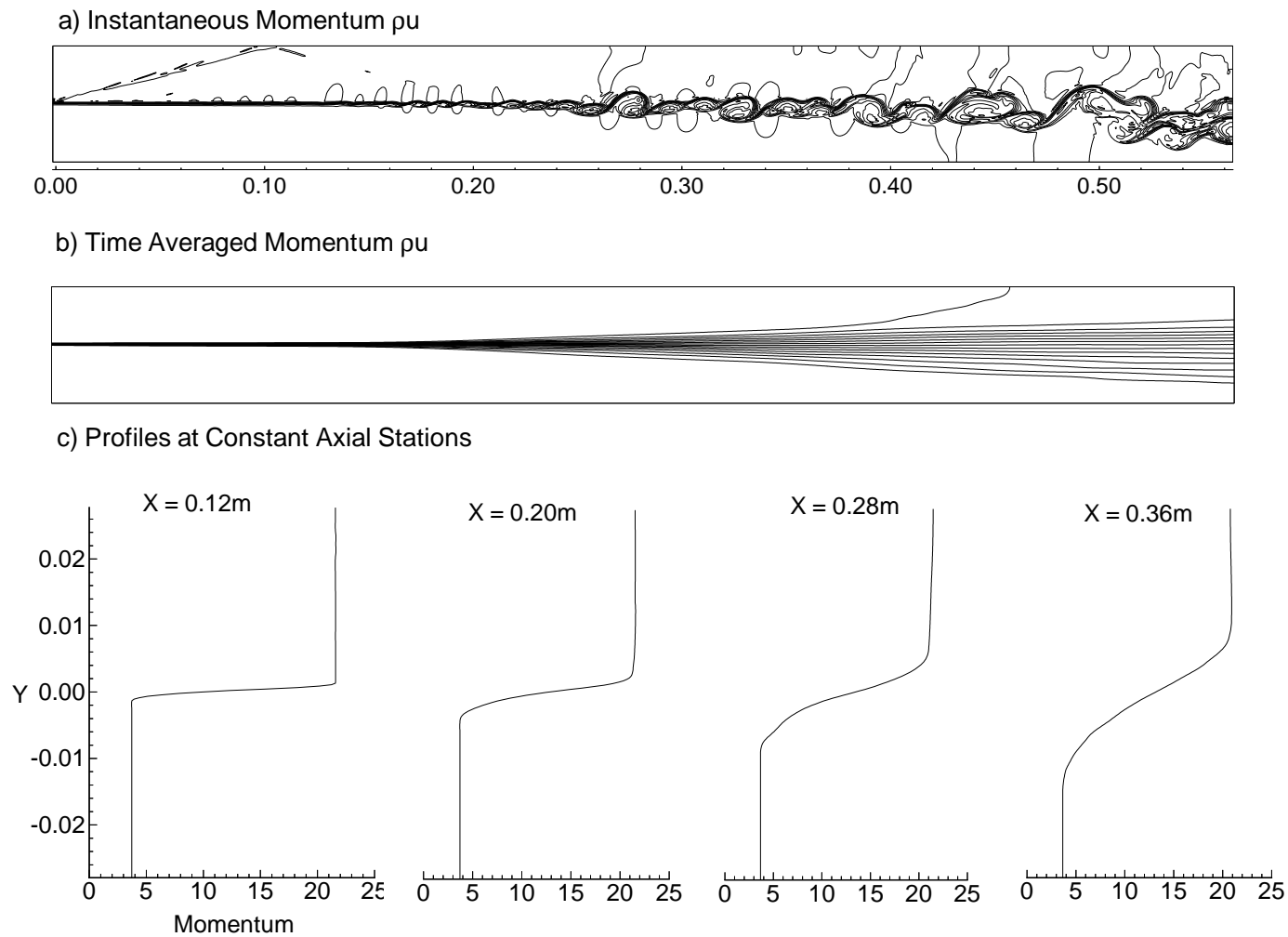


Figure 6.7. Conservative Variable Axial Mass Flux ρu (kg/sm^2) a) Instantaneous Mass Flux, b) Time Averaged Mass Flux Field, and c) Cross Channel Mass Flux Profiles at $X = .12m, .20m, .28m,$ and $.36m$.

The transverse mass flux fields provide the best insight into the shear layer growth bulge. In the time-averaged field two Mach waves can be seen clearly emanating from the splitter plate, one in each stream. The low speed Mach wave travels through the low speed stream to the wall, reflecting, traveling back to the shear layer and triggering a second high speed stream Mach wave. The Mach wave pattern in the high speed stream repeats several times along the length of the mixing channel. The strength of the vortices (positive and negative transverse pairs) along the shear layer is not monotonic, but varies with position. The Mach waves appear to trigger the added shear layer growth by their influence on the strength of the vortices. Several other notable features are the strength of the Mach waves that are readily identifiable in the early cross channel profiles ($X = 0.12$ and $0.20m$) and the peak in the ρv field in the range of 0.32 to 0.40 m position. Immediately following the peak in the time-averaged ρv field, the magnitude quickly diminishes and gradients rapidly spread out. It is in this diffuse region that the instantaneous contour lines suggest the presence of shocks associated with the vortices. Some researchers such as Guirguis et al. [22] have computed the shocks associated with non-pressure balanced shear layers. The total energy profiles give essentially no clues to the dynamic processes that are going on in this simulation. Viscosity in real flows will dampen the type of phenomena observed. The effects of viscosity and their influence on all aspects of the flow, especially the effect of wall boundary layers, are not addressed by this Euler simulation.

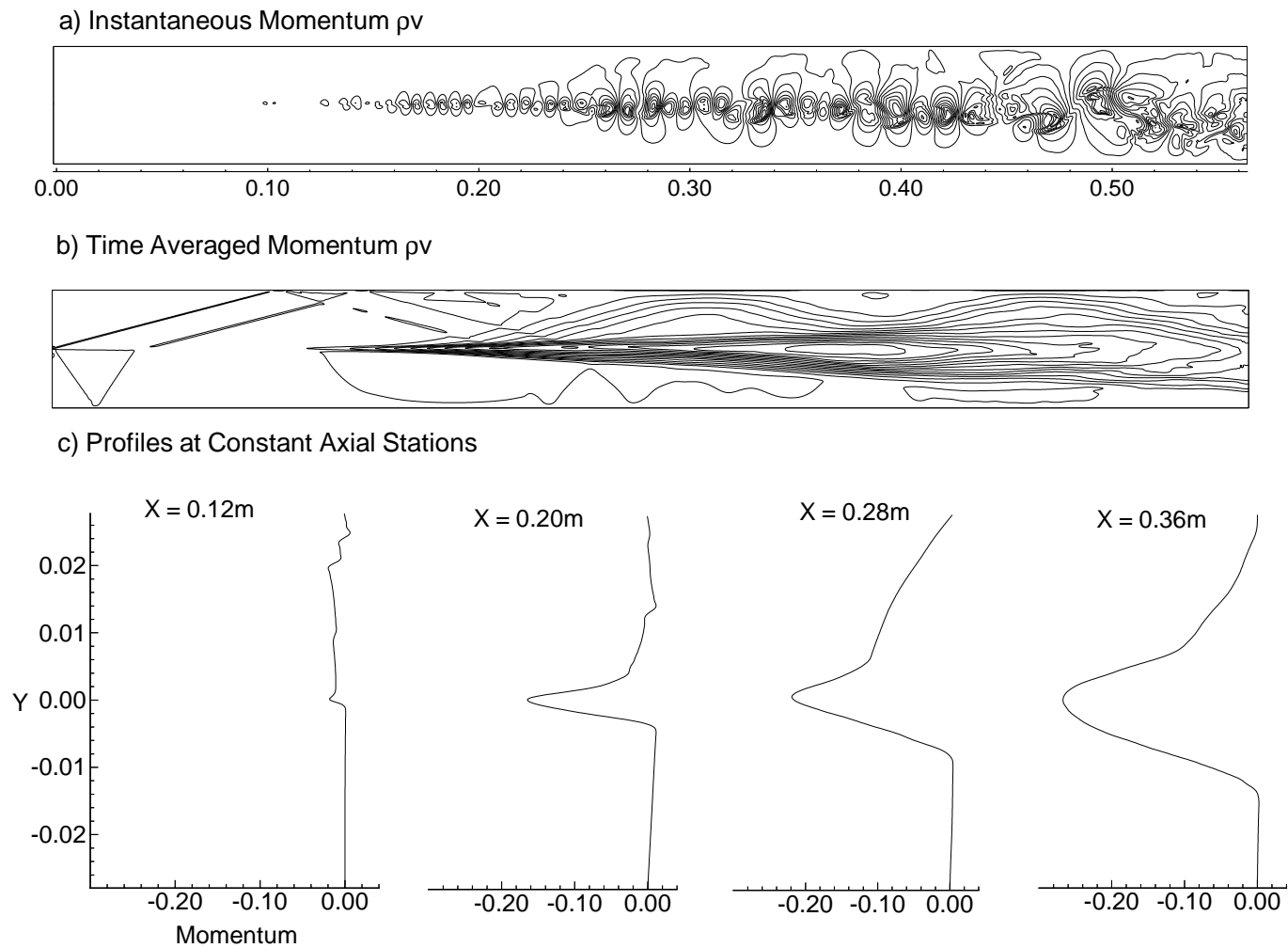


Figure 6.8. Conservative Variable Transverse Mass Flux ρv (kg/sm^2) a) Instantaneous Mass Flux, b) Time Averaged Mass Flux Field, and c) Cross Channel Mass Flux Profiles at $X = .12m, .20m, .28m,$ and $.36m$.

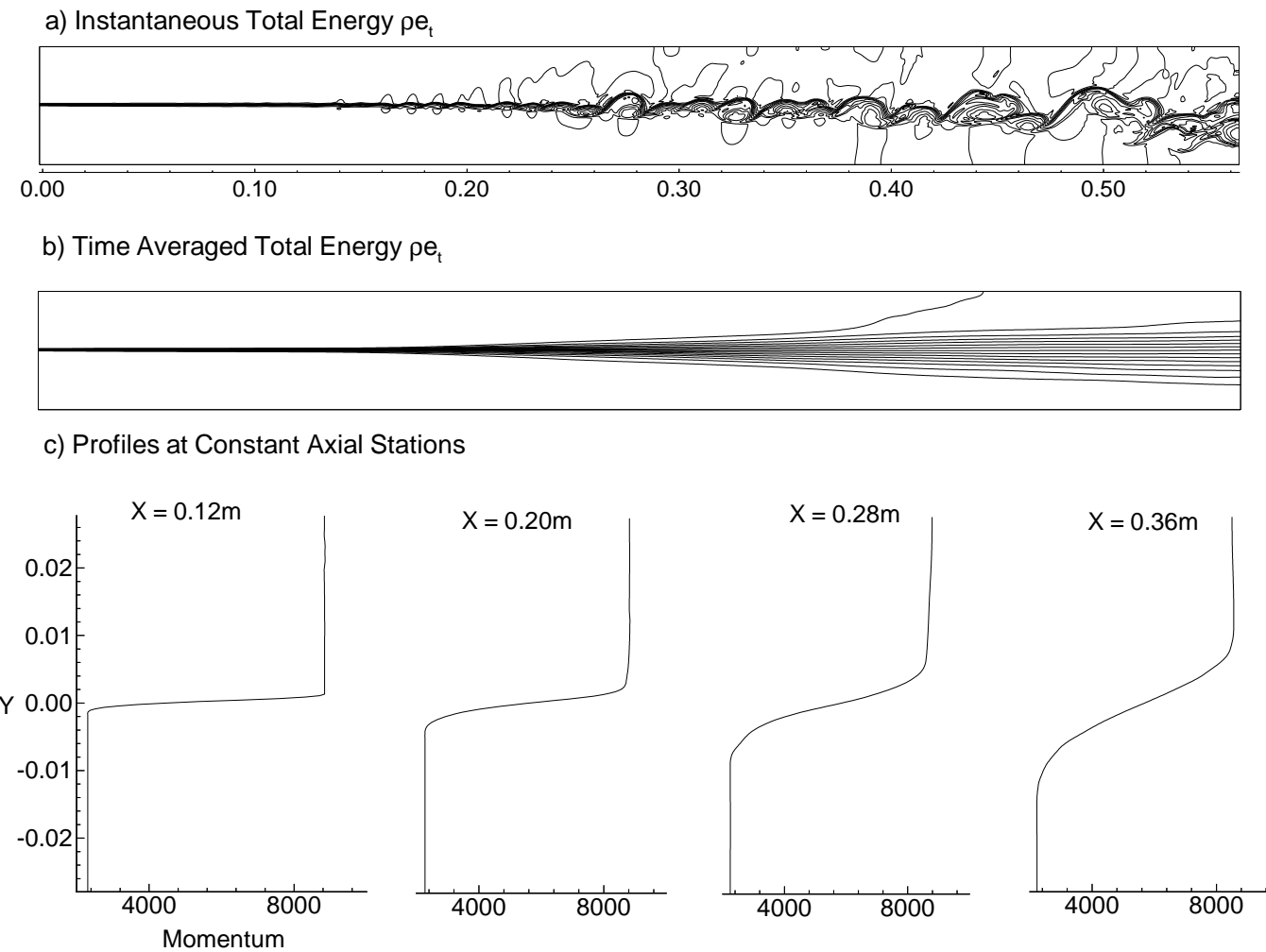


Figure 6.9. Conservative Variable Total Energy ρe_t ($Joule/m^2$) a) Instantaneous Total Energy, b) Time Averaged Total Energy Field, and c) Cross Channel Total Energy Profiles at $X = .12m, .20m, .28m,$ and $.36m$.

Time-Averaged Comparison With Experiment

The time-averaged spreading of the shear layer into the low energy stream is shown in Figure 6.10. The gradual rise in the low energy stream is believed to be the effect of the high speed stream pumping the channel flow.

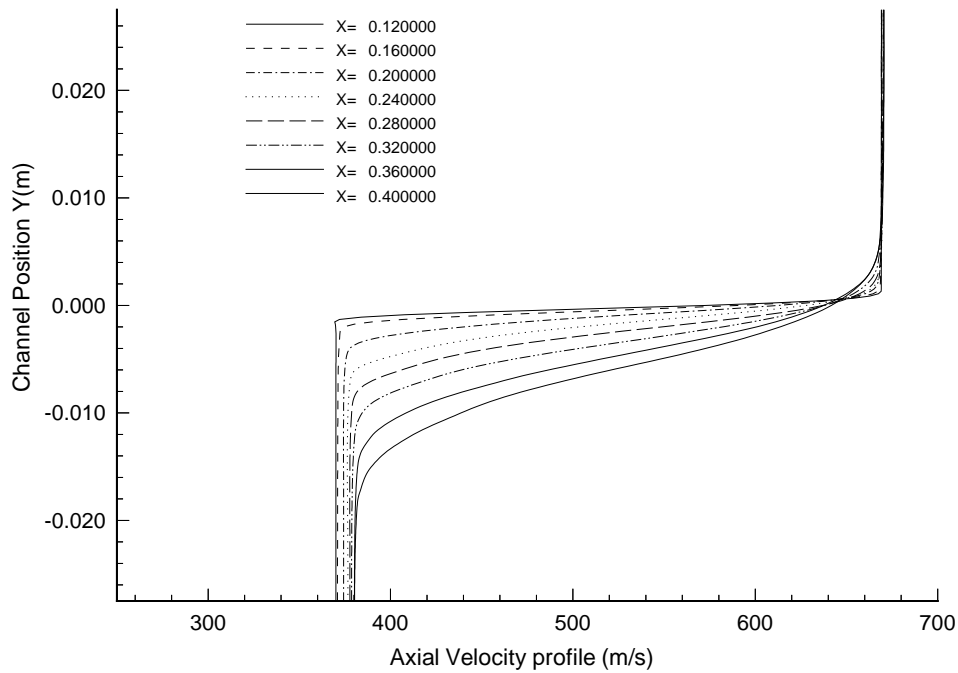


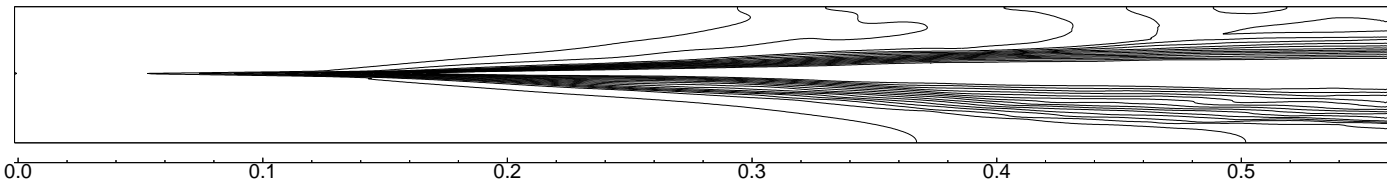
Figure 6.10. Axial Variation of Numerical Time-averaged Velocity Profiles.

Fluctuating Quantities

The mass flux perturbations and the Reynolds stress are displayed in Figure 6.11, Figure 6.12 and Figure 6.13. The axial mass flux fluctuations computed for both Case I and Case II grows to a maximum level and then remains constant. The cross channel profiles of the mass flux perturbations are similar in shape and magnitude trend to the turbulence intensities of the numerical simulation of Oh and Loth [49] and the experiments of Goebel and Dutton [16]. other experimenters such as Samimy and Elliot [61] report findings that show a different trend in the growth of the turbulence intensities. The mass

flux perturbations and turbulence intensities may be affected by the same influencing factors. One possible explanation for the differing observations is interaction of the shear layer with the domain, whether it is an experimental wind tunnel wall or a computational boundary. The axial turbulence intensity grows to a maximum and then holds a constant contour shape; but, $\rho v'$ and $\rho u'v'$ both show a process of growing to a peak and then dying down. This growth and decay process can occur several times within a normal test or computational domain. The decay process is strongly influenced by the shear layer interaction with the wall.

a) RMS Momentum Perturbation: $(\rho u)'$



b) Profiles at Constant Axial Stations

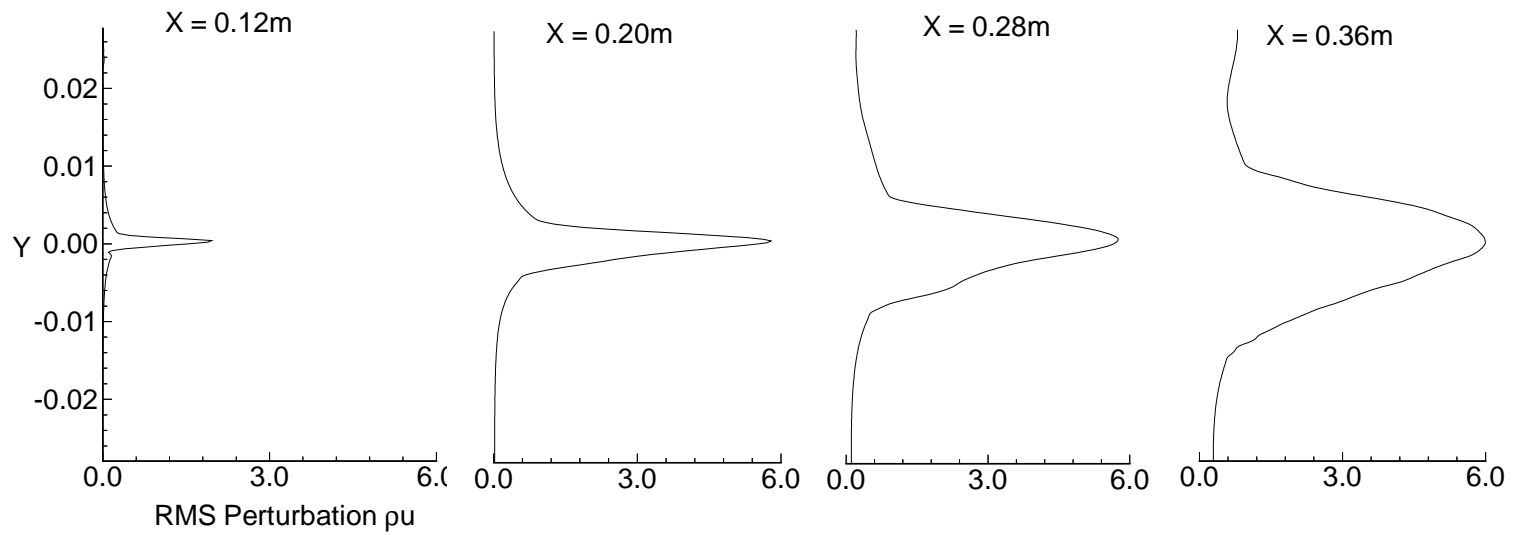
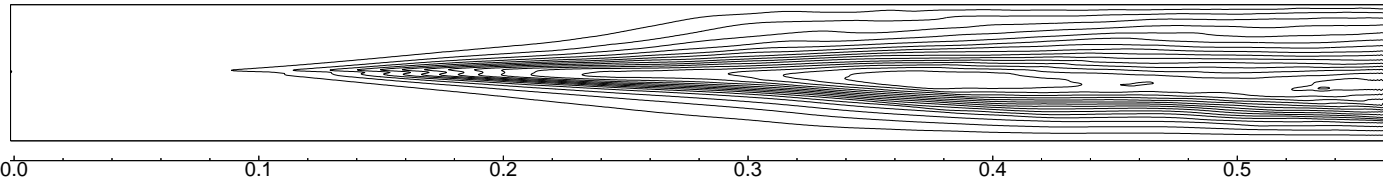


Figure 6.11. Case II $M_c = 0.64$ Axial Mass Flux Perturbation $\overline{(\rho u)'}'$: a) RMS Mass Flux Perturbation and b) Cross Channel Profiles at $X = .12m, .20m, .28m,$ and $.36m$.

a) RMS Momentum Perturbation: $(\rho v)'$



b) Profiles at Constant Axial Stations

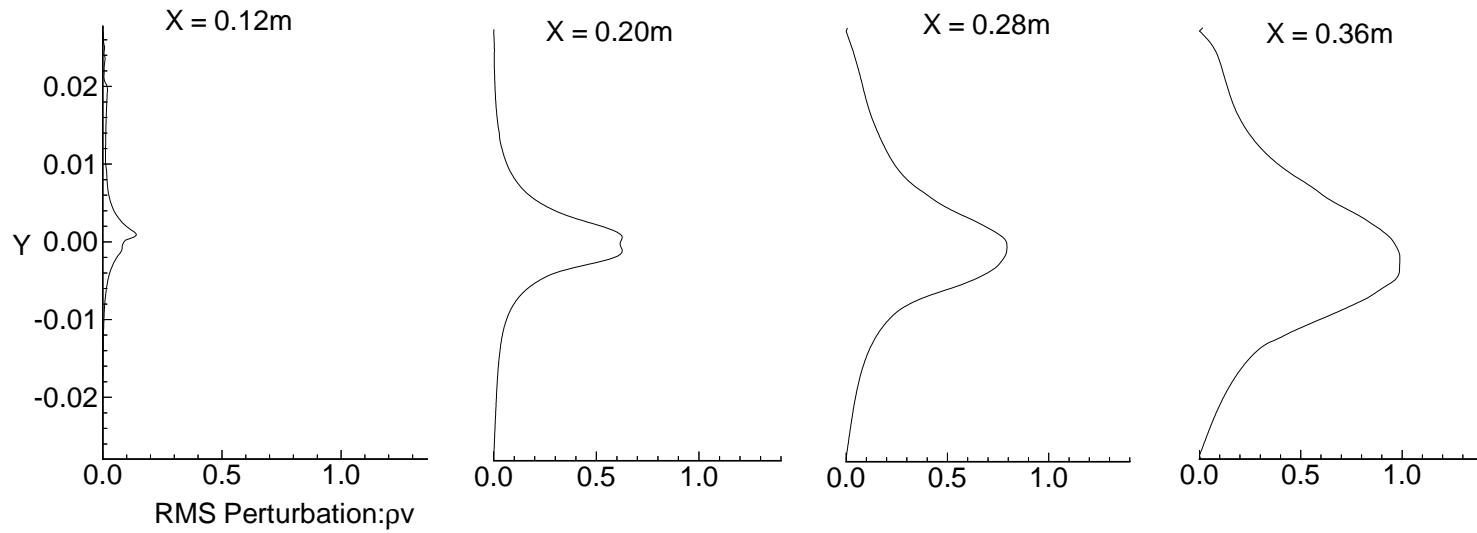


Figure 6.12. Case II $M_c = 0.64$ Transverse Mass Flux Perturbation $\overline{(\rho v)'}'$: a) RMS Transverse Mass Flux Field and b) Cross Channel Profiles at $X = .12\text{m}$, $.20\text{m}$, $.28\text{m}$, and $.36\text{m}$.

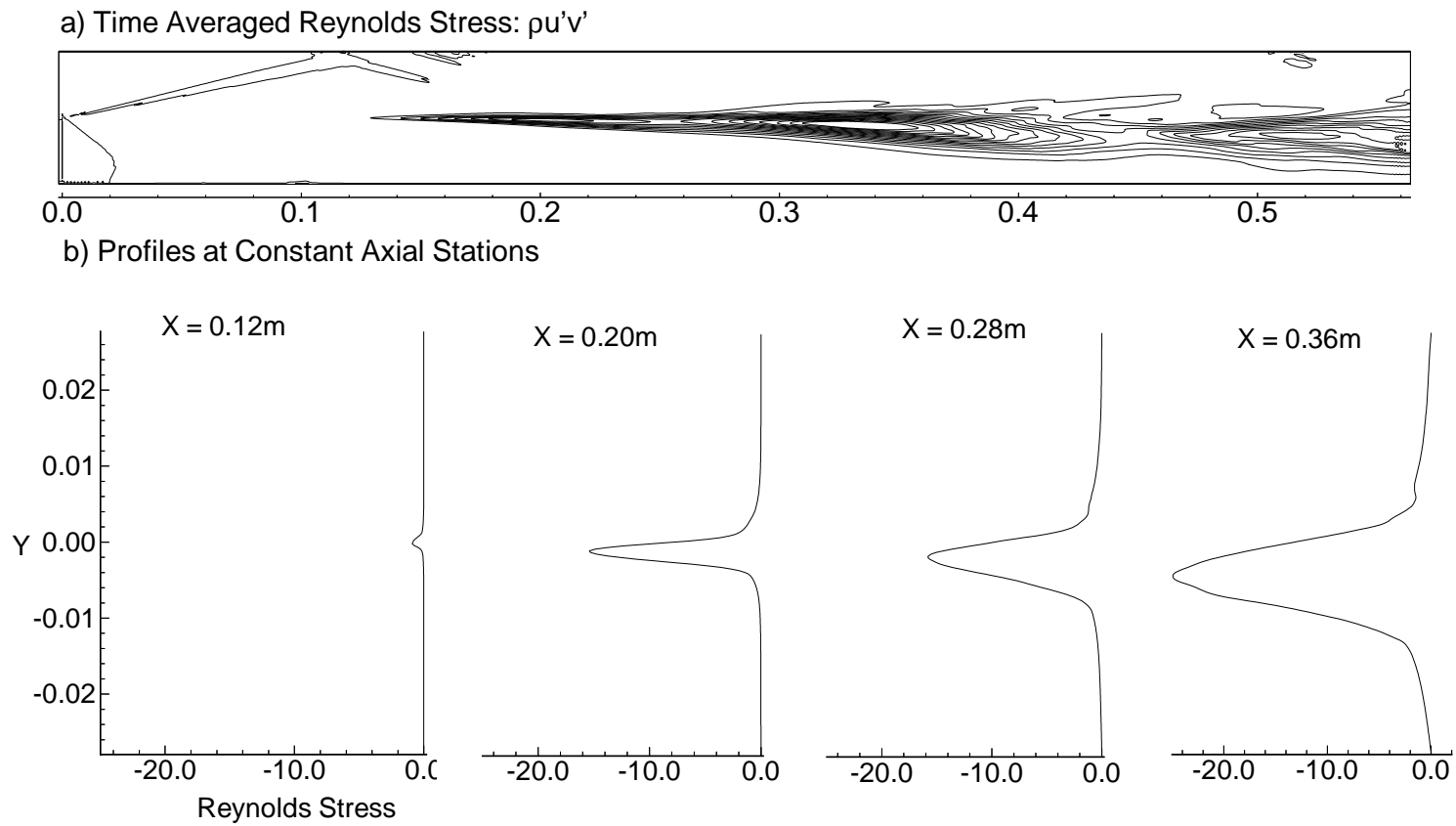


Figure 6.13. Case II $M_c = 0.64$ Time Averaged Reynolds Stress $\overline{\rho u'v'}$: a) Time-averaged Reynolds Stress Field, and b) Cross Channel Profiles at $X = .12\text{m}$, $.20\text{m}$, $.28\text{m}$, and $.36\text{m}$.

The predictions for the Case II shear layer conditions follow in a consistent manner the findings of the Case I simulation. Both simulations were aided by the foundation laid in the findings of the single frequency simulations. The four classes of simulations, including the three-dimensional simulation of Case I conditions, present a significant quantity of data, supporting and confirming the findings of other researchers. The simulations also provide explanations for unexplained behaviors that have been reported by experimental researchers. A complete discussion of the significant accomplishments, finding and suggested paths for future work is presented in the final chapter that follows.

Chapter 7

Conclusions

The research conducted for this thesis was a Direct Euler Simulation (DES) of the dynamic behavior of a confined supersonic shear layer. The fourth-order MacCormack 2-4 numerical scheme and a Cartesian grid system were used to provide high-resolution inviscid eddy simulations of the spatially evolving confined shear layer. The objectives were to improve physical understanding of shear layers, develop a simple technically clean approach that provided a high fidelity foundation for simulations and establish the validity of the simulations by direct comparisons with experimental measurements. In general, the objectives of this research were satisfactorily accomplished; the Euler code performed well, several significant developments and findings were discovered and the simulation results compared well with the experimental results. The following sections discuss the specific findings and new developments that were achieved in this research.

7.1 Objectives

The research conducted as part of this thesis has been successful in reaching the overall objective of developing a numerical simulation code capable of accurate modeling of confined supersonic mixing layers. The Euler code that was developed provides effective simulation of both the steady and dynamic behaviors of supersonic compressible shear layers. For the Euler equations the MacCormack 2-4 numerical scheme provides resolution of wave frequencies of up to 28,000 Hz for the two-dimensional simulation and 6,400 Hz for the three-dimensional simulation. The MacCormack method provides these resolution capabilities without loss to the dispersion relation characteristics of the waves. During code development Von Neumann stability analysis identified limitations of the MacCormack 2-4 method for flows with high Reynolds numbers, such as Martens' Case I and Case II conditions. Extension of the code to include viscous effects was also examined during the Von Neumann analysis. Unfortunately, the simulation and wave resolution goals could not

be achieved within the combined CFL and diffusion number limits due to computer memory and run-time limitations.

The Euler mode operation resulted in the development of an effective modification to the Jameson artificial viscosity algorithm; a new extrapolation method that has provided better stability than classical methods; and a new unsteady inflow excitation method that produces white noise disturbances. The excitation method has been effective in eliminating the need for a virtual origin to achieve streamwise comparison of experimental and numerical results in the two-dimensional simulations. The Euler mode operation has been a very successful development tool. However, the simulations greatest contribution, a very fine grain definition of both instantaneous and time-averaged variables, could not have been gained without the memory and speed benefits of massively parallel processing.

The availability of Gigabytes of memory and Gigaflop class computing speeds provide the basic capability that enables the use of fine grain grids that can resolve acoustic waves in air up to 28,000 Hz. Addition of memory capacity to an advanced computer is a relatively very straight forward process. It is the Gflop computing speed that made the 196,608 point grid of the two-dimensional simulations and the 5,242,880 point grid of the three-dimensional simulation an achievable task. Finally, the matrix based syntax of High Performance Fortran style programming language removes many hours and errors from the code development process. This research demonstrates that practical engineering problems can now be simulated directly with Euler methods. Continuing development in computing speeds and numerical methods should soon provide comparable simulation capability for viscous problems.

7.2 Numerical Methods

To provide the desired high-resolution of inviscid eddies it was necessary to resolve two types of phenomena, fluid dynamic waves and acoustic waves. Resolving the shear layer initial profile was the most severe fluid dynamics requirement. The method of Tam et al. [74] for analyzing the dispersion relation preservation capability of numerical stencils was used to show that the MacCormack 2-4 method needed 8 points per wave length to resolve a wave fully. Using a criteria of 10 points per wave length to fully resolve a wave, the final grid system for the two-dimensional Case I conditions fully resolved the inlet shear

layer, the fundamental Kelvin-Helmholtz instability and acoustic waves of up to 28 kHz. For the two-dimensional Case II conditions the inlet shear layer and the Kelvin-Helmholtz modes and acoustic waves up to 6 kHz were resolved fully. The only remaining issue was the size of the physical domain that could be resolved and that was determined by the grid. A common numerical issue in today's environment has been the order of accuracy needed to resolve waves fully. The fourth order accuracy of the MacCormack method was judged to provide the needed spatial accuracy needed for the Euler simulations. Real fluid effects of viscosity and boundary influences were expected to produce differences between the simulation results and the experimental data that could not be simulated even by the use of a higher order method.

The unsteady boundary conditions developed for the inlet have demonstrated white noise behavior which does not introduce favored frequencies into the solution. The new boundary conditions are significantly simpler than the sine series frequently used by investigators. The simple form requires only the amplitude of the inlet turbulence intensities be provided, which, for most experimental test facilities, are known moderately well. An important new capability provided by these unsteady boundary conditions is their ability to produce large scale behavior in its proper spatial location.

The utility of the Jameson artificial viscosity has been extended by a change in the second order damping switch developed during this research. Jameson's original method is not effective in flows which have very low pressure variation such as a pressure balanced shear layer. The density based switch can be used as effectively for many problems. It was developed by comparing switch behavior for the Riemann problem. Both switches have identical behavior patterns, differing only in magnitude. The normal coefficient tuning for the Jameson method corrects for any needed magnitude changes. The modified Jameson method was very effective for this research and should be equally applicable for other flows with variable density.

A new approach to finding extrapolation stencils was developed. Conventional stencils commonly produce unbounded estimates when vortices with large gradients pass through an extrapolated boundary. The new approach has produced stencils that rarely produce out-of-limit estimates. Also, conventional high order extrapolations are commonly centered at one-half to one cell position from the actual boundary. The new stencils also have

a consistent form that is centered at the boundary cell. The new stencils also do not require any assumptions and they are uniformly first order accurate, $O(\Delta x)$. The first order accuracy provides artificial damping at the boundary.

7.3 Simulation Physical Phenomena

Three measures were used to evaluate the ability of the Euler simulation to predict the physical behavior of shear layers 1) the ability to reproduce the FFT and power spectra, 2) the ability to predict the correct shear layer growth behavior and 3) the ability to predict accurate time-averaged field variables profiles. Overall comparison with the experimental data was excellent with differences generally attributable to either viscous effects or methods of data reduction. Accurate prediction of physical data by the simulation establishes the credibility of the simulation. Once established as valid, a simulation provides valuable insight into the flow's behavior from its detailed information that goes beyond anything available from the usually relatively sparse experimental data. Valuable insight into the shear layer was obtained by comparison between the instantaneous and time-averaged contour plots of the conservative variables and turbulence quantities.

Direct Euler simulation produced accurate dynamic modeling of the shear layer. The FFT and power spectra compared well with the experimental data. Both the experimental and the simulation frequencies matched those predicted from linear stability theory calculations. Comparison at two axial locations demonstrated the simulation's correct prediction of the peak frequency at each location and the relative changes between locations.

The shear layer growth profiles from experiment and simulation compared well but did show significant differences between Case I and Case II. For Case I conditions the numerical boundary-layer type (δ_{98}) thickness compared the closest to the experimental profile of Martens. The experimental shear layer thicknesses were determined graphically from Pitot profiles. Pitot profiles and visual thickness produced very similar profiles which explained why the experimental growth compared best with the numerical boundary-layer thickness type calculation. Viscous effects in the real flow reduce the maximum velocity gradient through the layer yielding a larger thickness than that computed from the inviscid calculations. For Case II conditions the lower growth rate resulted in a thinner layer thickness. Viscous effects were reduced due to slightly higher Reynolds number. The thinner

layer made graphical resolution more difficult. The combination of effects resulted in the Case II experimental vorticity and numerical vorticity profiles comparing moderately well. Overall for the two cases the growth profiles compared very well. The differences between experimental and numerical vorticity thickness were due primarily to viscous effects that reduced the velocity gradient in the real fluid and differences in the method of determining the profile thicknesses. The growth rates were normalized and compared to the results of other researchers using Papamoschou's normalized growth correlation. When compared on a normalized basis the numerical results compared well with the ideal profile of Ragab and Wu.

The time-averaged cross channel profiles of the axial velocity profile were compared with the experimental data with good overall comparison. Several shear layer inlet velocity profiles were explored early in the research to determine the influence of the splitter plate wake. For the very thin shear layer being simulated no profile provided better overall results than the hyperbolic tangent profile. The velocity profiles throughout most of the turbulent growth region showed the same shape and growth rates as the experimental data. Viscous effects deteriorated the comparisons at the far downstream locations. Viscosity modified the shear layer by producing nearly linear velocity profiles and boundary layer growth at the duct walls began to interact with the shear layer profiles.

The dominant amount of research conducted was based upon the two-dimensional simulations. These simulations provided a sound and effective development tool capable of being run relatively quickly. A typical two-dimensional simulation required about 10 hours of cpu time which took about two weeks to push through computer queues. The three-dimensional simulation was substantially more expensive to run and was run for about a fourth of the number of time steps as the two-dimensional simulations. The three-dimensional simulations provided the needed confirmation of the two-dimensional nature of the Case I conditions. Overall, the combination of two- and three-dimensional simulations provided an effective research combination.

7.4 Directions for Future Research

Possible directions for future research that stem from this research fall into two areas: first, suggested numerical research and second, suggested experimental research. The

suggested numerical research addresses four issues that naturally follow from this research. These are: a new solution algorithm to permit examination of viscous effects; grid optimization; fully three-dimensional mixing mechanisms in shear layers; and; shear layer growth enhancing mechanisms. The proposed future experimental research also addresses four areas for shear layer research: first, bench mark quality calibrated shear layer mapping; second, mapped single frequency excited shear layers; third, a systematic set of compressible shear layers beginning at fully two-dimensional flow and progressing into fully three-dimensional flow; and fourth, experiments investigating shear layer growth control. The suggested experimental research builds upon Martens' work and improves upon it as a basis of both new knowledge and simulation validation.

The first area for future numerical shear layer research is the development of a fourth-order numerical scheme that will permit simulation of high Reynolds number, viscous shear layers. The method should be optimized for parallel application so as to achieve the greatest possible speed. The Runge-Kutta integration method of Chyczewski [9] is suggested only using fourth order spatial differencing. The second area of suggested research is grid independence and optimization research. Grid independence research would look at how to cluster a grid to address the requirements of a multizone problem such as the shear layer. The zones would include the shear layer laminar growth area both axially and across the shear layer, the turbulent growth zone, and near the channel walls for confined shear layers. Grid optimization would look at issues of how to allocate a grid for such goals achieving a uniform resolution of frequency in the solution domain, adaptive grid and grid allocation optimization for three-dimensional simulations. The third area of research is a systematic series of simulations moving from a shear layer flow that is strictly two dimensional through a flow that has pronounced three-dimensional behavior. The research would be looking to determine issues of why growth rates slow with compressibility; is the third dimension adding an energy absorbing mechanism? Investigation of shear layer growth tripping mechanisms like Mach wave/shear layer interactions such as produced by a wavy wall. This research would include both growth enhancement and growth suppression. These four areas of numerical research present significant challenges for which the high performance computing environment at Penn State.

The proposed research in the numerical and experimental areas parallel each other to provide the maximum synergism to each project and the greatest overall accomplishment. The research areas have been simply stated but hold a multitude of paths, options and challenges as well as establish a center of excellence in shear layer research.

Appendix A

Von Neumann Stability Analysis

The stability limits of the MacCormack 2-4 finite difference scheme were examined in detail using Von Neumann analysis. The Von Neumann or Fourier analysis was applied to the linear convection equation, the linear diffusion (heat) equation and the combined linear convection-diffusion equation. The limiting values of the stability coefficients were derived for their respective amplification factors. Gottlieb and Turkel [18] gave the limit for Courant number as $\lambda = 2/3$ and the limit for the diffusion number as $r = 3/8$. The values derived in this investigation are in agreement with Gottlieb and Turkel's findings for the individual convection and diffusion equations.

For the Convection and diffusion equations, the limits for Courant and diffusion numbers occur at different frequencies. Consequently, the complex nature of the combined convection-diffusion equation and the predictor-corrector application of the schemes stencil lead to non-linear changes in the stability limits. The limits for the combined equation were found by holding the Courant number at the convective limit and absorbing non-linear effects in the viscous diffusion number. The resulting limits for the Courant and diffusion number are $\lambda = \frac{2}{3}$ and $r = \frac{3 + \frac{\sqrt{337}}{3}}{16}$, (≈ 0.57), respectively. The historical Von Neumann analysis of the second order MacCormack scheme by Fromm [15] added the requirement that the cell Reynolds number be less than two. This criteria was later corrected by Hirt [26] and relaxed to $Rey_{cell} \leq \frac{2}{\lambda}$.

The interrelationship between the Courant and diffusion numbers for the MacCormack 2-4 method also yields a cell Reynolds number criteria. The derived cell Reynolds number limit requires that Rey_{cell} be less than $\frac{3(-3 + \frac{\sqrt{337}}{3})}{8}$, (≈ 1.17). For the second order MacCormack method, Hirt took advantage of the form of the amplification factor equation to relax the original cell Reynolds number. Hirt applied the properties of the equation of an ellipse to relax the stability limit. The complexity of the MacCormack 2-4 scheme yields

a very complicated amplification factor equation that is neither simple nor constant. Consequently a more relaxed limit for the cell Reynolds number could not be readily identified. Detailed analysis of the Courant, diffusion and cell Reynolds numbers are given below.

A.0.1 Convection Equation

The spatial splitting of the MacCormack method allows each coordinate direction to use the one-dimensional stability limits. The one-dimensional limits yield a larger time step than may be found from the multi-dimensional limits. Accordingly the stability analysis was carried out for one-dimensional equations.

The linear convection equation is written,

$$\frac{\partial u}{\partial t} + \alpha \frac{\partial u}{\partial x} = 0 \quad (\text{A.1})$$

The MacCormack 2-4 method uses a second order forward difference in time and a fourth order central difference in space to represent the derivatives.

$$\frac{\partial u}{\partial t} = \frac{u_j^{n+1} - u_j^n}{\Delta t} \quad (\text{A.2})$$

and

$$\frac{\partial u}{\partial x} = \frac{u_{j-2}^n - 8u_{j-1}^n + 8u_{j+1}^n - u_{j+2}^n}{12\Delta x} \quad (\text{A.3})$$

The fourth order central difference in space is applied in a predictor-corrector split form. Applying these difference equations to the convection equation in the predictor-corrector sequence yields,

$$u_j^* = u_j^n + \alpha \frac{\Delta t}{6\Delta x} (-7u_j^n + 8u_{j+1}^n - u_{j+2}^n) \quad (\text{A.4})$$

$$u_j^{n+1} = \frac{1}{2} [u_j^* + u_j^n - \alpha \frac{\Delta t}{6\Delta x} (+7u_j^* - 8u_{j-1}^* + u_{j-2}^*)] \quad (\text{A.5})$$

Von Neumann or Fourier stability analysis is linear, allowing the analysis to be carried out for a single frequency. To illustrate the analysis, a single Fourier component of u_j^n is assumed to have the form,

$$u_j^n = U e^{\beta n \Delta t} e^{I k_m j \Delta x} \quad (\text{A.6})$$

where $I = \sqrt{-1}$, U is the amplitude coefficient, k_m is the m^{th} wave number in the x direction, $n \Delta t$ is the local temporal level and $j \Delta x$ is the local spatial position. The amplification factor G , where $U^{n+1} = G U^n$, is found after substituting the assumed form into the MacCormack 2-4 integration scheme. Using the definition of the Courant number, $\lambda = |\alpha| \frac{\Delta t}{\Delta x}$ where α is the maximum eigenvalue of the solution, G takes on the following form.

$$G = 1 - \frac{(7 - 8 e^{-Iz} + e^{-2Iz}) \lambda}{12} + \frac{(7 - 8 e^{Iz} + e^{2Iz}) \lambda}{12} - \frac{114}{72} \lambda^2 + \frac{64 (e^{-Iz} + e^{Iz})}{72} \lambda^2 - \frac{7 (e^{-2Iz} - e^{2Iz})}{72} \lambda^2 \quad (\text{A.7})$$

where $z = k_m \Delta x$. Equation A.7 is the exponential form of the amplification factor from one time step to the next, i.e. $e^{\beta(n+1)\Delta t} e^{I k_m j \Delta x} / e^{\beta n \Delta t} e^{I k_m j \Delta x}$ or in a compact notation e_j^{n+1} / e_j^n . Applying the exponential definitions of sine and cosine the above equation can be reduced and simplified to give

$$G = 1 + \frac{\lambda^2}{18} (1 - \cos(z)) (7 \cos(z) - 25) + I \frac{\lambda}{3} \sin(z) (4 - \cos(z)) \quad (\text{A.8})$$

Equation A.8 is identical to that derived by Gottlieb and Turkel [18]. The amplification factor equation now maps the behavior of the entire real frequency range into the finite domain $0 \leq k_m \Delta x \leq 2\pi$. The upper limit of the Courant number is defined by the Courant-Friedrichs-Lewy (CFL) conditional stability condition, the limit for which the modulus of the amplification factor must be bounded to less than or equal to one. The resulting Courant number for the convection equation is given by

$$\lambda \leq 2/3 \quad (\text{A.9})$$

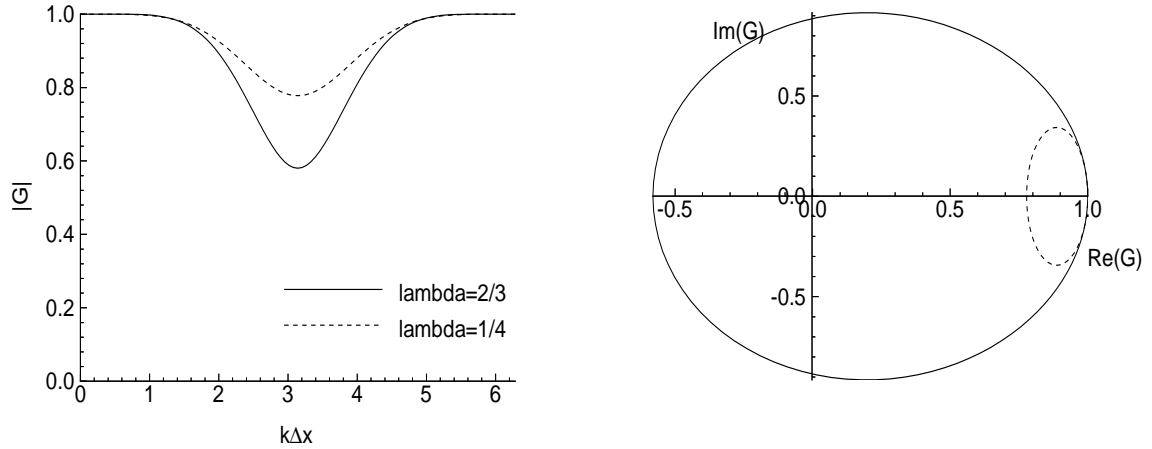


Figure A.1. Amplification Factor of the Convection Equation, $\lambda = 2/3$ and $\lambda = 0.25$

The formal requirement for stability can be expressed as $|G| \leq 1$. The stability criteria is shown in Figure A.1 for two Courant numbers; $\lambda = 2/3$, the maximum limit and $\lambda = 0.25$, the Courant number used throughout the computations of this research. The amplification factor is shown graphically in both polar and Cartesian coordinates.

A.0.2 Diffusion Equation

Stability analysis of diffusion terms was carried out using the diffusion or heat equation. Use of the diffusion equation simplified investigation of various methods of implementing the second order derivatives. None of these methods gave improved stability over the basic approach suggested by Gottlieb and Turkel [18].

The diffusion equation was written in hyperbolic form.

$$\frac{\partial u}{\partial t} - \frac{\partial}{\partial x} \left(\nu \frac{\partial u}{\partial x} \right) = 0 \quad (\text{A.10})$$

The form of Equation A.10 emulates the way the diffusion terms were implemented in the software and is also the form of implementation suggested by Gottlieb and Turkel. The inner derivative uses a first order one sided stencil. The outer derivative uses the MacCormack 2-4 fourth order stencil. The differencing of each first order one sided stencil is applied

in the opposite direction to the fourth order stencil to which it is being applied. As an example, backward differencing in the first order stencil was applied

$$E_v = \nu \frac{u_j^n - u_{j-1}^n}{\Delta x} \quad (\text{A.11})$$

to the forward differenced fourth order stencil.

$$u_j^* = u_j^n + \frac{\Delta t}{6\Delta x} (-7E_{v_j}^n + 8E_{v_{j+1}}^n - E_{v_{j+2}}^n) \quad (\text{A.12})$$

After applying the MacCormack scheme, the Fourier solution form of Equation A.6 and the diffusion number definition $r = \nu \frac{\Delta t}{(\Delta x)^2}$ were introduced. The resulting amplification factor has the form

$$G = 1 - \frac{180}{72} r + \frac{96(e^{-iz} + e^{iz})}{72} r - \frac{6(e^{-2iz} - e^{2iz})}{72} r + \frac{356}{72} r^2 - \frac{249(e^{-iz} - e^{iz})}{72} r^2 + \frac{78(e^{-2iz} + e^{2iz})}{72} r^2 - \frac{7(e^{-3iz} - e^{3iz})}{72} r^2 \quad (\text{A.13})$$

Applying the exponential definitions of sine and cosine, the above equation can be reduced and simplified to give

$$G = 1 + \frac{5}{2} r + \frac{8 \cos(z)}{3} r - \frac{\cos(2z)}{6} r + \frac{89}{18} r^2 - \frac{83 \cos(z)}{12} r^2 + \frac{13 \cos(2z)}{6} r^2 - \frac{7 \cos(3z)}{36} r^2 \quad (\text{A.14})$$

The formal stability requirement is expressed as $|G| \leq 1$. The amplification factor is shown graphically in Cartesian coordinates in Figure A.2. The symmetric behavior about π allows the upper limit of the diffusion number, r , to be easily found. For the diffusion equation the amplification factor is within stability limits when the diffusion number is

$$r = \nu \frac{\Delta t}{(\Delta x)^2} \leq \frac{3}{8}. \quad (\text{A.15})$$

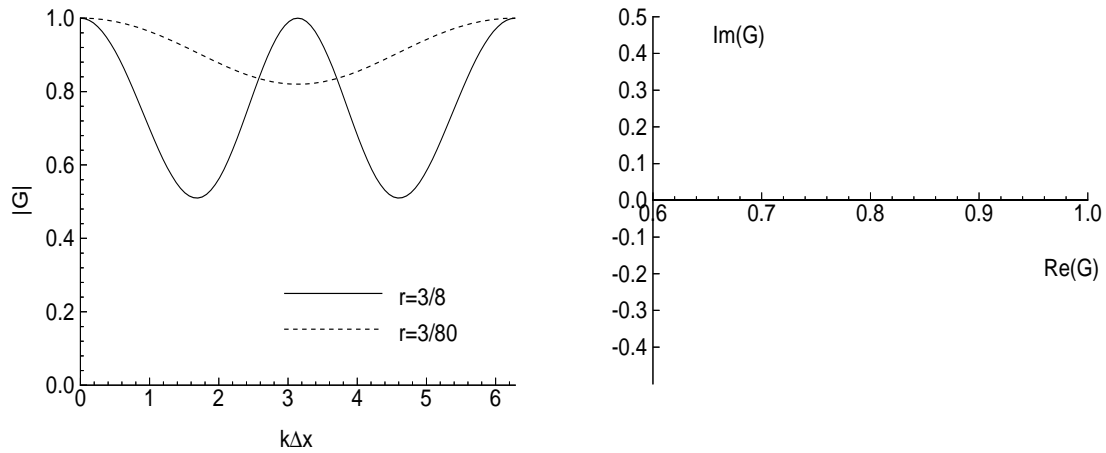


Figure A.2. Amplification Factor of the Diffusion Equation, $r = 3/8$ and $r = 3/80$

A diffusion number limit of $\frac{3}{8}$ was also reported by Gottlieb and Turkel [18]. As will be seen later, combining the convection and diffusion terms does not necessarily lead to the same limits for both these stability coefficients. The cause for the differences is based on the different frequencies at which these limits occur and non-linear effects due to the predictor-corrector application.

A.0.3 Convection-Diffusion Equation

The combined convection and diffusion equation written in hyperbolic form is given as

$$\frac{\partial u}{\partial t} + \alpha \frac{\partial u}{\partial x} - \frac{\partial}{\partial x} \left(\nu \frac{\partial u}{\partial x} \right) = 0 \quad (\text{A.16})$$

The MacCormack 2-4 scheme was applied in the same manner as for the convection and diffusion equations. Inserting the Fourier solution form of Equation A.6 yields the following amplification factor G .

$$G = 1 + \frac{48(e^{-iz} - e^{iz})\lambda}{72} - \frac{6(e^{-2iz} + e^{2iz})\lambda}{72} - 114\lambda^2 + \frac{64(e^{-iz} + e^{iz})\lambda^2}{72} -$$

$$\begin{aligned}
& \frac{7(e^{-2iz} - e^{2iz})\lambda^2}{72} - 180r + \frac{96(e^{-iz} + e^{iz})r}{72} - \frac{6(e^{-2iz} - e^{2iz})r}{72} - \\
& \frac{107(e^{-iz} + e^{iz})\lambda r}{72} + \frac{64(e^{-2iz} - e^{2iz})\lambda r}{72} - \frac{7(e^{-3iz} + e^{3iz})\lambda r}{72} + 356r^2 - \\
& \frac{249(e^{-iz} - e^{iz})r^2}{72} + \frac{78(e^{-2iz} + e^{2iz})r^2}{72} - \frac{7(e^{-3iz} - e^{3iz})r^2}{72} \quad (A.17)
\end{aligned}$$

Converting to a trigonometric basis Equation A.17 can be reduced and simplified to give

$$\begin{aligned}
G &= 1 - \frac{19\lambda^2}{12} - \frac{5r}{2} + \frac{89r^2}{18} + \frac{16\lambda^2 \cos(z)}{9} + \frac{8r \cos(z)}{3} - \frac{83r^2 \cos(z)}{12} \\
& - \frac{7\lambda^2 \cos(2z)}{36} - \frac{r \cos(2z)}{6} + \frac{13r^2 \cos(2z)}{6} - \frac{7r^2 \cos(3z)}{36} \\
& - \frac{4}{3} I \lambda \sin(z) + \frac{107}{36} I \lambda r \sin(z) + \frac{1}{6} I \lambda \sin(2z) \\
& - \frac{16}{9} I \lambda r \sin(2z) + \frac{7}{36} I \lambda r \sin(3z) \quad (A.18)
\end{aligned}$$

The interrelationship of the Courant and diffusion numbers was determined using the stability limit for the modulus of the amplification factor, $|G|^2 = 1$. The solution root that has a positive real value over the range of λ from zero to one is given by

$$r = \frac{(3 + \sqrt{9 + 64\lambda^2})}{16} \quad (A.19)$$

The combined convection-diffusion equation allows the diffusion number to rise above its diffusion equation limit. The diffusion number correctly approaches the diffusion equation limit as λ goes to zero. That minimum diffusion number has a value of $\frac{3}{8}$ or numerically 0.3750. The limit relationship between r and λ is shown in Figure A.3. The Courant number was held at its convection limit to give proper handling of the convective terms in the Euler/Navier Stokes equations. At the Courant number of $\frac{2}{3}$ the diffusion number limit becomes $r = \frac{3 + \sqrt{337}}{16}$, with an approximate numerical value of ≈ 0.57 . Two figures, Figure A.4 and Figure A.5, present the amplification factor for two Courant numbers and several diffusion numbers. Researchers Kennedy and Carpenter [30] have investigated several high order numerical methods including a series of extended MacCormack schemes. They found limits for the Courant and diffusion numbers to be 0.72 and 0.57, very close to those found here. However, as they note in their paper, the 2-4 schemes that they investigated are different

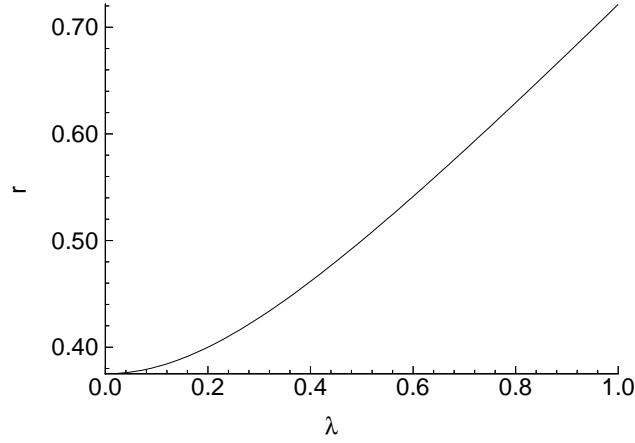


Figure A.3. Diffusion versus Courant Relationship for the Convection-diffusion Equation Using the MacCormack 2-4 method.

from those proposed by Gottlieb and Turkel. The complex nature of the amplification function is readily seen in both figures. Because of this complex behavior, the equation form could not be used to relax the cell Reynolds number limit as was done by Hirt.

The practical application of Equation A.19 is to solve for the maximum allowable time step. The time-step equation takes the form

$$t = \frac{3\nu\Delta x^2}{2(4\nu^2 - \alpha^2\Delta x^2)} \quad (\text{A.20})$$

The time-step equation can be recast in terms of the cell Reynolds number to give

$$\lambda = \frac{\frac{3}{2}Rey_{cell}}{(4 - Rey_{cell}^2)} \quad (\text{A.21})$$

Equation A.21 shows that the maximum allowable cell Reynolds number that gives a stable solution is controlled by the Courant number. Expressing the cell Reynolds number in terms of the Courant number give

$$Rey_{cell} = \frac{-3 + \sqrt{9 + 64\lambda^2}}{4\lambda} \quad (\text{A.22})$$

It can be shown easily that the cell Reynolds number has an upper limit of $Rey_{cell} = \frac{3(-3 + \frac{\sqrt{337}}{3})}{8}$, (≈ 1.17) at a Courant number of $\frac{2}{3}$. This is an even more severe limit than the

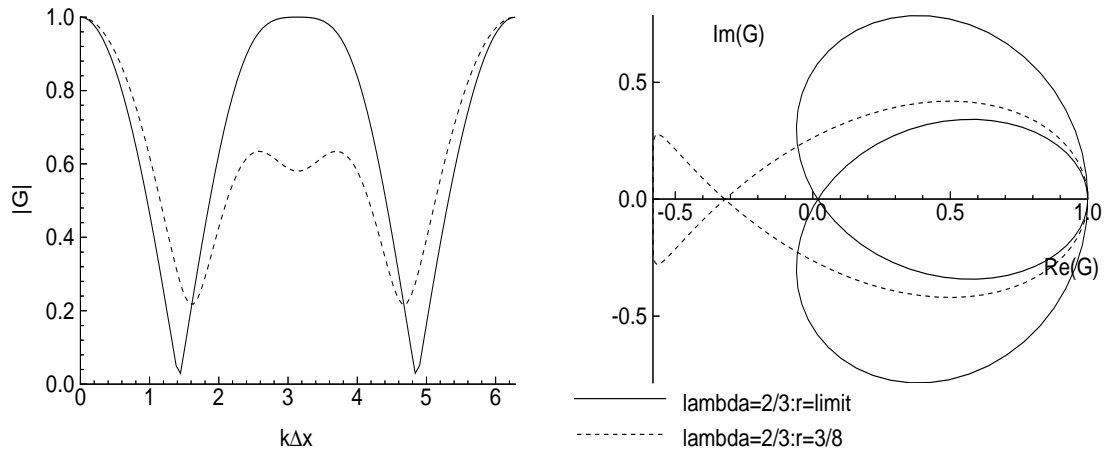


Figure A.4. Convection-Diffusion Amplification Factor for $\lambda = \frac{2}{3}$, $r = \text{max}$ and $r = \frac{3}{8}$.

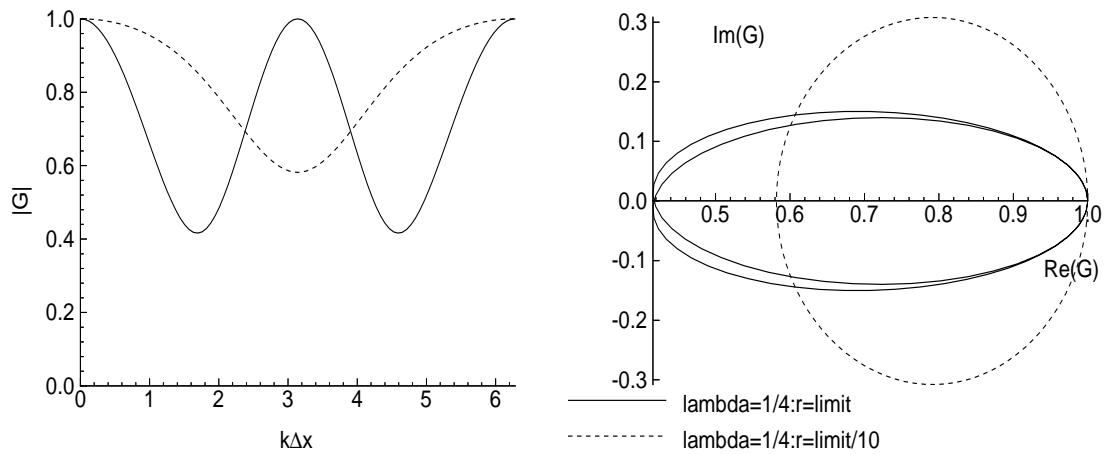


Figure A.5. Convection-Diffusion Amplification Factor for $\lambda = \frac{1}{4}$, $r = \text{max}$ and $r = \frac{\text{max}}{10}$.

apparent limit of $Re_{y_{cell}} \leq 2$ that appears in Equation A.21. The practical consequence of this severe cell Reynolds limit is that, for viscous flows, this method is only useful at very low Reynolds numbers.

REFERENCES

- [1] BAILEY, D. H., BARSZCZ, E., DAGUM, L., AND SIMON, H. D. NAS parallel benchmark results 10-94. Tech. Rep. NAS TR NAS-94-001, National Aeronautics and Space Administration, Oct. 1994.
- [2] BARRE, S., QUINE, C., AND DUSSAUGE, J. P. Compressibility effects on the structure of supersonic mixing layers: experimental results. *Journal of Fluid Mechanics* 259 (1994), 47–78.
- [3] BAYLISS, A., MAESTRELLO, L., PARIKH, P., AND TURKEL, E. Numerical simulation of boundary-layer excitation by surface heating/cooling. *AIAA Journal* 24, 7 (July 1986), 1095–1101.
- [4] BELL, J. H., AND MEHTA, R. D. Effects of imposed spanwise perturbations on plane mixing-layer structure. *Journal of Fluid Mechanics* 257 (1993), 33–63.
- [5] BLUMEN, W., DRAZIN, P. G., AND BILLINGS, D. F. Shear layer instability of an inviscid compressible fluid: Part 2. *Journal of Fluid Mechanics* 71 (1975), 305–316.
- [6] BOGDANOFF, D. W. Compressibility effects in turbulent shear layers. *AIAA Journal* 21, 6 (1983), 926–927.
- [7] BROWN, G. L., AND ROSHKO, A. On density effects and large structure in turbulent mixing layers. *Journal of Fluid Mechanics* 64 (1974), 775–816.
- [8] CHIEN, K.-Y., FERGUSON, R., KUHL, A. L., GLAZ, H. M., AND COLELLA, P. Inviscid simulations of turbulent shear layers - fluctuating flow profiles. In *Seventh Symposium on Turbulent Shear Flows* (Aug. 1989), p. 4.3.1 to 4.3.5.
- [9] CHYCZEWSKI JR., T. S. *A time-dependant, three-dimensional numerical study of supersonic rectangular jet flow and noise using the full navier stokes equations*. PhD thesis, The Pennsylvania State University, 1996.
- [10] CLEMENS, N. T., AND MUNGAL, M. G. Two- and three-dimensional effects in the supersonic mixing layer. *AIAA Journal* 30, 4 (1992), 973–981.

- [11] CLEMENS, N. T., AND MUNGAL, M. G. Large-scale structure and entrainment in the supersonic mixing layer. *Journal of Fluid Mechanics* 284 (1995), 171–216.
- [12] ELLIOTT, G. S., AND SAMIMY, M. Compressibility effects in free shear layers. *Physics of Fluids A* 2, 7 (1990), 1231–1240.
- [13] FAROUK, B., ORAN, E. S., AND KAILASANATH, K. Numerical simulation of the structure of supersonic shear layers. *Physics of Fluids A* 3, 11 (1991), 2786–2798.
- [14] FERZIGER, J. H. Estimation and reduction of numerical error. In *Quantification of Uncertainty in Computational Fluid Dynamics*, vol. FED-148. ASME, 1993, pp. 1–7.
- [15] FROMM, J. The time dependent flow of an incompressible viscous fluid. In *Methods in Computational Physics*, vol. 3. Academic Press, New York, 1964, pp. 345–382.
- [16] GOEBEL, S. G., AND DUTTON, J. C. Experimental study of compressible turbulent mixing layers. *AIAA Journal* 29, 4 (1991), 538–546.
- [17] GOTTLIEB, D. Strang-type difference schemes for multidimensional problems. *SIAM Journal of Numerical Analysis* 9, 4 (Dec. 1972), 650–661.
- [18] GOTTLIEB, D., AND TURKEL, E. Dissipative two-four methods for time-dependent problems. *Mathematics of Computation* 30, 136 (Oct. 1976), 703–723.
- [19] GREENOUGH, J. A., RILEY, J. J., SOETRISNO, M., AND EBERHARDT, D. S. The effects of walls on a compressible mixing layer. Tech. Rep. AIAA 89-0372, American Institute of Aeronautics and Astronautics, Jan. 1989.
- [20] GROPENGIESSER, H. Study on the stability of boundary layers and compressible fluids. Tech. Rep. NASA TT F-12, National Aeronautics and Space Administration, Technical Translations, 1970.
- [21] GROSCH, C. E., AND JACKSON, T. L. Inviscid spatial stability of a three-dimensional compressible mixing layer. *Journal of Fluid Mechanics* 231 (1991), 35–50.
- [22] GUIRGUIS, R. H., GRINSTIEN, F. F., YOUNG, T., ORAN, E. S., KAILASANATH, K., AND BORIS, J. Mixing enhancement in supersonic shear layers. Tech. Rep. AIAA 87-0373, American Institute of Aeronautics and Astronautics, Jan. 1987.

- [23] HACKETT, C. H. *Design and Analysis of a Low Reynolds Number Supersonic Shear Layer Facility*. Master's thesis, The Pennsylvania State University, 1989.
- [24] HAYDER, M., TURKEL, E., AND MANKABADI, R. Numerical simulation of a high mach number jet. Tech. Rep. AIAA 93-0653, American Institute of Aeronautics and Astronautics, Jan. 1993.
- [25] HIRSCH, C. *Numerical Computation of Internal and External Flows*. Wiley, New York, 1988.
- [26] HIRT, C. W. Heuristic stability theory for finite difference equations. *Journal of Computational Physics* 2 (1968), 339–355.
- [27] JACKSON, T. L., AND GROSCH, C. E. Inviscid spatial stability of a compressible mixing layer. *Journal of Fluid Mechanics* 208 (1989), 609–637.
- [28] JACKSON, T. L., AND GROSCH, C. E. Absolute/convective instabilities and the convective mach number in a compressible mixing layer. *Physics of Fluids A* 2, 6 (1990), 949–954.
- [29] KAMVISSIS, N. *Design, Calibration, and Shakedown Tests of a Low Reynolds Number Supersonic Shear Layer Facility*. Master's thesis, The Pennsylvania State University, 1992.
- [30] KENNEDY, C. A., AND CARPENTER, M. H. Several new numerical methods for compressible shear-layer simulations. *Applied Numerical Mathematics* 14 (1994), 397–433.
- [31] KINZIE, K. W. *Aeroacoustic Properties of Moderate Reynolds Number Elliptic and Rectangular Supersonic Jets*. Master's thesis, The Pennsylvania State University, 1991.
- [32] KISTLER, A. L. Fluctuation measurements in a supersonic turbulent boundary layer. *Physics of Fluids* 2, 3 (1959), 290–296.
- [33] KO, C. L., McLAUGHLIN, D. K., AND TROUTT, T. R. Supersonic hot-wire fluctuation data analysis with a conduction end-loss correction. *Journal of Physics E: Scientific Instrumentation* 11 (1978), 488–493.

- [34] LEEP, L. J., DUTTON, J. C., AND BURR, R. F. Three-dimensional simulations of compressible mixing layers: Visualizations and statistical analysis. *AIAA Journal* 31, 11 (1993), 2039–2046.
- [35] LESSEN, M., FOX, J. A., AND ZIEN, H. M. On the inviscid stability of the laminar mixing of two parallel streams of a compressible fluid. *Journal of Fluid Mechanics* 23 (1965), 355–367.
- [36] LESSEN, M., FOX, J. A., AND ZIEN, H. M. Stability of the laminar mixing of two parallel streams with respect to supersonic disturbances. *Journal of Fluid Mechanics* 25 (1966), 737–742.
- [37] LOCKARD, D., 1995. Private communication.
- [38] LOWERY, P. S., REYNOLDS, W. C., AND MANSOUR, N. N. Passive scalar entrainment and mixing in a forced, spatially developing mixing layer. Tech. Rep. AIAA 87-0132, American Institute of Aeronautics and Astronautics, Jan. 1987.
- [39] LU, P. J., AND WU, K. C. Numerical investigation on the structure of a confined supersonic mixing layer. *Physics of Fluids A* 3, 12 (1991), 3063–3079.
- [40] MANKBADI, R., HAYDER, E., AND POVINELLI, L. The structure of supersonic jet flow and its radiated sound. Tech. Rep. AIAA 93-0549, American Institute of Aeronautics and Astronautics, Jan. 1993.
- [41] MARTENS, S. *Enhancements to a Low Reynolds Number, Two-stream Supersonic Shear Layer Facility*. Master’s thesis, The Pennsylvania State University, 1992.
- [42] MARTENS, S. *An Experimental study of Compressible Mixing Layers*. PhD thesis, The Pennsylvania State University, 1995.
- [43] MARTENS, S., KINZIE, K. W., AND MCLAUGHLIN, D. K. Measurements of Kelvin-Helmholtz instabilities in a supersonic shear layer. *AIAA Journal* 32, 8 (1994), 1633–1639.

- [44] MARTENS, S., LOCKARD, D., MORRIS, P. J., AND McLAUGHLIN, D. K. An experimental and analytical investigation of the large scale instabilities in a supersonic shear layer. In *Tenth Symposium on Turbulent Shear Flows* (Aug. 1995).
- [45] MARTENS, S., AND McLAUGHLIN, D. Mixing enhancement using mach wave interaction in a confined supersonic shear layer. Tech. Rep. AIAA-95-2177, American Institute of Aeronautics and Astronautics, June 1995.
- [46] McLAUGHLIN, D. K., MARTENS, S., AND KINZIE, K. W. An experimental investigation of large scale instabilities in a low Reynolds number two-stream supersonic shear layer. Tech. Rep. AIAA 92-0177, American Institute of Aeronautics and Astronautics, Jan. 1992.
- [47] MOIN, P. Towards large eddy and direct simulation of complex turbulent flows. In *Computer Methods in Applied Mechanics and Engineering* (June 1991), vol. 87 2-3, pp. 329–334.
- [48] MORRIS, P. J., AND GIRIHARAN, M. G. The effect of walls on instability waves in supersonic shear layers. *Physics of Fluids A* 3, 2 (1991), 356–358.
- [49] OH, C. K., AND LOTH, E. Unstructured grid simulations of spatially evolving supersonic shear layers. *AIAA Journal* 33, 7 (1995), 1229–1238.
- [50] ORAN, E. S., AND BORIS, J. P. *Numerical Simulation of Reactive Flow*. Elsevier, New York, 1987, ch. 11.
- [51] OSTER, D., AND WYGNANSKI, I. The forced mixing layer between parallel streams. *Journal of Fluid Mechanics* 123 (1982), 91–130.
- [52] PAPAMOSCHOU, D. Structure of the compressible turbulent shear layer. Tech. Rep. AIAA-89-0126, American Institute of Aeronautics and Astronautics, Jan. 1989.
- [53] PAPAMOSCHOU, D., AND ROSHKO, A. The compressible turbulent shear layer: an experimental study. *Journal of Fluid Mechanics* 197 (1988), 453–477.

- [54] PLESNIAK, M. W., AND JOHNSTON, J. P. The effects of stabilizing and destabilizing curvature on a plane mixing layer. In *Transport Phenomena in Turbulent Flows*, M. Hirata and N. Kasagi, Eds. Hemisphere, New York, June 1988, pp. 377–390.
- [55] PRESS, W. H., FLANNERY, B. P., TEUKOLSKY, S. A., AND VETTERING, W. T. *Numerical Recipes*. Cambridge University Press, 1989, ch. 12.
- [56] QUIRK, J. J. A contribution to the great Riemann solver debate. Tech. Rep. ICASE 92-64, NASA, Nov. 1992.
- [57] RAGAB, S. A., SHEEN, S.-C., AND SREEDHAR, M. An investigation of finite-difference methods for large-eddy simulation of a mixing layer. Tech. Rep. AIAA 92-0554, American Institute of Aeronautics and Astronautics, Jan. 1992.
- [58] RAGAB, S. A., AND WU, J. L. Instabilities in the free shear layers formed by two supersonic streams. Tech. Rep. AIAA 88-0038, American Institute of Aeronautics and Astronautics, Jan. 1988.
- [59] ROGALLO, R. S., AND MOIN, P. Numerical simulation of turbulent flows. *Annual Review of Fluid Mechanics* 16 (1984), 99–137.
- [60] ROGERS, M. M., AND MOSER, R. D. Spanwise scale selection in plane mixing layers. *Journal of Fluid Mechanics* 247 (1993), 321–337.
- [61] SAMIMY, M., AND ELLIOTT, G. S. Effects of compressibility on the characteristics of free shear layers. *AIAA Journal* 28, 3 (1990), 439–445.
- [62] SAMIMY, M., REEDER, M. F., AND ELLIOTT, G. S. Compressibility effects on large structures in free shear flows. *Physics of Fluids A* 4, 6 (1992), 1251–1258.
- [63] SANDHAM, N., AND REYNOLDS, W. The compressible mixing layer: Linear theory and direct simulation. Tech. Rep. AIAA 89-0371, American Institute of Aeronautics and Astronautics, Jan. 1989.
- [64] SANDHAM, N. D., AND REYNOLDS, W. C. Some inlet plane effects on the numerically simulated spatially developing two dimensional mixing layer. In *Sixth Symposium on Turbulent Shear Flows* (Sept. 1987), pp. 22-4-1 to 22-4-6.

- [65] SANDHAM, N. D., AND REYNOLDS, W. C. Growth of oblique waves in the mixing layer at high mach number. In *Seventh Symposium on Turbulent Shear Flows* (Aug. 1989), p. 9.5.1 to 9.5.6.
- [66] SANKAR, L. N., REDDY, N. N., AND HARIHARAN, N. A comparative study of numerical schemes for aero-acoustic applications. In *Computational Aero- and Hydro-Acoustics*, vol. FED-147. ASME, 1993, pp. 35–40.
- [67] SARKAR, S. The stabilizing effect of compressibility in turbulent shear flow. *Journal of Fluid Mechanics* 282 (1995), 163–186.
- [68] SARKAR, S., AND LAKSHMANAN, B. Application of a Reynolds stress turbulence model to the compressible shear layer. *AIAA Journal* 29, 5 (1991), 743–749.
- [69] SOETRISNO, M., GREENOUGH, J. A., EBERHARDT, D. S., RILEY, J. J., AND SOETRISNO, M. An investigation of finite-difference methods for large-eddy simulation of a mixing layer. Tech. Rep. AIAA 89-1810, American Institute of Aeronautics and Astronautics, Jan. 1989.
- [70] STRANG, G. On the construction and comparison of difference schemes. *SIAM Journal of Numerical Analysis* 5, 3 (Sept. 1968), 506–517.
- [71] STRANG, W. G. Accurate partial differential methods. i: Linear cauchy problems. *Archive of Rational Mechanical Analysis* 12 (1963), 392–402.
- [72] STRANG, W. G. Accurate partial differential methods. ii: Non-linear problems. *Numerical Methods* 13 (1964), 37–46.
- [73] TAM, C. K. W., AND HU, F. Q. The instability and acoustic wave modes of supersonic mixing layers inside a rectangular channel. *Journal of Fluid Mechanics* 203 (1989), 51–61.
- [74] TAM, C. K. W., AND WEBB, J. C. Dispersion-relation-preserving finite difference schemes for computational acoustics. *Journal of Computational Physics* 107 (Aug. 1993), 262–281.

- [75] TANG, W., KOMERATH, N., AND SANKAR, L. Numerical simulation of the growth of instabilities in supersonic free shear layers. Tech. Rep. AIAA 89-0376, American Institute of Aeronautics and Astronautics, Jan. 1989.
- [76] TUNCER, I. H., AND SANKAR, L. N. Numerical simulation of 3-d supersonic free shear layers. Tech. Rep. AIAA 90-3958, American Institute of Aeronautics and Astronautics, Oct. 1990.
- [77] TURKEL, E. On the practical use of high-order methods for hyperbolic systems. *Journal of Computational Physics* 35 (1980), 319–340.
- [78] WILSON, R. V. *Numerical Simulation of Two-Dimensional Spatially Developing Mixing Layers*. Master's thesis, Old Dominion University, 1993.
- [79] WILSON, R. V., AND DEMUREN, A. O. Numerical simulation of two-dimensional spatially developing mixing layers. Tech. Rep. ICASE 94-32, NASA, May 1994.
- [80] WINANT, C. D., AND BROWAND, F. K. Vortex pairing: the mechanism of turbulent mixing layer growth at moderate Reynolds number. *Journal of Fluid Mechanics* 63 (1974), 237–255.
- [81] ZHUANG, M., DIMOTAKIS, P. E., AND KUBOTA, T. The effects of walls on a spatially growing supersonic shear layer. *Physics of Fluids A* 2, 4 (1990), 599–6004.